DISSERTATION

submitted to the

Combined Faculties of the Natural Sciences
and Mathematics

of the

Ruperto-Carola-University of Heidelberg,
Germany

for the degree of

Doctor of Natural Sciences

Put forward by

LENNART HUTH
born in Buchen (Odenwald)

Oral examination: 19th of December, 2018

A High Rate Testbeam Data Acquisition System and Characterization of High Voltage Monolithic Active Pixel Sensors

Referees:
Prof. Dr. André Schöning
Prof. Dr. Norbert Herrmann

Den vier wichtigsten Menschen in meinem Leben

ABSTRACT

New experiments, designed to test the Standard Model of particle physics with unprecedented precision and to search for physics beyond, push detector technologies to their limits. The *Mu3e* experiment searches for the charged lepton flavor violating decay $\mu^+ \rightarrow e^+e^-e^+$ with a branching ratio sensitivity of better than $1 \cdot 10^{-16}$. This decay is suppressed in the Standard Model to unobservable levels but can be sizable in models beyond the Standard Model. The *Mu3e* detector consists of a thin pixel spectrometer combined with scintillating detectors to measure the vertex, momentum and time of the decay particles. Requirements on rate and material budget cannot be fulfilled by classical pixel sensors and demand the development of a novel pixel technology: high-voltage monolithic active pixel sensors (HV-MAPS).

Two important steps towards a final pixel detector are discussed within the scope of this thesis: the characterization of two HV-MAPS prototypes from the MUPIX family and the development of a tracking telescope based on HV-MAPS with online monitoring, tracking and efficiency calculation for particle rates above 10 MHz.

Using the telescope it is shown that the transition from the small-scale MUPIX7 to the full-scale MUPIX8 has been successful. Sensor characterization studies of the MUPIX8 show efficiencies above 99 % at noise rates below 0.4 Hz/pixel over a large threshold range as well as a time resolution of 6.5 ns after time-walk corrections, thus fulfilling all *Mu3e* sensor requirements.

Additionally, the radiation tolerance of the MUPIX7 has been demonstrated up to a fluence of $1.5 \cdot 10^{15}$ 24 GeV p/cm^2.

ZUSAMMENFASSUNG

Neue Experimente, welche die Standardmodellvorhersagen mit beispielloser Präzision testen und nach Physik jenseits dieses Models suchen, reizen die Grenzen von Detektortechnologien ständig aus. Das *Mu3e*Experiment sucht den geladenen leptonfamilienzahlverletzenden Zerfall $\mu^+ \rightarrow e^+e^-e^+$ mit einer Verweigungsverhältnis Sensitivtät kleiner als $1 \cdot 10^{-16}$. Dieser Zerfall wird im Standardmodell auf nicht beobachtbare Werte unterdrückt, kann aber in Modellen jenseits des Standardmodells nachweisbar werden. Der *Mu3e* Detektor besteht aus einem dünnen Pixelspektrometer in Kombination mit szintillierenden Detektoren um den Zerfallpunkt, Impuls und die Zeit der Zerfallsteilchen zu vermessen. Die Anforderungen an Rate und Materialbudget können von klassischen Pixelsensoren nicht erüllt werden und erfordern die Entwicklung einer neuen Pixeltechnologie: Hochspannungsbetriebene aktive Pixelsensoren (HV-MAPS).
Zwei wichtige Schritte zu einem endgültigen Detektor werden im Rahmen dieser Arbeit diskutiert: Die Charakterisierung von zwei Sensor Prototypen aus der MuPix Familie und die Entwicklung eines Teleskops zur Rekonstruktion von Teilchenspuren auf Basis von HV-MAPS mit online-Überwachung, Spurrekonstruktion, Effizienzbestimmung, welches Teilchenraten von über 10 MHz verarbeiten kann.
Mit dem Teleskop wird gezeigt, dass der Übergang von kleinen zu großen Prototypen erfolgreich war. Die Sensoren zeigen eine Effizienz von über 99 % bei einer Rauschrate von unter 0.4 Hz/Pixel über einen großen Schwellenbereich, sowie eine Zeitauflösung von 6.5 ns nach einer *time-walk* Korrektur, womit alle *Mu3e* Anforderungen erfüllt werden.
Zusätzlich wurde die Strahlenhärte des MuPix7 bis zu einer Fluenz von $1.5 \cdot 10^{15}$ 24 GeV p/cm^2 demonstriert.

CONTENTS

OUTLINE OF THESIS

The thesis discusses particle tracking telescopes as a tool for integration and characterization studies of high-voltage monolithic active pixel sensors (HV-MAPS), which are developed for the *Mu3e* experiment. HV-MAPS are also under consideration for many other experiments, as they can be thinned down to 50 µm, are highly integrated and capable of high particle rates. Additionally, the thin active depletion region makes HV-MAPS naturally radiation tolerant and therefore interesting for HL-LHC detector upgrades.

In the introduction, a theoretical motivation for the Mu3e Experiment as a window to new physics is given (chapters 1 and 2). Subsequently, interactions of charged particles with matter are discussed (chapter 3), followed by a detailed introduction into pixel sensors. The two MUPIX prototypes characterized in this thesis are introduced next in chapter 4. Particle track reconstruction, the principle of device under test studies and a simulation based comparison between different track models, a straight line and a general broken line fit, conclude the introductory part (chapter 5).

The second part of the thesis introduces two particle tracking telescopes: the new MUPIX TELESCOPE, which was developed in the scope of this thesis to characterize and integrate HV-MAPS prototypes and the EUDET-type high resolution telescopes. The readout architecture, DAQ concept, monitoring and online efficiency calculation and a study of the systems limitations of the MUPIX TELESCOPE are presented in chapter 6. The concept, performance and resolution of the EUDET-type telescopes is discussed and the analysis concept for the sub-pixel studies is validated and the material budget estimates for the device under test are compared to measurements (chapter 7).

The third part of the thesis is focusing on the characterization of two HV-MAPS prototypes in laboratory and testbeam measurements. Testbeam facilities used to obtain the presented results are introduced at the beginning (chapter 8). Results from efficiency, noise, crosstalk and time resolution studies of the MUPIX7 are summarized in chapter 9. Detailed studies of the MUPIX8 are presented in chapter 10, including sub-pixel studies. The results from a published irradiation campaign are discussed in chapter 11 to conclude on the sensor studies. Lastly, a summary of the thesis and an outlook on further developments of HV-MAPS and the MUPIX TELESCOPE is presented in chapter 12.

Complex data acquisition systems are developed in a collaborative effort, involving many people.
The MUPIX TELESCOPE has been development first for the MUPIX6 and MUPIX7, based on the readout of the MUPIX3. The author has developed the first MUPIX TELESCOPE version in the scope of a master thesis. The new MUPIX TELESCOPE has been developed in the scope of this theses based on the first MUPIX TELESCOPE, with contributions from colleagues to the sensor steering. The author has implemented online data merging and storing as well as online tracking and efficiency calculation within the telescope and designed the online monitoring, which has been implemented by a supervised student. The software implementation of the direct-memory-access, as well as the coordinate transformation and the data format have been developed in close collaboration with group members. The required hardware for the MUPIX TELESCOPE has been developed by group colleagues in Heidelberg.
The author developed the analysis framework: the implementation of the track reconstruction, matching algorithm as well as the efficiency, noise, time resolution, clustering and crosstalk analysis.
Testbeam campaigns cannot be carried out without the support of colleagues from Heidelberg and Mainz, who contributed as telescope operators during all campaigns. The telescope commissioning for both prototypes has been conducted by the author during two testbeam campaigns. The data for the online monitoring and online efficiency study has been taken in absence of the author, who carried out the analysis. The data for the MUPIX7 and MUPIX8 studies has been taken in presence of the author.
The time-walk correction implementation and study is part of a master thesis from Heidelberg, which has been supervised by the author.
The irradiation campaign results summarized in thesis are based on a publication, where the author has been the main editor, who also carried out the analysis. The data has been obtained at a PSI testbeam campaign, which has been carried out together with colleagues from Heidelberg.

Part I

INTRODUCTION

Elementary particles and their interactions are described by the Standard Model of Particle Physics with outstanding precision. Despite having predicted many discovered particles in the last years, it is known to be incomplete. Gravitation, matter-antimatter asymmetries and neutrino oscillations are for example not included in the Standard Model. Numerous models try to extend the Standard Model to include these effects.

Beyond the Standard Model theories often predict new particles with masses above the Higgs mass. These particles motivate accelerator-based experiments, which increase the collision energy to become sensitive to the mass scale of new physics. However, the mass might be beyond the reach of direct detection experiments and new physics only manifests in small deviation in Standard Model processes. An increased luminosity by enhancing beam intensities allows for a search for highly suppressed effects with specialized detectors.

Mu3e is a precision experiments searching for new physics in charged lepton flavor violating muon decays motivated by the existence of neutral current lepton flavor violation. The *Mu3e* experiment is based on state of the art high-voltage monolithic active pixel sensors to track particles, pin down their interaction/decay positions and measure their momentum.

In the first chapter, the Standard Model and its limitations are discussed, followed by an introduction to the *Mu3e* experiment. Subsequently, particles interaction with matter is introduced. The concept of particle detection with silicon sensors is discussed next, followed by an introduction of the last two MuPix prototypes. The part is concluded with an overview of particle track reconstruction concepts, a discussion of two implemented track models , device under test studies and a comparison of two track reconstruction concepts.

1 THEORETICAL BACKGROUND

For more than three thousand years people have been unveiling the secrets of nature and natural science has developed into a broad field of research: Chemistry, biology, computer science, mathematics and physics. Physics is one of the most fundamental natural sciences with several research areas. Particle physics focuses on understanding interactions between the smallest constituents in nature, elementary particles, and radiation. Today, the particle nature of matter is well established and elementary particles and their fundamental interactions are covered by a common theory developed during the 20th century that has survived numerous experimental tests: The Standard Model of particle physics.

1.1 THE STANDARD MODEL OF PARTICLE PHYSICS

The Standard Model of particles physics (SM) is describing the elementary particles and their interactions. The SM has its roots in the sixties when the weak and electromagnetic interaction have been unified [1] and evolved during the seventies to its current form. The SM is one of the biggest success stories in modern physics, has been extensively tested and an extraordinary prediction power.
Figure 1.1 shows the particle content of the SM, grouped into quarks and leptons next to the gauge bosons. Quarks and leptons have half integer spin and are called fermions. They exist in three generations with increasing masses. Each generation consists of two quarks with an elementary charge of +2/3 and -1/3, a lepton with elementary charge -1 and the corresponding lepton neutrino, which has no elementary charge. An antiparticle exits for each fermion, with opposite quantum numbers. The first generation is stable and makes up everything visible surrounding us. The charged fermions of the other two generations are unstable and decay with varying lifetimes and over different channels into fermions of the first generation. Neutrinos are stable and massless in the Standard Model. A fermion and its anti-fermion can annihilate if they come into contact.
The three forces – electromagnetic, weak and strong – are mediated by spin 1 particles, so called (gauge) bosons. All fermions can interact weakly, via the exchange of W/Z bosons. Charged fermions can interact electromagnetically via the exchange of a photon. Quarks can interact strongly via gluons. The last missing piece is the Higgs boson, with a spin of 0, which is responsible for the spontaneous symmetry breaking of the electroweak interaction, giving rise to the masses of the W and Z. The Higgs has been discovered in 2012 at the large-hadron-collider (LHC) [4, 5] and completed the SM. Processes, which are allowed in the SM conserve certain quantum

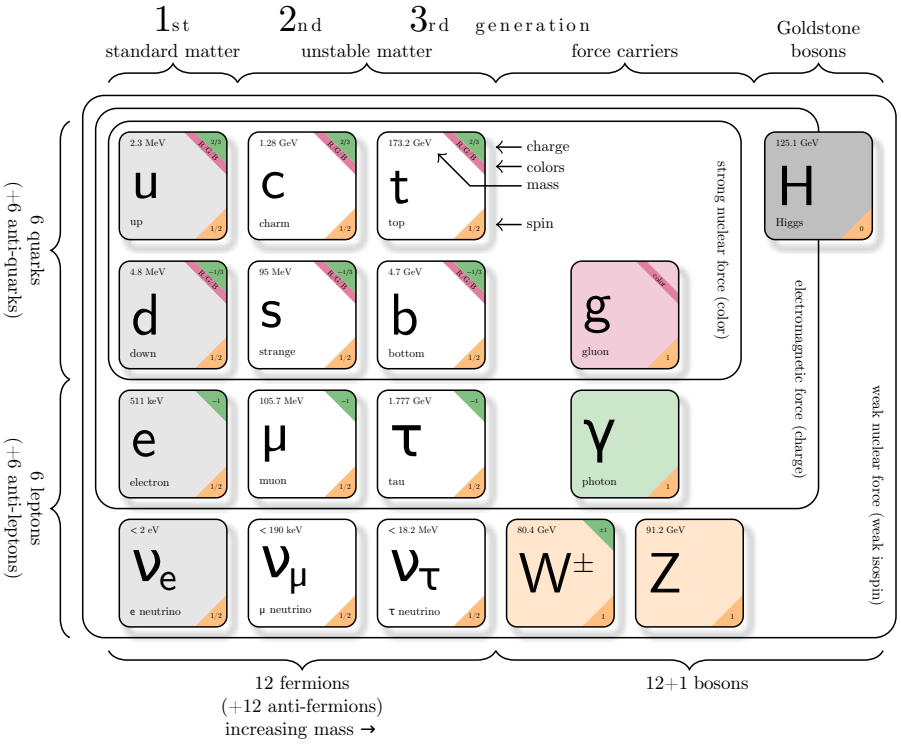

Figure 1.1: The Standard Model of Particle Physics. Taken from [2], based on [3].

numbers. The charge for example is conserved, but also the lepton flavor, lepton number and the spin.

1.2 MUON DECAYS IN THE STANDARD MODEL

Muons (and anti muons) are the charged fermions of the second generation. They are unstable, have a lifetime of 2.2 μs and decay exclusively via the weak interaction into electrons, neutrinos and photons [6]. Muons have a very limited number of possible decay channels. The Michel decay, see figure 1.2a, of an anti muon into two neutrinos and a positron

$$\mu^+ \rightarrow e^+ \nu_e \bar{\nu}_\mu, \tag{1.1}$$

is the dominant decay in the SM with a branching fraction of above 98 %. The second possible decay with a branching fraction of 1.4 % involves an additional photon $\mu \rightarrow e\gamma\nu\nu$. The involved gamma converts internally to an e^+e^- pair with a branching fraction of $3.4 \cdot 10^{-5}$ leading to the decay

$$\mu^+ \rightarrow e^+ e^+ e^- \nu_e \bar{\nu}_\mu. \tag{1.2}$$

This decay is referred to as internal conversion decay in the following.

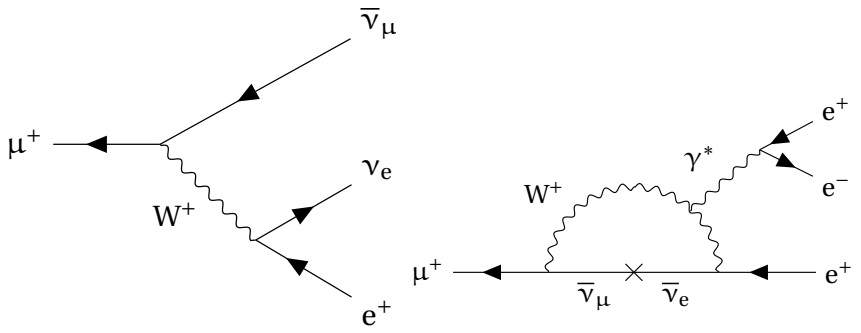

(a) Michel decay $\mu^+ \to e^+\overline{\nu}_\mu\nu_e$. (b) Loop level decay $\mu \to eee$.

Figure 1.2: Muon decays in the (extended) SM.

1.3 PHYSICS BEYOND THE STANDARD MODEL

Despite the excellent prediction power of the SM, not all observations are covered and a lot of free parameters are existing, which need to be experimentally determined.
One example is the oscillation of neutrinos between their flavor eigenstates, which has been measured by several experiments [7–9]. This is possible, if the three mass eigenstates are different, which in turn requires massive neutrinos. However, neutrinos are massless within the SM. To add neutrino oscillations, the SM needs to be extended to include massive neutrinos[1]. Including neutrino oscillation in an extended SM is still not sufficient to explain other observations.
How does gravity fit into the picture? How can we explain dark matter? Why are there three generations and not more? Why do we observe an asymmetry between matter and anti matter? All these questions give rise to novel theories going beyond the Standard Model (BSM).

1.4 PROBING THE STANDARD MODEL EXPERIMENTALLY

The open questions on the SM cannot be answered without experiments probing theoretical predictions. Two approaches are followed these days: indirect and direct searches. The latter are based on a further increase of the energy in particle beams and collisions to be able to directly probe higher and higher masses. Direct searches currently all rely on the LHC and the multi purpose detectors ATLAS, CMS (and LHCb). Data from these detectors is also used to measure properties of the SM.
In contrast to direct searches, indirect searches focus on finding small deviations from the SM predictions or search for decays, which are forbidden within the SM. Dedicated indirect searches have high mass scale reaches, as they use highly specialized detectors. However, these experiments typically only cover one process and are not as flexible as multi purpose detec-

1 Adding a heavy right-handed neutrinos for example gives rise to small masses for the left handed ones, the seesaw mechanism [10].

tors. Indirect searches like the *Mu3e* experiment are very promising portals to new physics.

1.5 CHARGED LEPTON FLAVOR VIOLATION

Charged lepton flavor is conserved in the SM at tree-level. However, on loop-level, charged lepton flavor can be violated (cLFV) by neutrino-oscillation in the extended SM, giving rise to decays like $\mu \rightarrow eee$, $\mu \rightarrow e\gamma$ or $\mu \rightarrow e$. Similar decays of $\tau \rightarrow \mu$ are also possible under the same prerequisite. Figure 1.2b shows a Feynman diagram for the loop level realization for the decay $\mu \rightarrow eee$. The branching ratio for loop diagrams is however heavily suppressed by the huge mass difference between the W^+ mass M_W and the neutrino mass difference m_{i1} [11]. The BR for the decay $\mu \rightarrow e\gamma$ is

$$BR(\mu \rightarrow e\gamma) = \frac{3\alpha}{32\pi} \left| \sum_{i=2,3} {U_{\mu i}}^* U_{ei} \frac{\Delta {m_{i1}}^2}{{M_W}^2} \right|^2 < 10^{-54}, \tag{1.3}$$

where $U_{\alpha i}$ are elements of the neutrino mixing matrix and α the fine structure constant.
The tiny branching ratio in the SM beyond any experimental reach in combination with the availability of high intensity muons beams makes muon decays attractive for precision searches. It is also natural to expect lepton flavor violation in charged currents, if it is violated in neutral currents.
The full Lagrangian for the decay $\mu \rightarrow eee$ is derived in [12]. In general, the decay can be mediated on tree or/and on loop level. To be less model dependent, it makes sense to look primarily on the new physics mass scale reach, which can be expressed with a simplified Lagrangian based on [11]. Introducing a common mass scale Λ and a parameter κ describing the ratio between loop and contact interaction contributions the mass scale reach can be plotted [13], compare figure 1.3. If new physics is manifested on loop level, the strongest limits can be set by searches for $\mu \rightarrow e\gamma$. Otherwise searches for $\mu \rightarrow eee$, which are sensitive to loop and tree level manifestations of new physics can set the strongest limits.

It is neither possible nor useful to list all existing theories which include cLFV but two examples are given. A prominent theory for cLFV on loop level are SUSY-GUTs [14], which predict enhanced branching ratio simply by smaller mass differences of the particles running in the loop, see figure 1.4a.
Four-fermion contact interactions require new bosons, which can mediate cLFV, like Little Higgs Models [15] or Z' models [16], see figure 1.4b.

As cLFV is a promising window to new physics, experiments searching for cLFV have a long history, see figure 1.5. The strongest current limits on cLFV are set by muon experiments, which are mostly hosted at the PSI in Switzerland, where the world's most intense muon beam is available. The decay $\mu \rightarrow eee$ has last been searched for in the 80s [17].

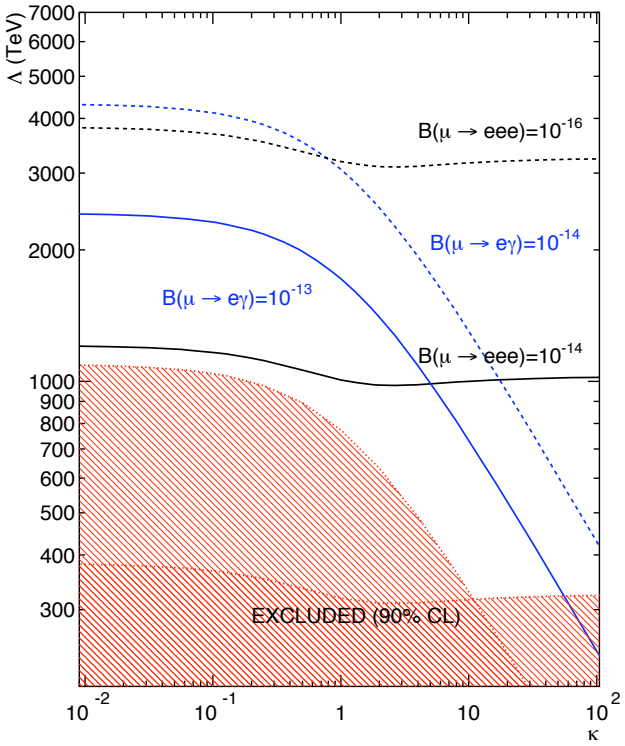

Figure 1.3: Mass scale reach Λ against κ, which describes the nature of new physics. The already excluded region is highlighted in red. The filled area is currently excluded and the lines show the expected exclusion limits by planned experiments. Taken from [11].

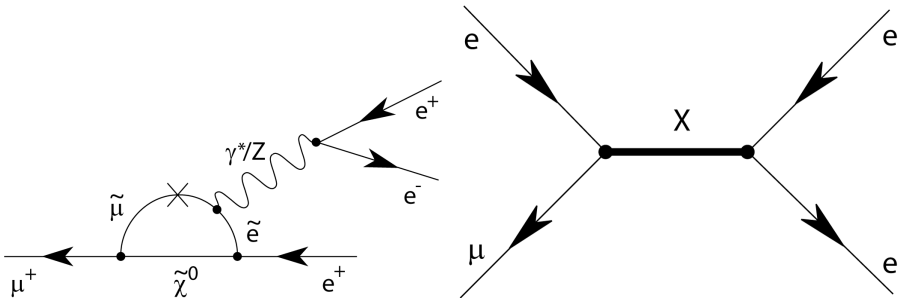

(a) SUSY loop

(b) Tree level μ → eee.

Figure 1.4: Muon decays in BSM.

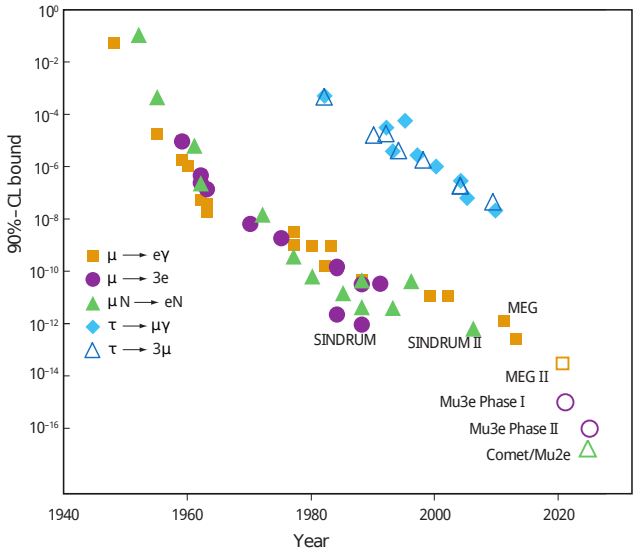

Figure 1.5: History of lepton flavor violating decays. Filled markers represent experiments, which have published data, empty markers show planned experiments. Taken from [18].

2

MU3E - MUON DECAYS AS A PORTAL FOR NEW PHYSICS

The last hunt for the decay $\mu \rightarrow eee$ by the SINDRUM collaboration in 1988 has set a limit on the branching ratio of $BR < 10^{-12}$ [17]. Although the MEG experiment has set an outstanding limit on $\mu \rightarrow e\gamma$ of $BR < 4.2 \cdot 10^{-13}$ (@90%CL) [19] putting strong constraints on $\mu \rightarrow eee$ on loop level, a new search for $\mu \rightarrow eee$ is well motivated due to additional tree level sensitivity. The technological development since then makes it possible to design an experiment with a higher sensitivity. *Mu3e* is the proposed successor and targets a branching ratio sensitivity of 1 in 10^{16} decays. Achieving this in a reasonable time necessitates a muon rate in the order of 10^9 muons/s, which cannot be be provided by any facility worldwide. However, a planned high intensity muon beam line [20] at PSI will be able to deliver the final rate. *Mu3e* is planned to be realized in two phases – phase I with highest possible muon stopping rate from an existing beamline of about $1 \cdot 10^8$ muons/s and a single event sensitivity target of 1 in 10^{15}. Phase II will increase the detector acceptance and utilize the proposed new beam line to reach the final sensitivity goal.
In the following, the signal and background characteristics, the detector concept, muon beamline, and the sub-detector systems are discussed for phase I.

2.1 SIGNAL AND BACKGROUNDS

Muons are stopped on a target and decay at rest. The two positrons and the electron from a signal decay are originating from a common vertex and are coincident in time. In addition, the total energy of the decay particles corresponds to the muon mass:

$$\sum_{i=1}^{3} E_i = m_\mu = 105.7\,\text{MeV} \tag{2.1}$$

The sum of the momenta has to vanish:

$$\sum_{i=1}^{3} \vec{p}_i = \vec{0} \tag{2.2}$$

Two important background processes exist.
The radiative muon decay with internal photon conversion into an e^+e^- pair, as introduced before. The branching fraction for this decay is $3.4 \cdot 10^{-5}$ [6][1]. All particles originating from one decay lead to a time and space coincident signal. A fraction of the energy is carried away by the two

1 measured for $p_t > 17\,\text{MeV/c}$.

neutrinos, which leave the detector without a trace, leading to missing energy. The branching fraction as function of the missing energy has been calculated in [21]. To suppress this background below $1 \cdot 10^{-16}$, a mass resolution of 0.5 MeV/c^2 is required.
The second background arises from the high muon rate: an overlay of two normal muon decays and an electron from another origin, like Bhabha scattering, photon conversion or Compton scattering, can mimic a signal decay. These backgrounds depend on stopping rate, acceptance and the material budget. In any case, they can be efficiently suppressed by excellent vertex-, time- and momentum resolution. Vertex- and momentum resolution are limited by the distance between target and tracking layers, as well as the multiple scattering in the detector layers and the target.
A background free operation during phase I requires an average momentum resolution of better than 1.0 MeV/c, without tails towards higher momenta and a time resolution of below 500 ps per reconstructed track according to detailed simulation studies [22].

2.2 DETECTOR CONCEPT

The detector concept and design is driven by the requirements to suppress background processes. The material budget has to be as low as possible to suppress multiple Coulomb scattering. Additionally, an excellent timing system is required to suppress combinatorial background. To measure charge and momentum, the detector is operated in a 1 T magnetic field. A sketch of the phase I detector is shown in figure 2.1: a muon beam is stopped on a hollow double cone target fabricated from Mylar [22]. The target is surrounded by two layers of pixels, which are used to determine the vertex position with maximal accuracy. Particles travel on a helix in the solenoid magnetic field and traverse a first timing layer made of scintillating fibres, placed as close to the two outer pixel layers as possible to minimize the impact of scattering in the fibres. Decay particles continue curling in the field and hit the outer layers again, either in the central part or in the recurl stations which are attached on both sides of the central detector. Combining the four hits in the outer layer improves the momentum resolution significantly. After recurling, the particles are absorbed in scintillating tiles below the recurl pixel layers, which will provide the final time measurement.
The complete detector is operated in a helium atmosphere. Active components of the detector are cooled by multiple gaseous helium flows. Helium is chosen as an optimal compromise between cooling power, scattering length and operational safety.
The phase II detector will add two additional recurl stations. The different components are introduced in the following. All numbers are extracted from [22], if not stated otherwise.

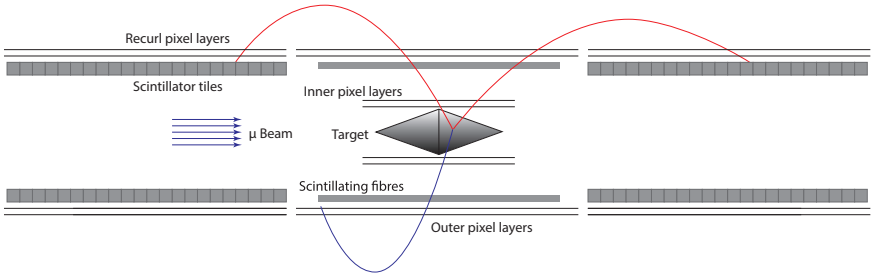

Figure 2.1: Transverse view of the *Mu3e* phase I detector with a $\mu \rightarrow eee$ decay.

2.2.1 *Target, beamline and magnet*

Creating and transporting the muons to the detector, as well as stopping them requires an advanced beam line and target concept. 590 MeV/c protons from the high intensity proton accelerator [23] hit a carbon target and create pions, which in a large fraction are created as surface pions. Surface pions are at rest on the surface of the target and decay into muons with a lifetime of 26 ns [6]. The difference between the muon and pion mass defines the muon momentum of approximately 34 MeV/c. These muons are collected by a magnet and transported to the experiment with the compact muon beam line [24].
The target has the shape of a hollow double cone and is as aforementioned made of Mylar foil with a thickness of approximately 80 µm. The shape is optimized to obtain an efficient muon stopping with minimal transverse material to precisely reconstruct the decay particles properties.

2.2.2 *Timing system*

The timing detector consists of two separate systems. A scintillating fibre detector in the central part provides a time resolution of 500 ps [25] at a moderate material budget. The recurl stations are equipped with scintillating tiles, which have a time resolution of below 100 ps [26], further suppressing combinatorial background.

2.2.3 *Pixel tracker*

The pixel tracker is responsible for vertex and momentum measurements. Due to the tight material budget limits, high-voltage monolithic active pixel sensors (HV-MAPS, see chapter 4), thinned to 50 µm are chosen. The HV-MAPS prototypes are named MUPIX and unify readout and active volume on one single chip. The detector layers consist of modules, which

in turn are fabricated from sensor ladders with 6 (18) MUPIX sensors for the inner (outer) layers. The sensors are connected via *Single-point Tape Automated Bonding* [27] with thin high density interconnection flex print. Traces for power and signal connections are fabricated from aluminum.
The layers are arranged in double pixel layers. The central detector consists of two double layers, the recurl station of one double layer. The radial positioning is optimized for tracking of low momentum electrons with a momentum below 53 MeV/c (half the muon mass). The inner layers are located as close to the target as possible to reduce extrapolation uncertainties. The radius of the outer layers is chosen such, that a majority of the particles is performing a half circle before being detected again, thus reducing the influence of multiple scattering, which can be neglected to first order after half a turn [13].

2.3 READOUT CONCEPT

Mu3e will run without a hardware trigger, as the life times of the muons and pions smear out the beam structure and create a quasi continuous beam. Having no trigger requires a streaming data acquisition and the reconstruction of all events online to select interesting events. Data from the three detector subsystems is merged on FPGA boards and short time slices of the full detector are sent to a filter farm with powerful GPUs, where a fast tracking and vertexing algorithm is implemented to select events of interest. Selected events are sent to storage and are available for offline analysis. The filter farm reduces the incoming data from roughly 100 Gbit/s [22] to 50 – 100 MB/s, corresponding to a compression factor of 142 [28].

3

PARTICLE DETECTION

Revealing the nature of particles by measuring their properties is essential to compare theoretical predictions with reality. Particle detectors are used to tag the presence of a particle and measure certain properties. Measuring a particle requires an interaction of the particle with the detector material, which creates a detectable signal. However, interactions change the particles momenta and energy. If more interactions take place, the detectable signal increases. Particle detection is therefore always a trade between disturbing the measured particle and ensuring high detection efficiencies. Detectors can be divided in several groups: Energy measurements via e.g. Calorimeters, determine the energy of a particle by absorbing the total kinetic energy and stopping the particle in sensitive material. Timing detectors are used to precisely measure event times, like scintillators combined with silicon photomultipliers. Measuring a charged particles momentum in presence of a magnetic field is done by position sensitive devices, like pixel sensors. They also allow to extrapolate the particles trajectory to its origin. Modern detectors often combine several functionalities in one device.
The different interactions of particles with matter, as well as effects due to high particle fluences over long time, radiation damage, are discussed in the following. Subsequently, pixel sensors are introduced, focusing on monolithic active pixel sensors. The chapter concludes with an introduction to crosstalk and charge sharing induced clusters in monolithic pixel sensors.

3.1 PARTICLE INTERACTION WITH MATTER

A particle traversing matter will interact with it. As discussed in section 1.1 different particles can interact in different ways. Weak interactions are not discussed, as electromagnetic and strong interactions dominate. All charged particles can interact electromagnetically, only hadrons (particles consisting of quarks, tied together by the strong force) can interact via the strong interaction. However, the strong interaction has a short range and is therefore suppressed. Electromagnetic interactions are, due to the larger interaction range, dominant for charged particles, which are measured in tracking systems. The absence of a net charge makes neutrons hard to detect and explains their long mean free path length in matter. Both interactions lead to two effects: the particles loose energy, which is deposited in the material and are deflected. The former is essential to detect particles and discussed first, the latter an unwanted, but unavoidable, side effect discussed later.

A very compact summary of particle interaction, on which this section is based, can be found in [6].

3.1.1 *Energy deposition*

Particles can deposit energy in matter by ionization of atoms, excitation of atoms, Bremsstrahlung, Cherenkov- and transition radiation. The latter two are not relevant for tracking systems. Bremsstrahlung is only relevant for light charged particles (electrons and positrons). The relative fraction of these processes depends on the particle species, the energy and the detector material's properties.
Energy loss is a stochastic process and cannot be predicted on a particle by particle basis. The number of interactions as well as the interaction strength are fluctuating. However, average energy losses are understood to a high level of detail and discussed separately for heavy and light particles, to accurately address Bremsstrahlung.

HEAVY PARTICLES The mass stopping power (essentially a density dependent energy loss per distance) of heavy particles is summarized in figure 3.1, exemplary for positive muons on a copper target. The maximal energy transfer in a single collision for a particle with mass M is given by [6]

$$W_{max} = \frac{2m_e c^2 \beta^2 \gamma^2}{1 + 2\gamma m_e/M + (m_e/M)^2}, \tag{3.1}$$

with electron mass m_e, speed of light c, relative speed $\beta = v/c$ and the Lorentz factor $\gamma = 1/\sqrt{1-\beta^2}$. The mean energy loss of moderately relativistic particles with $0.1 < \beta\gamma < 100$ is dominated by ionizing energy losses and well described by the Bethe-Bloch formula [29]

$$-\left\langle \frac{\mathrm{d}E}{\mathrm{d}x} \right\rangle = K z^2 \frac{Z}{A} \frac{1}{\beta^2} \cdot \left[\frac{1}{2} \ln\left(\frac{2m_e c^2 \beta^2 \gamma^2 W_{max}}{I^2} \right) - \beta^2 - \frac{\delta(\beta\gamma)}{2} \right], \tag{3.2}$$

with the particles energy E, constant $K = 4\pi N_A {r_e}^2 m_e c^2$,with the classical electron radius r_e and the Avogadro number N_A. The material thickness is x, the dielectric constant ϵ_0 and the mean excitation potential $I \approx 10\mathrm{eV} \cdot Z$. $\delta(\beta\gamma)$ takes the density effect[1] into account, which suppresses the logarithmic rise for higher energies. Additional parameters a the incident particles charge z, the detector materials atomic number Z and its atomic mass A. The energy loss has a minimum at $\beta\gamma$ of approximately 3. Particles in this range are called minimum ionizing particles (MIPs).
However, the mean energy loss is heavily affected by very rare events with large single collision energy, which shift the mean to higher values. A better description for the energy loss in a detector is the most probable energy loss, which is significantly lower than the mean loss given by the Bethe-

1 Polarization of the traversing media limiting the field extension.

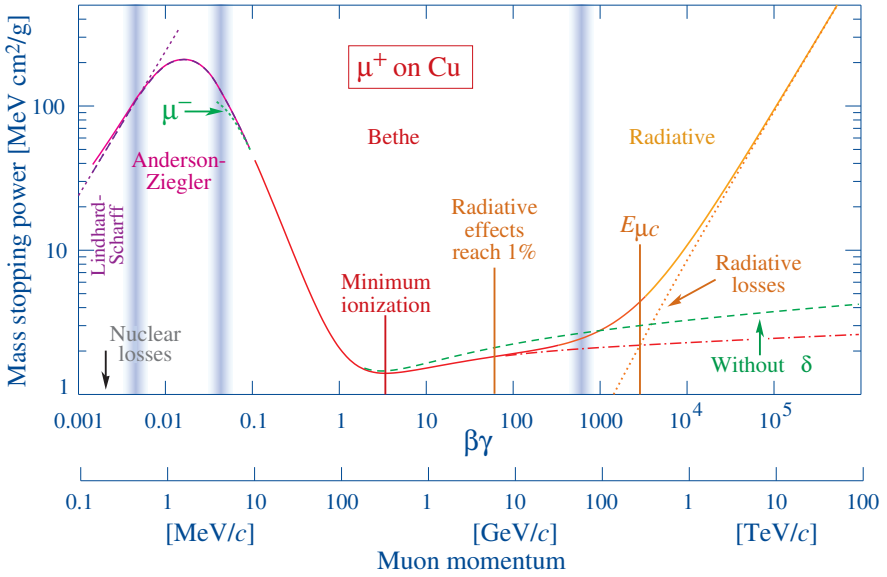

Figure 3.1: Mass stopping power for positive muons on a copper target. The energy loss is minimal in the Bethe region – particles within this momentum range are called minimum ionizing particles. Taken from [6].

Bloch equation. The discrepancy between Bethe-Bloch and the most probable loss is reduced for thicker sensors. Particle physicists usually describe the energy loss with a Landau distribution. However, a straggeling function with a mean value Δ_p/x and a full width half maximum w suits the energy loss better [30], as visualized in figure 3.2a for 500 MeV pions in silicon. The difference to the Bethe-Bloch mean energy loss for a MIP is shown in figure 3.2b. Especially for thin layers, the most probable loss is up to 40 % below the mean loss.

ELECTRONS AND POSITRONS The energy loss of electrons and positrons differs from the energy loss of heavy particles, as they have the same

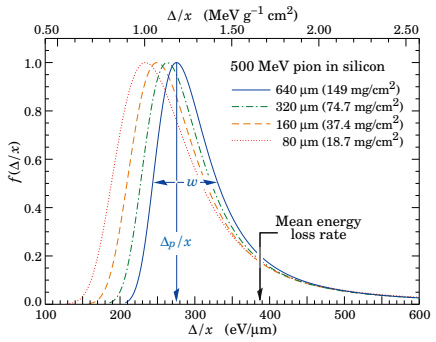

(a) Charge deposition for 500 MeV pions in silicon

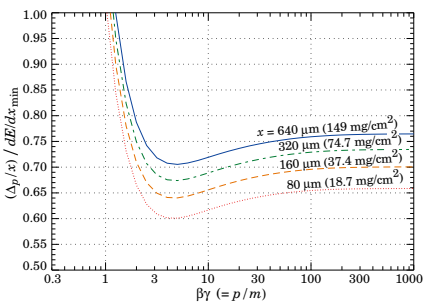

(b) Most probable energy loss scaled to mean loss of a MIP

Figure 3.2: Energy loss fluctuations in silicon. Taken from [6].

mass as the atomic electrons they free in the process of ionization. In contrast to moderately relativistic heavy particles, electrons and positrons can also significantly loose energy by bremsstrahlung. Ionization is the dominant energy loss component at low energies and bremsstrahlung becomes dominant for higher energies, see figure 3.3. Scattering with an energy transfer of more than 0.255 MeV is defined as Bhabba (positrons) and Møller (electrons) scattering in figure 3.3.
Electrons are bound to the atoms and at least the binding energy needs to be deposited to free the electrons. Additional energy transfer increases the momentum of the free electron. The atomic- and impact electron are quantum mechanically indistinguishable particles. A full energy transfer has therefore the same effect as no interaction at all (the electrons simply exchange positions). The maximal energy transfer is therefore only half the kinetic energy:

$$W_{max} = \frac{m_e c^2(\gamma - 1)}{2} \tag{3.3}$$

For electrons, the mass stopping power can be calculated from the first moment of the Møller cross section, assuming free atomic electrons [6]:

$$-\left\langle \frac{\mathrm{d}E}{\mathrm{d}x} \right\rangle = \frac{1}{2} K \frac{Z}{A} \frac{1}{\beta^2} \cdot \left[\ln \frac{m_e c^2 \beta^2 \gamma^2 \left(m_e c^2 (\gamma - 1)\right)}{2 \cdot I^2} + (1 - \beta^2) - \frac{2\gamma - 1}{\gamma^2} \ln 2 + \frac{1}{8} \left(\frac{\gamma - 1}{\gamma} \right)^2 - \delta \right], \tag{3.4}$$

The above equation is very similar to equation 3.2. Similarly, the stopping power for positrons can be calculated from the first moment of the Bhabha equation. Alternatively, the mean energy loss of electrons can be approximated by the equation from Berger and Seltzer [31]:

$$-\left\langle \frac{\mathrm{d}E}{\mathrm{d}x} \right\rangle = \rho \frac{0.153536}{\beta^2} \frac{Z}{A} \left[B_0(T) - 2 \ln \frac{I}{mc^2} - \delta \right] \tag{3.5}$$

The term $B_0(T)$ is the momentum dependent stopping power of the material, which differs between electrons and positrons due to Fermi statistics.
Electrons and positrons not only loose energy by ionization, but also by electromagnetic radiation due to deceleration by deflection in the field of a nucleus, so called bremsstrahlung. Bremsstrahlung losses for electrons/-positrons above 10 MeV are described by

$$-\frac{dE}{dx} = -\frac{E}{X_0}, \tag{3.6}$$

with the material dependent radiation length X_0. It is defined as the average distance a high energy electron or positron is traveling until its energy is reduced to $1/e$ of the initial energy. Detailed calculations of the radiation length can be found in [32, 33] and are approximated by [6]

$$X_0 = \frac{716.4}{Z(Z+1) \ln \frac{287}{\sqrt{Z}}} \frac{1}{\rho}. \tag{3.7}$$

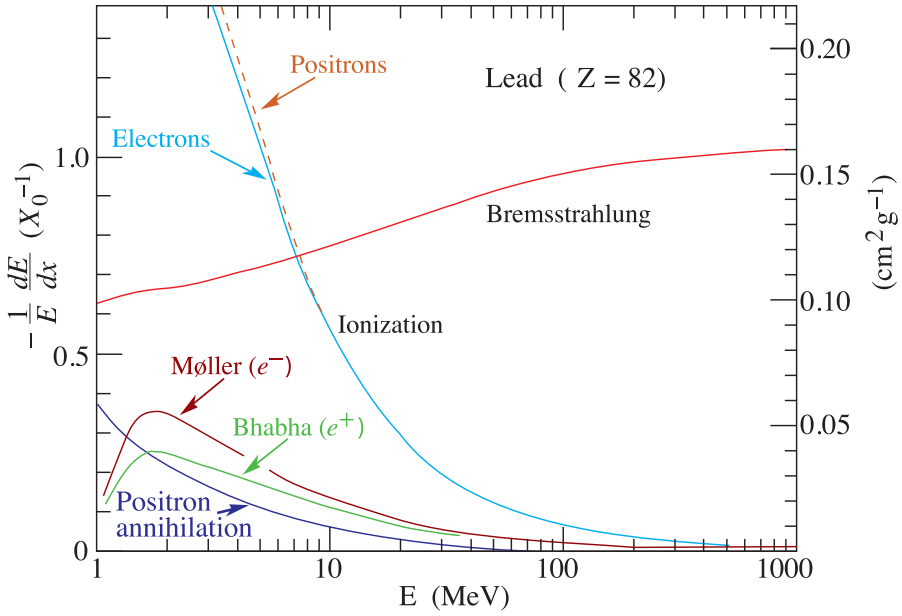

Figure 3.3: Mean energy loss of positrons/electron in lead. The dominant contributions are ionization and bremsstrahlung. Scattering is considered ionization, if the single collision energy loss is below 0.255 MeV, otherwise Bhabba and Møller. Taken from [6].

Bremsstrahlung photons convert to an electron-positron pair, which in turn looses energy - an electromagnetic shower is initialized. The created particles are detectable in the next tracking layer and can cause ambiguities in track reconstruction.

3.1.2 *Multiple Coulomb scattering*

Electromagnetic interactions lead not only to changes in the particles energy, but also in the direction of the particles. Each single interaction deflects the charged particle by a small angle, see figure 3.1.2. Coulomb scattering at the nuclei are described by the Rutherford cross section. For thin layers, the offset y_{plane} due to scattering in the material can be neglected and only the change in direction θ_{plane} is relevant.
Traversing through material leads usually to many small angle scatters creating a scattering angle distribution with a Gaussian core and tails from rare hard scatters. The projected width of the scattering angle distribution is

$$\theta_0 = \theta_{\text{plane}} = \frac{1}{\sqrt{2}}\theta_{\text{space}}. \tag{3.8}$$

The RMS of the central 98 % of the scattering distribution can be described by the Highland-formula [34]:

$$\theta_0 = \frac{13.6\,\text{MeV}}{\beta c p} z \sqrt{\frac{x}{X_0}} \left[1 + 0.038 \ln\left(\frac{x}{X_0}\right)\right] \tag{3.9}$$

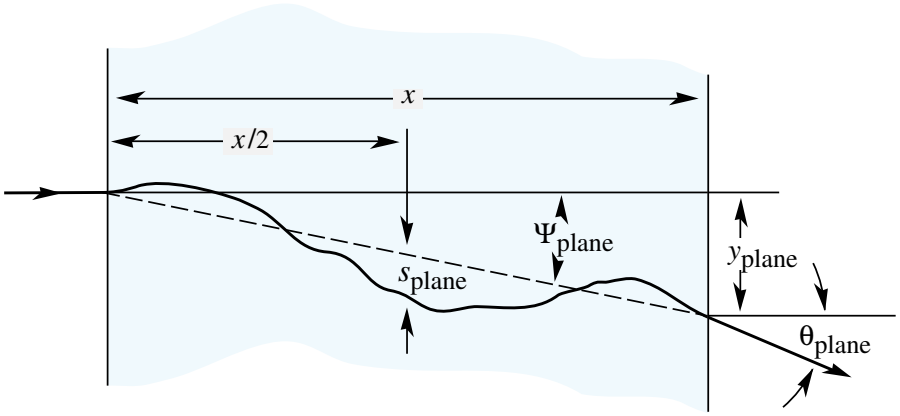

Figure 3.4: One dimensional sketch of the scattering in material with a thickness of x. The change in direction is described by θ_{plane}, the offset $y_{\text{plane}} = \sin(\theta_{\text{plane}}) \cdot x$. Taken from [6].

The variables are identical to the equation before. x/X_0 is the thickness of the material in radiation length. For stacked detector layers, the total scattering length is calculated by summing over all materials and using the total radiation length. For compounds and mixtures, the radiation length is simply given by [6]

$$1/X_0 = \sum w_j/X_j. \tag{3.10}$$

w_j and X_j are the fractional weights and radiation lengths of the elements.

3.1.3 *Radiation damage*

Energy deposition influences the structure of the traversed material. Being exposed to a large particle flux for a longer time can damage materials - so called radiation damage. Fluence, the integrated particle flux per surface, is used to quantize radiation damage. In principle, two types of damage exist: Ionizing and non-ionizing damage.

Ionizing energy loss damage: Ionizing energy loss (IEL) damages the sensor oxide surface and boundaries (Si-SiO_2) and electronics within the sensors due to ionizing the material.

Non-ionizing energy loss damage: Non-ionizing energy loss (NIEL) damage describes hard scatters in the bulk material of the sensor, which can displace atoms (vacancies) and move atoms to different intermediate lattice positions. The latter ones are usually unstable, but can build stable defects with other impurities. For convenience, the NIEL damage is usually scaled to the damage of a 1 MeV neutron flux. Particle fluences are therefore typically given in 1 MeV n_{eq}/cm^2.

IEL damage is reversible, heating the sensor will cure some damage. Contrary, NIEL damage is changing materials irreversibly. Direct collisions cre-

ate vacancies which in turn can create clusters of vacancies. Due to electromagnetic interactions, the probability to create point defects is significantly higher for charged particles compared to neutrons. Following the argumentation of the **NIEL-Hypotheses**, all bulk damage effects can be described by point and cluster defects and their occurrence probability. This allows for a energy dependent direct comparison between bulk damage from protons, neutrons and electrons. An energy dependent damage function $D(E)$ can be defined [35]:

$$D(E) = \sum_i \sigma_i(E) \int_{E_d}^{{E_R}^{max}} f_i(E, E_R)\, E_{\mathrm{dam}}(E_R)\, dE_R \tag{3.11}$$

E and E_R are the incoming particle and recoil atom energies. Index i runs over all possible cross sections σ_i and $f_i(E, E_R)$ denotes the probability to create a recoiling atom with energy E_R. $E_{\mathrm{dam}}(E_R)$ is the energy available for defect creation. For neutrons with an energy of 1 MeV $D_n(1\,\mathrm{MeV}) = 95\,\mathrm{MeVmb}$ holds. For each energy-particle combination, the damage can be scaled with the hardness factor κ to the damage of 1 MeV neutrons. κ depends on the material, energy E and particle species x [36]:

$$\kappa = \frac{\int_{E_{min}}^{E_{max}} D_x(E)\Phi(E)\,dE}{D_n(1\,\mathrm{MeV}) \int_{E_{min}}^{E_{max}} \Phi(E)\,dE} \tag{3.12}$$

$\Phi(E)$ is the particle flux. The hardness factor for 24 GeV protons (energy of the protons at the PS irradiation facility) for example is $\kappa = 0.6$ [37]. However, the hardness factor is assuming a constant volume. For sensors without a full depletion, like HV-MAPS discussed below, the hardness factor is an underestimation of the radiation damage impact, as the depletion zone thickness increases with irradiation and therefore the amount of active material irradiated.

3.2 PIXEL SENSORS

Pixel sensors are semiconductor solid state detectors, with a pixelated active area. Typical materials are silicon and germanium. All presented sensors in the scope of this thesis are based on silicon, which is therefore the focus of the following introduction. The most important silicon properties are summarized in table 3.1. To understand the working principle of a silicon pixel sensor, a short introduction to semiconductor physics is given, followed by a discussion of different pixel sensor architectures.

3.2.1 *Semiconductor physics*

Semiconductors have unique conductivity properties, arising from the small energy gap between bound electrons in the valence band and quasi-free electrons in the conduction band. Without any thermal excitation at absolute zero temperature (0 K), all electrons are bound in the valence

Property		Value
Atomic number	Z	14
Mass		28.09 U
Density	ρ	2.3 g/cm^3
Dielectric constant	ϵ	11.9
Crystal structure		Diamond
Band gap	direct	3.4 eV
	indirect	1.2 eV
Intrinsic charge density		$1.01 \cdot 10^{10}$ cm^{-3}
Specific resistivity		$2.3 \cdot 10^5\,\Omega$cm
Radiation length		9.36 cm
Mean e-h pair creation energy		3.65 eV
Electron mobility	μ_e	1450 cm^2 V/s
Hole mobility	μ_h	500 cm^2 V/s
Lifetime electron	τ_e	$> 100\,\mu$s
Lifetime hole	τ_h	$> 100\,\mu$s

Table 3.1: Summary of selected silicon properties, adopted from [38].

band. With increasing temperature, thermal excitations become possible: an electron can be lifted to the conduction band, where it can travel freely. The missing electron leaves an empty spot in the crystal structure, a so called hole. The hole attracts electrons – if an electron from adjacent bonds fills up the hole, it leaves another one behind, resulting in a charge movement in the valence band. Excited electrons can be trapped by a hole in the valence band again, the process of recombination.
The number of available free charge carriers at room temperature for silicon is about 12 orders of magnitude lower for silicon compared to ordinary conductors, where essentially every atom contributes one electron in the conduction band.

The intrinsic conductivity of semiconductors can be manipulated by so called doping, where impurities are added to the crystal structure. These implants create intermediate energy levels between valence and conduction band, easing thermal excitation. Implanting atoms with one additional valence electron (atoms with five electrons for silicon doping), allows for one more free electron to the conduction band due to thermal excitation, increasing the conductivity of the semiconductor. Atoms with additional electrons are referred to as donors and semiconductors with donors are called n-doped. Similarly using implants with one electron less (atoms with three electrons for silicon doping) leads to additional holes. These atoms are referred to as acceptors and the processed semiconductor material is called p-doped.

Bringing the surface of an n-doped and a p-doped piece of silicon in contact is creating a pn-junction, which can be used as a diode. The asymmetry in the number of free charge carriers in the conduction band in both regions induces diffusion of electrons from the n-doped region into the p-doped part. In parallel holes diffuse in the other direction. The additional electrons in the p-doped part will recombine with the large amount of available holes and vice versa. The acceptor and donor atoms, will stay at their lattice position, creating an electric field along the pn-junction. The electric field opposes the diffusion and an equilibrium between thermal diffusion and field induced drift is created. The junction region has a strong electric field and is free of mobile charge carriers. The effects at a pn-junction can be reduced or enhanced by applying an additional bias voltage across the pn-junction. Connecting the p-doped part to a positive level and the n-doped to a negative leads to a reduction of the depletion zone - the co called forward bias. If the potential barrier is vanishing, the pn-junction gets fully conductive.
Swapping the polarity is called reverse biasing: The external levels force the depletion zone to grow. The thickness w of the deletion zone in bias U_0 for acceptor (donor) concentrations $N_A(N_D)$ is calculated in [39, 40], based on [41] :

$$w = \sqrt{\frac{2\epsilon_0 \epsilon U_0}{e} \frac{N_A + N_D}{N_A \cdot N_D}} \overset{N_A \ll N_D}{\propto} \sqrt{\frac{U_0}{N_A}} \tag{3.13}$$

For industrial processed wafers, the real doping concentration is often not quoted, but the specific resistivity ρ_s

$$\rho_s = \frac{1}{\mu_h \, e \, N_A} \tag{3.14}$$

is given and the depletion zone thickness can be written as

$$w = \sqrt{2 \, U_0 \, \epsilon \, \epsilon_0 \, \mu_h \, \rho_s}. \tag{3.15}$$

The pn-junctions capacity can be interpret as a parallel plate capacitor with a capacity

$$C_{pn} \propto 1/\sqrt{U_0}. \tag{3.16}$$

A reverse biased diode can be used as active material for the detection of traversing particles.

3.2.1.1 *Charge collection in a pn-junction*

Charged particles traversing through a pn-junction create electron-hole pairs in silicon, as discussed in section 3.1, see figure 3.5. The electron-hole pairs can be split into two groups: Inside the depletion zone and outside. The latter either diffuse around and recombine or travel into the depletion zone. Inside the depletion zone, the electrons and holes are separated by the electric field and drift towards the contact points. The drifting charges create an electric field, which in turn induces charges on the collection

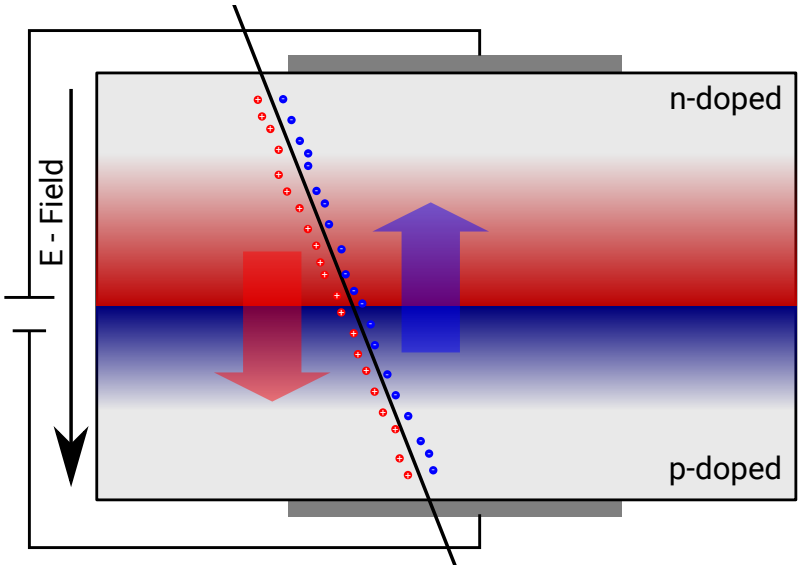

Figure 3.5: Reverse biased pn-junction with a traversing particle creating electron-hole pairs along the path.

electrodes placed on top of the n-doped part. These mirror charges are amplified and used to detect traversing particles.
The drift velocity v_d is

$$v_d = E \cdot \mu_{e/h}, \tag{3.17}$$

depending on the mobility $\mu_{e/h}$ and the field strength E. The average field in the parallel plate capacitor picture is given by

$$E = \frac{U_0}{w}. \tag{3.18}$$

For fields above $1 \cdot 10^5$ V/cm, the drift velocity saturates at roughly $3 \cdot 10^6$ cm/s [41]. For higher fields charge multiplication while drifting can occur leading to a significant increase in detectable signal as well as the risk of an easier diode breakdown. For a sensor with 20 Ωcm resistivity and a bias voltage of –80 V, the depletion zone has a thickness of approximately 15 µm, leading to an average field of $5.3 \cdot 10^4$ V/cm, which is already very close to the saturation limit. The resulting drift velocity for electrons (holes) is $3.4 \cdot 10^5$ cm/s ($1.1 \cdot 10^5$ cm/s). Assuming the drift velocity to be constant over the depletion zone, it takes $4 \cdot 10^{-10}$ s ($1.2 \cdot 10^{-9}$ s) to traverse the depletion zone for electrons (holes).
However, the field is linear rising to the contact point and decreasing afterwards. Performing an integration along the E-field profile, assuming constant mobility [39] leads to:

$$t_d = \frac{2 \cdot \epsilon}{\mu_e N_D} \cdot \ln(1 - 0.98) = \frac{2\epsilon}{\rho_s} \ln(0.01) \tag{3.19}$$

As the integration is not taking inertia into account holes and electrons would never reach the edge. Therefore the integration is stopped at 98 %

of the path. The remaining minor distance can be ignored. For the above example, the resulting time is $4 \cdot 10^{-9}$ s, with ρ_s being the resistivity. Both calculations result in fast charge collection time. However, the calculated time is always the time for the electron traversing the full depletion zone and the majority of the charge is collected faster, improving the expected average collection time. Nevertheless, this gives a rough estimate of the limit of the technology in the order of a nanosecond.

3.2.1.2 *Radiation damage effects in silicon*

Radiation damage, discussed in section 3.1.3, has several impacts on the charge collection and electrical properties of silicon.

Acceptor and donor creation Lattice defects are typically charged and can create acceptors or donors. During irradiation the effective doping concentration of the bulk material changes, changing the required voltage for a full sensor depletion and the charge collection properties. Existing acceptors/donors can be neutralized by radiation and new ones can be created. It is even possible, that the doping type is changing: n-type silicon can turn into p-type, the so called type inversion. Type inversion happens already at fluences of $1 \cdot 10^{13}\,\mathrm{n_{eq}/cm^2}$ for high substrate resistivity [38]. Acceptor like defects can capture valence electrons and contribute to negative space charge (like p-type substrates).

Excitation centers If the energy level of the defects are located between valence and conduction band, the creation of a thermal electron-hole pair is eased, which creates larger leakage currents in the sensor. Increased leakage currents increase the sensors noise levels. Additionally, the sensors temperature is increasing, which in turn increases leakage currents - a chain reaction called thermal runaway, which can be prevented by active sensor cooling.

Trapping Defects can capture electrons and holes – so called trapping. Captured charges are either static or released with a different time constant as in non-irradiated silicon. Trapping essentially reduces the free path length and therefore the available signal if the life time of the captured electrons/holes is larger than the signal shaping time. This effect only becomes important, if the free path length is reduced to the order of the depletion thickness.

Surface damage IEL damage on the sensor surface influences mainly the boundaries between Si-SiO_2. Damage in the non-conductive oxide layers is persistent, as the hole mobility is extremely low - they are quasi static. Over time, the oxide can charge up, which is influencing the behavior of the transistors, potentially even creating parasitic transistors. Modern micro structured technologies are naturally less effected, as the oxide layers

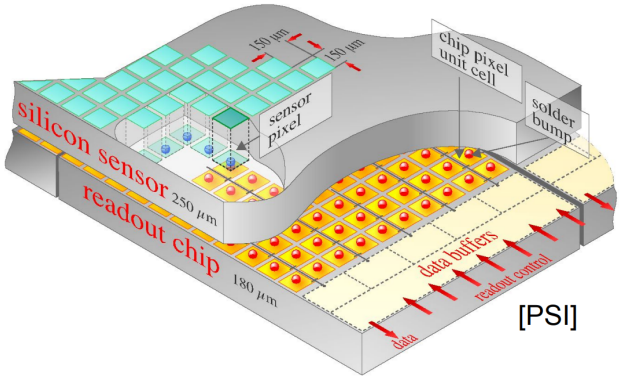

Figure 3.6: Sketch of the CMS pixel sensor as an example for a hybrid pixel technology. Taken from [42].

are only a few nanometer thin and trapped charge can tunnel out. Additionally, the critical transistors can be designed *round*, which suppresses the leakage currents significantly.

3.2.2 *Hybrid pixel sensors*

Hybrid pixel sensors consist of two silicon layers: One layer is used as active detection layer, which is connected to a readout chip via bump bonds. The active layer consists usually of an n-doped substrate with a segmented p-layer on one side. The readout chip matches the segmentation in the p-layer and each segment is connected to its individual readout cell with a bump bond. An exemplary picture of a hybrid sensor is shown in figure 3.6.

Having two silicon layers has several advantages, but also some drawbacks: Active and readout wafer can be fabricated in different processes, the readout chip can be fabricated in a smaller feature size process as the sensor. Additionally, the thick sensor allows for large depletion voltages, high signals and fast charge collection. The pixel size can be very small, if needed. Drawbacks are the large material budget due to the large amount of silicon combined with the solder bumps, which typically consist of high Z materials like indium. Fabrication is also rather complicated and expensive.

Hybrid sensors have performed excellent and been used as vertex detectors in most detector systems during the last 30 years.

3.2.3 *Monolithic active pixel sensors*

Monolithic avtive pixel sensor (MAPS) follow the concept of active pixel sensors (APS), which have been developed for imaging purposes. APS have an active cell next to a readout cell in the same material - leading to a small active sensor fraction of only 30 %. This issue is overcome by MAPS, where active readout electronics are implemented directly into the sensor, leading to almost fully active sensors. MAPS have been used for example in the

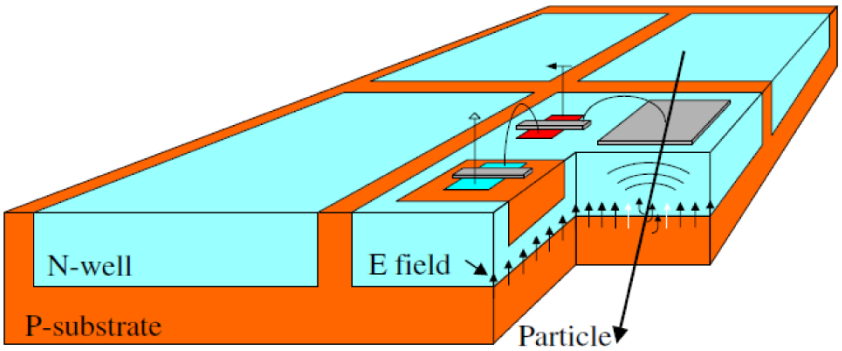

Figure 3.7: Schematic drawing of a four pixel submatrix of a HV-MAPS [44].

STAR [43] experiment at RHIC.
Production cost for MAPS are moderate, as they are fabricated in commercial CMOS processes, with high availability. MAPS have the disadvantage of being slow. For most MAPS charge is collected via diffusion instead of drift.

3.2.4 *HV-MAPS*

High-voltage monolithic active pixel sensors [44] have been proposed to overcome the charge collection time issue of MAPS, by combining the advantages of MAPS and hybrids. Figure 3.7 shows the idea behind the concept. HV-CMOS processes in which HV-MAPS are fabricated, feature the possibility of deep n-wells in a p-substrate. Segmentation into pixels is realized via a regular grid of n-wells. Active readout electronics, e.g amplifiers and line drivers are implanted in the n-well. Biasing the p-substrate creates a depletion zone in the order of $10-30\,\mu m$. The non-depleted part of the p-substrate is inactive and can be removed without reducing the sensors performance, allowing for $50\,\mu m$ thin sensors.
Digitization, readout, data serialization and LVDS links can be also implemented on the same chip, usually in a small dedicated part at one side of the sensor, the periphery.

3.3 CAPACITIVE COUPLING AND CROSSTALK

The concept of HV-MAPS includes a separation between analog and digital electronics as aforementioned. Digitization is done in the periphery of the sensor[2]. Therefore the analogue signal from each active pixel has a point to point connection line to its partner cell in the digital part. A sketch of a typical line layout is shown in figure 3.8. Line width w and d_L are typically in the order of 300 nm, the height h is $0.6-1\,\mu m$ and the metal layer distance $1\,\mu m$, based on numbers from a similar process [46].

2 Recently, a large-scale HV-MAPS prototype with in-pixel discrimination, the ATLASPIX, has been received and is performing excellent [45].

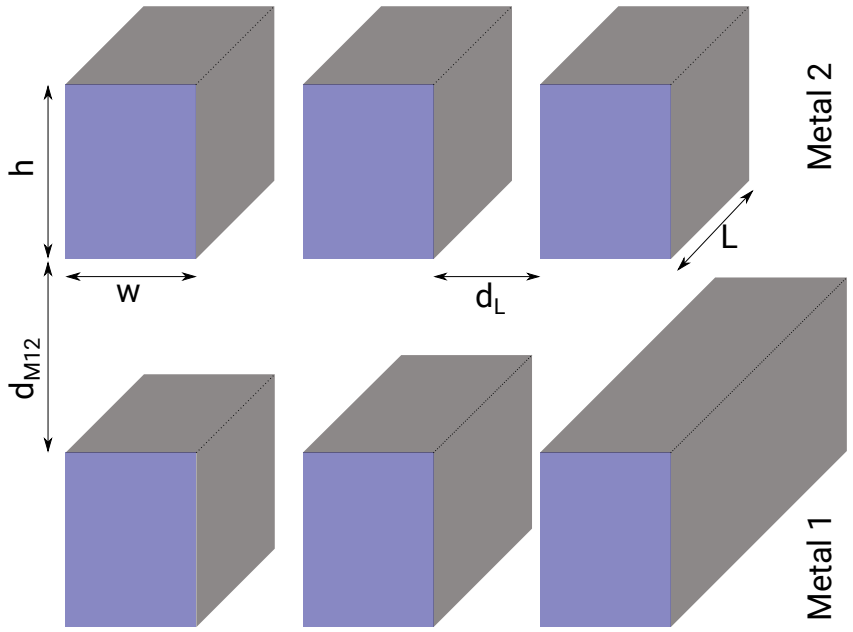

Figure 3.8: Sketch of a two metal layers transmission lines layout with the most important distances labeled.

Transmitting signal over the lines will introduces signals on the neighboring lines, so called capacitive coupling. The coupling strength is determined by the frequency of the transmitted signal as well as the capacity of the two involved lines. Thus coupling between to parallel lines can be approximated in first order by a high pass filter – high frequencies are less attenuated than lower frequencies, as the impedance of a capacitor becomes small for high frequencies. The amplitude $U_{sig}(t)$ of a typical signal pulse an be approximated by CR-RC filter [41]

$$U_{sig}(t) = U_0 \frac{\tau_2}{\tau_2 - \tau_1} \cdot \left(e^{\frac{-t}{\tau_2}} - e^{\frac{-t}{\tau_1}} \right), \tag{3.20}$$

if the time constants of the high-pass τ_1 and low-pass τ_2 fulfill $\tau_2 > \tau_1$. The induced current on the neighboring line $I_{xt}(t)$ is given by

$$I_{xt}(t) = C \frac{dU_{sig}(t)}{dt} = C_{ij} \frac{\tau_2}{\tau_2 - \tau_1} \cdot \left(\frac{-1}{\tau_2} e^{\frac{-t}{\tau_2}} + \frac{1}{\tau_1} e^{\frac{-t}{\tau_1}} \right), \tag{3.21}$$

with the interline capacity C_{ij}. The current on the neighboring line is maximal at the start of the signal pulse and switches signs at the peaking time of the signal pulse. The crosstalk signal amplitude $U_{xt}(t)$ can now be calculated as

$$U_{xt}(t) = Z \cdot I_{xt}(t) = Z C_{ij} \frac{\tau_2}{\tau_2 - \tau_1} \cdot \left(\frac{-1}{\tau_2} e^{\frac{-t}{\tau_2}} + \frac{1}{\tau_1} e^{\frac{-t}{\tau_1}} \right), \tag{3.22}$$

with the impedance $Z = i\omega C_{line} = i2\pi f C_{line}$. The impedance is frequency dependent. High frequencies induce a larger signal amplitude compared

to lower frequencies. The rise and fall times of the signals give an indication of the involved frequencies. The rise time is typically one order of magnitude shorter than the fall time. The rising edge is therefore dominating the crosstalk pulse.
The capacity between lines i and j can be described in a parallel plate capacitor picture:

$$\mathrm{C}_{ij} = \frac{\epsilon\, h\, L_{ij}}{d_{Lij}} \tag{3.23}$$

L_{ij} is the parallel length of the two lines, h the height of the lines and d_{Lij} is the distance between the lines. Typically, these capacities are in the order of 2 pF. The distance between two lines can be as small as 300 nm. The capacity between two metal layers k and l can be described by

$$\mathrm{C}_{kl} = \frac{\epsilon\, w\, d_{M_{kl}}}{d_{Lij}}, \tag{3.24}$$

with w being the width of a line, d_{Lij} the parallel length again and $d_{M_{kl}}$ the metal layers spacing. The resistance is assumed to be constant.
Capacitive coupling affects the transmission in two ways:

Line crosstalk: Large signal amplitudes will induce larger signals on the neighboring lines, which can trigger a hit in the neighboring cells. These events are referred to as (line) crosstalk in the following. This can happen on both sides, if both neighboring lines are close enough to the line with the initial signal. Smaller signal detection thresholds make crosstalk events more likely.

Signal losses: Small signals loose the same signal amplitude fraction due to capacitive coupling as large signals. However, small signals, which barely reach the threshold amplitude can get lost due to capacitive losses.

Both effects can be reduced by lowering C_{ij} and C_{kl}. The simplest way to reduce these effects is to increase the distance between lines, which is, of course, not feasible for large sensors with high channel densities. The production process defines h, d_{Mkl} and a minimal width $w_{min} \leq w$. The only remaining free design parameter is the length of parallel line, which can be reduced by optimizing the lines layout to avoid long lines being next to each other. Potential improvements are discussed in section 10.3.1.

3.4 CLUSTERING

It is not guaranteed that particles hit only one single pixel - they might traverse the sensor under a shallow angle and/or traverse through the region at the edges of pixels. These events can trigger more than one pixel per particle and lead to cluster of hits. Assuming perpendicular impacts and a regular pixel layout (quadratic pixels with common corners) the largest possible cluster spans over 4 pixels, if the particles hits exactly the corner

of a pixel. Charge diffusion is too slow and will not trigger a hit. Therefore it it ignored here. In the rare case of a very hard scatter of a traversing particle, a so called δ-electron [6] can be created, which travels a significant distance through silicon. δ-electrons can create significantly larger clusters and put severe temporary load on sensor readout.
The cluster size essentially depends on three parameters: The required charge to detect a particle, the deposited charge and the width/shape of the ionization profile. From the previous chapter it is known, that the charge deposition can be estimated with a Landau distribution. The ionization profile is approximated by a cylinder with a Gaussian intensity distribution around the true particles trajectory, based on the large fluctuations of single collision energy loss and the short mean free path of low momentum electrons in matter [47]. The charge in individual pixel cells can be calculated as

$$Q_{cell} = Q_p A \int_{x_{min}}^{x_{max}} \int_{y_{min}}^{y_{max}} e^{0.5\left(\frac{x-\mu_x}{\sigma}\right)^2} e^{0.5\left(\frac{y-\mu_y}{\sigma}\right)^2} dx\,dy, \tag{3.25}$$

with the total charge Q_p and the pixel extension along x (y) x_{min} (y_{min}) to x_{max} (y_{max}). The ionization σ_{ion} defines the Gaussian width $\sigma = \sigma_{ion}/\sqrt{2}$. Parameter A normalizes the two dimensional Gaussian to one:

$$\frac{1}{A} = \int_{-\infty}^{\infty} \int_{-\infty}^{\infty} e^{0.5\left(\frac{x-\mu_x}{\sigma}\right)^2} e^{0.5\left(\frac{y-\mu_y}{\sigma}\right)^2} dx\,dy. \tag{3.26}$$

An exemplary map, showing the locations of simulated clusters with sizes of up to four is shown in figure 3.9. In the central region of the pixel cell, only single clusters are created, while along the edges double clusters show up. In the corner, quadruple clusters are located, surrounded by small regions with triple clusters. The probability to create a cluster depends, similar to the crosstalk probabilities, on the the charge deposition and therefore the signal amplitude and on the threshold for signal detection. In addition, the cluster size is position dependent and influenced by the σ of the ionization profile.

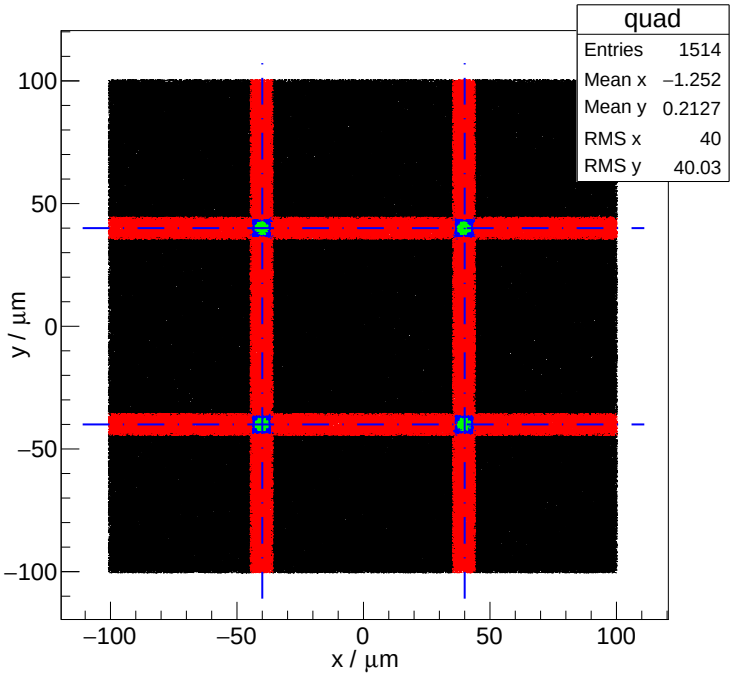

Figure 3.9: Simulated positions of cluster with different sizes: Single clusters are drawn as black dots, double cluster in red, triple cluster in blue and quadruple in green. The dashed blue lines mark the pixel edges. A detection threshold of 10 % and a charge cone σ of 3 µm are assumed.

4

HV-MAPS FOR *MU3E*

The MUPIX HV-MAPS prototype family is developed for the *Mu3e* experiment. The sensor prototypes are produced in the AMS H18 and aH18 process [48]. The main gate length is 180 nm. For signals and power distribution 6 metal layers are available. The default substrate resistivity is 20 Ωcm.
Substrate resistivities different from the default are only available for engineering runs, but not for the less expensive, shared multi-project-wafer runs. For the MUPIX8, several resistivity substrates have been used to fabricate sensors. A list of used substrate resistivities is shown in table 4.1, together with the naming scheme for the following studies.
Active electronics are implemented in deep n-wells in the p-substrate bulk. The boundary between the n-well and the p-substrate can be biased, creating an increased depletion zone, which is used as active detection volume. Digitization and readout are located in the inactive bottom part of the sensor, the periphery. The analog signals are sent to the digital partner cells on a point-to-point connection line.

4.1 MUPIX7

The MUPIX7 is the first small-scale prototype including all features required to operate it in the *Mu3e* experiment: the readout state machine is fully integrated on the ASIC alongside a high-frequency clock generator, based on a phase-locked loop (PLL) and a voltage controlled oscillator (VCO). VCO and PLL provide a phase stable clock relative to an externally applied reference clock. The data read out by the state machine is serialized and transmitted to the outer world with up to 1.6 Gbit/s. The MUPIX7 features a 32×40 pixel matrix with a pixel size of $103 \times 80\,\mu m^2$. Each pixel cell is made up by a 3×3 diode array, with the central diode housing the in-pixel electronics. There is a digital partner cell for each active cell in the digital periphery of the sensor.
The sensor is not designed to be radiation tolerant.

Name	20 Ωcm	80 Ωcm	200 Ωcm	1000 Ωcm
Resistivity range[Ωcm]	10 – 20	50 – 100	150 – 400	400 – 1500

Table 4.1: Substrate resistivities for the MUPIX8, together with the resistivity range.

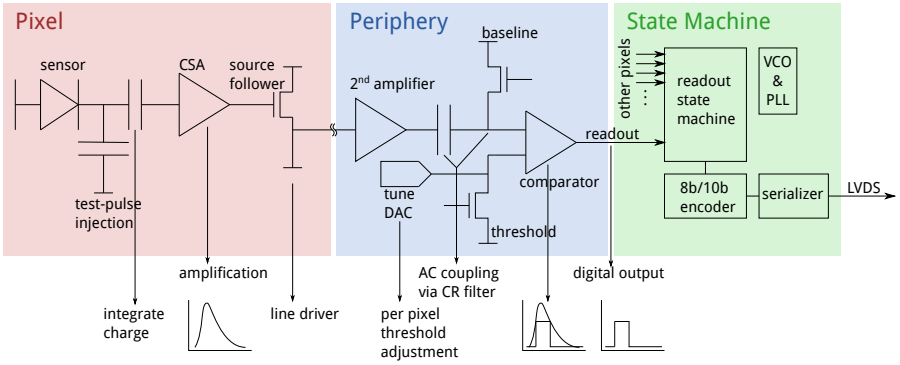

Figure 4.1: Sketch of MuPix7 readout.

4.1.1 *Readout scheme*

The MUPIX7 readout is shown in figure 4.1: charge deposited in the sensor is amplified by a charge sensitive amplifier in the pixel itself and sent to the periphery via a source follower. In the partner cell in the periphery (blue), the signal is again amplified and discriminated against a threshold, which can be finely adjusted for each pixel with a 4 bit digital-to-analog converer (DAC) value, a so called tuneDAC. Detectable signals are negative pulses relative to a baseline of typically 800 mV. An 8 bit timestamp is assigned to each hit. The digital hit information is read out by an on-chip state machine, 8 bit/10 bit encoded, serialized and sent out over an LVDS link.
The readout state machine [49] starts with copying the hit with the lowest row number of each column. While copying the hits to the readout buffers, a 24 bit counter, running at the timestamp frequency, followed by link synchronization words are sent. The hits are transmitted subsequently. After reading out up to one hit per column, the hits with the lowest row number per column are copied to the readout buffers again. This architecture does not preserve the chronology of the read out hits.
The timestamp frequency is coupled to the reference clock - it is limited to half the external clock speed, which in turn defines the serial data frequency. For the nominal data speed of 1.25 Gbit/s the timestamp frequency is limited to 62.5 MHz.

Transmission lines

As aforementioned, each analog cell is connected to its digital partner cell via a point-to-point connection line. The transmitted analog signal is amplified again in the periphery making this scheme prone to crosstalk. Events with the both line neighbors detecting a signal is called triple (line) crosstalk. All events where only one additional hit is detected are referred to as double (line) crosstalk. If such events happen with a high probability, it will significantly increase the required data bandwidth for the sensors.

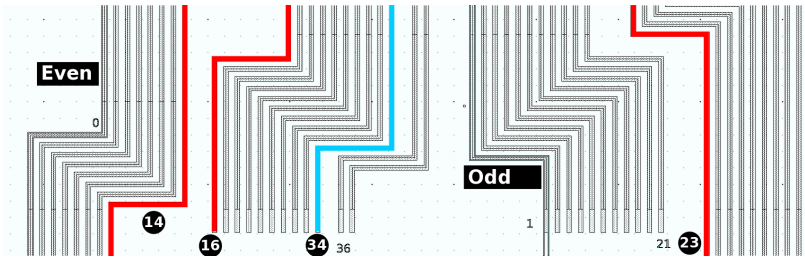

Figure 4.2: Layout of the connection lines between active and digital cell together with the line numbers. Even and odd pixel lines are separated on the chip. The lines are equidistant, excluding the highlighted ones. Taken from [50].

The total hit rate R_h with an average double (triple) crosstalk probability P_d (P_t) for a particle rate R_p is

$$R_h = (1 + P_d + 2 \cdot P_t) R_p, \tag{4.1}$$

assuming full detection efficiency. The probability for double and triple crosstalk events not only scales with the signal amplitude and the line length, but also with the applied detection threshold. The line layout is sketched in figure 4.2. The digital cells have only half the width of the active pixels, allowing for a double pixel structure per column in the digital part. All even pixels connect to the left digital column, all odd ones to the right. The line spacing is equal for all lines, excluding the highlighted ones, which have a significantly larger spacing. All lines have the same length, i.e. they are routed over the full sensor matrix.
This line structure creates a very distinct crosstalk pattern: The pixels ±2 in the same column of a hit can fire due to line crosstalk, as shown in figure 4.2.

Sensor I/0 and configuration

The MUPIX7 has a set of on-chip digital-to-analog-converter (DAC), which are responsible for the behavior of the sensors. A full DAC list can be found in Appendix C, detailed discussion of the functionality in [51]. Additionally, each pixel cell has an individual tuneDAC to adjust the discriminator threshold to correct for pixel-to-pixel variations. The configuration is done via a shift register. The bits to configure the sensor are simply clocked into the shift register. Triggering a load signal copies the values of the shift register to corresponding RAM cells for permanent storage.
Hit data is streamed on one differentially serial link.

4.2 MUPIX8

The MUPIX8 is the first large-scale HV-MAPS and the direct successor of the MUPIX7. The pixels have a size of $81 \times 80\,\mu m^2$ and are arranged in a 128×200 pixel matrix, with a total size of approximately $1 \times 2\,cm^2$. Compared to the MUPIX7, several modifications on the chip are implemented: MUPIX8 is segmented into three parts with column ranges from 0-47, 48-95 and 96-127. Each sub-matrix has its own state machine, following the same readout logic as the MUPIX7. The timestamp range is increased to 10 bit and the timestamp frequency is not directly coupled to the readout speed. The maximal timestamp frequency corresponds to the frequency of the reference clock – typically 125 MHz. The pixel has a single diode. The in-pixel amplifier has been reworked and the second amplifier in the periphery is sacrificed, creating positive pulses on top of the baseline. Additionally, a second comparator and a 6 bit timestamp are introduced, which is used to measure the time-over-threshold (ToT), see below. Both comparator thresholds are again fine adjustable with a 2(3) bit DAC respectively.
MUPIX8 features four serial differential data links, three of them can be used to stream data from the sub-matrices individually, while the fourth link is either used to duplex another link or send multiplexed data from the complete chip at a reduced readout speed. A similar design is foreseen for the final chip to match the different requirements for the inner and outer layers of the *Mu3e* pixel tracker.
Matrix A (0-47) implements the same line driver as the MUPIX7, based on a source-follower. Matrices B and C implement a current driver, which is introduced to reduce the crosstalk, as the larger sensor size increases these effects. Unfortunately, a significantly reduced timing performance of matrices B and C has been observed, which could be attributed to a flaw in the design. All following characterization studies focus on matrix A.
The readout state machine is essentially identical to the MUPIX7 state machine [52]. The sensor I/0 and configuration is also similar to the MUPIX7 and discussed in detail in [53].
The HV-MAPS concept has also attracted interest for other applications in high radiation environments, like the HL-LHC. To fulfill radiation tolerance standards, critical parts of the sensor feature a radiation hard design - all critical transistors are circular to reduce the influence of oxide damage from IEL.
The circuitry of the analog and digital cell is sketched in figure 4.3.

TIME-WALK CORRECTIONS

The two comparators combined with the two timestamps can be used in three different configurations, which are intended to be used to correct for the larger delay of smaller signals, time-walk. One threshold is used to raise a hit flag – threshold 1. The timestamps are stored in different ways:

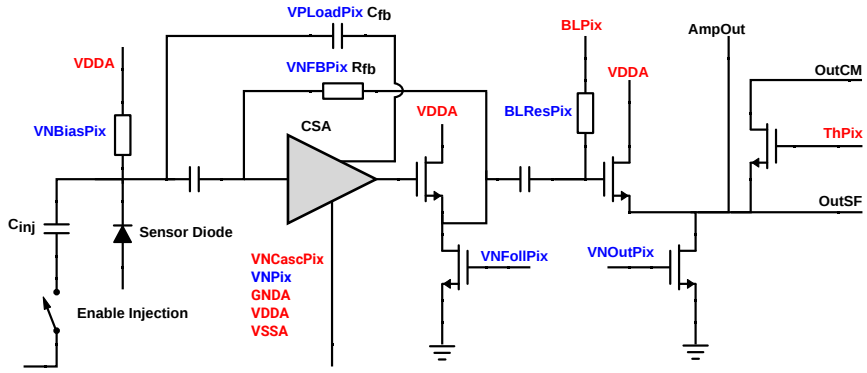

(a) Analog cell

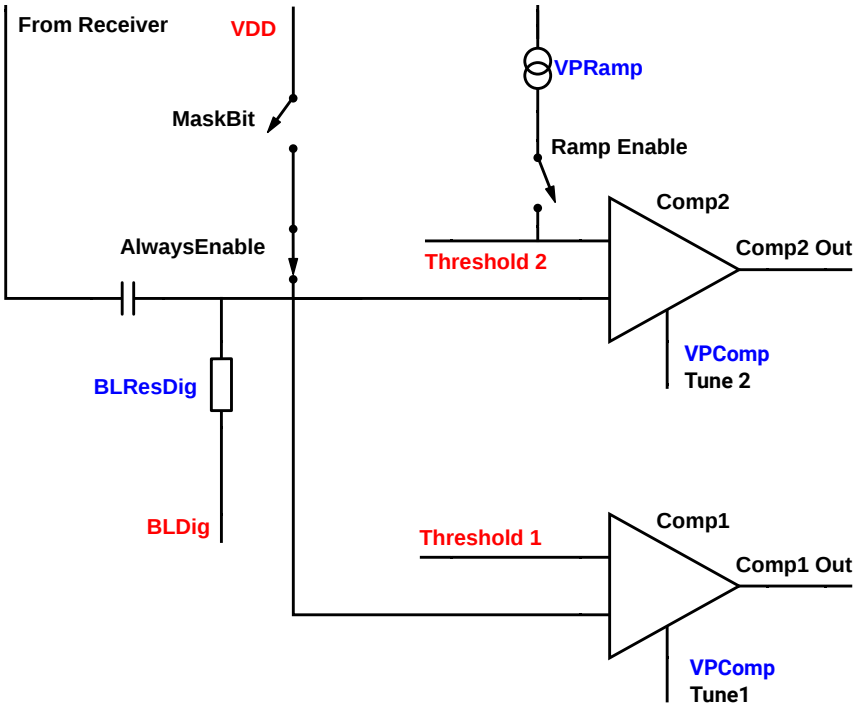

(b) Digital cell

Figure 4.3: Layout of the analog and digital cell of the MUPIX8. Adopted from [54].

ToT: The ToT method sets both thresholds to the same level. The 10 bit timestamp is sampled if the signal passes threshold 1 and the 6 bit timestamp is sampled when the signal goes below threshold 2 again. The difference between the two timestamps can be calculated offline and represents a ToT.

ToT with ramp: This method is very similar to a normal ToT: If the signal passes the threshold 1, the 10 bit timestamp is sampled and a potential starts to increase linearly in time (the steepness is selectable with a DAC). As soon as the signal falls below this rising potential, the 6 bit timestamp is stored. This approach has the advantage of creating shorter ToTs, which can be sampled with a higher frequency. In addition, the pulse and the potential cross each other under an angle, making it less prone to noise.

Two thresholds: The last method provides an online, on-chip time-walk reduction by taking threshold 1 to validate the signal, while the 10 bit timestamp is sampled by the second threshold, which can be set close to the noise level of the pixel. Time-walk is small for very small thresholds and therefore automatically reduced. The 6 bit timestamp is sampled on the falling edge of the signal after passing threshold 2 again. The two threshold method has the advantage of combining online time-walk reduction and measurement of the charge.

The design implemented in MUPIX8 has one drawback: The hit flag is always raised on the rising edge of the signal. For typical readout speeds, the hit is often read out before the falling edge passes the threshold which latches the 6 bit timestamp. In the case of an too early readout, the 6 bit timestamp is the time of readout and not correlated to the amplitude. The problem can be circumvented by a severe reduction of the readout frequency, which can not be done for the *Mu3e* experiment, nor is desired in the telescope readout. Therefore the ToT information could not be reliable used in the telescope DAQ. Characterization is carried out in laboratory and dedicated testbeam measurements [54] and summarized later.

TRANSMISSION LINES Crosstalk on the signal transmission lines is also an issue in the MUPIX8. In contrast to MUPIX7, not all lines are routed over the full matrix, but only to the corresponding row. This creates a row dependence of the coupling. Additionally the double readout column structure from the MUPIX7 is abandoned, as the digital cells are significantly larger due to the time-walk compensation circuitry. Crosstalk to one neighboring line cannot be distinguished from charge sharing between two pixel cells on an event by event basis anymore. Nevertheless capacitive coupling is going to create asymmetries between horizontal and vertical cluster sizes, which can be exploited to determine crosstalk.
Crosstalk between the two metal layers has not been observed for MUPIX8.

Capacity between the lines The line routing density is extremely high, as up 200 signal lines are required per column, an the pixel pitch is only 81 µm. 2 metal layers are reserved for these lines, which are, of course, finite in height, width and length. The maximal average line center distance is only 810 nm. Equation 3.23 can be used to calculate the capacity between two transmission lines. However, the height of the transmission lines as well as the metal layer thickness and spacing are confidential. The line width is given by 280 nm. The minimal edge-to-edge distance is 320 nm [55]. For simulation studies [56], a capacity of 2 pF is assumed for the longest lines, resulting in signal with 20 % of the primary amplitude on the neighboring line. As the capacity scales with the line length, the coupling can be expressed as function of the row number r:

$$\text{coupling}(r) = 0.2 \cdot \frac{r}{200} \tag{4.2}$$

Crosstalk will be only visible, if the induced signal is over the detection threshold. Therefore, a linear rise of the crosstalk probability is expected, starting at a certain row for the MUPIX8.

5

PARTICLE TRACK RECONSTRUCTION

In particle physics experiments tracking detectors are used to reconstruct the momentum, charge and direction of charged particles in the presence of a magnetic field. Gaseous or solid state detectors register ionizing energy deposition of traversing charged particles. Tracking information can be used for particle identification and verticies can be reconstructed by extrapolating several tracks back to a potential common position.
Combining hits from multiple tracking layers to a track give rise to a combinatorial problem, which is typically solved by applying a track model that describes the particle trajectory. A set of hits, which can be assigned to a trajectory is called track candidate. Track candidates, which pass quality checks and are kept are referred to as tracks in the following.
Fitting a trajectory requires knowledge of the measurement uncertainties. Each position measurement has an uncertainty σ_m, which is in the case of a pixel tracker for example induced by the pixel pitch $p_{x/y}$: $\sigma_m = p_{x/y}/\sqrt{12}$. Exploiting charge sharing reduces σ_m. The second unavoidable uncertainty is due to multiple Coulomb scattering. Each tracking layer will disturb the particles trajectory adding an uncertainty on the scattering angle σ_{MS}. Finally, energy losses in the layers are changing the curvature of the particle, especially for electrons/positrons which can radiate (bremsstrahlung).
Depending on the particle momentum and detector material different track fits taking the dominant uncertainties in their regime into account can be used.
In principle, track reconstruction can be split into three steps, where the first two steps can be interconnected: Hit assignments, trajectory reconstruction and track selection. The total number of track candidates n_{tc} is given by

$$n_{tc} = \prod_{i=0}^{n} n_i, \tag{5.1}$$

with n_i being the number of hits on plane i, assuming that particles leave a hit in all layers. High hit multiplicities dramatically increase the combinatorial problem asking for an improved candidate selection. Therefore seeded approaches are favored in most modern experiments. These approaches start with an initial particle trajectory, which is based on a subset of layers. The trajectory is then propagated from layer to layer and only hits which are within the uncertainty of the propagation are accepted.
For a seeded approach, the track fit is typically performed while assigning the hits. Unseeded approaches apply a track fit to all track candidates. As an agreement parameter between track candidate and fit, a χ^2 using a proper track model is used in both cases.

Multiple particle trajectory or noise hits create ambiguities, which can result in an wrong assignment and a faulty reconstruction of verticies or particle momenta. An arbitration between track candidates is required as last step. The best track candidate is selected, typically based on a χ^2 comparison, and candidates with the same hit are rejected.

In general, track reconstruction methods are either based on local or global approaches. An example for a global method is the Hough transformation [57]. Hits are transformed from a measurement space to a track parameter space. Hits, which correspond to a particle track will cluster in the parameter space. However, this fit is rather coarse, does not take scattering uncertainties into account. Variations in the magnetic field of a detector for example cannot be taken into account.
An example for a local methods are iterative and seeded methods, like the Kálman filter [58]. Starting with a track seed, the information of the tracking layers is added one after the other, without having to recompute the previous steps. This method has the drawback of requiring a seed at the beginning and that the seed search is very time consuming. The covariance matrix is only known for the position of the last added hit. Accessing the covariance matrix at any other position requires a full refit.

In the scope of this thesis, track reconstruction is used exclusively for test beam measurements, without a magnetic field. The initial particle momentum/energy is known and particles usually only have a small momentum spread easing the treatment of multiple coulomb scattering. The pixel sensors are arranged in stacked layers, called particle tracking telescopes, as shown in figure 5.1. A potential ambiguity, where a hit cannot be unambiguously assigned to a track is highlighted with the red ellipse.
Compared to standard track reconstruction algorithms, several simplifications are made in the following to ease the reconstruction of tracks in telescope, because of the low hit multiplicity. Track candidates are selected without any seed and all possible combinations are fitted. A track candidate requires a hit on every tracking plane, if a hit on one layer is missing, the track is rejected. The measurement uncertainty of a hit is as aforementioned $\sigma_{x/y} = p_{x/y}/\sqrt{12}$. As spatial uncertainty of clusters[1], single hit uncertainties are assumed, overestimating the measurement uncertainties. Clusters are assigned to only one track. In the case of an ambiguity, the track candidate with the smaller χ^2 value is selected. Energy loss of particles is usually very small and not considered in the fits.
In the following, the used coordinate systems are introduced and two track fits – a straight line and a general broken line – are discussed. Subsequently, the principle of device under test studies is explained . Results obtained by a Monte-Carlo study from the two track fits are compared at the end.

Vectors are written as $\mathbf{v}$, matrices as $\boldsymbol{M}$ and variables as v hereafter.

1 Clusters are defined as hits on a layer with touching corners/edges in the same event.

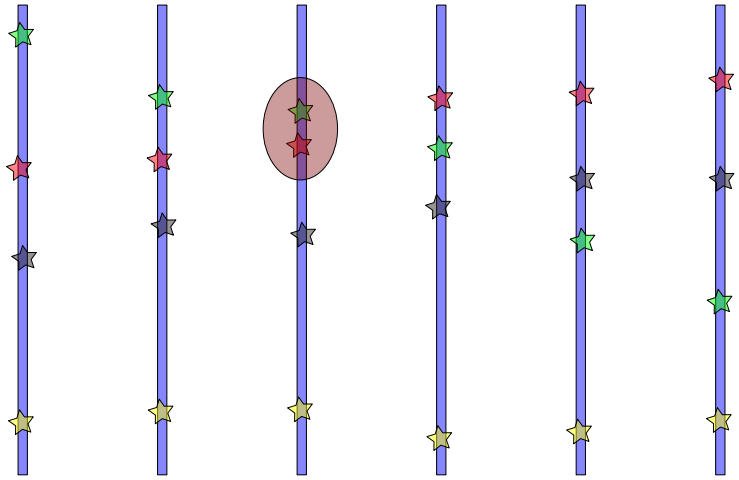

Figure 5.1: Sketch of a six layer detector with four traversing particles. The colored stars mark the hit positions on the sensor layers. The red ellipse marks two hits which could potentially be assigned to the wrong particle trajectories.

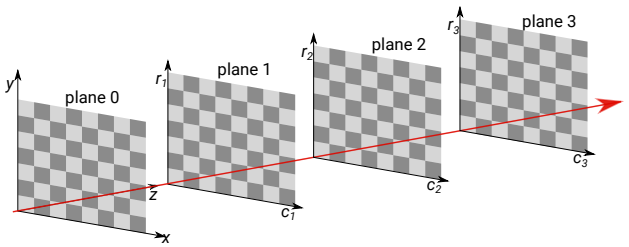

Figure 5.2: Sketch of the coordinate system. (*x,y,z*) is the global coordinate system defined by the column and row axis of plane zero. The particle beam defines z and is drawn red. The local coordinate systems (*c,r,0*) for planes are shown for the other planes. For simplicity, no rotations are shown.

5.1 GEOMETRY AND COORDINATE SYSTEMS

Combining hits to tracks requires knowledge of the plane positions relative to each other. One distinguishes between local-, essentially the sensor layers, and global coordinate system. The chosen coordinate systems are sketched in figure 5.2.

The global coordinate system is defined as a left handed coordinate system with the z-axis pointing in beam direction. The x and y axis are defined based on the first pixel sensor layer in the setup. The origin is set to the pixel center of pixel (0,0). The x axis is defined along the column direction of the pixel matrix, see figure 5.2. The y axis is defined along the row direction of the pixel sensor. Points in the global coordinate system are denoted as $\mathbf{x} = (x, y, z)^T$.
The local coordinate system is also left handed and defined for each sensor layer. The column and row axes define the xy plane again and the z

axis is the normal vector to this plane. The origin is set to the center of pixel (0,0). The local coordinates are given in units of pixels and denoted as $\mathbf{u} = (c, r, 0)^T$.

Coordinate transformation

The local coordinate systems can be shifted and rotated relative to the global coordinate system. To move from a local coordinate position $\mathbf{u}$ to the global position $\mathbf{x}$ and back, transformations are defined. The transformation is defined by the function $\mathbf{G}(\mathbf{u})$

$$\mathbf{x} = \mathbf{G}(\mathbf{u}) = \boldsymbol{Q}\,\mathbf{u} + \mathbf{t}, \tag{5.2}$$

with a shift $\mathbf{t}$ and $\boldsymbol{Q}$ being a 3x3 transformation matrix, assembled from two parts. A diagonal 3x3 matrix $\boldsymbol{P}$ to convert column and row numbers to distances on the plane. Afterwards a 3x3 rotation matrix $\boldsymbol{R}$ is applied.

$$\boldsymbol{Q} = \boldsymbol{R} \cdot \boldsymbol{P} \tag{5.3}$$

The pitch matrix $\boldsymbol{P}$ is defined as

$$\boldsymbol{P} = \begin{pmatrix} p_x & 0 & 0 \\ 0 & p_y & 0 \\ 0 & 0 & 1 \end{pmatrix}. \tag{5.4}$$

As rotation bases, the 3-2-1 Euler Angles [59] are used, which is also known as the yaw-pitch-roll ($\psi - \theta - \phi$) sequence. First, a rotation around the z-axis is performed.

$$\boldsymbol{R_z} = \begin{pmatrix} \cos\psi & \sin\psi & 0 \\ -\sin\psi & \cos\psi & 0 \\ 0 & 0 & 1 \end{pmatrix}. \tag{5.5}$$

The rotated coordinate system is then rotated around the new y-axis. The new system is finally rotated around the x-axis:

$$\boldsymbol{R} = \boldsymbol{R_x R_y R_z} \tag{5.6}$$

Finally, the coordinate origin difference is taken into account by a shift of

$$\mathbf{t} = \begin{pmatrix} \text{offset}_x \\ \text{offset}_y \\ \text{offset}_z \end{pmatrix}. \tag{5.7}$$

Converting back from global to local coordinates can be the done by calculating the inverse affine transformation function $\mathbf{G}'$

$$\mathbf{u} = \mathbf{G}'(\mathbf{x}). \tag{5.8}$$

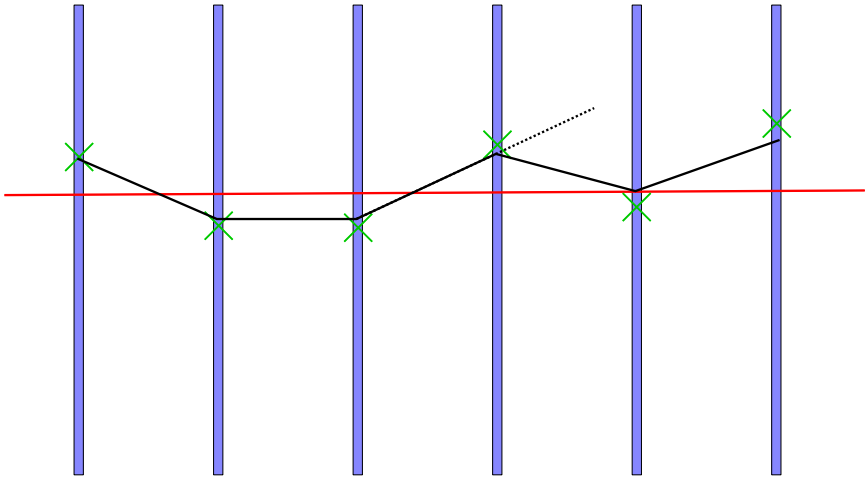

Figure 5.3: Sketch of a particles trajectory with multiple scattering through six tracking layers. The particle hits are marked as green crosses. A Straight line fit is sketched in red, while the result of a GBL is indicated in black.

The inverse transformation can be calculated as

$$\mathbf{u} = \mathbf{G}'(\mathbf{x}) = \boldsymbol{Q}^{-1}\mathbf{u} - \boldsymbol{Q}^{-1}\mathbf{t}. \tag{5.9}$$

The described transformation functions are implemented in the `Transform3D` class of the `genvector` package of `ROOT` [60]. The implementation is described in more detail in Appendix A.

5.2 TRACK MODELS

Track Models describe a particles' trajectory through a tracking system. Depending on the particles momentum, the pixel size, the number of layers, their material budget and the computational resources different track models can be used. In the case of high momentum particles and low material, multiple scattering can be ignored. The main uncertainty in this case is introduced by pixel sizes. The higher the material budget and the lower the particles momentum, the more important multiple scattering becomes and the less relevant becomes the pixel size. This relation drives the track model selection. In the following two different track models, a straight line fit ignoring multiple scattering and a general broken line fit taken multiple scattering into account are introduced and compared. Figure 5.3 shows an exemplary particles trajectory and the approximation by two different track models.

5.2.1 *Straight line fit*

A particle track without multiple Coulomb scattering in absence of a magnetic field is described by a straight line:

$$\mathbf{f}(z) = \mathbf{a} + \mathbf{s} \cdot z \tag{5.10}$$

z denotes the z-position in the global coordinate system. $\mathbf{a}$ represents an initial x/y-position in the global coordinate system at $z = 0$, while $\mathbf{s}$ describes a two dimensional slope. A χ^2 definition can be formulated as

$$\chi^2 = \sum_{i=0}^{n_{planes}} \left(\frac{(p_{x,i} - (a_x + s_x \cdot z_i))^2}{{\sigma_{i,x}}^2} + \frac{(p_{y,i} - (a_y + s_y \cdot z_i))^2}{{\sigma_{i,y}}^2} \right), \tag{5.11}$$

with i being the plane index, n_{planes} the number of reference planes, $\mathbf{p_i} = (x_i, y_i, z_i)^{\mathrm{T}}$ being the pixel centers in global coordinates. The measurement uncertainties $\sigma_{x/y,i}$ are given by $p_{x/y_i}/\sqrt{12}$. Calculating the derivatives of equation 5.11 with respect to the track parameters and setting them equal zero leads to a minimal χ^2. The set of derivatives can be rearranged in a matrix form

$$\begin{pmatrix} \sum_{i=1}^n x_i \\ \sum_{i=1}^n (x_i \cdot z_i) \\ \sum_{i=1}^n y_i \\ \sum_{i=1}^n (y_i \cdot z_i) \end{pmatrix} = \begin{pmatrix} \sum_{i=1}^n z_i & \sum_{i=1}^n 1 & 0 & 0 \\ \sum_{i=1}^n {z_i}^2 & \sum_{i=1}^n z_i & 0 & 0 \\ 0 & 0 & \sum_{i=1}^n z_i & \sum_{i=1}^n 1 \\ 0 & 0 & \sum_{i=1}^n {z_i}^2 & \sum_{i=1}^n z_i \end{pmatrix} \cdot \begin{pmatrix} s_x \\ a_x \\ s_y \\ a_y \end{pmatrix}, \tag{5.12}$$

which can be analytically solved and provides the best estimates for the track parameters. An exemplary straight line fit result is sketched in red in figure 5.3.

The main advantages of the straight line fit are firstly, that it can be calculated analytically, resulting in a non iterative and fast implementation. Secondly it is very robust against outliers and noise hits. The resulting precision of the reconstructed particles trajectory is, of course, not as precise as in track models which take multiple scattering into account.

5.2.2 *Alternative fits*

For lower momentum particles and an increased precision, multiple scattering has to be taken into account. Several methods and implementations are available. A general-broken-line fit (GBL) [61] implementation for the Mu3e experiment in the watson-framework [62] is used in the telescope framework. The GBL takes uncertainties from multiple scattering at the sensor layers as well as measurement uncertainties from finite pixels sizes into account. It is an iterative method defined as linearized corrections on a reference seed trajectory. For a telescope setup, the reference track is for example the line extracted from the straight line fit discussed above.

At each scatterer (active and inactive pixel layers) a two dimensional offset $\mathbf{u} = (u_1, u_2)$ is defined. Multiple scattering leads to kinks $\mathbf{K}$ at each plane with a variance $\mathbf{V}_k$. A χ^2-function is defined by the sum of the $\chi^2$of measurement offsets χ^2_m and kinks χ^2_k:

$$\chi^2(x) = \chi^2_m + \chi^2_k = \sum_{i=1}^{n_{meas}} \mathbf{r'}_i^T \boldsymbol{V}_{m,i}^{-1} \mathbf{r'}_i + \sum_{i=2}^{n_{scat}-1} \mathbf{k}_i^T \boldsymbol{V}_{k,i}^{-1} \mathbf{k}_i, \tag{5.13}$$

$\mathbf{r'}$ are the residuals in the curvilinear[2] system and correspond to the residuals between extrapolation and measurement in the case of perpendicular tracks in a telescope. The GBL performs small linear parameter corrections along the reference tracks to take scattering at the sensor planes into account. The small corrections are propagated along the reference track and depend for layer $\mathbf{u_i}$ only on $\mathbf{u_{i-1}}$, $\mathbf{u_{i+1}}$ and the momentum. The idea of a GBL fit is sketched in figure 5.3 as a black line.
For a detailed description of the exact mathematical formulation see [61].
Alignment of detectors can be done based on tracking information. A GBL based alignment is developed for the *Mu3e* detector [63], utilizing millepede-II. The idea behind this alignment procedure is to perform a parallel fit of all local and global parameters, based on a linear least square method. The *Mu3e* alignment software is used to align the telescope as a proof of concept.

5.3 DEVICE UNDER TEST STUDIES USING TRACKING INFORMATION

Devices under test (DUT) studies based on reference trajectories are key to characterize detector prototypes. A track is extrapolated/interpolated to position of the DUT. The extrapolated position is matched to hits on the DUT to determine the efficiency and the noise.
The extrapolation, matching and efficiency determination is discussed for the two track models.

5.3.1 *Track extrapolation*

The propagation of tracks and the extrapolation to the device under test is model dependent.

Straight track

For a straight line track, the intersection point between the fitted line and the sensor can be easily calculated, if surface deformations can be ne-

2 A curvilinear coordinate system is a Cartesian coordinate system traveling along the particles trajectory. z always points in the direction of movement.

glected. The local xy directions are determined by column and row addresses and the plane in the global coordinate system is defined as:

$$\mathbf{p}(u,v) = \mathbf{p}_0 + \mathbf{p}_{01} \cdot u + \mathbf{p}_{02} \cdot v, \tag{5.14}$$

where $\mathbf{p}_{01}$ and $\mathbf{p}_{01}$ are the span vectors of the DUT plane in global coordinates obtained from the following coordinate transformation:

$$\mathbf{p}_{01} = \left(\boldsymbol{G}\left((1,0,0)^T\right) - \boldsymbol{G}\left((0,0,0)^T\right)\right) \tag{5.15}$$

$$\mathbf{p}_{02} = \left(\boldsymbol{G}\left((0,1,0)^T\right) - \boldsymbol{G}\left((0,0,0)^T\right)\right) \tag{5.16}$$

The intersection of track and plane can be calculated by solving

$$\mathbf{a} + \mathbf{s} \cdot z = \mathbf{p}_0 + \mathbf{p}_{01} \cdot u + \mathbf{p}_{02} \cdot v \tag{5.17}$$

for z_{DUT} to determine the z-coordinate of the intersection point, which does not necessarily correspond to the DUT plane offset, if the the plane is rotated:

$$z_{DUT} = \frac{(\mathbf{p}_{01} \times \mathbf{p}_{02}) \cdot (\mathbf{a} - \mathbf{p}_0)}{-\mathbf{s} \cdot (\mathbf{p}_{01} \times \mathbf{p}_{02})} \tag{5.18}$$

The intersection $\mathbf{p}_i$ in global coordinates is then given by

$$\mathbf{p}_i = \mathbf{a} + \mathbf{s} \cdot z_{DUT} \tag{5.19}$$

Applying the coordinate transformation gives the point on the plane in local coordinates.

GBL

In the used GBL implementation a DUT is implemented as a scatterer without a measurement [62]. The track intersection point is calculated by propagating the linear corrections of the reference track to the device under test plane.

5.3.2 *Hit matching*

Extrapolated track intersections $\mathbf{p}_i$ are matched to hits $\mathbf{h}_j$ on the DUT to determine the hit detection efficiency or the spatial resolution. If the distance between an extrapolated track and a hit is smaller than a set cut value the hit is assigned to the track. Figure 5.4 visualizes the matching: A cylinder with a radius corresponding to the maximal allowed distance (radial cut, search window) is defined around the extrapolated position in global coordinates. Possible rotations of the DUT in the global coordinate system are taken into account by projecting the search radius to the local plane coordinate system. The cylinder projection on the DUT changes then from a circle to an ellipse. For tracks with more than one assignable hit, the closest one to the track is chosen. The matching algorithm goes through all

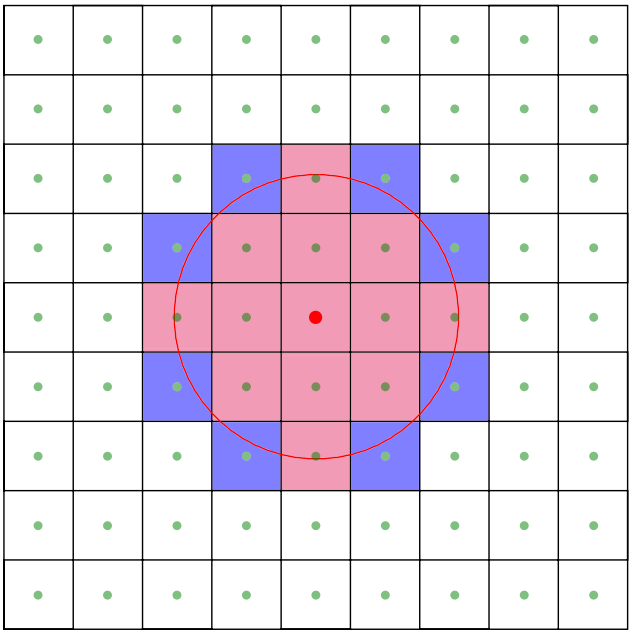

Figure 5.4: Sketch of the matching drawn in the global coordinate system. The red dot marks the intersection point and the red circle the radial search window. The light red pixel cells are matched in a first step, the white pixels excluded in the second matching step and the blue accepted in the last step.

combinations of track intersections and hits on the DUT one after another. For simplicity, the principle is described for perpendicular tracks here, the calculations for rotated DUTs is shown in Appendix A.
Pixels are described by pixel coordinates, which are defined to be the center of a pixel, but have a size. A hit can be matched to a track if the search radius and the pixel cell area overlap. Hits on the DUT are grouped into three categories. The first are hits with the pixel center in the search radius:

$$d = \sqrt{\sum_{k=0}^{1} \left(\mathbf{p}_{i\,k} - \mathbf{h}_{j\,k}\right)^2} <= r_c \tag{5.20}$$

These hits are assigned to tracks in a first step. The second category are pixel with a distance to the track intersection larger than the search radius plus half a pixel diagonal $\text{diag}_{pixel}/2$:

$$d = \sqrt{\sum_{k=0}^{1} \left(\mathbf{p}_{i\,k} - \mathbf{h}_{j\,k}\right)^2} > r_c + \frac{\text{diag}_{pixel}}{2} \tag{5.21}$$

The last category of pixel has a pixel center distance to the intersection, which is between the first to cases:

$$cut < d <= r_c + \frac{\text{diag}_{pixel}}{2} \tag{5.22}$$

For these hits the overlap of the search radius with the pixel cell has to be calculated. This is computational expensive and therefore done as last step by searching for an intersection of the search radius with one of the pixel edges. The implementation is discussed in Appendix A.
The last step becomes especially important for asymmetric pixel sizes or rotated DUTs, where a simple radius cut in the local plane is not sufficient.

5.3.3 *Efficiency calculation*

The ratio between the number of tracks which are matched with a hit k and the total number of tracks N corresponds to the sensor efficiency ϵ:

$$\epsilon = \frac{k}{N} \tag{5.23}$$

The uncertainty on the efficiency is given by binomial statistics, as the efficiency can be interpret as a positive outcome of a Bernoulli trial. Therefore the likelihood function is a binomial distribution:

$$L(\epsilon|k,N) = \binom{N}{k}\epsilon^k(1-\epsilon)^{N-k} \tag{5.24}$$

An appropriate error can by calculated in a Bayesian approach by the `TEfficiency` class from the `ROOT` library [60]: in the case of efficiency measures, the posterior probability is defined as the probability of ϵ being the correct efficiency given the measurements k, N: $P(\epsilon|k,N)$

$$P(\epsilon|k,N) \propto L(\epsilon|k,N) \times Prior(\epsilon) \tag{5.25}$$

In the provided framework, the prior is set to one [3]. The posterior is then, with $\binom{N}{k}$ dropped, as it is only used for normalization

$$P(\epsilon|k,N) \propto \epsilon^k(1-\epsilon)^{N-k}. \tag{5.26}$$

The efficiency error can now be calculated by finding the interval with the smallest Δx width over the posterior distribution fulfilling a certain confidence level ($C.L.$) requirement:

$$\frac{\int_x^{x+\Delta x}\epsilon^k(1-\epsilon)^{N-k}\,d\epsilon}{\int_0^1\epsilon^k(1-\epsilon)^{N-k}\,d\epsilon} = C.L. \tag{5.27}$$

The upper limit is now given by $x+\Delta x$ and the lower by x. The $C.L.$ is set to 0.683 ($\approx 1\sigma$ for a Gaussian) for all presented studies and the introduced errors here are referred to as binomial errors in the following.

3 In principle the prior is defined as $Prior(\epsilon) = \frac{1}{B(\alpha,\beta)}\epsilon^{\alpha-1}(1-\epsilon)^{\beta-1}$. However, in the current implementation, $\alpha = \beta = 1$ is chosen, $B(\alpha,\beta)$ is a normalization and the term can be simply dropped.

The calculated efficiency can be influenced by noise. This can induce a bias towards high efficiencies, if the noise rates are too high. For a known efficiency ϵ_k smaller than 1, the potential influence of noise on the measured efficiency ϵ_m can be defined as

$$\epsilon_m = \epsilon_k + (1-\epsilon_k)\cdot\epsilon_n, \tag{5.28}$$

with ϵ_n being the probability to match a noise hit, which is given by

$$\epsilon_n = \frac{\pi r_{cut}^2}{A_p}\overline{n_p}\cdot t_{window}. \tag{5.29}$$

$\overline{n_p}$ is the average noise rate per pixel, see below, A_p the area of a pixel and t_{window} the time window to search for matching hits.
For typical cut values of $r_{cut} = 400\,\mu\text{m}$, $t_{window} = 240\,\text{ns}$ and a pixel area $A_p = 81\text{x}80\,\mu\text{m}^2$, ϵ_n is below 1 % up to $\overline{n_p} \approx 500\,\text{Hz}$.

5.3.4 *Noise and beam related background*

Typically, not all hits on the DUT are assigned to a track, so called unmatched hits/cluster. These hits can originate from two sources: Beam related background and sensor noise. The latter is either created by leakage currents in the sensing diode or noise in the circuity. Beam related background are hits from particles, which are not reconstructed either due to geometrical mis-alignment or inefficiencies on the reference layers. The sensor noise is also an important parameter of pixel sensors, as it influences the required bandwidth to stream out the data and the multiplicities for track reconstruction.
The sensor noise can be measured without any particle source. However, the sensor noise can change during operation due to increased activity. To first order, all hits $n_{hits_{nm}}$, which are not assigned to a track can be counted as noise hits. Dividing this number by the runtime Δt and the number of pixels N_p leads to the average pixel noise rate

$$\overline{n_p} = \frac{n_{hits_{nm}}}{N_p\,\Delta t} \tag{5.30}$$

However, this is an overestimation of the noise, as three important effects are ignored: Cluster, geometrical acceptance and tracking inefficiencies.

Hit cluster and crosstalk: Traversing particles can fire more than one single pixel. Additionally crosstalk can further enhance the number of triggered pixels per particle. It is necessary to apply a clustering algorithm before calculating the noise. The charge sharing characteristics are sensor dependent and the clustering algorithm needs to be adapted to these differences. For MUPIX prototypes, all hits from a frame (essentially a time slice of 1 µs, see chapter 6), which have touching corners or edges are grouped into one single cluster. If a hit from a cluster is matched, the complete clus-

ter is excluded from the noise determination and therefore $n_{hits_{nm}}$ has to be replaced by the number of unmatched clusters $n_{cluster_{nm}}$.

Geometrical acceptance and scattered particles: Particles can scatter from outside the reference systems acceptance into the DUT plane and create a real particles' hit without a reference track. Similarly, mechanical misalignment can lead to regions on the DUT, without any reference tracks. If the reference sensors size is similar to the DUT size, this effect is even more pronounced. Both effects can be reduced by defining a region of interest (ROI) in the inner part of the pixel by e.g. excluding the outer three columns and rows from the analysis.

Inefficiencies on the reference planes: The reference sensors might not be fully efficient. Therefore, not all particles traversing the reference system can be tagged. The tracking efficiency ϵ_t is

$$\epsilon_t = \prod_{i=0}^{n_{planes}} \epsilon_i, \tag{5.31}$$

with the individual planes efficiencies ϵ_i. The tracking layers should be as efficient as possible to avoid large tracking inefficiencies. The number of missed track N_{missed} is given by

$$N_{missed} = \frac{N}{\epsilon_t} - N, \tag{5.32}$$

with the total number of reconstructed tracks N. This effect can be easily corrected by subtracting the expected number of missed tracks from the noise clusters.

A more precise noise calculation including these effects has the following form:

$$\overline{n_{p_{ROI}}} = \frac{n_{cluster_{nm\,ROI}} - N_{missed}}{N_{p_{ROI}} \Delta t}. \tag{5.33}$$

5.4 COMPARISON BETWEEN TRACK MODELS

GBL and straight line fits are benchmarked in the following based on a Monte-Carlo study. Mis-reconstruction probability, tracking efficiency and computational time are compared for telescopes consisting of up to 8 layers in the following setup: planes are equidistant spaced with 5 cm. Each layer has 48×200 pixel and a pixel pitch of $81 \times 80\,\mu$m, corresponding to the MUPIX8 dimensions. The planes have a thickness of 2.5 % x/X_0, are perfectly aligned relative to each other and assumed to have a 100 % hit detection efficiency.
Electrons with a momentum of 4 GeV and a Gaussian beam profile with a σ of 4 mm are simulated. The initial beam divergence is set to zero for simplicity. Only multiple coulomb scattering on the layers is simulated –

energy loss, bremsstrahlung and δ-electrons are not included and the probabilities for charge sharing and crosstalk are set to zero. If a particle is scattered outside the sensor acceptance, the event is anyways kept. To increase the combinatorics, several events can be merged to increase the particle density. Noise is assumed to be randomly distributed over the sensor and added just before the reconstruction. The Monte-Carlo truth information is, of course, only used for evaluation of the results quality.
The aforementioned track candidate requirements are applied: a hit on each layer and ambiguities are resolved by rejecting the tracks with worse χ^2.

Computation time

The computation time is benchmarked by processing an identical number of particles, with different multiplicities per event. In total 100k particles are simulated of which 37k are reconstructible.
The time spent for reconstruction is summarized in table 5.1 for different configurations. Additionally, the time spent for the for hit assignment, fitting, χ^2– sorting and ambiguity resolving is shown, which strongly depends on the implementation. A higher number of planes leads to longer computation times. Increasing the number of tracks per frames leads to a dramatic increase in computation time as the combinatorics is given the number of tracks to the power of planes, see equation 5.1. The required time to perform a GBL fit is significantly larger compared to the time required to perform a simple straight line fit[4]. For higher multiplicities the time difference between the two fits decreases as the track sorting and resolving ambiguities becomes dominant over the fitting time. From the time perspective a straight line fit is favored over a GBL.

Track quality

The quality of a reconstructed track is defined by the χ^2. To compare the fit quality of the two models as a function of the plane number, the $\chi^2{}_{red} = \chi^2/ndf$ of events with only one particle per event and no noise hit is shown in figure 5.5. Telescope setups with 4 to 8 layers are simulated. In all cases, the χ^2 values for true hit combinations are below 10 for all reconstructed track candidates. The distributions for the GBL have a mean value of 1 and are much more narrow compared to the distributions for the straight line. The χ^2distributions for the straight line also have increasing mean values with increasing included layers, due to increased material and more scattering from the added layers.
The visible spikes, especially for a four layer system are moiré pattern [64] due to the large pixel size and the limited number of planes. More planes reduce the moiré effects.

4 Running in debug mode slows down the GBL by another factor 40 compared to a release build.

		reconstruction		reconstruction and ambiguity resolving	
planes	tracks	Straight line	GBL	Straight line	GBL
planes	[1/frames]	[ms]	[ms]	[ms]	[ms]
8	1	128	4084	133	5396
8	2	3243	21755	3811	64204
8	3	25450	170192	307973	483128
8	4	103339*	689422*	2175010*	3399140*
6	1	105	3818	118	5005
6	2	729	6755	729	15184
6	3	2714	16755	5192	48392
6	4	7403	41449	44244	130381
6	5	16261	93122	241746	284169
4	1	80	3781	86.5	4374
4	2	176	3780	174	5440
4	3	342	4076	342	7498
4	4	631	4952	692	10935
4	5	975	6242	1302	15426
4	10	4924	22850	24165	70825
4	15	13456	46279	359230	204387

Table 5.1: Time to process 100000 particles (37000 reconstructible particle trajectories) for different particle and noise multiplicities. The implemented sorting algorithm is faster for the GBL tracks. Therfore, the reconsturction and filtering, i.e. ambiguity resolving becomes faster for the GBL for high multiplicities. The simulated data samples are identical for both reconstruction methods. Values with (*) are produced with a smaller sample and scaled to 100000 particles.

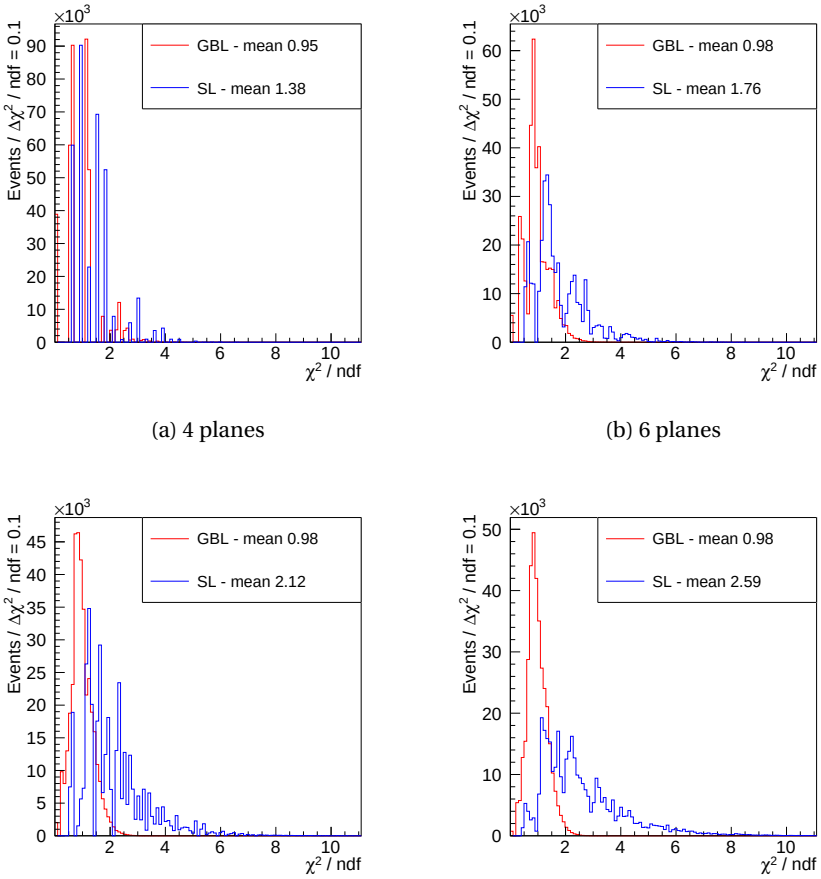

(a) 4 planes

(b) 6 planes

(c) 7 planes

(d) 8 planes

Figure 5.5: χ^2 distributions for track candidates in telescopes with different number of planes. Single particle events without noise are used as input, so only true combinations are shown.

Including multiple coulomb scattering makes the GBL more precise, resulting in the expected more narrow distribution.

Fake tracks

Fake tracks, due to mis-reconstruction of an event, are not always matchable and will therefore decrease the measured sensor efficiency. The fake track probability depends on the number of tracks per event and the number of noise hits per plane. In general fake tracks are expected to have a worse χ^2 than correct hit combinations. However, the nice χ^2 distributions in figure 5.5 do not guarantee good χ^2 separation of fake- and correct tracks. The χ^2 distribution for reconstructed track candidates after removal of ambiguities is evaluated exemplary for a six layer telescope in figure 5.6. Different noise occupancies on all planes ranging from 1 to 3 hits per plane and event are shown. These noise rates are already a

conservative scenario for MuPix sensors[5]. The sample contains 36567 reconstructible electrons. The Monte-Carlo truth information is used to separate the candidates with correctly assigned hits from track candidates with noise hits. Figure 5.6 shows the correct and fake candidates for different noise occupancies. Both fits have a good separation between correctly assigned track candidates and the majority of mis-reconstructed track candidates. If by chance a noise hit on one plane is suited better for the fit, the track parameters are similar to the true one. These tracks cannot be rejected by any means. The $\chi^2$of the GBL is systematically smaller, as shown above. For a χ^2 cut of 5 for the GBL and 10 for the straight line a good suppression of fake tracks is achieved.

Depending on the χ^2 cut, which selects tracks from candidates, different reconstruction efficiencies and fake track contaminations are obtained, as visualized in figure 5.7, where the reconstruction inefficiency is plotted against the fraction of fake tracks in the sample for the configuration from figure 5.6. The dashed lines correspond to the straight line fits and the solid lines to the GBL fit. The spectra look very similar for all three noise rates. The shift towards higher fake track probabilities and larger tracking inefficiencies is induced by the removal of track candidates while resolving ambiguities. Nevertheless, tracking efficiencies of 99.8 % with less than 0.2 % background contamination are achieved, with a tight χ^2 cut for conservative noise levels. As already indicated in figure 5.6, the optimal χ^2 cut values are 10 for the straight line fit and 5 for the GBL.

5 Sensor noise in the order of 10 kHz and an event length of 1 µs result in 0.01 noise hits per frame and plane.

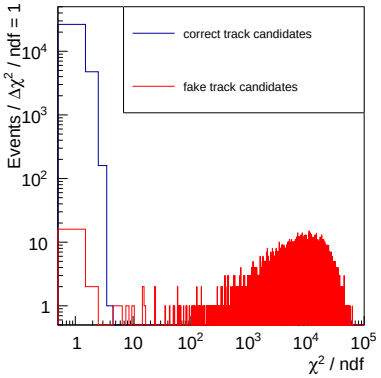

(a) GBL with 1 noise hit per plane

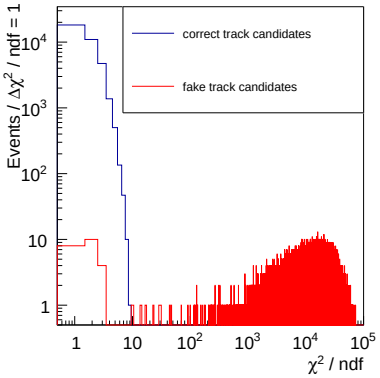

(b) SL with 1 noise hit per plane

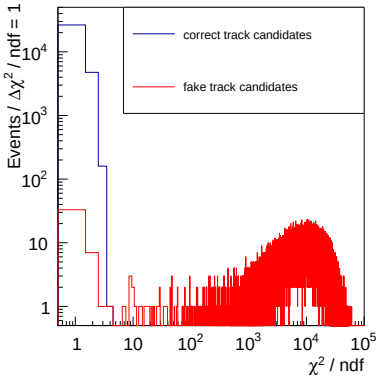

(c) GBL with 2 noise hit per plane

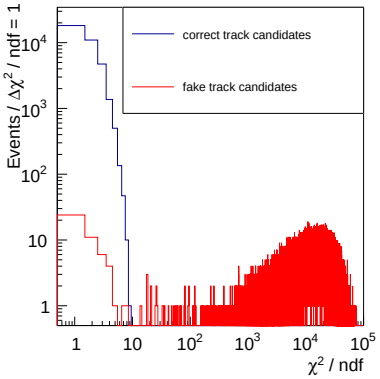

(d) SL with 2 noise hit per plane

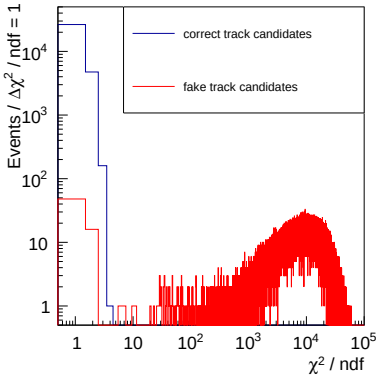

(e) GBL with 3 noise hit per plane

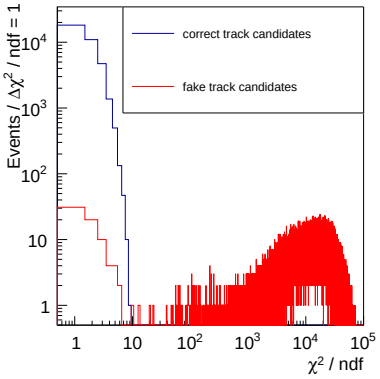

(f) SL with 3 noise hit per plane

Figure 5.6: χ^2distribution of track candidates with correctly assigned hits (blue) and candidates with at least one wrongly assigned hit (red) for different noise rates. The GBL is shown on the left and the straight line on the right. One particle per event and 1-3 noise hits per plane are simulated.

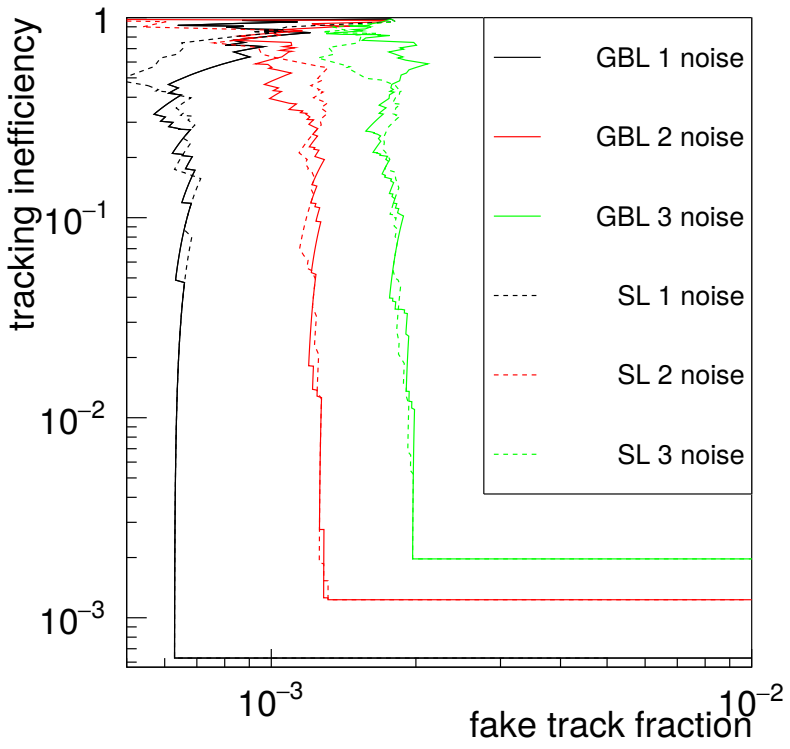

Figure 5.7: Tracking inefficiency against the fraction of mis-reconstructed tracks for different per pixel noise rates as function of the applied χ^2 cut. Solid lines are GBL results and dashed lines straight line results. Ambiguities are resolved by rejecting the track candidate with the worse χ^2.

Part II

TRACKING TELESCOPES

The feasibility of new DAQ systems and sensor concepts, proposed for experiments searching for new physics, need to be proven on a smaller scale before being used in final experiments. Particle tracking telescopes are perfectly suited to do both: DAQ concepts tailored to the readout scheme of new pixel sensors can be used to read out several layers of pixels. In parallel, a dedicated layer can be systematically studied using the other layers as reference.
Two tracking telescope approaches are described in part II: the new MUPIX TELESCOPE and the EUDET-telescope. The MUPIX TELESCOPE is optimized for high particle rates with low momentum, runs without any hardware trigger and can be used at any existing facility. Additionally it provides a precise reference timing system. The EUDET-telescopes are high precision telescopes, which can be used to study spatial effects on the micrometer scale. They have no time measurements, use an external trigger and are not capable of high rates.

6 MUPIX TELESCOPE

6.1 CONCEPT

To carry out integration studies as well as efficient testbeam campaigns, without relying on locally installed systems, a particle tracking telescope consisting of HV-MAPS [65, 66] has been designed and completely reworked in the scope of this thesis: the so called MUPIX TELESCOPE, see figure 6.1. The MUPIX TELESCOPE consists of four to eight layers of MUPIX sensors of which up to four are connected to an FPGA inside the DAQ-computer, see figure 6.2.
In contrast to most other systems, the MUPIX TELESCOPE has a streaming DAQ without any hardware trigger. The synchronized sensors stream all hit data to an FPGA. Data is processed in the FPGA and software, and finally stored on disk, without discarding hits. Two scintillating tiles framing the pixel layers serve as additional precise time reference, with a resolution of roughly 1 ns, to study the timing performance of pixel sensors within the MUPIX TELESCOPE. To simplify the operation, a graphical user interface (GUI) is included in the telescope DAQ. An eight plane telescope using the same software DAQ and the *Mu3e* front-end board to configure and steer the MUPIX has been developed based on the MUPIX TELESCOPE as a next step towards the *Mu3e* pixel tracker and is discussed in [53].
Based on the identical threading and data processing scheme another GUI has been constructed, which is optimized to study a single MUPIX - the SINGLE SETUP. In the scope of this thesis, the DAQ system has been reworked, improved and adapted to two new MUPIX prototype generations. Up to three MUPIX TELESCOPES in parallel have been used to take data at several testbeams in Mainz (MAMI), Geneva (CERN-SPS), Hamburg (DESY-II) and Villigen (PSI-HiPa). Operating several telescopes in parallel makes optimal use of the testbeam time.
In the following, the hardware, DAQ-concept, data flow and format , sensor

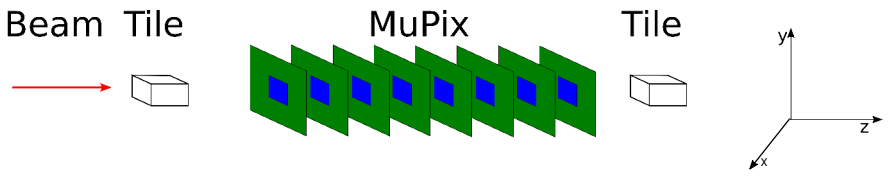

Figure 6.1: Sketch of the MUPIX TELESCOPE layout with the default left handed coordinate system. Eight sensor layers (blue) are mounted on PCBs (green) and framed by two scintillating tiles (empty boxes).

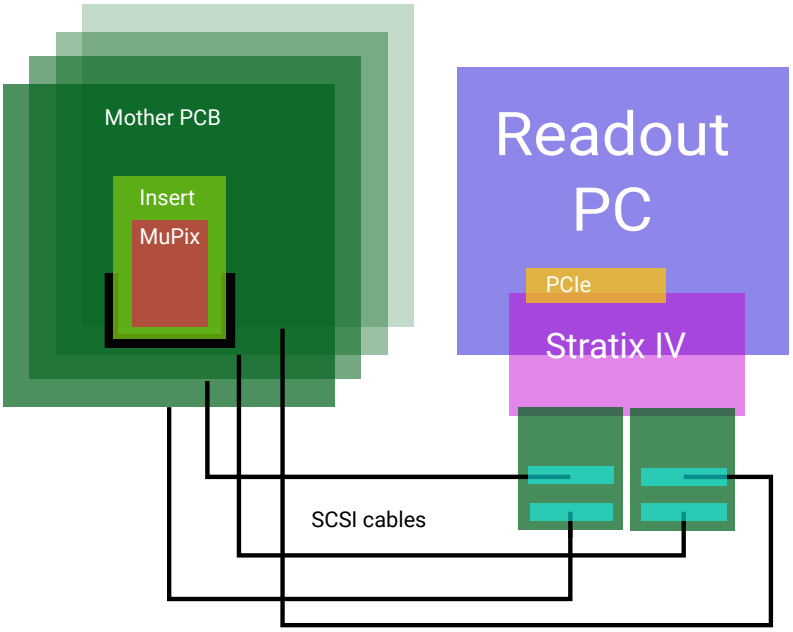

Figure 6.2: Schematic drawing of the hardware setup required to operate the telescope: A readout computer (blue) hosts an Stratix IV development kit (pink), which is connected over a PCIe socket (yellow). The Stratix IV development kit has two HSMC ports, which are equipped with an adapter card with two SCSI-III ports. Each SCSI-III port can be connected to a MUPIX8 mother PCB, to which MUPIX sensors, mounted on an insert PCB, can be connected.

steering and quality management are presented in detail. Subsequently, the performance during beam campaigns as well as the data analysis procedure are discussed.

6.2 HARDWARE COMPONENTS

To read out sensors, the MUPIX TELESCOPE requires several hardware components. A sketch of all hardware components is shown in figure 6.2: the MUPIX sensors are either directly glued and bonded to supply boards, the Mother PCBs, or placed on an insert, which is connected to the same Mother-PCB. The PCB in turn is connected to the readout FPGA (Stratix IV development kit [67] over a SCSI-III cable and an SCSI-III to HSMC adapter card. The FPGA connects to the readout PC via a PCIe interface.

Insert: The insert [68] is a simple extension of the Mother PCB, which provides a last filtering stage for the supply voltages and several test points to directly access configuration outputs of the MUPIX8.

Mother PCB: The Mother PCB [69] has a connector to the insert as well as a set of pads which can be used to directly glue and bond the sensors to the PCB. Therefore, the same filtering components and test points as on the insert are present. Adjustable supply voltages with low ripple and

injection pulses are generated on the board. LVDS receivers transform the differential slow control signals to single ended ones required by the MUPIX8. LVDS transmitters are used to send the read-back values of the sensor to the FPGA. The four data links of the MUPIX8 can be connected either to SMA ports or to a repeater chip, which allows to drive the data over longer differential cables.

SCSI-III to HMSC: The adapter card connects to up to two mother PCBs via a SCSI-III connection and the FPGA via a HSMC port. It receives the differential read-back signals and transforms them to single ended signals for the FPGA. The four data links are either connected to the LVDS-receivers or the fast inputs (8.5 GBit/s receivers [67]) of the FPGA. The fast inputs are used per default. Single ended control signals from the FPGA are converted to differential signals and sent to the mother PCB. Four NIM inputs on the adapter card can be connected to timing systems. An additional RJ-45 connector is used to communicate with the EUDET-telescopes, which are discussed later.

FPGA: A Stratix IV development kit [67] running custom firmware is used to receive the data from up to four sensors, only limited by the number of available input/output-connections on the HSMC banks. A detailed description of the firmware and the FPGA itself can be found in [53] - only the components related to the data path and sensor steering are described in the following section.

6.3 DATA ACQUISITION SYSTEM

The data acquisition system is built around a custom multi-threaded PC program and a commercial FPGA development kit running custom firmware. The goal of the DAQ system is to provide a stable and fast readout of the sensors, together with a graphical user interface to steer the sensors and monitor the performance. Additionally the DAQ is designed to be easily adaptable for new MUPIX generations. The MUPIX TELESCOPE has not only been used to study MUPIX prototypes, but also to study another monolithic prototype developed for ATLAS (the ATLASPIX), which has a similar readout scheme.
Having a fast DAQ requires a strict separation between components, which are involved in the actual data taking and user steered processes. In addition, bottlenecks have to be avoided, which is only possible, if the workload on all components is comparable. With these conditions is mind, the DAQ is optimized for the MUPIX.
Communication between the FPGA and the CPU is realized with *registers* and *memories* mapped to the PCIe bus as bus addressable registers (BARs). One set of 64 32 bit *registers* is writable by the FPGA, the other by the host CPU, while reading is always possible from both sides. The *registers* are used to steer the FPGA and to transfer status information of the firmware. Similarly there are two *memories* of 256 kB, one FPGA- and one host-writable. Data transmission to the 256 kB *memory* is realized via

polling, where the PCIe bandwidth cannot be efficiently used as every data transfer requires CPU interaction, see below. An fast alternative data transmission, via direct-memory-access (DMA), which is also suitable for *Mu3e*, is also implemented and proven to be functional [28, 70]. DMA is not using the FPGA-writable memory, but writes data to a pre-allocated space in the RAM of the PC, without keeping a copy of the data on the FPGA.
To cope with high rates, if DMA is not used, an on-FGPA DDR3-memory is available. Up to 500 MB can be buffered without loosing data, which is essential for stable test beam data taking. All received hit addresses and timestamps are also histogrammed on the FPGA.
The detailed software layout, data -flow, -format, sensor-steering, GUI and online monitoring are discussed in the following.

6.3.1 *DAQ software*

The DAQ software is split into six tasks: Data readout, reformatting , storing, monitoring, efficiency calculation and a graphical user interface. All tasks cannot be performed by a single CPU core efficiently. To distribute the load onto multiple cores, a multi-threaded scheme is used. However, running several threads in parallel, which need to exchange data and information can quickly become memory unsafe, as the threads do not know of each other and can potentially access the same memory in parallel. This can be avoided by using a thread safe[1] memory management, which is explained in detail later. Several libraries for multi-threaded software are existing and `qt4` [71] is chosen, as it combines multi-threading with a graphical user interface creation tool. Additionally it offers thread communication. Finally, it has a vibrant community with commercial application ensuring long term support on all platforms. A block diagram of the software is shown in figure 6.3.

The core is the so called `Mainwindow`, which also provides the GUI (see subsection 6.3.5). Graphical access to the *registers/memories* as well as the sensor configuration is implemented as `Dialogs`, which are essentially pop-up windows, running in the same thread as the `Mainwindow`. Communication between a `Dialog` and the `Mainwindow` is realized with `Signal-Slot` connections provided by a `qt` package: a signal in either the `Dialog` or the `Mainwindow` is connected to a slot on the receiving side. An internal event loop checks the status of the slots frequently, if the `Dialog/Mainwindow` is not busy, or if it is explicitly requested. The signal/slot communication is thread safe, but rather slow, as an acknowledgment is required. However, running signal/slot communication with several kHz is possible. Additional `Dialogs` are used to display tuning files, pixel masking, link status and monitoring, which increases the flexibility and clarity of the GUI.
The `Mainwindow` is also responsible to start/stop and control all other

1 Thread safe software can be used/accessed by several threads without memory/access violations.

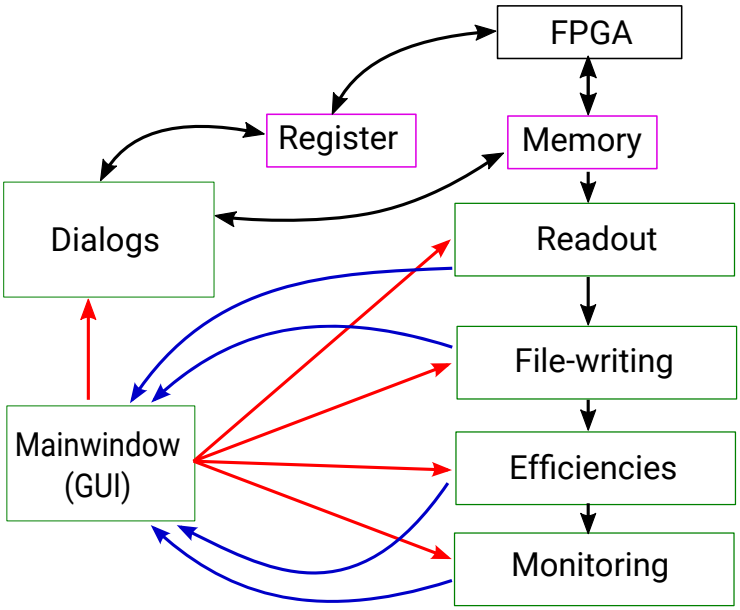

Figure 6.3: Block diagram of the software. The green framed boxes are threads and the magenta ones the memories. Black arrows indicate data transfers, red arrows mark steering, blue ones control/status information. The FPGA is not part of the software, but included for completeness.

threads. The principle is similar to the communication with the `Dialogs` and based on signal/slots. However, in contrast to `Dialogs`, *threads* are inactive until an event loop is started. A signal from the `Mainwindow` calls the execution of an endless loop. Stop signals will only be processed, if somewhere in the endless loop an explicit request to check for incoming signals is included. Unfortunately, checking for theses signals is slow and cannot be done too frequently. Therefore, the request is only called after a certain number of rounds n in the event loop[2]. If the stop signal is received and processed, the endless loop is exited and the thread goes back into an idle state. The threads in turn can also send signals with messages, status updates or errors to the `Mainwindow`, which reacts to them.

Data transfer between threads is queued – as soon as the processing is done, data is pushed into a FIFO queue. The next thread can read from the queue in turn. An optimal transfer can be achieved, if the threads can write and read in parallel, without blocking the queue - so called lock-free. Lock-free queues, with only one thread being allowed to write data, the *producer* and one to read, the *consumer* are called lock-free single-producer-single-consumer (SPSC) queues and available in the `boost` library [72]. The size of the queues is chosen to be large enough to buffer up to 500 MB data, which is the usual run size of the telescope, to avoid any data losses or back pressure. The queues after the data is written to disk are short to avoid long latency for the monitored data. Events are discarded and do not appear in

2 Depending on the data load n is adapted for different conditions.

the monitoring whenever the queue has been full. This principle makes any pre-scale obsolete – the monitoring processes as many events as possible.
Integers, declared atomic[3], are used to display rates of incoming data, as well as writing speed and the filling status of queues, which are used to buffer data and transfer it to the next thread. In the latter case for example, every time one element is pushed into a queue, one number is counted up, whenever one is consumed, another one counts down. The filling status is calculated in the `Mainwindow` with a rate of 1 Hz by simply calculating the difference between the numbers. Compared to CPU frequencies, 1 Hz is slow and not going to reduce the readout speed significantly.

6.3.2 *Data path*

The data path is sketched in figure 6.4. It consist of three steps: FPGA processing, data transfer and software processing.

FPGA PROCESSING Hit data is streamed from the MUPIX to the FPGA. The FPGA receives, 8 bit/10 bit decodes and deserializes the data. The timestamps can be optionally gray-decoded on the FPGA. The data of the sensors is either 4-to-1 multiplexed, to create a single data stream from the four links of a sensors, and sorted by their timestamps using the online hit sorter [2] or sent to a Multilink readout [53] entity. In both cases hit blocks are created. Hit blocks contain hits with a timestamp range of 128 timestamps in the case of the sorted readout. For the multilink readout hit blocks contain hits from one MUPIX readout cycle. The block structure is described in the next section. Empty frames can be dropped already on the FPGA to reduce the overhead.

DATA TRANSFER The FPGA is connected via the PCIe bus with the computer. Reading out the data requires a data transfer from a peripheral device memory the main memory. Two main transmission schemes are existing and can be used in the telescope DAQ: programmed I/O or direct-memory-access (DMA).
Programmed I/0 (also referred to as polling) is a CPU driven data transmission scheme, where read and write requests for small packages of data are instructed by software. Polling creates a large overhead because reads require two transmissions on the PCIe bus, which are typically sequential. It is used as the default transmission scheme, as it is rather easy to implement.
On the contrary, DMA offers a fast data transmission. Data is written to a fixed and pre-allocated physical memory. The CPU is informed once in a while by the device either via so called interrupt messages or a separate status memory about the writing status. A device driver in turn reacts to the

3 Atomic means that the integer can be read/written only by one thread at a time - if a second thread wants to read/write the number, it has to wait until the first thread is finished

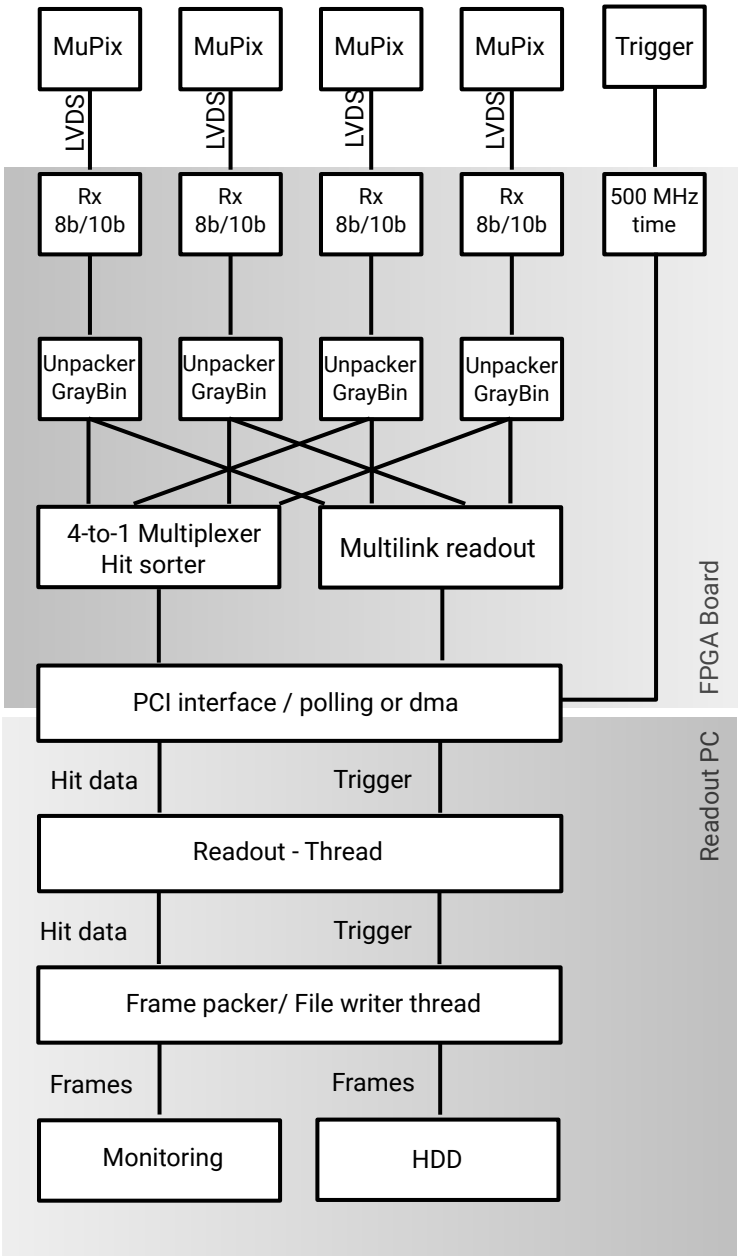

Figure 6.4: Data path of the MUPIX TELESCOPE: LVDS data from the sensors is received (Rx), deserialized and 8 bit/10 bit decoded. The Unpacker deserializes the data and creates one (two) 32 bit words per MUPIX7(MUPIX8) hit with an optional Gray decoding of the timestamps. The hits can be either 4-to-1 multiplexed and sorted by time or read out link by link via the PCIe interface. The PC receives the data blocks and splits them into hits and triggers, which are subsequently merged and synchronized to `telescope frames` with common time. The `telescope frames` are written to disk and forwarded to the online monitoring. Drawing based on [2].

interrupts and informs the DAQ software that e.g. a new data block is ready to be processed. The technicalities of DMA as well as the software and firmware implementation are summarized in [28]. Recently, DMA without interrupts has been implemented in the MUPIX TELESCOPE [73] to further decrease the transmission overhead.

SOFTWARE PROCESSING The software processing takes care of the data flow through the software and shares the work between several threads. The data flow is presented and the memory management is discussed.
Data is received by a dedicated thread, the *readout thread*. The *readout thread* either constantly checks for new fully written data events, indicated by a FPGA-writable *register* value, which is updated after the FPGA has finished writing a block, for polling data or interrupts for DMA. Polled data is split into the different block types, copied to a different memory location as the FPGA-writable *memory* is rather small. Pointers to the data are forwarded to the next thread, the *filewriter*. In the case of DMA, interrupt blocks with a fixed size of 256 kB are forwarded to a *data-processor thread*, which handles the data splitting and takes care of blocks, which might be split over the interrupt block border. The *filewriter* merges different blocks with similar time sent by several FPGAs into a final data object, the `telescope frame`, which is directly stored on disk for offline analysis. `Frames` are in turn forwarded to an *online efficiency thread*, which reconstructs tracks, if the `frame` has hits in all reference layers, and performs a full hit matching as introduced in section 5.3.2. Finally, data is forwarded to an *online monitoring thread*, where several monitoring histograms are provided, see subsection 6.3.6. At the end, the data is deleted from the main memory.

Memory management

The memory management of the DAQ system is build around two ring buffers containing either blocks[4] or `frames` and data queues between the threads, see figure 6.5. The maximal element size of the first buffer is 3870, given by the maximal event size for a sorted block, which is $2 \cdot n_{hits} + 6$ with a maximal hit number of 1920 and a few safety words in the case of changes in the header. The frames are assumed to contain up to a thousand hits and a hundred trigger timestamps. The buffer element size is accordingly scaled - however, this is continuously changed to adapt for different particle rates.
To optimize the processing speed, hit blocks and `frames` stay always at the same memory position, only pointers to the elements are passed from one thread to another. The transfer of the pointers is queued, as aforementioned.

4 A block is essentially an array of 32 bit words with varying size. In software, blocks are stored in `vector<32bit>`.

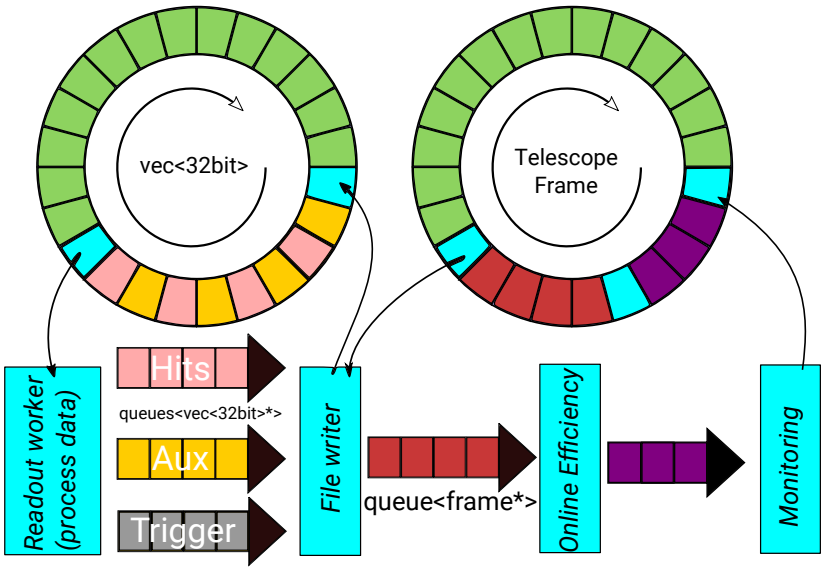

Figure 6.5: Sketch of the memory management and queueing system of the telescope DAQ operating in the polling mode: The data is stored in two ring buffers, one containing `vector<32bit>` values, the other one `telescopeframes`. The data is not moved, only pointer are send from thread to thread with lockfree queues. After processing, the data is deleted from the main memory and the ringbuffer elements can be used again.

The *readout thread* is connected to three SPSC queues as producer. Events from the FPGA are copied to elements of the first ring buffer and pointers are forwarded to the hit block queue. Additional information blocks can be optionally written to a second queue. Pointer are not used for the trigger reference timestamps, which are 64 bit words. On modern computer architectures, pointers are always 64 bit – there is no advantage of using pointers for triggers. The trigger words are pushed into the third queue. The *filewriter* is connected to three SPSC queues for each *readout worker*, from which it consumes events and merges the data into blocks of common timestamps, see subsection 6.3.7. The consumed events are cleared and the according ring buffer elements are freed. The merged data is written to elements of the second ring buffer and pointers to the `frame` are pushed into another queue. The *online efficiency thread* consumes these event pointers, performs tracking and efficiency calculation, and pushes the events in the last queue to the *monitoring thread*, where the event pointers are cleared and the ring buffer element freed.

6.3.3 *Data format*

Each MUPIX generation and readout mode has specific blocks. All block types have a begin/end of block marker and an block counter, together with block specific additional header information.

The exact hit and trigger block structure is shown for MUPIX8 data in Appendix B, only the most important features are discussed here.
The most significant bit of all words has a value of zero, excluding the beginning and end of block markers to avoid confusion.
Sorted and multilink readout blocks contain an on-FPGA sampled timestamp running at 125 MHz, which can be used to determine the overall runtime. Both blocks contain a variable number of hits. Sorted blocks can contain up to 1920 hits, as for every of the 128 timestamps in each block up to 15 hits can be read out. The multilink readout block contain a maximum of 64 (48) hits for the MUPIX7 (MUPIX8), as only one hit per column can be read out in one readout cycle of the MUPIX. All MUPIX8 hits consist of an 8 bit column, 8 bit row address and 16 bit time information. The readout of several sensors requires additional chip/link labels which in turn require additional bits. As all memories are implemented in 32 bit units, a hit will always fill up two words. The first word contains chip and link identifiers and address marker and column/row address; the second word the same chip and link identifiers, a time marker and the timestamps. The remaining bits are used to transfer overflow information for the sorted readout or are set to zero.
The trigger blocks are simpler: the header only contains a beginning of block marker and a block counter, followed by an 64 bit trigger timestamps sampled with a 500 MHz clock and split into two words again. The trailer simply contains an end of block marker.
The block structure for MUPIX7 data is slightly different and discussed in [2, 53].

6.3.4 *Sensor steering*

The steering scheme of the MUPIX8 telescope is shown in figure 6.6: the DACs for the MUPIX prototypes as well as the reference voltages on the mother-PCB can be set and adjusted in the GUI. When setting the DACs, the values are transferred to a dedicated software class, the `MupixSensor` [74], which handles the bit order and positioning in the shift registers. The bits are then written to the registers and send to the FPGA word by word. MUPIX8 has a significantly increased number of configuration bits, which asks for a faster configuration method, as the register based transfer is becoming too slow. Therefore an alternative method utilizing the host *writable memory* has been implemented [53], allowing for fast sensor configuration. In both cases, the values are received by the *MuPix8 Sensor Slow Control* entity on the FPGA, which sends the bit stream to the MuPix with a selectable frequency. The bit stream is written to shift registers and loaded into on-chip storage.

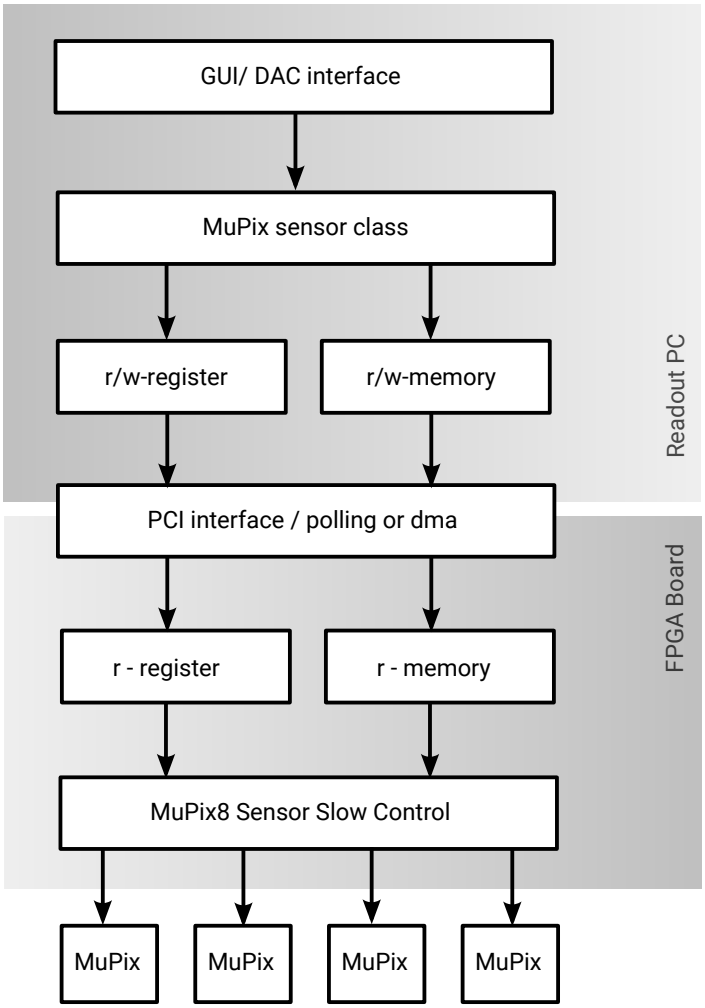

Figure 6.6: Sensor steering scheme for the MUPIX8 telescope: The DAC values are changed in the GUI, interpreted by a dedicated sensor class and transferred to the FPGA via the *register* or *memory*. The DACs are interpreted by the *MuPix8 Sensor Slow Control* entity of the FPGA and clocked into the shift registers of the MuPix with a selectable frequency.

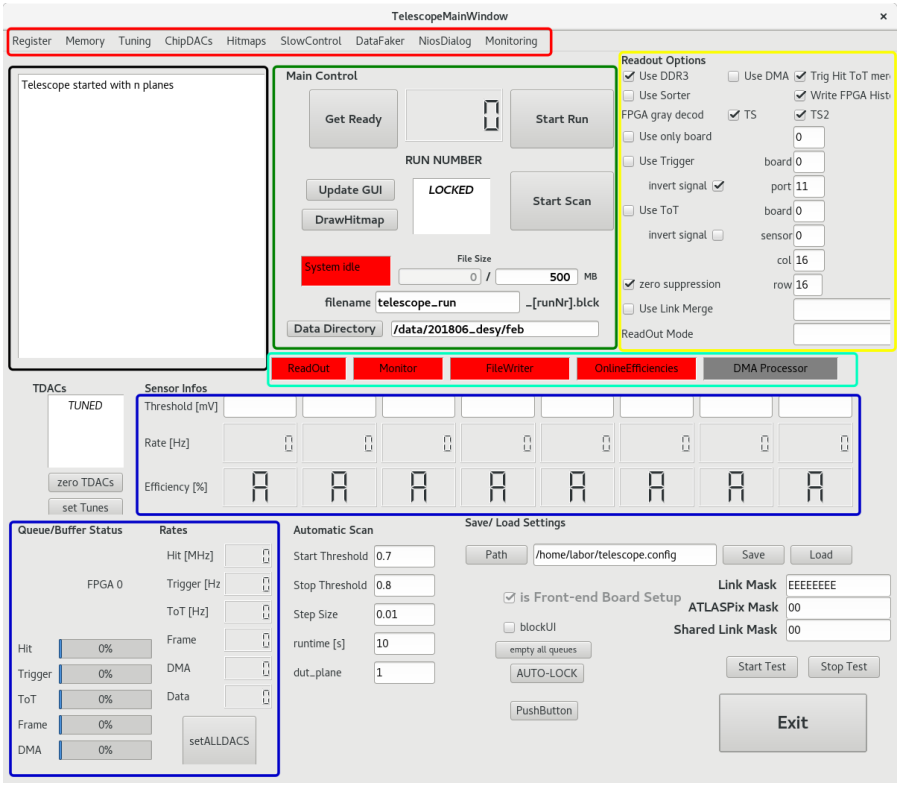

Figure 6.7: Screen shot of the telescope GUI

6.3.5 *Graphical user interface*

To improve the setup usability, the sensors need to be steered and read out utilizing a graphical user inferace (GUI). The GUI for the MuPix7 telescope is discussed already in [75]. To address the changes for MuPix8, the complete DAQ system, including the GUI, has been restructured. A screenshot of the GUI for the MuPix8 telescopes is shown in figure 6.7. The most important components are highlighted and presented below:

- *Drop down menu:* Highlighted in red. The drop down menu bar gives access to several `Dialogs`:
  - **Register:** Opens the register `Dialog` to access the *read/read-write registers* and to update them.
  - **Memory:** Displays the content of the *read memory*.
  - **Tuning:** Defines the input paths for the tuning files for all sensors.
  - **Chip DACs:** Opens a `Dialog` to change and set the chip and board DACs. The device under test and the reference layers have individual windows.
  - **Hitmaps:** Currently not in use.
  - **Slow Control:** Interface to slow control devices, which are accessed via a slow control software protocol developed at PSI,

the midas-slow-control-bus [76]. The power supplies, temperature and humidity sensor can be read out via this interface.

  - **Data Faker:** Opens the steering window for the on-FPGA MUPIX8 emulator [68].
  - **Nios Dialog:** Display the link status of the attached sensor via an NIOS-interface running in a softcore on the FPGA [53].
  - **Monitoring:** Opens the monitoring `Dialog`.

- *Main control:* Highlighted in green. Provides all buttons and functionality to operate the setup with default settings. The buttons are self-explanatory and grouped around a run number-LCD display.

- *Message Box:* Highlighted in black: Prints messages from all threads and `Dialogs`.

- *Readout options:* Highlighted in yellow. Selection window for the different readout options. The ones used for MUPIX8 readout are listed below:
  - **Use DDR3:** Select if the the DDR3 on the FPGA is used.
  - **Use DMA:** Enable/disable DMA.
  - **Trig Hit ToT merger:** Create `telescope frames` from the block data
  - **Use Sorter:** Selected if the data is time sorted, unchecked for multilink read out.
  - **Write Histograms:** Write the FPGA-histograms to disk at the end of each run.
  - **FPGA gray decode:** Can be checked to decode the timestamps on the FPGA.
  - **Use Trigger:** Checked if the tiles are connected to the system. Board and port are used to select the trigger inputs. Invert is checked to select active high or low levels.
  - **Use ToT:** Checked if also the analog ToT is sampled. Only used for MUPIX7,
  - **Zero suppression:** Empty hit blocks are rejected in the *readout worker* if this is checked.

- *Thread status:* Highlighted in turquoise. Status displays for the different threads. The boxes are red if the threads are idle and green if they are running and busy. The system idle is just the exclusive or of all individual threads.

- *Monitor displays:* Highlighted in dark blue. The rates and efficiencies of all all layers and the set thresholds are displayed in the central part. The display scales automatically with the number of sensors in the telescope. The bottom left part of the GUI displays the trigger, hit,

block, data and frame rates of the telescope. The Queue/Buffer Status indicates the filling level of the data queues between the threads.

6.3.6 *Online monitoring*

The online monitoring is essential to control the data taking during testbeam campaigns. The monitoring is split into three parts: Online tracking and efficiency calculation for the DUT, filling correlation, sensor and trigger histograms and a `Dialog` to display a selection of all histograms. The `Dialog` implements a `ROOTApplication`, which draws a canvas into the `Dialog`. The histograms can be adjusted interactively within this `Dialog`, i.e. they are scalable. As filling `ROOT` histograms is slow, all information is stored in pre-allocated vectors and only filled into the histograms once a histogram update is requested from the `Dialog`. A screen-shot of the monitoring `Dialog` is shown in figure 6.8: The left column is used to control the monitoring itself by defining the size of the histograms and the refresh timers for the displayed histograms. The central column shows checkable lists of available histograms to be displayed. The right column displays the selected histograms with scroll down bar. A list of available histograms is given below:

Available monitoring histograms

- **Sensor-Histograms:** Contains hit maps, multiplicities, timestamps and timestamp bit distributions.
- **Correlation-Histograms:** Contains correlations maps and difference histograms between column, row and timestamps of two sensor layers.
- **Trigger-Histograms:** Contains trigger timestamps and bits folded to 10-bit running at 125 MHz.
- **Trigger-Correlation Histograms:** Contains correlation maps and difference histograms between a trigger input and the timestamps of the sensor and a shadow map of the sensor, the hit position of a time correlated hit.
- **Efficiency Histograms:** Contains the efficiency map, matched hit distances, track positions and timestamps of matched hits as well as tracks.

6.3.6.1 *Online tracking and efficiency calculation*

The DUT performance is the most critical information during a testbeam campaign. To optimally monitor the DUT, a dedicated thread is used to perform an online straight line fit through the reference layers in exactly

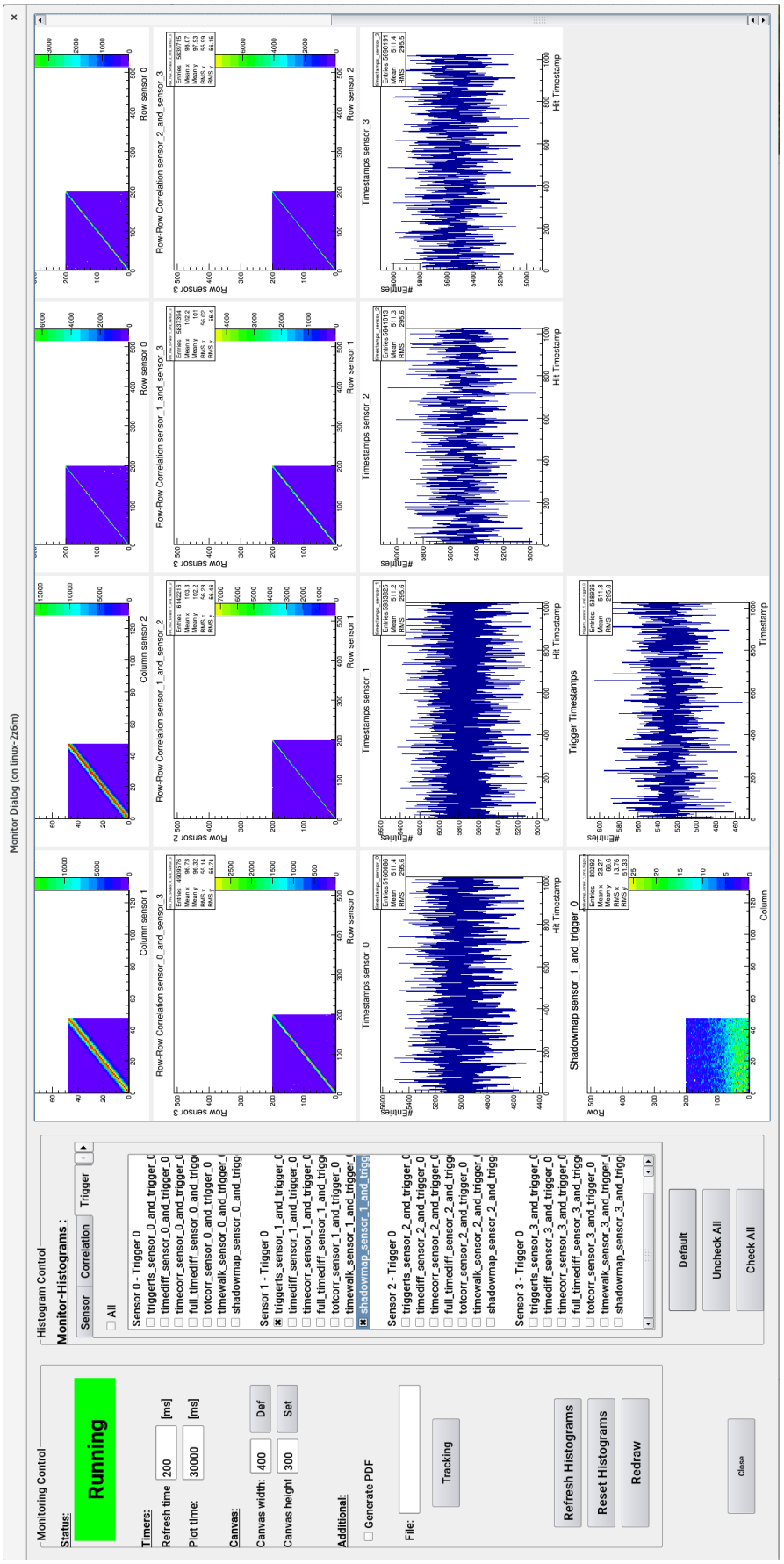

Figure 6.8: Screenshot of the online monitoring during a testbeam campaign at DESY-II in March 2018. The left two columns show control interfaces and the right part displays the selected monitoring histograms.

the same way as in the offline analysis (see chapter 6.5) based on a geometry containing the measured z-distances and no shifts or rotations[5]. The mechanical alignment has typically a precision in the order of 200 µm. The coarse alignment requires a rather loose cut on the χ^2.
Track map, efficiency map and matching distances histograms can be accessed via the above discussed Dialog and the full matching analysis histograms are stored in a separate root file at the end of each run. Additionally, the average efficiency for subsets of 1000 processed tracks is printed out, giving simple, fast and precise feedback.

6.3.7 *Online block sorting*

Blocks from different FPGAs, with hit and reference tile timestamps information, are merged in the *file writer*. All blocks have a timestamp, which is assigned on the FPGA. The sorting always requires one event from each block source. Hit blocks are used to define the range of allowed timestamps. The hit block timestamp is running at 125 MHz, which corresponds to the timestamp frequency of the MUPIX8. The earliest hit timestamp, with the lowest 10 bits set to zero, is used as reference for the merging. Hit blocks and trigger are added to the frame, if their timestamps, again with the lowest 10 bits set to zero, are identical with or smaller as the reference. After adding an element, the next element in the queue is read and also compared. A block is completed if all timestamp of the blocks are larger than the reference timestamp.

6.4 DATA TAKING

Taking data asks for a well defined initial state of the DAQ system. Pressing the Start Run button calls a routine, which ensures a correct start up, consisting of several steps:

1. Disable the FPGA readout.
2. Empty all queues and reset all counters.
3. Putting the FPGA in readout-reset, emptying the DDR3 memory on the FPGA, setting the readout mode.
4. Configuring the sensors according to the values in the `ChipDACs Dialog`.
5. Store the configuration in a log file.
6. Activate the event loops for all threads (starting with the last one in the data queue).
7. Wait until all threads acknowledged the start.

5 As soon as a software alignment is performed the geometry can be updated with x/y shifts and rotations

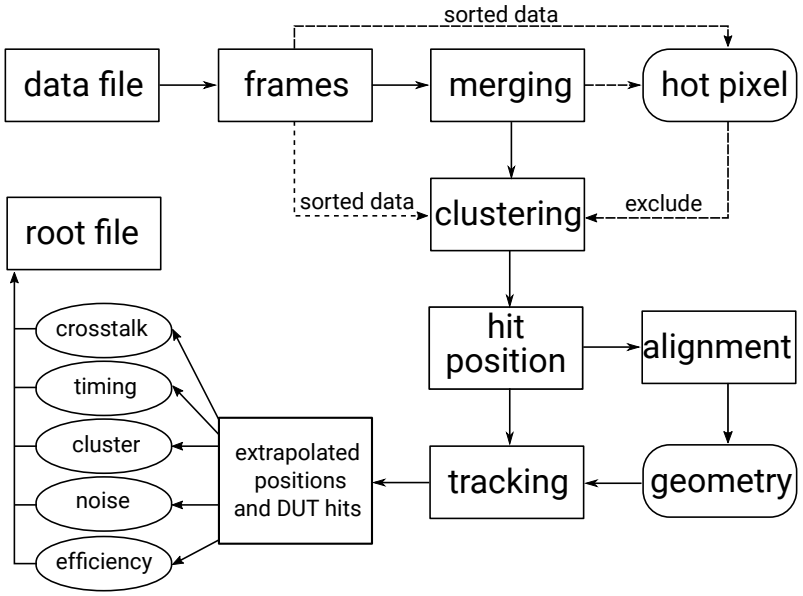

Figure 6.9: Analysis procedure for data obtained with the MUPIX TELESCOPE.

8. Releasing the FPGA resets.

Similarly, the stopping procedure, which is either called after clicking on the button again or at changing the data file after reaching the maximum file size, is defined as follows:

1. Disable the FPGA readout.
2. Stop the threads (starting with the first one in the data queue).
3. Wait until all threads acknowledged the stop and have quit the event loops.
4. Start the readout again, if the data taking has not been stopped manually.

6.5 ANALYSIS PROCEDURE

Successful data taking implies online and offline analysis of the data. Therefore an analysis framework has been been developed, parallel to the DAQ system, tailored to the data structure and pixel sensor analysis requirements and reusing the online monitoring histograms efficiently. The analysis is based on individual `frames` and sketched in figure 6.9: the data file is opened and the `frames` are extracted. If data has been obtained with the multilink readout, the `frames` contain always individual sensor information and are merged according to their frame timestamps. Masking[6] hot pixels for the analysis is the second, optional, step. Clustering and extraction of the particle hit position, the barycenter of the cluster, is done

6 Masking means to exclude the pixel from the analysis.

next. The processed `frames` are now ready for detector alignment, which can be either done manually in several iterations or using the alignment software for the *Mu3e* experiment based on millepede-II [63]. The latter leads to a more precise alignment and has the option to align for rotations around the beam axis, which became relevant with larger sensor sizes. It is also more complex and time-consuming. In both cases, shifts along the x and y-axis are corrected and the z positions of the planes are fixed to the measured values, as they are only loosely constrained by both alignment methods. The alignment results are stored in a geometry file.
After a successful alignment, the pre-processed hits are used for DUT studies using reference tracks, as described in section 5.3. In addition to an efficiency-noise analysis, studies concerning the time resolution, cluster sizes and crosstalk are done with the matched hits on the DUT. All results are stored as histograms, re-using many histograms from the online monitoring, in a `ROOT` file. The analysis procedure can also be applied on a set of runs to increase the available statistics.
Threshold scans (or a scan of any other parameter) are plotted by extracting average values from the `ROOT` files and combining them. The threshold (parameter) values are automatically extracted from the run configuration files.
Intermediate results from the analysis procedure are presented in section 7.2.

6.6 MONITORING PERFORMANCE

The two core components of the monitoring – control histograms and efficiency calculation – have been studied during two beam times at two different facilities (MAMI and PSI beamline $\pi E1$), which are introduced later. The extremely high rate at MAMI is used to study rate dependencies and reveal the limits of the histogramming. In parallel, the rate at which data is written to disk is studied. The online efficiencies are evaluated based on data obtained at PSI.

Rate dependency: Higher particle rates increase the pressure on the monitoring. The maximum frame rate created on the FPGA can only be transferred by DMA and has been tested at a dedicated campaign at MAMI, where particle rates of over 10 MHz can be provided without issues. The monitoring for both readout modes – sorted and multiplexed – has been stress tested in an eight layer telescope using the *Mu3e* front-end board [53]. The run time of the online monitoring in the case of DMA can be longer than the data taking time, if the data is buffered in the main memory. Therefore `frame` timestamps cannot be used to determine the run time of the monitoring. The monitored rate can be calculated using a UNIX timestamp, which is written to every ten-thousandth frame and the entries in the monitoring histograms. The particle rate is reconstructed from the frame timestamps of the data blocks and the number of hits in

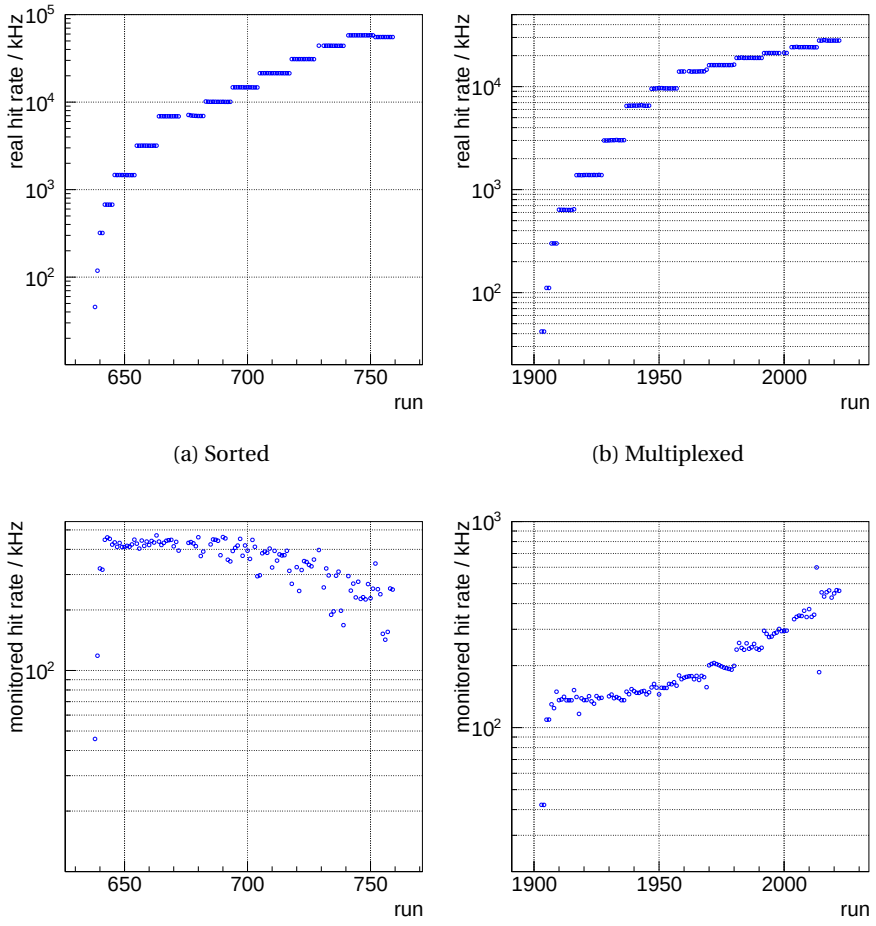

(a) Sorted

(b) Multiplexed

(c) Sorted

(d) Multiplexed

Figure 6.10: **Top:** Total rate in the telescope for different readout modes versus the run number. **Bottom:** Rate of processed hits in the monitoring.

the data file. Figure 6.10 summarizes the runs used for the performance comparison. Total hit rates of up to 60 MHz (see figure 6.10a) in the sorted mode and up to 30 MHz (see figure 6.10b) for the multiplexed readout are recorded. The rate of processed hits in the monitoring tool is shown in figures 6.10c and 6.10d. For low rates, the left side of the two plots, the monitored rate is limited by the actual particle rate. For higher rates, the readout modes result in different curves: The processed hit rate is decreasing with rate as the combinatorics to fill/draw all correlation histograms increases for sorted data. In contrast to the sorted mode, the rate of processed hits is constantly increasing as hit blocks become more likely to contain more than one hit, decreasing the data overhead.

The monitored rate versus the mean hit multiplicities per frame is shown in figure 6.11. The rate increases linearly with the multiplicity for the multiplexed data, as explained above. Sorted data has significantly higher multiplicities as the data from all 8 sensors over a longer timestamp range is

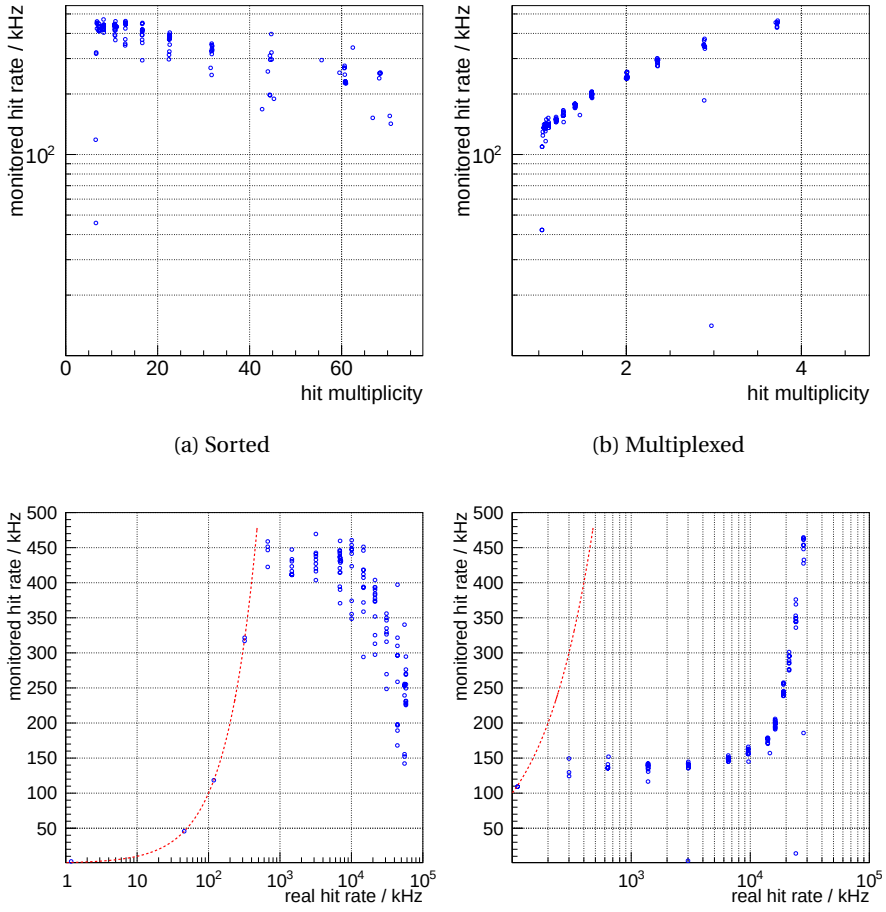

(a) Sorted (b) Multiplexed

(c) Sorted (d) Multiplexed

Figure 6.11: Monitored hit rate as a function of the average frame multiplicity (**top**) and the particle rate (**bottom**). The dashed line in the bottom plots correspond to the 100% efficient monitoring.

stored in one block. A decrease in the monitored rate with increasing multiplicity due to higher combinatorics is observed.

Plotting the monitored hit rate as as a function of the real hit rate reveals more structure depending on the readout mode: At low hit rate up to approximately 350 kHz, the monitored rate for sorted data is corresponding to the hit rate, compare figure 6.11c. For particle rates up to 10 MHz, the multiplicity per frame is not increasing significantly and roughly 450 KHz hits can be monitored. Going to the highest rates leads to decrease in the monitored rate, again due to combinatorics in the correlations. Multiplexed data shows a constant region from 1 to 10 MHz, where essentially only one hit per frame is recorded [53] and the disk writing limits the frames transmitted to the monitoring, see figure 6.11d. For higher rates, the multiplicities increase and the overhead is reduced, resulting in higher monitored rates.

The last tested detail is the file-writing speed. Figure 6.12 shows the time

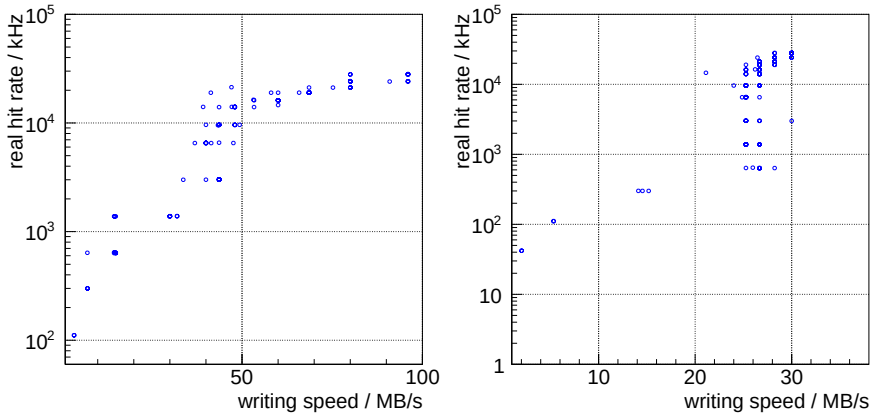

(a) Sorted (b) Multiplexed

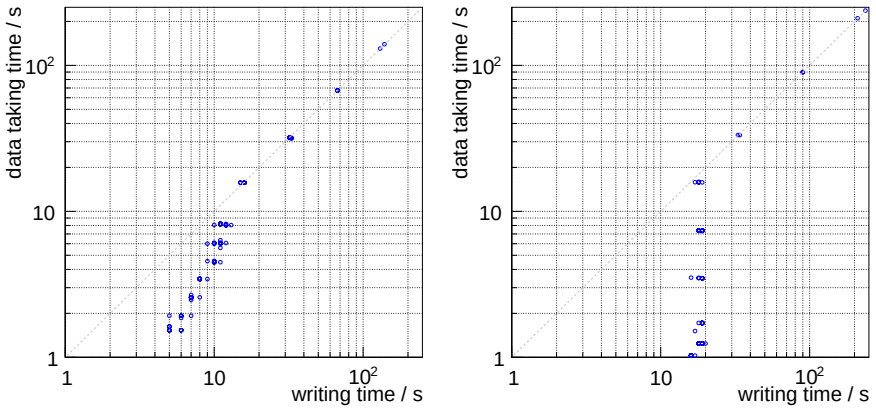

(c) Sorted (d) Multiplexed

Figure 6.12: **Top:** File writing speed versus the hit rate. **Bottom:** Data taking time as a function of the time required to write a data file.

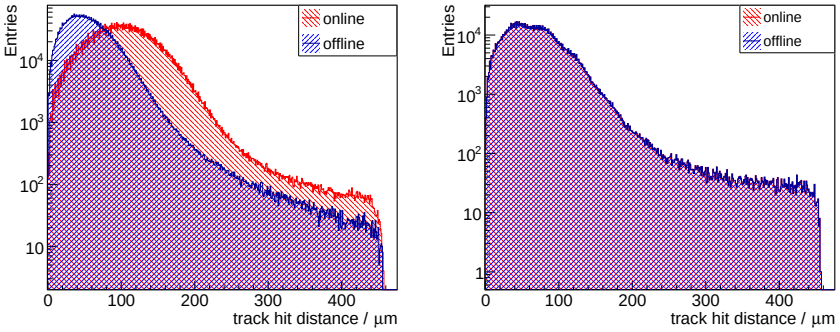

(a) Non aligned online efficiency

(b) Aligned online efficiency

Figure 6.13: Comparison of the online and offline matching distance for two exemplary runs with and without aligned geometry for the online processing. Offline, aligned geometries are used.

to write a 500 MB file as a function of the time it took to take the data and the writing speed as function of the hit rate. Two effects are visible: In both readout modes, the data can be written to disk as fast as it is transmitted from the FPGA up to a certain hit rate. Afterwards, the writing speed cannot keep up with the data rate. Sorted data can be written with a speed of up to 100 MB/s, multiplexed with a speed of up to 30 MB/s. The lower writing speed for the multiplexed data is due to less efficient data structure. Creating the frames takes longer than writing them to disk. In the most extreme cases, writing takes a factor 3 (20) longer than taking the data for the sorted (multiplexed) mode.

Online efficiencies: Online efficiencies provide an outstanding sensor performance monitoring, which allows to choose ranges, for example in a threshold scan, efficiently. During a campaign at PSI, the online efficiencies have been systematically monitored for a four layer telescope setup. One threshold scan has been performed with a geometry without corrections for mechanical mis-alignment and one with a correct geometry, which has been extracted offline from data of the first run. Figure 6.13 shows the matching distance for an exemplary run for the off- and online analysis, with identical cut configurations for the two scans. Offline matching distances are larger compared to the online distances if the mechanical mis-alignment is not taken into account, as expected. For a distance cut of 400 µm the difference in calculated efficiency however is small. If the correct alignment is applied during data taking, the shapes of online and offline matching distances are identical. For the presented data set 99.64 % of the taken data has been analyzed online. The fraction of processed events is, of course, depending on the hit rate and the number of layers. The DDR3 memory on the FPGA throttles the data rate to 22.5 kHz track rate. For higher rates, the processed fraction will shrink, without slowing down the data taking, as the data is already written to disk when mon-

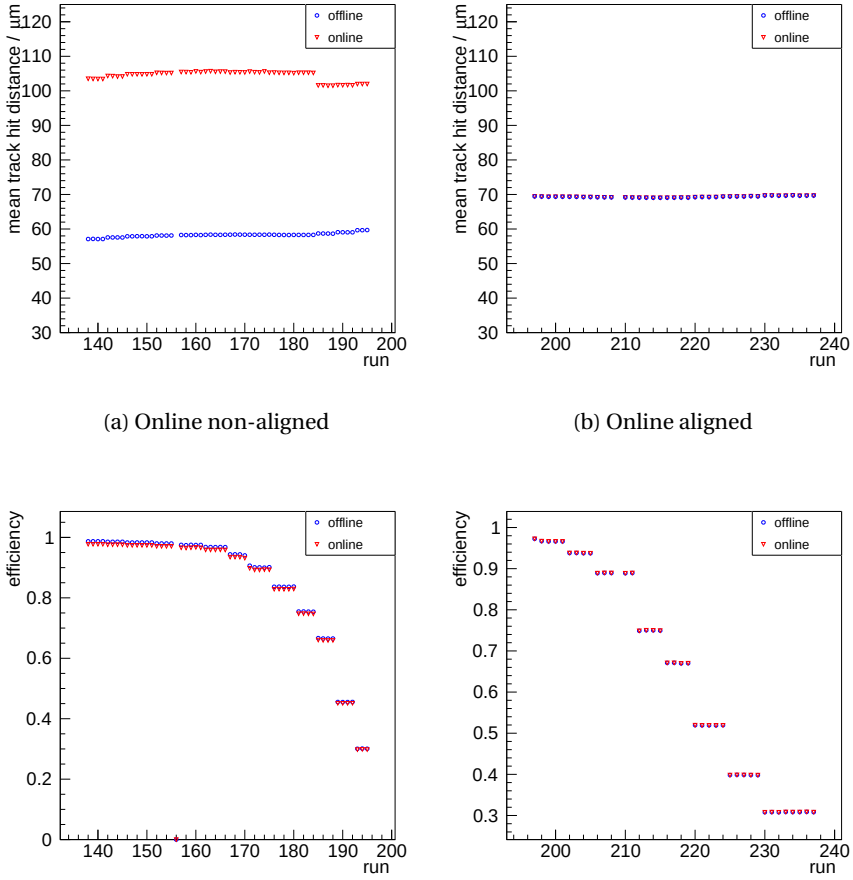

(a) Online non-aligned

(b) Online aligned

(c) Online non-aligned

(d) Online aligned

Figure 6.14: Comparison between online and offline efficiency calculations. All offline results are obtained with a correct alignment. **top:** Mean hit track distance for the on and offline data analysis. **bottom:** Efficiency as function of the run number for to threshold scans.

itored. The online monitoring, which is the next step directly after the online efficiencies and processes 96.32 % of the data written to disk.

The mean track hit distance as a function of the run is shown in the upper part of figure 6.14 for the two scans. The mean distance is almost halved for the offline analysis for the first scan, see figure 6.14a and identical to the online differences, if the correct geometry is applied, as expected. The efficiency is accordingly correlated: Running with an aligned geometry reproduces the online results offline. Using a non-aligned geometry underestimates the efficiency by less than 1 % due the search window cut of 400 µm.

7 EUDET-TELESCOPES

The DESY-II testbeam [77] facility provides a precise reference tracking telescope called EUDET-telescopes [78] based on six layers of MIMOSA-26 [79] MAPS sensors. They are fully integrated into the EUDAQ framework [80]. The EUDAQ-framework is a network based DAQ system that offers the possibility to integrate essentially any DUT. It also handles data storage, online monitoring and run control.

MIMOSA-26 sensors

The MIMOSA-26 sensors have a pixel pitch of $18.4 \times 18.4\,\mu m^2$, have 512 columns and 1152 rows, resulting in an total active area of $\approx 2\,cm^2$. The sensors are read out in a rolling shutter mode, with all columns being read out in parallel for each row. Each readout circle, looping over all rows, takes 115 µs. The signal detection threshold is set to a value corresponding to six times the RMS of the sensor noise[1]. Hit-data is digitized on chip and zero suppressed.

Testbeam layout

EUDET-telescopes consist of a total of six layers and are arranged as shown in figure 7.1. The up and down-stream reference triplets are put as close as possible to the DUT to minimize effects from multiple scattering. The spacing in the two arms is set to approximately 15 cm, as equidistant spacing leads to the best resolution on the DUT for very high momenta. A set of four scintillators coupled to PMTs is used to generate a coincidence trigger.

7.1 EUDAQ TESTBEAM DAQ SYSTEM

Data taking using the EUDET-telescopes is based on the EUDAQ software framework and a central trigger logic unit (TLU) to assign common IDs to traversing particles. The TLU features a coincidence unit, which creates an AND coincidence of up to four signals (typically the four scintillators framing the MIMOSA-26 planes). After finding a coincidence, the TLU sends a trigger with a 14 bit ID (TLU-ID) to all hardware components of the test setup. The coincidence input is vetoed until all hardware components have acknowledged the trigger and processed the data. Afterwards the next trigger can be processed.

1 Tuning files for different noise levels are provided by the facility

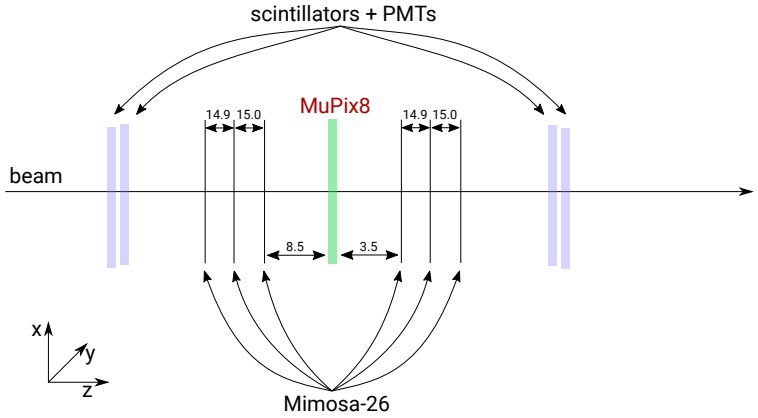

Figure 7.1: Layout of the Mimosa telescope. Four scintillators frame the six reference pixel sensors and the device under test. The given distances are in cm and represent the setup of the DESY II beam test campaign in March 2018. The DUT is mounted on a rotational xy-stage.

The EUDAQ software framework is sketched in figure 7.2: a central run control is in charge of controlling all hardware components. Each hardware component runs on a local machine and has a so called producer. The producers are connected with the run control via TCP/IP sockets. All producers need to have a set of mandatory steering functions, which can be called by the run control: Start/stop run and configure.
After starting a run, the producers send data sorted by TLU-IDs to a central data collector. The data collector waits until events from all subsystems are received and writes the data, sorted by TLU-IDs to disk. Additionally, the data can be forwarded to an optional monitoring unit. Error and status messages from all producers and the run control are collected in a log collector.

MuPix *integration*

To integrate a MuPix into the EUDAQ framework, a producer and a data converter are required. The latter is responsible to transform the `telescope frame` data into the EUDAQ data format and back.
The producer for the MuPix8 is realized as a separate thread in the Single Setup, see figure 7.3. It is implemented as an interface between the Single Setup and the EUDAQ. Start/stop signals are forwarded to the `Mainwindow`, which in turn starts and stops the readout. The data is not written to disk with the *file writer*, but forwarded to the *EUDAQ producer*,

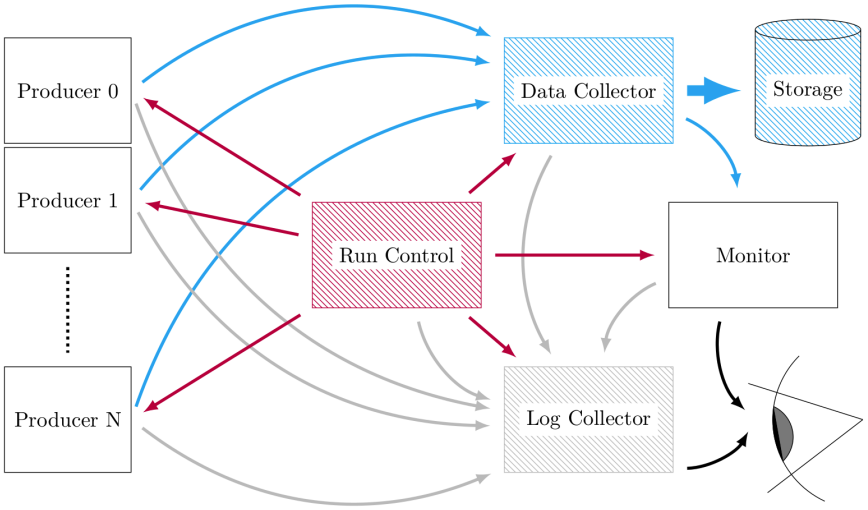

Figure 7.2: Layout of the EUDAQ DAQ system [81]. Each hardware component, has a producer running on a local host. The run control configures the subsystems and steers the readout via TCP connection. The prodcuers send data to the data collector, where the data is merged and send to storage and monitoring.

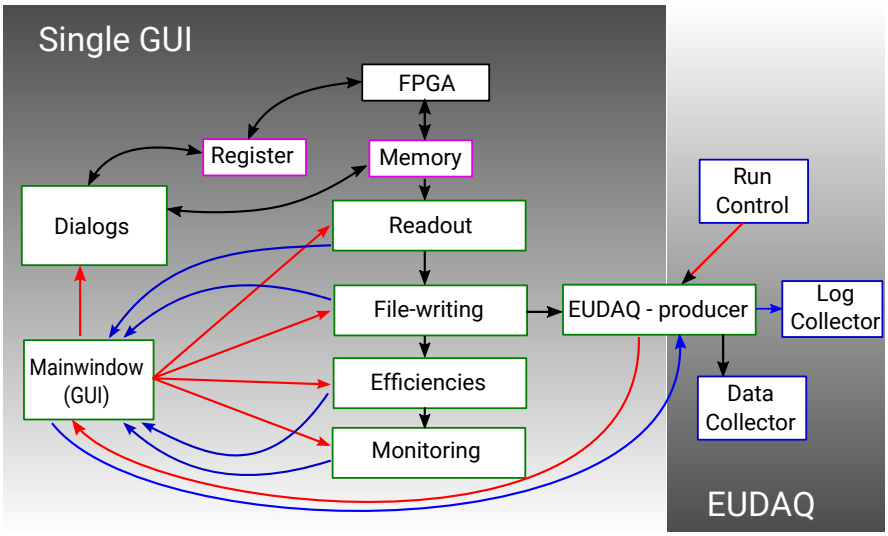

Figure 7.3: Block diagram of the EUDAQ integrated MuPix DAQ. The EUDAQ-producer serves as an interface between the EUDAQ and the MuPix DAQ. The blue rectangles are EUDAQ components. The green ones are threads within the Single Setup and the magenta ones are *memories*. The black arrows indicate data flows, the red ones steering and the blue ones status information.

which buffers the data until a TLU-ID is received[2]. Upon receiving a TLU-ID, the buffered `frames` are merged to one EUDAQ standard event and sent to the data collector. Due to a feature in the firmware of the TLU, it can happen, that TLU-IDs are skipped. If a TLU-ID is skipped, the `EUDAQ producer` sends an empty dummy frame to avoid back pressure in the Data Collector. These events are marked and ignored in later analysis.
Error and status messages are sent over the *EUDAQ producer* to the central log collector.
To perform detailed time resolution studies, the coincidence of the EUDET-type scintillators is sampled with a 500 MHz counter on the FPGA of the MUPIX8 DAQ. This is required to exactly assign hit timestamps to the triggers.
The FPGA in the SINGLE SETUP computer handles the handshake with the TLU and transfers the TLU-IDs to the readout PC, encoded as trigger with a special ID.

7.2 ANALYSIS PROCEDURE

The analysis procedure is based on to the MUPIX TELESCOPE analysis procedure and fully reuses the tracking and matching code. The raw data stored by the EUDAQ Data Collector is converted into a ROOT tree with the column and row addresses of each hit. For the MUPIX8, additionally, the time and time-over-threshold information is stored. In a second step a noisy pixel removal is applied. The noise rates of the MIMOSA-26 are unknown. Therefore all pixels, which have a factor five more hits than the average pixel are removed on the reference planes and on the DUT-plane. The noisy pixel removal reduces the tracking combinatorics significantly and avoids biases in the alignment. In the last pre-processing step, clustering on all layers is applied to achieve the highest hit position precision on the reference layers. The results are summarized in figure 7.4 for layer 2 and run 209: 251 pixels are masked and removed in the first step, reducing the total number of hits by a factor five. Due to an average cluster size of 1.9 for layer 2, the amount of hit candidates per plane is halved again, resulting in one million remaining particle hits per plane and run.

Above procedure is also applied for the DUT layer. Figure 7.5 summarizes the results of the clustering step. The MIMOSA-26 reference layers, see figure 7.5a, have significantly higher average cluster sizes between 1.8 and 1.98 compared to the MUPIX8, which has average cluster size of approximately 1.15. This is consistent with expectations from the different pixel sizes.

2 The MUPIX prototypes are significantly faster compared to TLU and MIMOSA-26. Therefore the TLU-ID is delayed in the data stream.

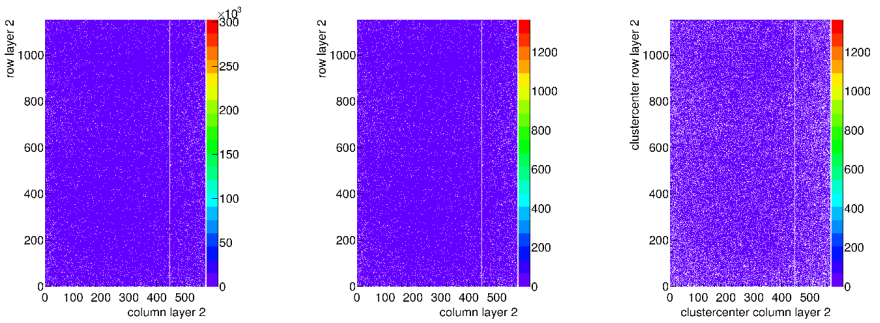

(a) Raw hitmap. (b) Hitmap without noisy pixel. (c) Clustermap.

Figure 7.4: Exemplary hit- and clustermaps for reference layer 2 of run 209. Removing 251 noisy/hot pixels out of 589824 pixels reduces the total hit amount by a factor five. An average cluster size of about 1.9 further reduces the data sample to approximately 1 million potential particles. The vertical line in the figures is created by a non working column, where the row position is always set to the same values. Note the different z-scales.

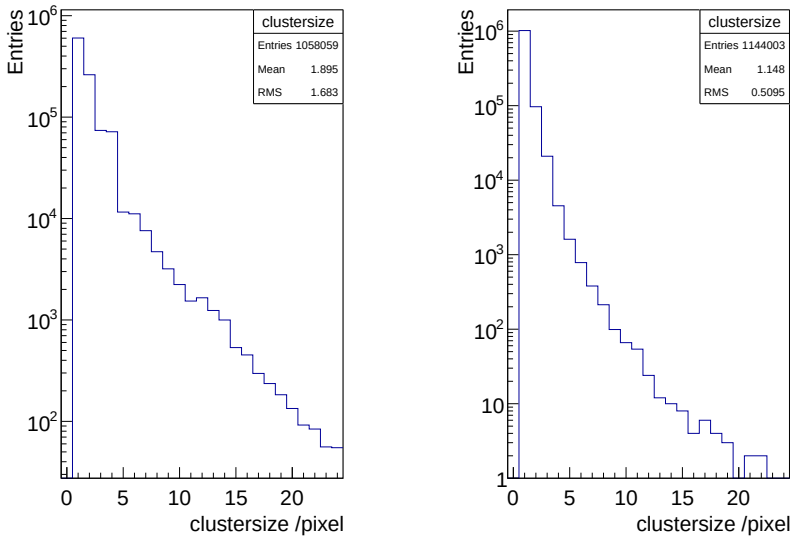

(a) Mimosa. (b) MUPIX8.

Figure 7.5: Cluster size for MIMOSA-26 reference layer 2 and MUPIX8-DUT.

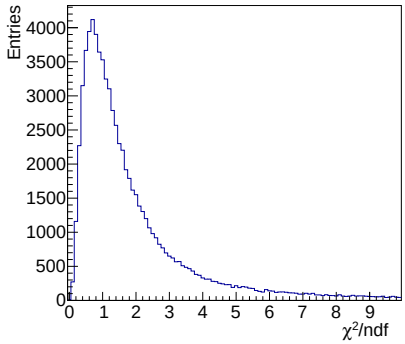

Figure 7.6: χ^2 distribution obtained for GBL-tracks after millepede-II alignment.

7.3 ALIGNMENT

The pre-processed data is used to reconstruct particle trajectories. However, as the planes are not perfectly aligned mechanically, a software alignment has to be applied. To optimize the precision of the alignment of the reference planes, dedicated alignment runs without DUT are taken. A pre-alignment is applied using the correlations of the x and y positions of different layers. This allows for a precision of roughly 300 µm for each plane, sufficient to apply a track based alignment, based on the alignment code for the *Mu3e* detector [63]. To avoid confusion, events with exactly one cluster on each plane are selected and a GBL fit is applied. A specific binary format which can be read by millepede-II [82] is created and the mis-alignment is automatically corrected. The alignment parameters, x and y positions and rotations, are released step by step: First, only shifts in x and y are allowed, while in a second step only rotations around the beam axis (see section 5) are allowed. In a third step, z-rotations and x/y-shifts are allowed simultaneously. The mean values of the residuals are well below 1 µm. The residuals have an RMS below 3 µm. The χ^2 distribution for reference tracks is shown in figure 7.6.

For the characterization runs the DUT is aligned in a similar fashion as the reference system: The DUT is pre-aligned using correlations and events with one track pointing onto the DUT are selected. The closest hit to the extrapolated track intersections is assigned to the track and the unbiased residual is analyzed, with the alignment parameters of the reference being fixed. At first, x/y shifts are corrected. Subsequently rotations around the z axis are taken care of and in a last step, also rotations around x/y are corrected. The resulting alignment is shown exemplary in figure 7.7. The $x(y)$ residual is below 2.3 µm (3 µm) and has a width of 27.6 µm (28.6 µm), which is consistent with the expected pixel resolution of 23.4 µm (23.1 µm) and non accounted scattering on the layers. The slightly worse resolution for the y residuals can be explained by a tiny rotation which is not accounted for.

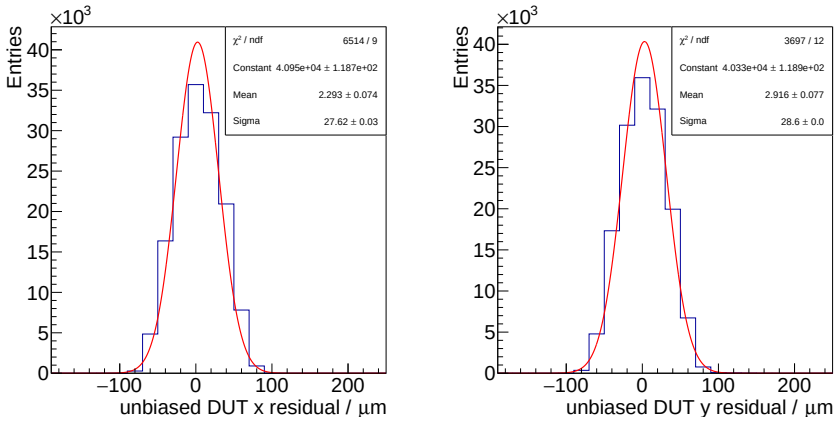

(a) X residual (b) Y residual

Figure 7.7: Unbiased residuals for a combination of runs 452 to 505 and a reference track cut of $\chi^2 < 40$.

Both residuals are plotted against both sensor axes in figure 7.8. A linear fit to the central region with sufficient statistics shows, that the rotations are well under control with a mean residual drift below 1.8 µm over the sensor, which corresponds to an alignment error of 0.1 mrad. The telescope pointing resolution is studied in the following section in more detail.

Alignment stability

Small movements of the telescope planes can spoil the pointing resolution. Therefore, the stability is checked by studying the residuals over a set of runs. Figure 7.9 shows the biased residuals of the reference planes as well as their RMS using straight track fit. The mean residuals are stable on the 1 µm level over a complete set of runs.

The different RMS values for the layers are explained by the geometry: Layers 0 to 2 and 3 to 5 build triplets of very thin sensors, see figure 7.1. The straight track fit without scattering ignores the DUT and multiple scattering. The two triplets can be considered as two hits at the center of gravity of the triplets. This leads to an anti-correlation between the outer triplet layers, see figure 7.10a. A linear fit to the correlation results in a slope of approximately -1 with an offset corresponding to the alignment error. Figure 7.10b shows the x residual correlation for the inner layers of both telescope arms. The horizontal and vertical structure is created by the loose χ^2cut.

7.3.1 *Resolution*

The telescope resolution is crucial to resolve effects on very small scales like inefficiencies at certain positions of the device under test. Better res-

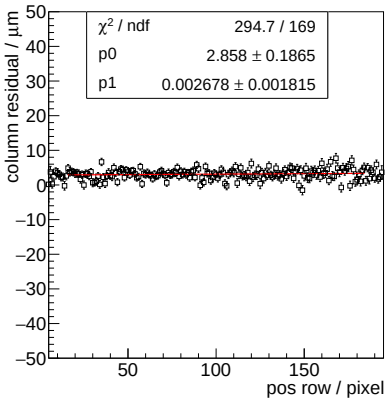

(a) Column residual along the pixel row.

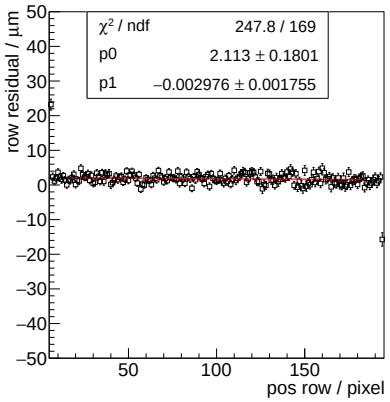

(b) Row residual along the pixel row.

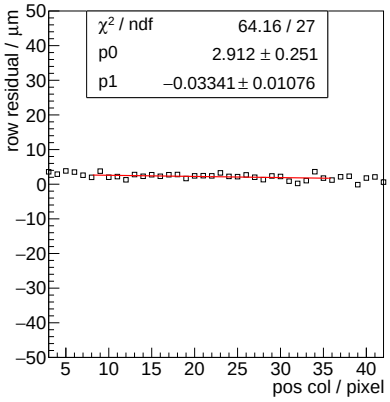

(c) Column residual along the pixel column.

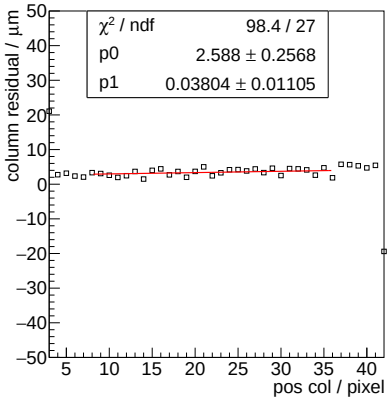

(d) Row residual along the pixel column.

Figure 7.8: Column and row residuals against the column and row positions for runs 452 to 505 an a reference $\chi^2 < 40$. Each combination is fitted with a linear function. The largest rotation creates a residual drift of only 1.8 µm over the sensor.

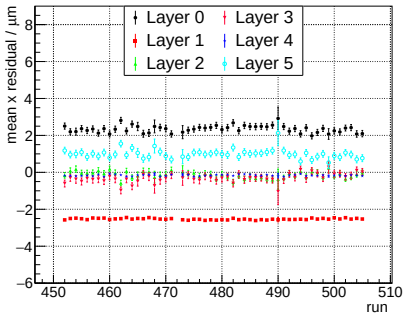

(a) x residual.

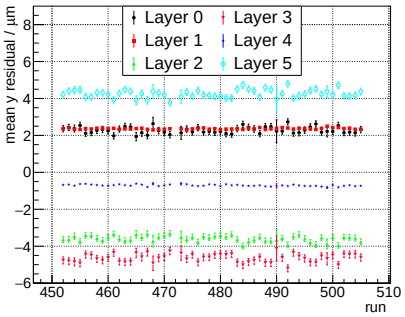

(b) y residual.

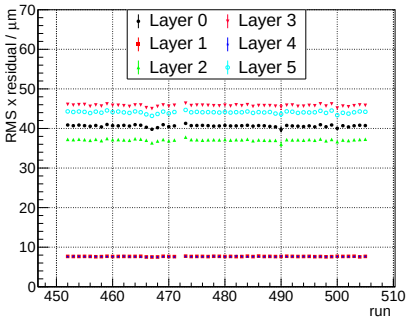

(c) RMS of x residual.

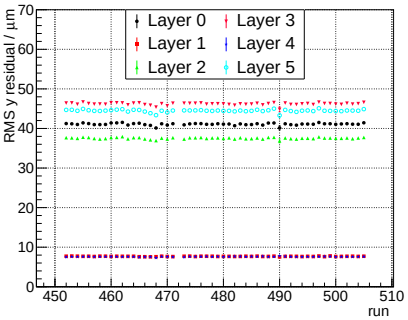

(d) RMS of y residual.

Figure 7.9: Biased residuals and their RMS width against the run number. The residuals are stable on the 1 µm level over the complete run set.

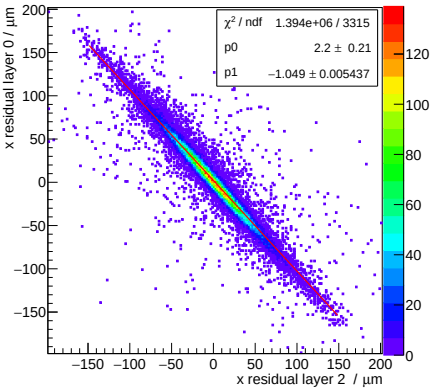

(a) Residuals of layer 0 vs layer 2

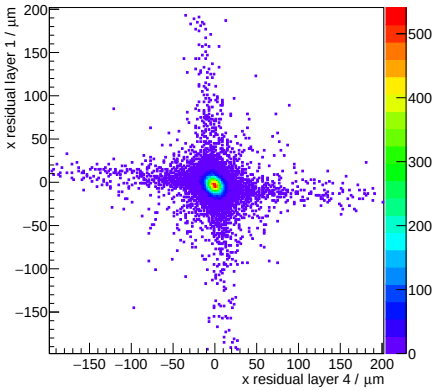

(b) Residuals of layer 1 vs layer 4

Figure 7.10: Correlation between the x residuals of the tracking layers. (a) shows the correlation of layers 0 and 2, exemplary for a set of outer triplet hits. (b) shows the correlation between the inner layers of both triplets, which dominate the track fit.

olutions allow more detailed sensor studies. Therefore different extrapolation/interpolation methods are tested and compared.
The Gaussian fit to the unbiased residuals in figure 7.7 is sufficient for alignment, but it cannot be used to determine the telescope's pointing resolution. The pointing resolution is determined using the matching residuals along the x and y axis. For a perfect telescope with infinitesimal resolution and a fully efficient, it would reassemble a box with the pixel pitch as width. A box function is a combination of two step functions:

$$\text{box}(x) = \begin{cases} 0 & \text{if } (|x-c|) > w/2 \\ 1 & \text{if } (|x-c|) \leq w/2 \end{cases} \tag{7.1}$$

with the w being the width of the box and c the center. A finite resolution smears out the edges, which can be described by an error function, which also referred to as s-curve:

$$\text{erf}(x) = \frac{2}{\sqrt{\pi}} \cdot \int_0^x e^{-y^2} dt \tag{7.2}$$

An error function can be used to describe only one pixel edge located at position $x = 0$. To fit both edges with one fit, the pixel center position c, a scaling factor A and the resolution σ are introduced, leading to the following function for $w >> \sigma$:

$$f(x) \approx A \left[\text{erf}\left(\frac{w/2 - |x-c|}{\sigma\sqrt{2}} \right) + 0.5 \right] \tag{7.3}$$

Three different resolutions are plotted in figure 7.11 exemplary. For larger values of σ, e.g. worse resolution, the edges are smeared out more. In the following, different track extrapolation methods are evaluated and compared based on the resolution σ and number of tracks N as well as the resolution power $\sigma/\sqrt{(N)}$ as a function of the χ^2cut.

7.3.1.1 *Interpolation with a straight track*

The resolution of a straight line fit through all six layers strongly depends on the χ^2-cut: Tighter cuts lead to tracks with smaller average residuals and less accepted scattering. However, the DUT can be rather tick and large angle scatters are likely to occur. For a χ^2-cut of 10 the resolution is shown in figure 7.12. The resolution, if the pixel size is a free parameter of the fit, along x/y is 6.6(5) µm/6.1(5) µm and the fitted pixel pitch is correct within 1 µm, compare top plots in figure 7.12. The number of reconstructed tracks is orders of magnitude lower compared to the tracks which could be used for alignment, see figure 7.7. The effect of the χ^2-cut is shown in figure 7.13: The resolution decreases with looser cuts (7.13a), consistent with the interpretation of allowing larger scattering angles and the observed increase in reconstructible tracks, (7.13b). The resolution power can be used to find the optimum between resolution and available statistics and is shown in

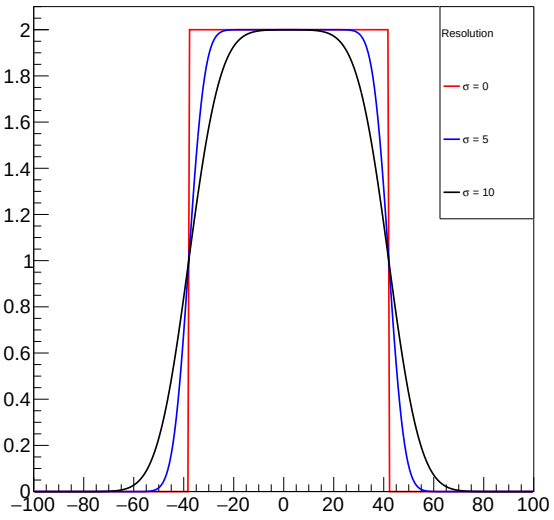

Figure 7.11: Visualization of the resolution fit function for different resolutions.

figure 7.13c. The minimum is located around a χ^2 of 500, where the resolution is in the order of 25 µm. This is unacceptable for a precision analysis, as one typically looks for effects on a scale below 10 µm. The necessary high resolution decreases the available amount of tracks too much and makes a simple straight line fit an unsuitable fit method for the analysis.

7.3.1.2 *Extrapolation with scattering at the DUT*

The EUDET-telescopes provide up- and downstream arms with three pixel layers each. This is sufficient to perform a straight line fit on both arms. Tracks from both sides with a $\chi^2 < 10$ are extrapolated to the DUT-plane. If the intersection points are closer than a certain distance to each other, the center of both intersections is used as extrapolated track position. This method is referred to as double-triplet fit. Ambiguities are resolved by selecting the track pair with smaller distance. Figure 7.14 shows the resulting pointing resolution for a maximal distance of 30 µm between the two extrapolated intersections. With 6.54(3) µm/6.20(3) µm along the x/y axis, the pointing resolution is comparable to the straight line fit from above at a $\chi^2 < 10$. The number of reconstructed tracks, however, is a factor 350 larger. The fitted pixel pitch also agrees with the known size within 1 µm. Fitting from both sides has the additional advantage of being independent of the thickness of the device under test, as long as the displacement of the particle while traversing the DUT can be neglected .
Even if the maximal allowed distance between the up- and downstream extrapolation is increased, the resolution decrease is moderate as shown in figure 7.15a. The number of reconstructed tracks flattens out starting at a maximal allowed distance of 30 − 40 µm. Similarly to the straight line fit

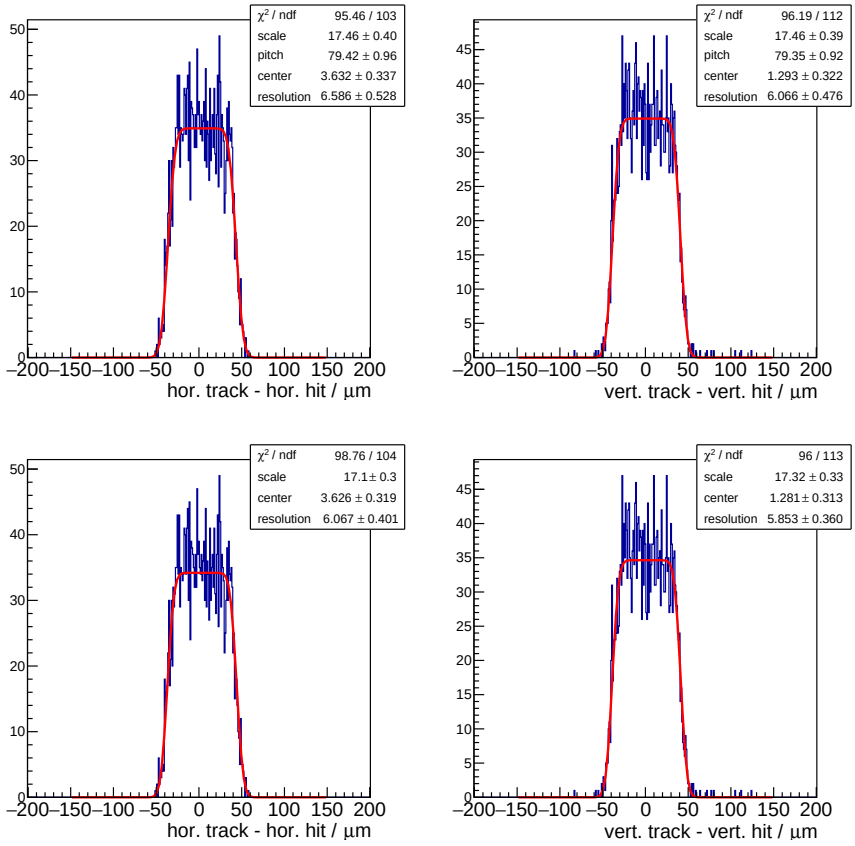

Figure 7.12: Pointing resolution on the device under test for a straight line fit through all six reference layers with a $\chi^2 < 10$. The two top plots leave the pixel pitch as a free parameter, while the two bottom plots are fitted assuming the known pixel pitch. Runs 452 to 505 are combined. Empty bins are ignored in the fit and lead to different ndf for the horizontal and vertical fits.

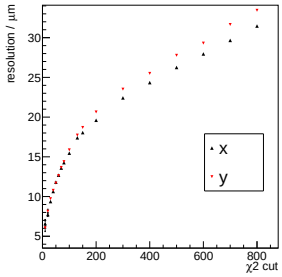

(a) Resolution

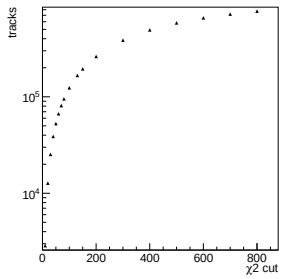

(b) Number of reconstructed tracks

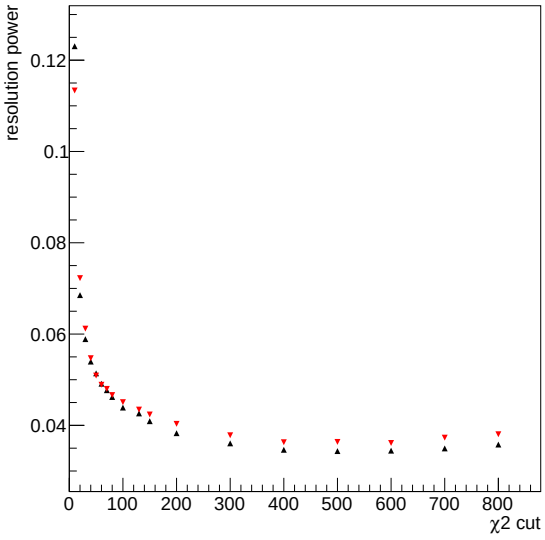

(c) Resolution power

Figure 7.13: Influence of the χ^2cut on the resolution and the number of reconstructed tracks for runs 452 to 505. The resolution power is shown on the right.

through six layers, the resolution power can be defined as a function of the maximal allowed distance, see figure 7.15c. The minimum is broad and located around a maximal distance of 35 µm. For the following analysis a maximal distance of 30 µm is chosen to be conservative.

Using only one of the two telescope arms results in a significantly reduced resolution, as the constraint from the second side is missing and is therefore not considered for the sensor analysis.

7.3.2 *Device under test material measurement*

The procedure introduced above using both arms individually allows not only to reconstruct the intersection point with high precision, but also the kink angle on the device under test which can be used to compare the measured scattering distribution with the expectation from the estimated material budget. A comparison between the results and expectations can be used to verify the reconstruction method. After being verified, it can be used to check the material calculations. The angles in x and y are independent and can be calculated from the slope differences:

$$\theta_p = \arctan(s_u) - \arctan(s_d) \approx s_u - s_d \tag{7.4}$$

θ_p is the planar scattering angle and $s_{u/d}$ are the up- and downstream slopes. For small angles, the $\arctan(t)$ is approximately t. The average

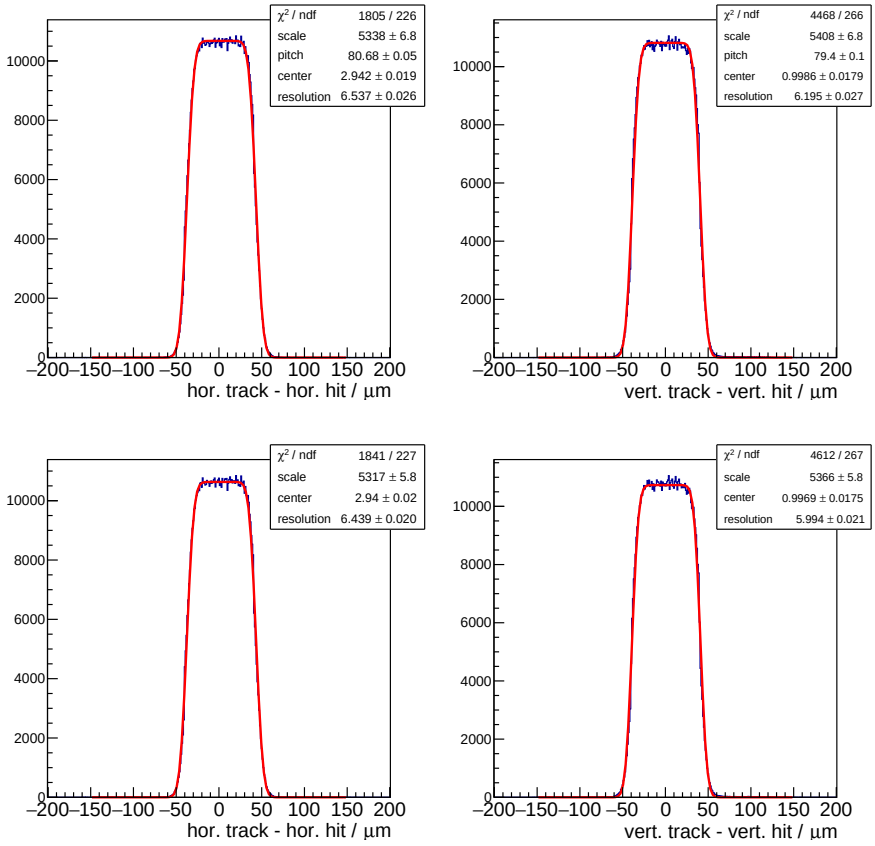

Figure 7.14: Pointing resolution on the device under test for the double-triplet fit with a maximal spacing of 30 µm. The two top plots leave the pixel pitch as a free parameter, while the two bottom plots are fitted assuming the known pixel pitch. Runs 452 to 505 are combined. Empty bins are ignored in the fit and lead to different ndf for the horizontal and vertical fits.

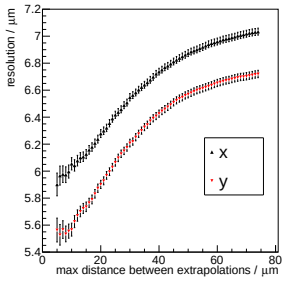

(a) Resolution

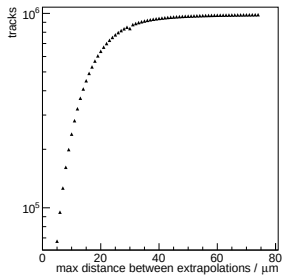

(b) Number of reconstructed tracks

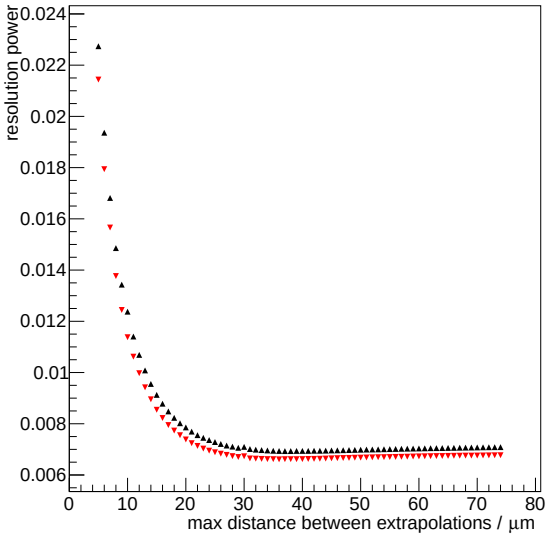

(c) Resolution power

Figure 7.15: Influence of the maximal distance between the up- and downstream arm tracks of the telescope on the pointing resolution and the number of reconstructed tracks for runs 452 to 505. The resolution power is shown on the right.

scattering angle is vanishing and its width is given by θ_{MS}, as defined in section 3.1.2. To fit the distribution of kink angles along x and y simultaneously a two dimensional Gauss-function is used:

$$g(\theta_x,\theta_y) = 2 \cdot Ae^{-0.5\left(\frac{\theta_x-\mu_x}{\sigma_x}\right)^2} e^{-0.5\left(\frac{\theta_y-\mu_y}{\sigma_y}\right)^2} \tag{7.5}$$

A describes the normalization, $\sigma_{x/y}$ the scattering angle width in x/y and $\mu_{x/y}$ are the mean scattering angles to take mis-alignments into account.

The estimated material budget of the devices under test is shown in table 7.1. The width of the scattering distribution for positrons with a momentum of 4 GeV and the estimated material budget from the March'18 campaign is $\theta_{MS} = 4.8 \cdot 10^{-4}$ rad. Figure 7.16 shows a 3D plot of the scattering angles with a two dimensional Gaussian fit. The mean scattering angle in both dimensions are below $5 \cdot 10^{-5}$ rad. The $x(y)$-width is $5.029(4) \cdot 10^{-4}$ rad ($5.058(4) \cdot 10^{-4}$ rad), which agrees within 5 % with the expectations from the material budget estimation.

Similarly, the material budget estimation from the June'18 setup can be compared to the measurements, where the reduced particle momentum increases the scattering angle and levels the smaller material budget. Performing the same fit on the data a $x(y)$-width of $4.66(1) \cdot 10^{-4}$ rad ($4.70(1) \cdot 10^{-4}$ rad) is extracted. This is systematically larger than the theoretical prediction, due to an incomplete material budget calculation, as the

	thickness [mm]	scattering length [mm]	$\frac{x}{x_0}$ [‰]	θ_{MS} exp. [10^{-4} rad]
March'18 setup 4 GeV				
MuPix8	0.725	93.7	7.7	
Insert	1.55	159	9.7	
PCB	1.55	159	9.7	
total			**27.1**	**4.8**
June'18 setup 3 GeV				
MuPix8	0.1	93.7	1.1	
Insert	1.55	159	9.7	
PCB	0	159	0	
total			**10.8**	**3.9**

Table 7.1: Material budget for the DUT at DESY. The glue between sensor and PCB is neglected.

scattering in air and the glue are ignored. Both have an increased influence due to the reduced beam momentum.
Nevertheless, the results underline that the fit model is well suited for a precision analysis and can even be used to determine the overall scattering length of the device under test. Adding the position information allows to check the homogeneity of sensor thickness.

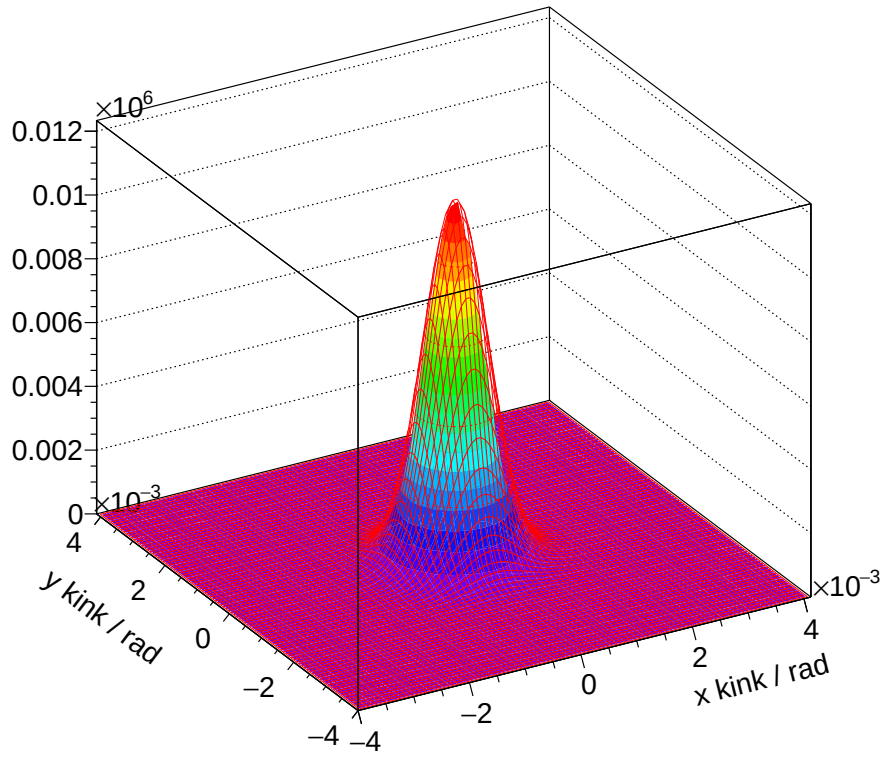

Figure 7.16: 2-dimensional distribution of the kink angles on the DUT in colors with an 2-dimensional Gauss fit for runs 452 to 505 from the March'18 campaign using 4 GeV positrons.

Part III

SENSOR CHARACTERIZATION

Sensor characterization in the laboratory and by using particle beams is crucial for the development of new sensor technologies and detectors. HV-MAPS, proposed for *Mu3e*, have moved from small-scale prototypes to full-scale sensors recently. This transition involved several challenges, especially in the signal routing schemes and the power distribution.
At the beginning of part III an overview of the testbeam facilities used for characterization studies is given. Selected results of the small-scale MuPix7 and a detailed study of the large-scale prototype MuPix8 are presented next. Both sensors are compared. The part is concluded with a summary of an irradiation campaign of the MuPix7.

8 TESTBEAM FACILITIES

Testbeam facilities offer the unique opportunity to test sensor prototypes in a realistic environment. They are optimally suited to study the hit detection efficiency, which cannot be done properly in laboratory measurements with radioactive sources.
The majority of characterization results presented in the following chapters has been obtained at testbeam facilities providing different particles species, momentum ranges and rates, which are introduced in the following. In the scope of this thesis 14 campaigns, mainly at DESY, PSI and MAMI have been carried out.

8.1 DESY-II TESTBEAM

The DESY-II testbeam facility [77] is located in Hamburg. DESY-II serves as pre-accelerator for the PETRA-III storage ring, which is in turn used as x-ray radiation source. DESY-II is used to accelerate electron bunches to an energy of 6 GeV. Three testbeam lines can provide either electron or positron beams originating from converted bremsstrahlung beams from a carbon fibre target in the DESY-II ring. A dipole is used to select the particle species and the energy ranging from $1-6$ GeV. Rates in the order of a few kHz/cm^2 are available.

8.2 πM1 AND πE1 TESTBEAM AT PSI

Contrary to DESY-II, the πM1 and πE1 beam lines at PSI [23] provide a mixed particle beam consisting of pions, electrons, muons and protons, with pions being the dominant component.
Two ring cyclotrons accelerate protons, pre-accelerated by a Cockcroft-Walton, to an energy of 590 MeV with a current of up to 2.4 mA corresponding to 1.2 MW beam power – the most powerful beam in the world. The protons are guided serially to two targets, where secondary particles are created. Each target is surrounded by several beam lines, which guide the secondary particles to the experimental sites.
The rather low momentum of the initial protons limits the available momentum in the πM1 and πE1 area to about 500 MeV/c. However, the beam momentum is usually set to approximately 300 MeV/c, close to the MIP momentum of pions. The high intensity of the primary proton beam allows for high particle rates in the testbeam area.

8.3 X1 TESTBEAM AT MAMI

The Mainz Microtron (MAMI) [83, 84] is a three stage racetrack microtron providing a continuous beam of electrons, which can be polarized on request. Maximal energies of 1.5 GeV can be provided in the last stage, with a highly focused beam with less than 1 mm diameter. After the second stage, electrons with an energy of 885 MeV can be extracted and transferred to an x-ray test facility. The extraction beamline is open and allows for test system installation. The machine can provide several 10 MHz particle rate. The high rate on the small area makes MAMI an optimal facility to stress test DAQ systems and sensors.

9 MUPIX7 STUDIES

The MUPIX7 is the first prototype studied in the scope of this thesis. Detailed characterization studies during testbeam campaigns as well as in the laboratory are already summarized in several Bachelor, Master, doctoral theses and publications [28, 50, 51, 54, 75, 85–88]. The MUPIX TELESCOPE DAQ has been developed and improved throughout these characterization studies.
Selected results of these characterizations are summarized in the following to provide a basis for understanding the challanges, improvements and performance differences of the MUPIX8. Based on the MUPIX TELESCOPE and a testbeam campaign at PSI the DAC settings have been optimized with respect to power dissipation and are published in [50]. The sensors time resolution has been measured to be 14.2 ns [50]. Crosstalk studies have also been presented in [50]. The influence of sensor rotations has been evaluated during a campaign at DESY-II.
All presented measurements have been done with sensors tuned to a noise rate of 1 Hz/pixel without beam. The cuts have been analyzed systematically in [75] and it could be shown, that a search radius of 800 µm is sufficient to also include the tails of scattering effects, without becoming noise influenced due to the time cut of ±48 ns for the hit matching. The time cut on the reference track is set to ±16 ns.

POWER DISSIPATION OPTIMIZATION

To fulfill the Mu3e cooling requirements, a maximal power dissipation for the pixel sensor of 400 mW/cm^2 can be tolerated. The power dissipation is heavily setting dependent, driven by the DAC settings steering the current sources for the amplifier and comparator. To ensure a high hit detection efficiency, the DAC values have been set to their maximum value at the beginning of the sensor characterization, as one naively expects the best performance if the amplification is maximized. The full list of DAC settings can be found in Appendix C.
The DAC settings at the beginning of the studies consume 1 W/cm^2, which is above the cooling limit. The sensors can be operated efficiently, see figure 9.1. To reduce the power dissipation of MUPIX7, the amplifier and comparator steering DAC values are reduced in several steps. Three different settings with reduced power consumption down to 225 mW/cm^2 are tested.
The results of threshold scans for the four DAC settings are summarized in figure 9.1. Obviously, the DAC settings with the highest power consumption are not optimal, especially at higher thresholds, a larger efficiency re-

duction is observed. The lowest power dissipation settings lead to a reduced overall response, comparable to the highest power settings. The settings with 300 mW/cm^2 and 400 mW/cm^2 show the best performance. The noise behavior of the four threshold scans is also varying. All have a flat region in common that is created by beam background which is not subtracted in these measurements. At a certain threshold (0.75 V for the 300 mW/cm^2 scan for example) the noise starts to rise exponentially. These points correspond to the tuning thresholds at which the sensors per pixel noise rate is optimized to be 1 Hz/pixel.
As less power consumption is advantageous for any detector system, and especially Mu3e, the 300 mW/cm^2 are used as default DAC settings for further characterization studies. These settings have been varied in a small range in a more systematically way in [86], to further improve the sensor's performance with the conclusion that only small improvements in the power consumption are possible without decreasing the efficiency. The operational region fulfilling the *Mu3e* requirements, i.e. efficiency above 99 %, is small, even with optimized settings.

MEASUREMENTS WITH ROTATED SENSORS

In contrast to test beam measurements, particles usually penetrate the sensors under different angles. This has several implications: On the one hand, the charge deposited in the effectively larger depletion zone increases and thus the maximum signal height. On the other hand, the charge is more likely to split between two pixels if the tracks are not vertical. This can reduce the amount of charge deposited in a pixel as long as the effective path is not doubled. By varying the DUT rotation and calculating the probability to create a charge sharing cluster, the thickness of the depletion zone can be calculated [28]. The effect of tilting the sensor is shown by threshold-scans under different angles in figure 9.2 for 4 GeV positrons. The tested sensor is fully efficient already for perpendicular tracks. Increased charge sharing probabilities for rotated sensors do not reduce the efficiency of a sensor that is already fully efficient in vertical impacts. Therefore, the signal height increase dominates over the increased charge sharing and the threshold dependency of the efficiency is reduced for larger rotations. The effective depletion thickness is doubled for a rotation angle of 60°. For a rotation of 60°, the sensor stays above 99 % efficiency over a range of 90 mV, compared to 15 mV for the unrotated sensor. A similar improvement in the signal height is expected by changing the substrate's resistivity from 20 Ωcm to 80 Ωcm.

CROSSTALK

Line crosstalk is measured by exploiting the topological pixel patterns, which can be tagged easily. The probability of triple crosstalk is exemplary shown in figure 9.3 as a function of the row address. The distribution is flat

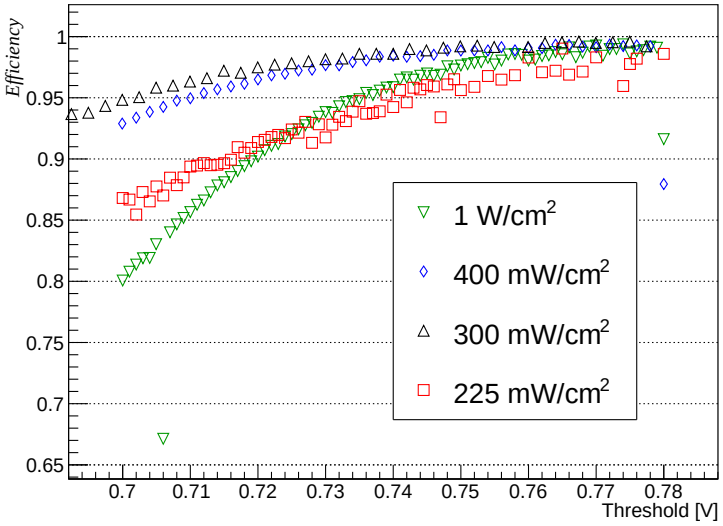

(a) Efficiency

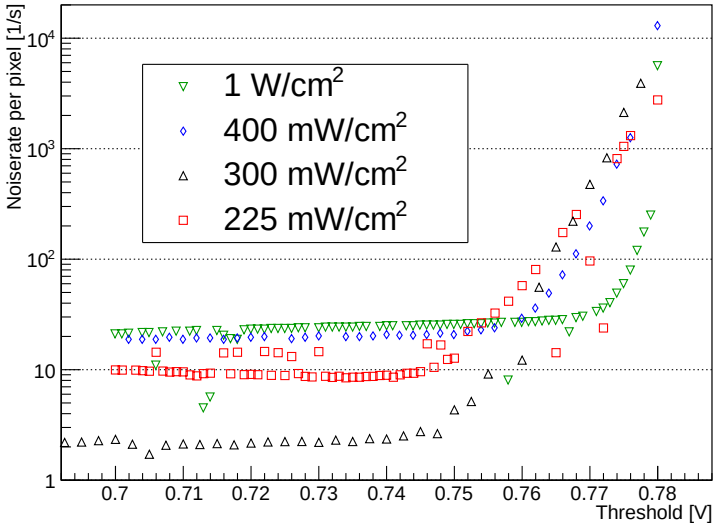

(b) Noise

Figure 9.1: Efficiency and noise as function of the threshold for different DAC settings with the calculated power dissipation. Data has been taken with 300 MeV/c pions and electrons. Note that the two stage amplification leads to negative pulses and the baseline is set to 800 mV. Taken from [50].

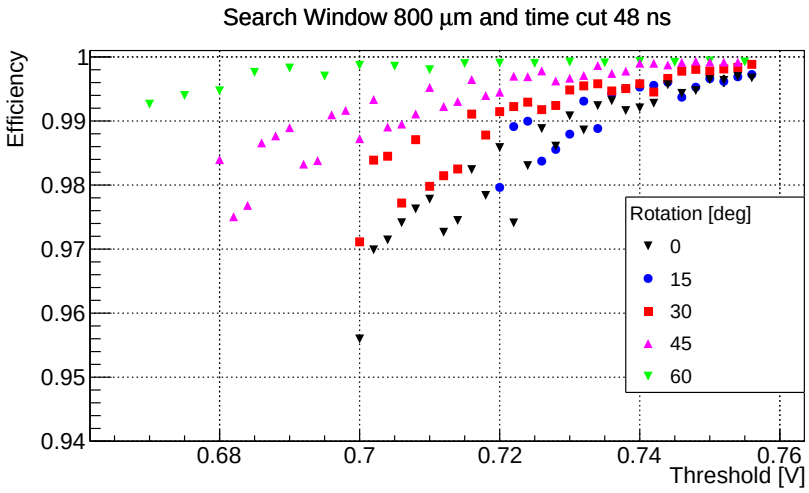

Figure 9.2: Efficiency as function of the threshold for different rotation angles.

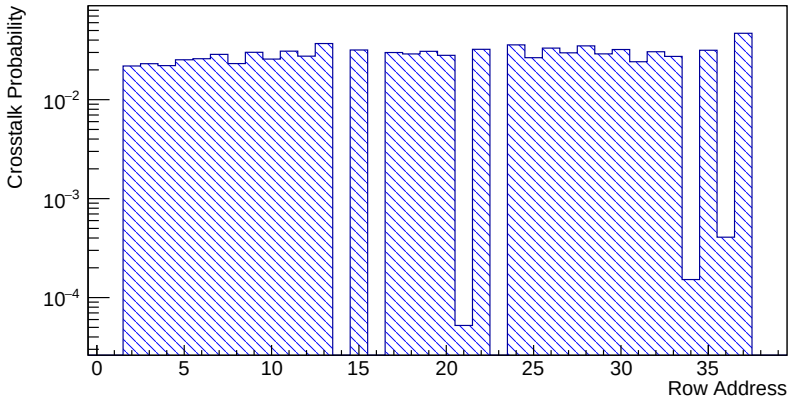

Figure 9.3: Triple crosstalk probability for the different rows. Taken from [50]

over the sensor with some dips. These dips nicely match pixels with connection lines with a larger distance to the neighbors, as shown in figure 4.2. The distance between the connection line of pixels 34 and 36 is roughly twice the normal spacing, which already suppresses visible crosstalk by more than one order of magnitude. The spacing between the lines from pixels 21 and 23 is four times the normal spacing and crosstalk is suppressed by two orders of magnitude. Pixels 14 and 16 have the largest spacing and do not show any crosstalk.

In [86], the crosstalk as function of the threshold is studied. Double crosstalk events occur with a probability of up to 20 %, triple crosstalk events with a probability of up to 10 %.

10 MUPIX8 STUDIES

MUPIX8 is the first-large scale HV-MAPS prototype and characterized in the laboratory as well as during testbeam campaigns at PSI and DESY-II. The obtained results are discussed in the following and compared to the previously presented results from the MUPIX7. For all presented measurements, the power dissipation of the MUPIX8 is approximately 180.8 mW/cm^2 if not stated otherwise. Sacrificing the second amplifier explains the reduction compared to the MUPIX7. The full DAC list can be found in Appendix D.

10.1 LABORATORY TESTS

The laboratory tests of the MUPIX8 are discussed in detail in [54, 68, 89], in particular the sensor commissioning. Therefore, only measurements that are relevant to understand the following testbeam analysis are presented here.

RESPONSE TO RADIOACTIVE SOURCES Two radioactive sources have been used to test the sensor response: Fe^{55} and Sr^{90}. The latter mimics a particle and is used to measure depletion zone dependent signal size. The Fe^{55}-source is an ideal calibration source with three mono-energetic x-ray lines: $k_{\alpha 1}$ at 5.899 keV, $k_{\alpha 2}$ at 5.889 keV and k_β at 6.49 keV [90]. The latter is suppressed by one magnitude. Absorbed x-rays create a tiny charge cloud and therefore a depletion thickness independent signal. In silicon, the formation of a electron-hole pair requires an average energy of 3.65 eV. The iron source therefore creates 1635 electron-hole pairs on average.
In contrast to Fe^{55}, Sr^{90} decays into yttrium via β^--decay, with a decay energy of 0.546 MeV, with a half-life of 29 years [91]. Yttrium in turn undergoes another β^--decay to zirconium with a half-life of 64 hours and a decay energy of 2.28 MeV. Zirconium is essentially stable ($t_{1/2} \approx 2 \cdot 10^{19}$ years). The β^--decay electron can mimic[1] a particle traveling through the sensors depletion zone. However, the energy spectrum of β^-decays is continuous and the low momentum of the electrons lead to large fluctuations in the energy deposit (compare figure 3.3).
Figure 10.1a shows the response of three different sensors on a iron source, corrected for noise. An error function like shape, also referred to as s-curve, is visible for two sensors, with a clear turning point for sensor 084-3-25. Sensor 084-2-03 becomes sensitive to the iron source at lower thresholds of 70 mV, compared to 100 mV for the other two.
The response on a Sr^{90} source for the same sensors is shown in figure 10.1b.

1 Electrons can be stopped and deposit significantly more energy in the material than a MIP.

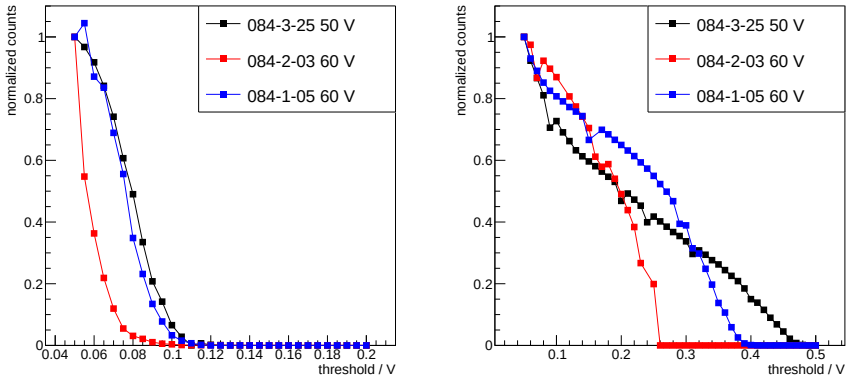

(a) Fe^{55} (b) Sr^{90}

Figure 10.1: Response of three different MUPIX8 sensors to an Fe^{55} and a Sr^{90} source.

The response varies again between the three sensors, but all are sensitive to the signal at higher thresholds compared to the measurements with the iron source. Sensor 084-2-03 is sensitive from 250 mV on, the other ones already at thresholds above 400 mV. The difference between sensors 084-3-25 and 084-1-05, which is not present in the iron measurements, is due to the difference in resistivity – 084-3-25 has a 200 Ωcm substrate, while 084-1-05 is fabricated on an 80 Ωcm substrate. Higher substrate resistivities have a larger depletion zone for identical bias voltages resulting in potentially larger signals. Despite the fluctuations, the Sr^{90} measurements give a rough estimate on the expected signal height for MIPs in the order of 300 – 400 mV.

LINE CROSSTALK The amplitude of capacitive coupling, as discussed in section 3.3, can be studied by injecting charge into a pixel of column zero and measuring the signal height of the analog output[2] on neighboring rows. The amplitude of the analogue output of the MUPIX8 due to an injected signal of about 400 mV, corresponding to an upper limit of the expected signal height from MIPs, in neighboring and next-to-neighboring pixels is shown for several rows in figure 10.2. A clear row dependency is observed: Higher rows show larger signals in the neighboring pixels - consistent with the interpretation of larger coupling due to longer parallel transmission lines. Rows 135 and 100 show no coupling to their lower neighbors, because the line spacing is significantly higher. For Row 10, the coupling capacity is too small to create a signal, that can be distinguished from noise. For the longest line tested, row 197, there is even a small effect on next-to-neighboring pixels visible.
At a typical operation point with a threshold of 50 mV, line crosstalk signals

2 The direct amplifier signal cannot be accessed, the output of the line driver is wired to a pad.

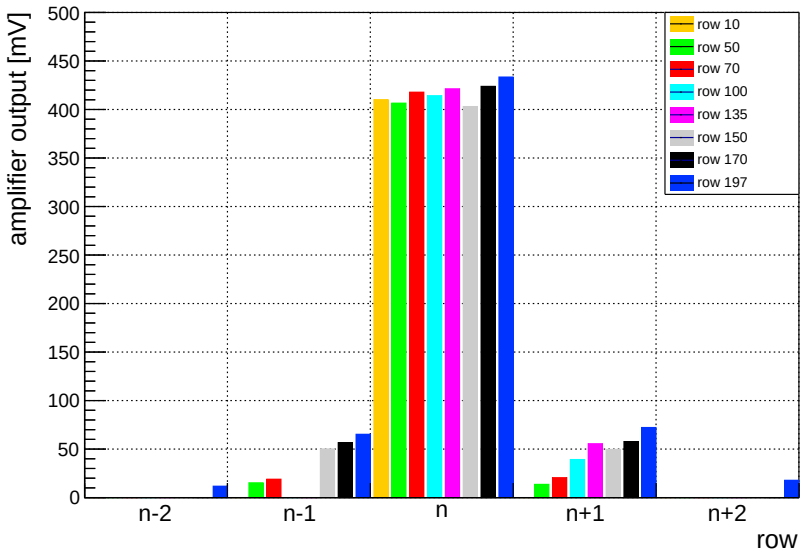

Figure 10.2: Coupling to neighboring and next-to-neighboring pixels for signals injected into pixels in column zero. Taken from [54].

from rows smaller than 135 are not high enough to trigger the discriminator with an injection of 400 mV and will not be stored. For the highest rows it can happen that clusters with a size of three are created.
These measured amplitudes nicely match the expected crosstalk amplitudes from simulations [56] for lines with only one neighbor. The time difference between the analog output and the injection signal, the latency, is studied using an oscilloscope. Similar latencies for the crosstalk and the actual signal are observed, consistent with the simulation. This effect can be explained by stronger coupling of fast signals with higher frequencies leading to typical sharp and short crosstalk pulses.

10.2 TEST BEAM MEASUREMENTS

Four campaigns at DESY have been carried out to characterize and understand the performance of the MUPIX8 as well as to show its integrability. Up to three MUPIX TELESCOPES have been used in parallel to optimally use the available particle beam: One telescope with four planes, one with three MuPix planes and an ATLASPix as DUT [45] and one telescope based on the *Mu3e* front-end board (FEB) with four to eight layers of MuPix sensors, see figure 10.3. The high flexibility of the MUPIX TELESCOPE allows studies of different configurations with different prototypes using identical software.
All setups are aligned with a mechanical precision in the order of 150 µm. An automated track based software alignment, discussed in section 6.5, is applied to correct for the remaining alignment offsets as well as for rotations around the beam axis. The final biased tracking residuals are below

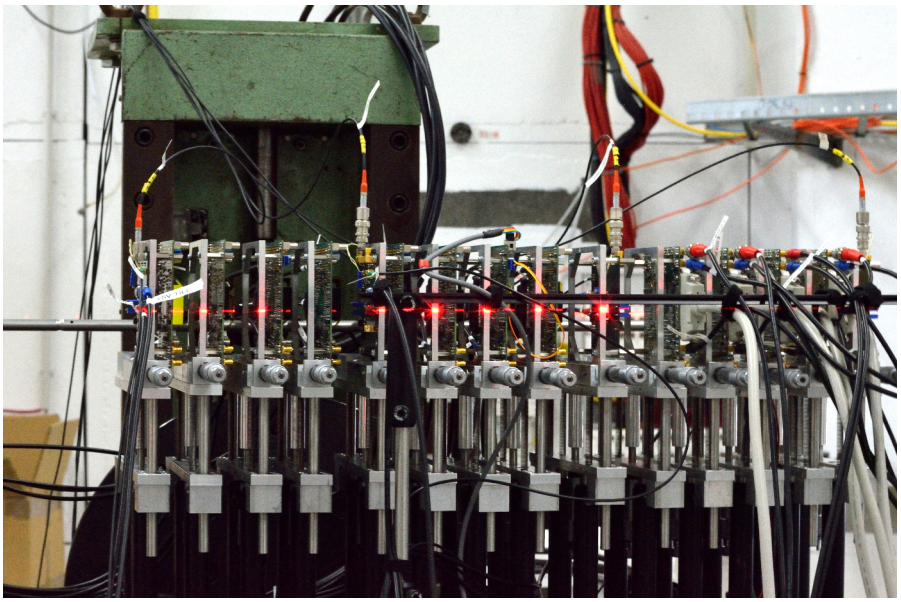

Figure 10.3: Picture of the setup from the March'18 test beam. 11 layers of MUPIX8, one ATLASPIX and four scintillating tiles (connected by red lemo connectors) are set up. The red horizontal laser is used for mechanical alignment and switched off during data taking. Particles enter the setup from the right side.

4 µm, see figure 10.4 exemplary .

10.3 SENSOR STUDIES

The MUPIX8 characterization studies discussed in the following start with a detailed study of crosstalk, clustering, noise, efficiency and time resolution of dedicated exemplary sensors, followed by a study of sub-pixel effects. Different sensors with varying thickness, resistivity and from the pre- and final production are compared at the end. The data samples are summarized in table 10.1. All presented studies are performed with a hit matching radius of 400 µm, a time cut on the hit for the reference tracks of ±80 ns, a time cut on potential matching candidates of ±160 ns and without removal of noisy/hot pixels, if not mentioned otherwise. The time cut for the reference tracks are chosen to be tighter than the time cut of the hit matching to ensure a clean sample. The matching radius cut is chosen tighter as for the power optimization study of the MUPIX7 as the beam momentum is higher.

10.3.1 *Cluster size and crosstalk*

Even though crosstalk and charge sharing are two different effects, they are directly connected in the MUPIX8. Both influence the average cluster size. Charge sharing can create clusters with a size of up to four due to particles,

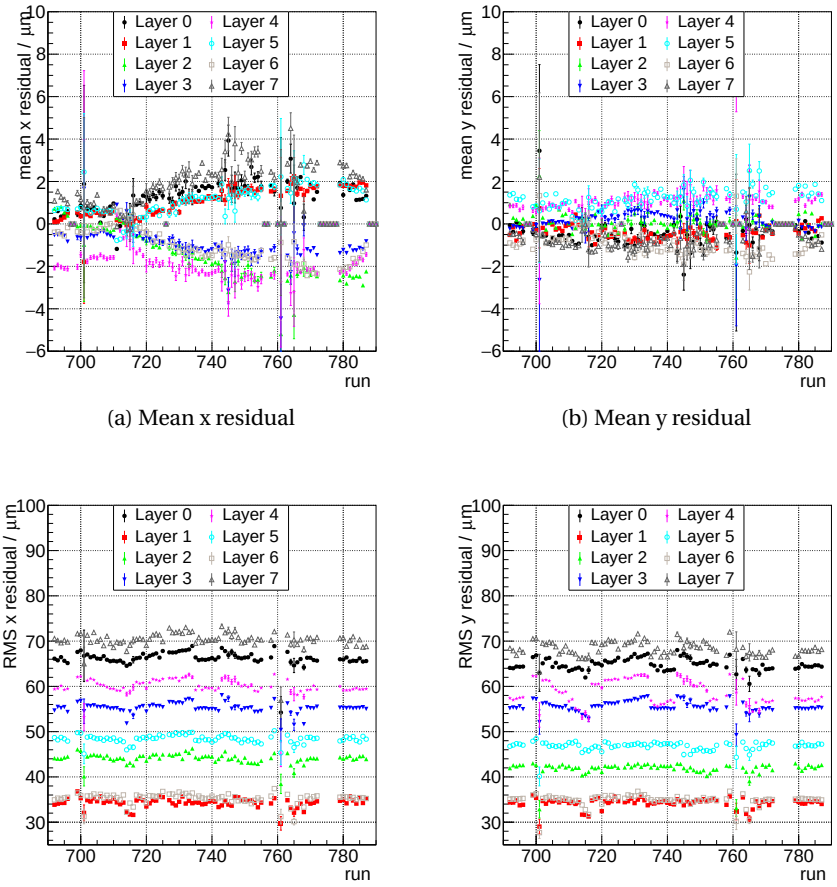

(a) Mean x residual

(b) Mean y residual

(c) RMS x residual

(d) RMS y residual

Figure 10.4: Residuals for runs 609 to 790 of the FEB telescope from the June'18 beam time. The mean values for x (a) and y (b) residuals are below ± 4 µm. Run 713 is used for alignment. The residual widths (bottom) are constant over time.The outer two layers are least constraint and have the largest width. Points with an residual of exactly zero are short runs without beam.

Sensor ID	Resistivity [Ωcm]	Thickness [µm]	Bias [-V]	Setup
		Final production		
084-3-08	080	62.5	50	MUPIX TELESCOPE
265-1-03	080	62.5	50	MUPIX TELESCOPE
084-3-22	200	100	50	MUPIX TELESCOPE
084-3-25	200	100	15, 30, 50	MUPIX TELESCOPE
		Pre-production		
084-1-05	080	725	50	MUPIX TELESCOPE
084-2-06	080	725	50	FEB Telescope
084-1-10	080	725	50	FEB Telescope
084-2-03	080	725	50	MUPIX TELESCOPE
232-1-15	200	725	50	MUPIX TELESCOPE
084-3-21	200	725	50	FEB Telescope
084-3-18	200	725	50	FEB Telescope
232-1-04	200	725	50	FEB Telescope
084-3-04	200	725	50	FEB Telescope
084-3-30	200	725	50	FEB Telescope

Table 10.1: Summary of all characterized MUPIX8 samples, which have been tested during the Test beams at DESY. The sensor ID has the following naming sheme based on the inserts on which they are mounted: type-batch-number. The setup column denotes the used setup for characterization: Frontend board telescope (FEB telescope) or MUPIX TELESCOPE.

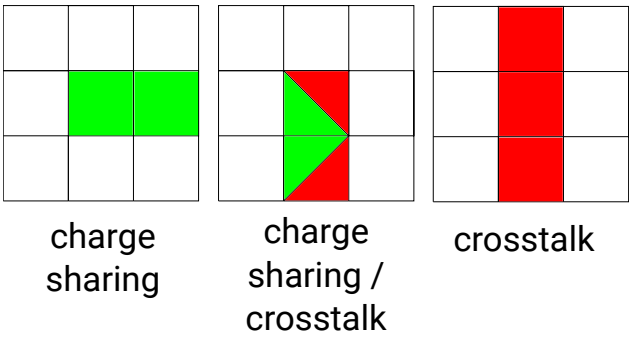

Figure 10.5: Sketch of one dimensional double and triple clusters and their potential origin.

which deposit their charge close to the pixel edges/corners. In contrast, crosstalk is the capacitive coupling between two point-to-point connection lines from the active analog cells to the digital part, which are routed parallel. Therefore, crosstalk artificially increases the average cluster size. In contrast to MUPIX7, the transmitted analog signals are not amplified again before discrimination in the design of the MUPIX8, as discussed in section 4.2. To perform an accurate cluster size study, the crosstalk has to be understood and subtracted first.

Crosstalk

During beam measurements, it is impossible to distinguish between crosstalk events and a physical cluster created by a traversing particle on an event by event basis. In contrast to MUPIX7, there is also no clear pattern created by crosstalk which can be tagged. The only option is to study asymmetries between clusters along row and column. Clusters with a column or row extension of more than two cannot be created by a single particle traversing the sensor. An exception are δ-electrons from rare hard scatters. Figure 10.5 illustrates the potential clusters with column/row extension of one. Charge sharing creates the same amount of double clusters along columns and rows, because the pixels are essentially square [3].

Figure 10.6 summarizes the matched cluster size distribution for clusters with a row/column extension of one. An enhancement of double and triple clusters can be observed along the rows. The probability of creating crosstalk events with size $i > 1$, as a function of the ratios of total amount of horizontal (hits with common row number) clusters n_{sum_h}, vertical (hits with common column number) clusters n_{sum_v} and entries at $n_{v/h}(i)$ is calculated as:

$$P_{xt}(i) = (n_v(i)/n_{sum_v} - n_h(i)/n_{sum_h} \tag{10.1}$$

3 pixel size: $81 \times 80\,\mu m^2$. Calculated crosstalk values have therefore a relative systematic error of below 2 %, which is small compared to the statistical uncertainty.

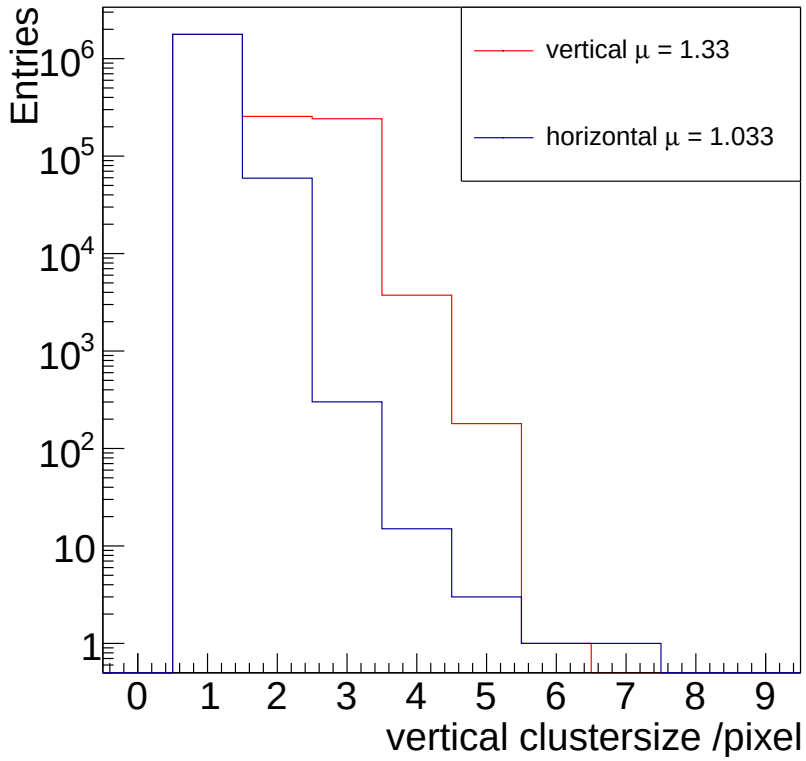

Figure 10.6: Vertical (horizontal) cluster size distribution for matched clusters with an horizontal (vertical) extension of one for data taken at -50 V bias and a threshold of 50 mV. A strong enhancement of double and triple clusters is visible for vertical clusters. The average cluster size is added to the legend.

The probability to create a double or triple cluster is then

$$\begin{aligned} P_{xt}(2) &= 157670/1390810 - 37510/1120470 = 0.079, \\ P_{xt}(3) &= 148022/1390810 - 198/1120470 = 0.106. \end{aligned} \tag{10.2}$$

However, these are only integrated numbers and do not take variations over the sensor into account. Figure 10.7 shows the position of all matched clusters next to single, double and triple clusters. Cluster are homogeneously distributed over the sensor, compare figure 10.7a. Selecting clusters with a certain size reveals structures: the single clusters are located mainly on the bottom half of the sensor, while the double and triple clusters are located in the top part of the sensor. These observation are explained by the increasing connection line length and therefore larger interline capacities and a stronger coupling. For triple clusters, an additional column dependence becomes visible. The MUPIX8 has an unintended voltage drop of approximately 200 mV between the supply voltage pads and the biasing block of the chip. This reduces the voltage at the comparator and enhances sensitivity of the comparator to a voltage drop of

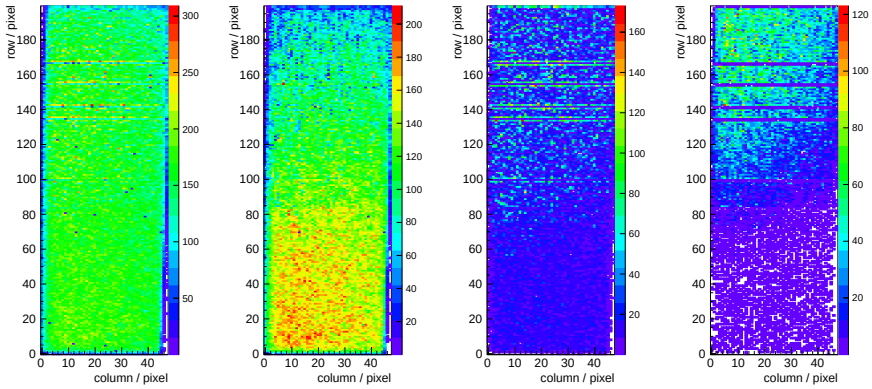

(a) all cluster (b) Cluster size = 1 (c) Cluster size = 2 (d) Cluster size = 3

Figure 10.7: Clusterposition for matched clusters with a multiplicity of 1, 2 and 3 and an overview for all matched clusters. A threshold of 50 mV and a bias of -50 V is used.

approximately 10 – 20 mV along the column axis [92]. This feature will be solved for upcoming prototypes. For MUPIX8, an increased comparator DAC value reduces the dependence, see section 10.3.3.

To further quantize the effect, the probabilities to create a double or row crosstalk event can be plotted as function of the row position, see figure 10.8. The probability to create double (triple) crosstalk as a function of the row address can be calculated by the difference between vertical and horizontal clusters, scaled by the sum of clusters for each row r:

$$P_{xt_{2/3}}(r) = \frac{n_{v_{2/3}}(r) - n_{h_{2/3}}(r)}{n_{total}(r)} \tag{10.3}$$

At the top and bottom row, where the only possible double/triple clusters can be horizontal, the above formula is not valid. No triple clusters are visible for the top row in figure 10.8b and a large negative probability for double clusters is visible in figure 10.8a. Rows 0 and 199 are therefore excluded from the studies.

To create a crosstalk event for a given threshold, the connection lines need to have a certain parallel length. For the data set shown at an threshold of 50 mV, the minimal line length to create visible crosstalk is reached around row 70. The triple crosstalk probability is linearly rising, the double crosstalk probability is rising up to row 100 and stays flat afterwards. The flattening can be explained: the charge deposition is Landau distributed and the signal amplitude is charge dependent. Therefore, also the crosstalk signal height will vary and a higher signal amplitude is more likely to trigger both neighbors. With increasing row number, the required deposited charge to create crosstalk hits on both lines is reduced. In parallel, there are always pixel-to-pixel fluctuations, which change the effective detection threshold of each pixel as well as the signal amplitude for a given charge

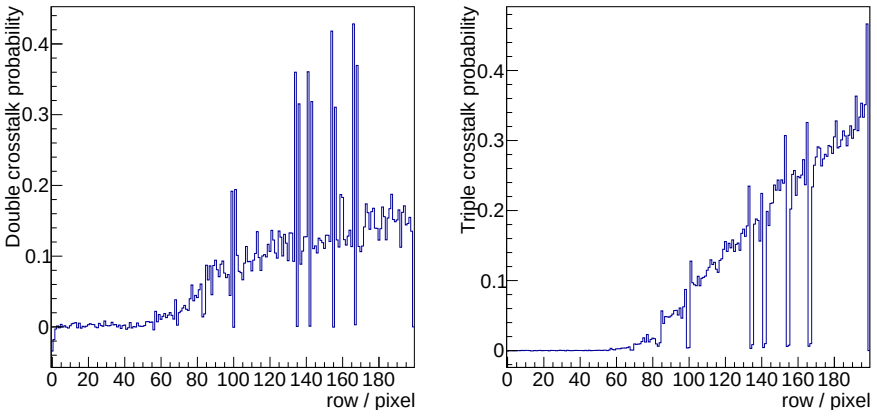

(a) Double (b) Triple

Figure 10.8: Probability to create a double or a triple crosstalk event as function of the row address of the cluster's barycenter. A threshold of 50 mV and a bias of -50 V is used.

deposition. The combination of both effects creates a band in the charge spectrum, which triggers double crosstalk.

The spikes/dips in both spectra are located at rows where the line spacing is larger. Two pixels p_i and p_{i+1} with a large line spacing cannot be the barycenter of a triple cluster, thus creating two pixel wide dips in the triple crosstalk spectra. In parallel to the reduction of triple crosstalk for these pixels, an enhancement of the double crosstalk events in p_i and p_{i+2} is observed, which is also reflected in figure 10.7c. The positions of the dips in the triple crosstalk nicely coincide with the pixels with larger line spacing extracted from the MUPIX8 layout.

Single and double crosstalk probabilities can be fitted, if the above mentioned spikes and dips are excluded. For the triple cluster spectrum, a linear function with a threshold, motivated by the linear capacity increase with the row number and a detection threshold, is used to describe the data:

$$\mathrm{P}_{\mathrm{xt}_3}(r) = \begin{cases} P_0 & \text{if } r < \mathrm{row}_{\mathrm{thres}} \\ P_0 + (r - \mathrm{row}_{\mathrm{thres}}) \cdot s & \text{if } r >= \mathrm{row}_{\mathrm{thres}} \end{cases} \tag{10.4}$$

$\mathrm{row}_{\mathrm{thres}}$ is the first row where crosstalk becomes visible and P_0 is a constant to take statistical fluctuations in the crosstalk free region below the threshold into account. The data is well described by the fit as shown in figure 10.9. Pixel-to-pixel variations cause slightly varying effective thresholds for each pixel. Therefore a certain signal is sufficient to trigger a signal in one pixel but not in the other one. The distribution is Gaussian, without any row dependence [92]. The double crosstalk spectrum can be fitted by an error function, defined in equation 7.2, see figure 10.10, as the signal is increasing with row. The data agrees well with the fit model. The σ of the error function can be interpreted as a variation of the pixel response.

To conclude the crosstalk analysis of the MUPIX8, the threshold depen-

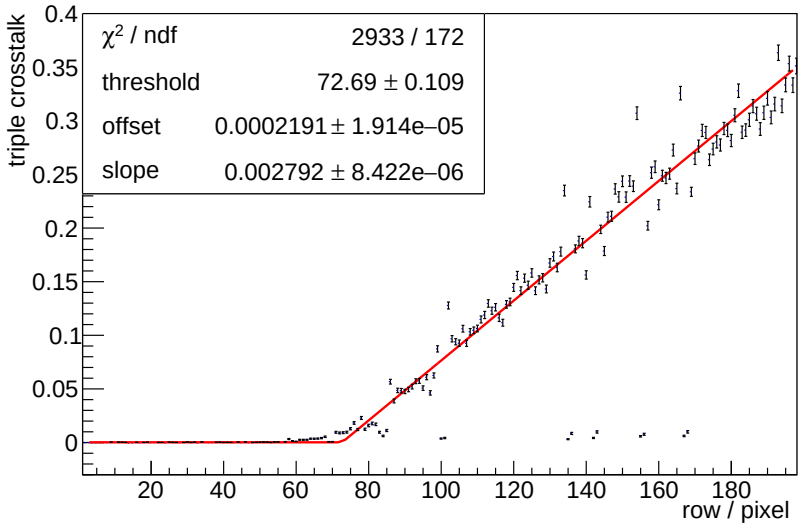

Figure 10.9: Triple crosstalk probability as a function of the threshold. Data is fitted with the function defined in equation 10.4. The points with a probability of zero above row 80 are due to increased line spacing and excluded from the fit.

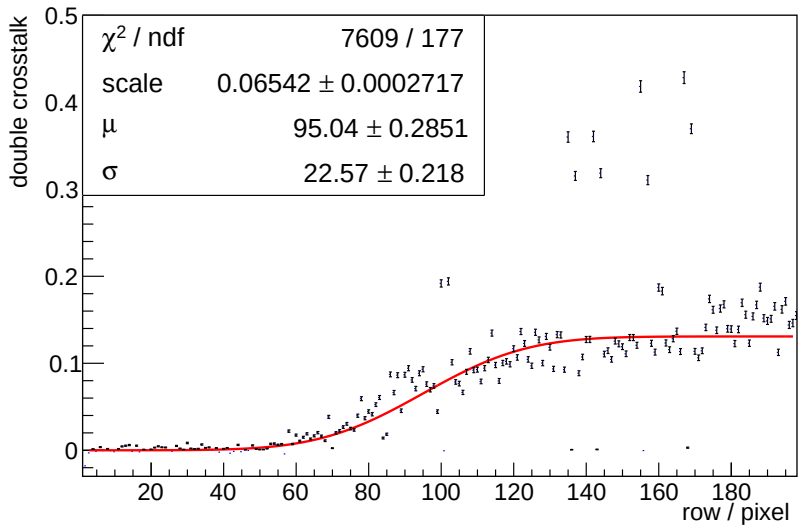

Figure 10.10: Double crosstalk probability as function of the row position. Data is fitted width an error function. Points with too high probability above row 80 have a large line spacing to one neighbor, resulting in an increased double crosstalk probability as triple crosstalk is suppresses. These points are excluded from the fit.

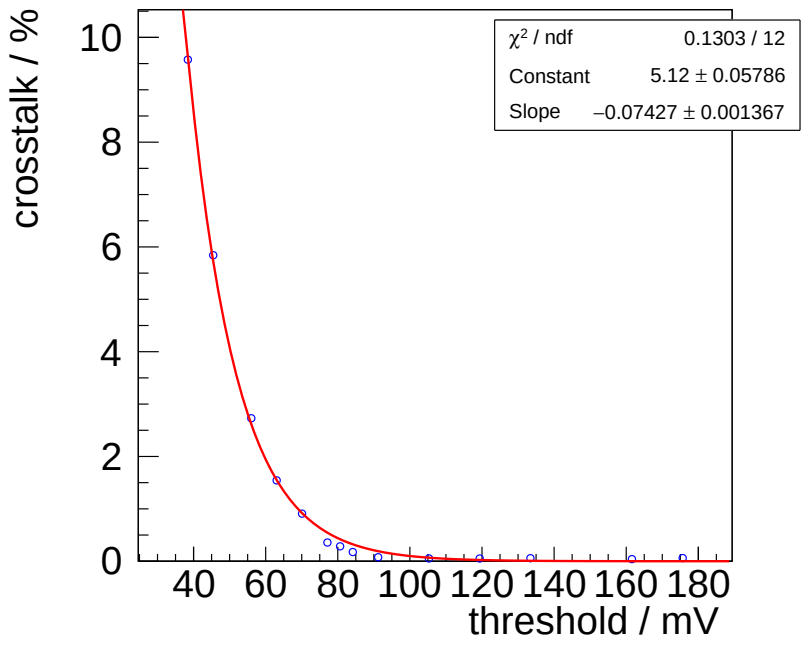

Figure 10.11: Summed probability to create a double or triple crosstalk event averaged over the full matrix for sensor 084-2-03 as a function of the hit detection threshold. Data is well described by an exponential function.

dence of the mean crosstalk probability is shown in figure 10.11 for a detailed threshold scan of sensor 084-2-03. The behavior is exactly as expected – for high thresholds no crosstalk can be seen, as the capacitive coupling creates too small pulses to be detected. For lower thresholds, roughly 90 mV for the presented sensor, the crosstalk signals are more likely to be above threshold. Lowering the threshold further increases the crosstalk probability for a fixed row. Additionally, lower rows show crosstalk, reflected by a reduction of $\text{row}_{\text{thres}}$ for lower thresholds. Empirically, an exponential function suits the data well.

Clustering

The average cluster size is strongly crosstalk influenced as discussed above. The effect of charge sharing is however important as it influences the sensors resolution and the required bandwidth to stream the hit data out. The latter one is also increased by crosstalk. Figure 10.12a shows the average cluster size as function of the threshold for sensor 084-2-03 including crosstalk. High thresholds decrease the probability to create a cluster by charge sharing as they require a more equally distributed charge and are also prone to inefficiencies. For lower thresholds, the average cluster size increases, because less charge is required to create a hit. In addition, line

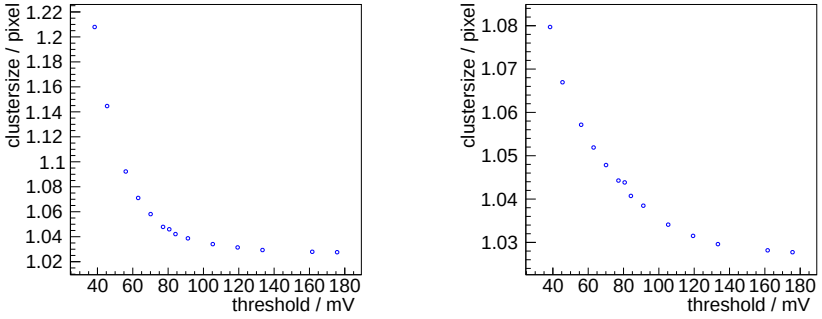

(a) Cluster size of raw data

(b) Cluster size after cross talk removal

Figure 10.12: Cluster size of matched clusters for sensor 084-2-03 as a function of the threshold with and without crosstalk. The bias voltage is –60 V.

crosstalk further enhances clusters. The average pure crosstalk cluster size is given by

$$\mu_{xt} = (1 - P_{xt_2} - P_{xt_3}) \cdot 1 + 2 \cdot P_{xt_2} + 3 \cdot P_{xt_3} = 1 + P_{xt_2} + 2 \cdot P_{xt_3}. \qquad (10.5)$$

Subtracting μ_{xt} from the average cluster distribution leads to the average cluster size for charge sharing, see figure 10.12b. The presented sensor has an average cluster size of up to 1.08.

Charge sharing creates less clusters compared to crosstalk at low thresholds for the MUPIX8. For future prototypes, the influence of crosstalk can be removed by an optimized line layout, which avoids long parallel lines next to each other. The dips in the spectra of the MUPIX7 show, that doubling the spacing between two connection lines is already sufficient to suppress crosstalk by over an order of magnitude. The line spacing for the MUPIX8 lines without crosstalk is a factor 10 larger than the average spacing. Twice the line spacing has the same effect on the capacity as halving the parallel length. An optimized layout avoids long parallel lines and can be realized for example by an alternating line layout between long and short lines.

10.3.2 *Efficiency and noise*

Efficiency and noise, together with time resolution, are the most important figures of merit for pixel sensors. Efficiency and noise are calculated as described in section 5.3.3 and plotted exemplary for sensor 084-2-03 at a threshold of 56 mV in figure 10.13. The efficiency is above 99.8 % over the complete sensor. By eye visible inefficiencies only occur at the sensor edges due to physical mis-alignments and scattering effects. To ensure not to be biased by effects at the sensor edges, for all following results a region of interest is defined excluding the outer three columns and rows. Pixel (8/91) is an inefficient pixel and also has less noise compared to the pixels

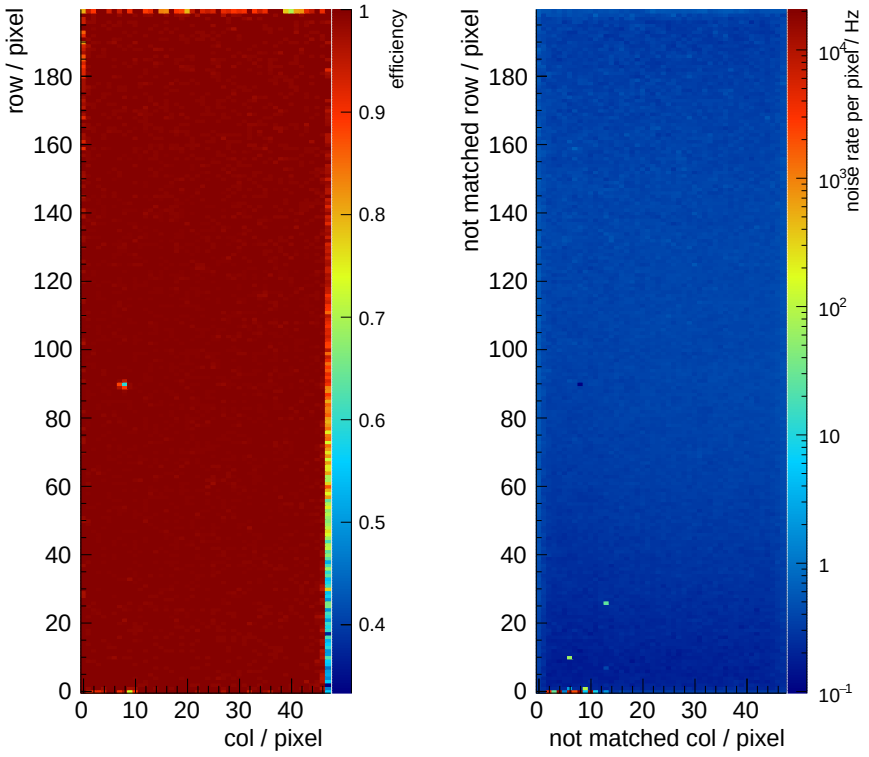

(a) Efficiency (b) Noise

Figure 10.13: Efficiency and noise maps for sensor 084-2-03 at a threshold of 56 mV and a bias of –60 V.

surrounding it. The reduced performance can be caused by a shift in the reference voltages for that pixel or by a reduced amplification. Most pixels have a noise rate of approximately 0.3 Hz. Exceptions are pixels in row zero, close to the fast digital logic, which have high noise rates of over 10 kHz and two additional noisy pixels in the bottom right corner of the chip. Similar effects have not been observed for other sensors and are specific for sensor 084-2-03.
The row/column, bias voltage and threshold dependency of sensor 084-2-03 are studied in detail in the following. Subsequently, the signal height and the line crosstalk are discussed.

ROW AND COLUMN DEPENDENCY Crosstalk as described in the previous section reduces the signal height linearly with the row number. The reduced signal amplitude also affects the signal detection efficiency. Figure 10.14a shows the mean efficiency as a function of the row. The mean efficiency is above 99.6 % over the complete sensor. However, a small but significant decrease of the efficiency of 0.10(1) % over the chip is revealed if the data is fitted with a linear function.

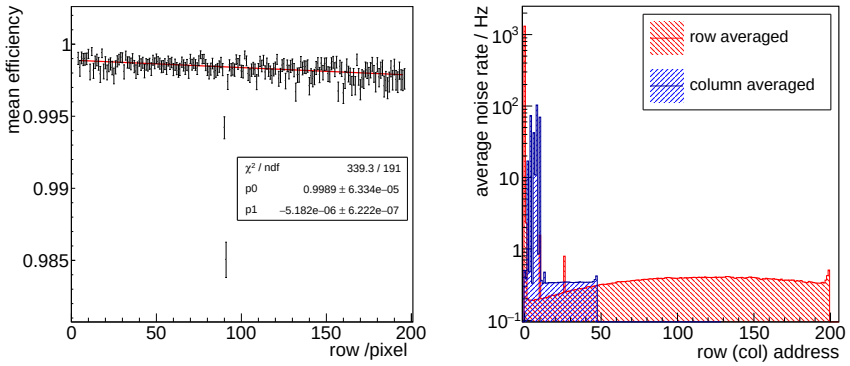

(a) Efficiency (b) Noise

Figure 10.14: Efficiency and noise projections for sensor 084-2-03 at a threshold of 56 mV and a bias of –60 V. The efficiency projections is fitted with a linear function.

The column averaged noise in figure 10.14b spikes at the column addresses of the noisy pixel mentioned above and is flat otherwise. The row averaged noise is related to the beam profile, which becomes visible as the sensor is four times higher than wide. The tracking efficiency is approximately 95 % for the presented scan. The correction for beam related backgrounds, scattered particle and tracking inefficiencies, as it is shown in equation 5.33 is not done position dependent but averaged over the full sensor. Thus the beam profile is not removed in the noise projection. The noisy pixels also create spikes in this distribution. Both distributions show an increase at the boundaries due to tracking inefficiencies at the sensors' edges, which is not spoiling noise rates within the region of interest.

THRESHOLD DEPENDENCY Noise and efficiency are threshold dependent. For higher thresholds, reduced efficiencies and noise rates are expected. Figure 10.15a shows the results for an exemplary threshold scan of sensor 084-2-03 at –60 V bias. The sensor has an efficiency of above 99 % in a threshold region of 45 mV and stays below 10 Hz noise per pixel over the full scan, fulfilling the *Mu3e* specifications over a larger threshold range. The noise is dominated by a small number of noisy pixel, which would be masked if the sensor is operated in a detector[4]. Noisy pixel have been masked during offline analysis to study their impact on efficiency and noise. Masked pixels cannot contribute to clusters as well as noise and cannot be assigned to tracks. The resulting efficiency and noise curves are shown in figure 10.15b. The small efficiency reduction due to the pixel masking is barely visible by eye – in contrast to the change in noise. The noise rate stays well below 0.5 Hz over the complete scan region and is

4 This was not possible during this testbeam due to technical issues, which have been solved for later beam times.

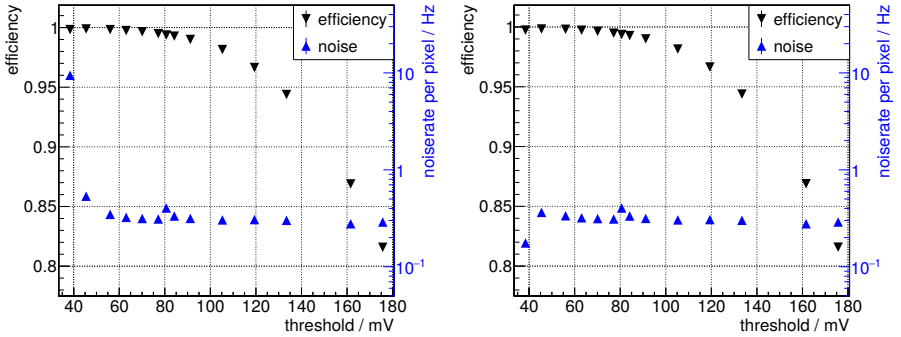

(a) Efficiency and noise without pixel masking

(b) Efficiency and noise with pixel masking

Figure 10.15: Efficiency and noise as a function of the threshold voltage for sensor 084-2-03 at a bias voltage of –60 V with and without software masking of hot pixels. Up to 25 pixels have been masked, see figure D.2 in the appendix. The increased noise rate at a threshold of 80 mV is attributed to a reduced tracking efficiency due to a non-optimal configured plane.

dominated by the masking threshold. The noise rate is reduced for lowering the threshold from 45 mV to 40 mV due to additional masked pixels for example.

BIAS VOLTAGE The efficiency not only changes as a function of the threshold but also as a function of the bias voltage. To first order, the depletion zone grows proportional to $\sqrt{U_{bias}}$. A thicker depletion zone results in more collectible charge, which creates larger signals, leading in turn to larger efficiency plateaus. Figure 10.16 shows threshold scans at different bias voltages of –5 V, –15 V and –50 V for sensor 084-3-25, which has a substrate resistivity of 200 Ωcm. For a bias of –5 V, an average efficiency of 96 %, constantly decreasing with increasing thresholds is observed. A small efficiency plateau is visible for a depletion voltage of –15 V. For the highest tested bias of –50 V, the sensor is over 99 % efficient up to a threshold of above 100 mV.
A higher bias has not been possible for this sensor, because the leakage currents dramatically increase for higher bias voltages. In general, the breakdown happens when the E-field becomes too large locally. The exact location of the breakdown is currently under investigation. One candidate are the bias substrate contacts, which seem to be critical in a simulation [55].

SIGNAL HEIGHT DETERMINATION The efficiency as a function of the threshold can be fitted with an s-curve in order to determine the average signal height of the sensor, as well as fluctuations over the sensor under the assumption of reaching an efficiency of 100 % at an threshold of zero, see figure 10.17. The average signal height from the fit is 228.2(1) mV with

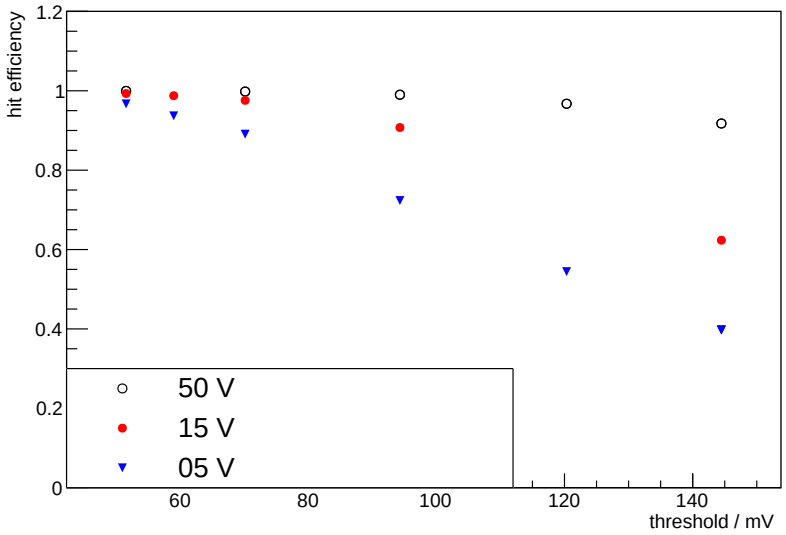

Figure 10.16: Efficiency as a function of the threshold for three bias voltages for sensor 084-3-25. Binomial errors are included but too small to be visible. Data has been taken with 4 GeV positrons.

a width of 59.1(1) mV. Assuming a linear correlation between signal height and number of primary electrons, the signal corresponds to roughly 5300 primary electrons, based on the iron results (70 mV for 1635 electrons). The expected depletion zone thickness from equation 3.15 for a bias of –60 V and a substrate resistivity of 80 Ωcm is 27 µm. A MIP looses on average 0.4 keV/µm [6], leading to approximately 3000 primary electrons. This discrepancy could be explained by a superposition of several effects: a non-linear response, charge multiplication in the depletion zone by avalanche effects and a higher resistivity of the wafer (80 Ωcm wafers have s specified range from 50 – 100 Ωcm). A systematic calibration with x-rays at different energies is required to validate the linearity assumption[5]. The depletion zone thickness can be measured with a edge transient current technique setup [93].

SIGNAL LOSSES DUE TO CROSSTALK The previously determined signal height is averaged over the sensor. Crosstalk will reduce the signal height with increasing row addresses, as already indicated in figure 10.14a. Fitting a linear function to the efficiency projection along the row for all thresholds, see figure 10.18a, confirms the indication: the efficiency decreases over the sensor length. The decrease is larger for higher thresholds, consistent with the interpretation of signal reduction due to crosstalk, which becomes more severe for larger thresholds. From the linear fits in figure 10.18a, the efficiency at rows 0, 100 and 199 can be calculated and plotted as function of the threshold, see figure 10.18b. The mean signal height

5 In [54] indications for a non-linear response to an injection are observed.

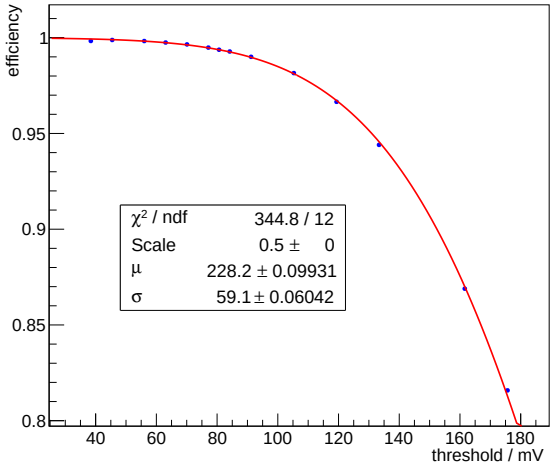

Figure 10.17: Efficiency as a function of the threshold, fitted with an s-curve. Binomial errors included. Data has been taken with 4 GeV positrons.

decreases with increasing row number, which gives an estimation on the coupling between two lines. The mean signal at row zero is 235.75 mV and at row 199 221.93 mV – a reduction of 6 %. The loss in signal amplitude is frequency dependent, as already seen in laboratory measurements and simulations. The measurements with the analogue amplifier output show a signal height of about 20 % of the injected signal height for row 199. However, the crosstalk pulse is shorter than the signal pulse, as only the high frequency components of the signal contribute significantly. The total energy is conserved. Therefore, the small amplitude reduction results in a sharp crosstalk pulse with measurable amplitude.
The crosstalk is not only dependent on the row position, but also on the column position, as also visible in the cluster position maps (see figure 10.7). The latter cannot be explained by the line length and is more likely to be introduced by a drop in the supply voltages on the sensor. Data samples with increased supply voltages show reduced effects along the column address, emphasizing a voltage drop in either the digital or the analogue part of the sensor. It is not possible to disentangle the source of this effect any further based on the presented data, especially as no access to the analogue signal is given for any other column than the first one. However, it is known from the designers, that the comparator is sensitive to the power drop in the used DAC configuration [92].

10.3.3 *Time resolution*

The last studied parameter is the time resolution. Only clusters, which are assigned to a track and have a multiplicity of one are used in the following studies. The timestamps t_{hit} of the hits are compared to the time of a co-

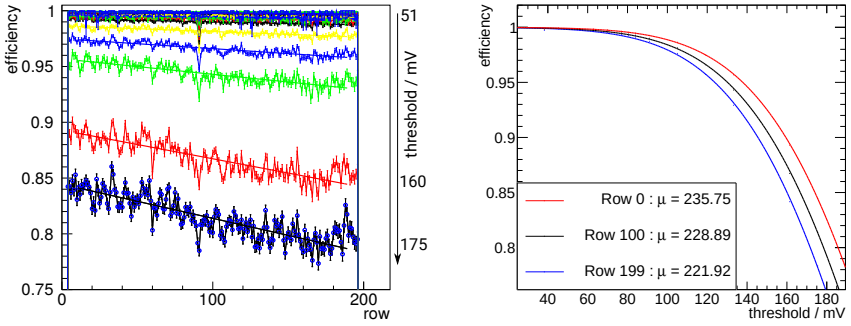

(a) Efficiency along the rows for a threshold-scan

(b) Extrapolated efficiency as function of the threshold for different rows

Figure 10.18: Efficiency for sensor 084-2-03 at a bias of –60 V. The efficiency projections are fitted with linear function. From the fit results extracted exemplary efficiency curves as function of the threshold are fitted with an s-curve. Data taken with 4 GeV positrons.

incidence of two scintillating tiles t_{ref}, which is sampled with 500 MHz on the FPGA. The difference $\Delta t = t_{hit} - t_{ref}$ is plotted and a Gaussian is fitted to the core of the difference histogram. The σ of the Gauss defines the time resolution. It needs to be better than 20 ns to fulfill the *Mu3e* sensor specification. The time resolution of sensor 084-3-25 at a threshold of 51 mV, shown in figure 10.19, is studied in the following. The time resolution of the full sensor is 20.02(1) ns. The small bumps, for example at a time difference of 220 ns, are created by particles, which only hit the reference tile, which is larger than the sensor. In the DAQ, these reference timestamps from earlier bunches are assigned to the next frame recorded. The relative time difference corresponds to 13 turns of the DESY-II. Compared to the MUPIX7, the time resolution is surprisingly bad. However, the area of the MUPIX8 about 20 times larger. Therefore the power distribution, parasitic on chip resistors and capacities are more critical.

The worse time resolution compared to MUPIX7 can be understood by studying the time resolution of all pixels individually. Two effects are observed: Firstly, the average time difference between the pixel and trigger time, shown in figure 10.20a, is increasing with column and row number. This average difference can be interpreted as a delay. Secondly, the individual pixel resolution, see figure 10.20b, depends only little on the position. The average pixel time resolution is 13.72(4) ns, with a spread of only 1.96(2) ns, see figure 10.20d, which is similar to the MUPIX7. The difference to the average time resolution of the sensor has to be created by delay variations over the sensors and pixel-to-pixel fluctuations. Delays are explained by the same effects as the signal height/crosstalk changes over the sensor in the last section: The delay along the row axis is also due to increased capacities on the transmission lines, while the delay along the column direction is caused by the distribution of the timestamps in the

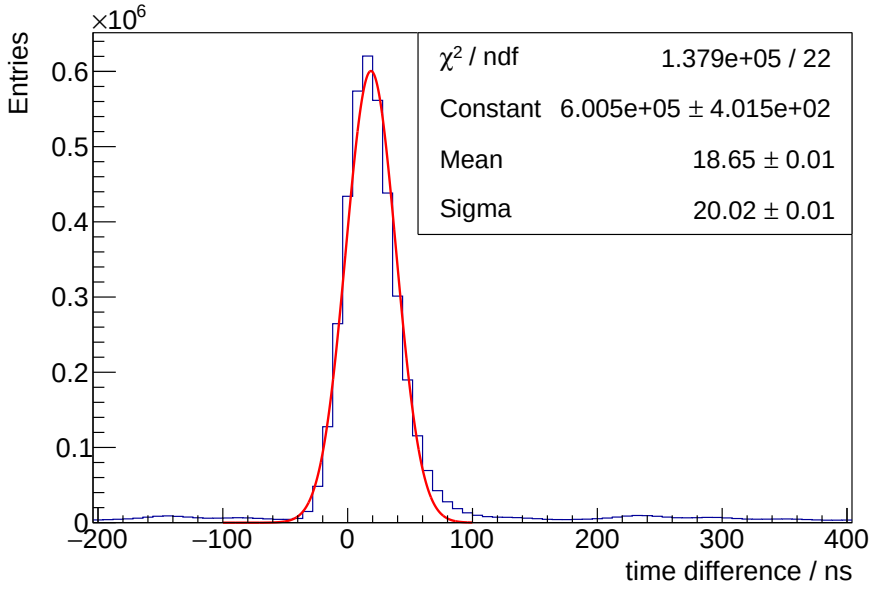

Figure 10.19: Time difference between scintillating tile reference and hit timestamp for matched clusters with a multiplicity of 1 of sensor 084-3-25. A Gaussian is fitted to the central region of the distribution. The bias voltage is set to −50 V. The small visible bumps in the spectrum are created by particles, which only hit the tiles.

digital logic. The timestamps are created in the left part of the periphery and distributed over the digital part. The expected delay is below 2 ns over the column length [92]. In addition, drops in the power can cause performance gradients over the sensor.

The delays can be corrected for to improve the sensors time resolution. To test the feasibility of different approaches, four correction methods have been implemented in the offline analysis:

- **Individual pixel correction:** The delay of each pixel is corrected individually, after the per pixel delay $\mu(c,r)$ is fitted. The corrected time difference is then:

$$t_{cor}(c,r) = t_{hit} - \mu_{pixel}(c,r) - t_{ref} \tag{10.6}$$

  Correcting each individual delay is the most precise technique, as it is independent of pixel-to-pixel variations.

- **Sector corrections:** Pixels can be grouped into sets of e.g. 8×8 pixels and the average delay $\mu_{sec}(c/8, r/8)$ of each group can be used to correct the timestamps in the same way as for the individual pixel correction.

$$t_{cor}(c,r) = t_{hit} - \mu_{sec}(c/8, r/8) - t_{ref} \tag{10.7}$$

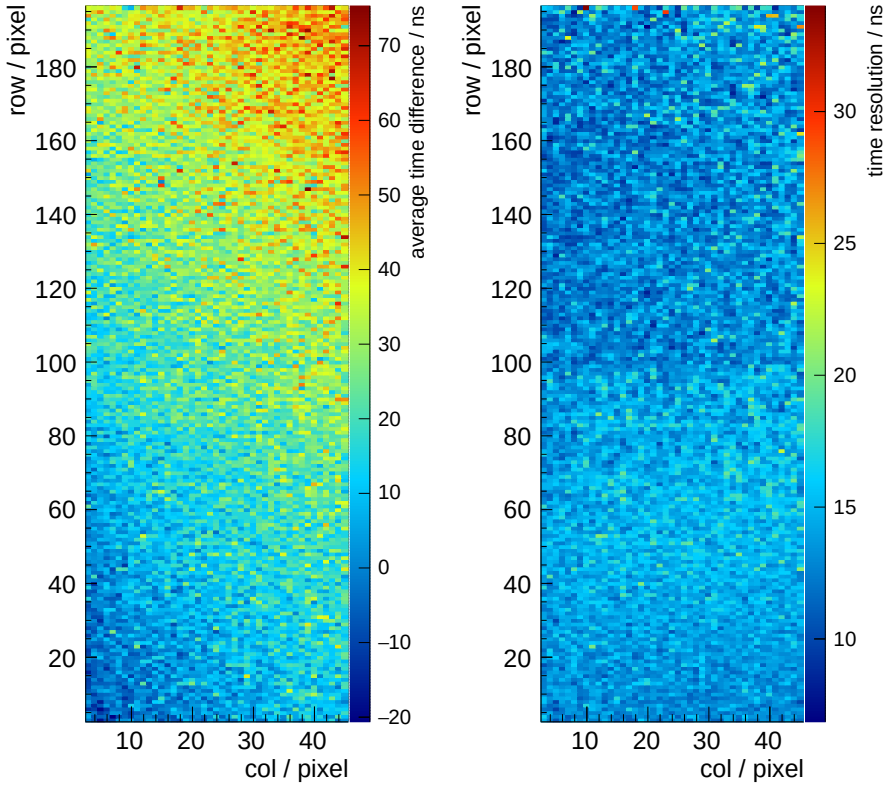

(a) Average time difference map

(b) Time resolution map

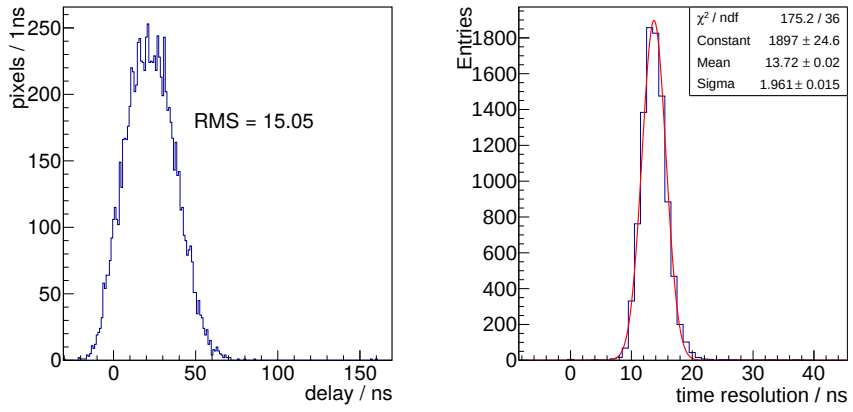

(c) Average time difference histogram

(d) Resolution histogram

Figure 10.20: **Top:** Average time difference and time resolution maps of sensor 084-3-25 at a bias voltage of –50 V. The resolution is expressed as Gaussian sigma.
Bottom: Histogrammed individual time resolution and average time difference. The pixel resolution histogram is fitted with a Gaussian.

- **Parametrized corrections:** A general correction can be defined as:

$$t_{cor}(c,r) = t_{hit} - \mu(c,r) - t_{ref} \tag{10.8}$$

$\mu(c,r)$ is a correction, which depends on the column and row position and can be written as

$$\mu(c,r) = d_0 + d_r \cdot r + d_c \cdot c + d_{rr} \cdot r^2 + d_{cc} \cdot c^2 + d_{rc} \cdot c \cdot r + \mathcal{O}^3(c,r). \tag{10.9}$$

$d_0, ..., d_{rc}$ are constant correction factors. The correction can be split in different components: constant, linear, correlated/quadratic and higher orders. A constant correction is not influencing the time resolution and therefore dropped. The simplest parametrized approach is to perform a one dimensional correction along column or row, hereafter referred to as column/row correction , where $\mu_{col}(c) = d_c \cdot c$ and $\mu_{row}(r) = d_r \cdot r$ holds.
Correcting only along column/row ignores the other direction and leads to a non-optimal correction. A full linearized correction is given by

$$\mu_{lin}(c,r) = d_r \cdot r + d_c \cdot c. \tag{10.10}$$

The effect of correlations $d_{rc} \cdot c \cdot r$ and the quadratic terms in column and row can be analyzed by performing the linearized correction first and studying the corrected average timestamp difference as functions of cr, c^2 and r^2, compare Appendix D. No significant influences have been found.

Figure 10.21 shows the average time difference between trigger and hit times after applying the linearized corrections. The width of the distribution significantly decreases compared to the initial spread in figure 10.20c. However, the width is still 7.20(1) ns, which sets a lower limit for the time resolution of the sensor for global corrections. The fluctuations are larger in the top right part of the sensor due to reduced statistics. Non-linear corrections are negligible as aforementioned.

The time resolution results are summarized in figure 10.22. The column only correction gives a small improvement of about 0.7 ns compared to 3.3 ns of the row delay correction. Combining both corrections leads to a further improvement and a resolution of 15.72(1) ns. Dividing the MUPIX8 into sectors with 8×8 pixels also leads to a significant improvement in the time resolution to 15.76 ns, comparable with the resolution after the linearized corrections. Correcting each pixel delay individually leads to best performance with a resolution of 14.34(1) ns, see figure 10.22e, which is close to the distribution of the average time resolutions.
The better time resolution for the individual pixel correction method com-

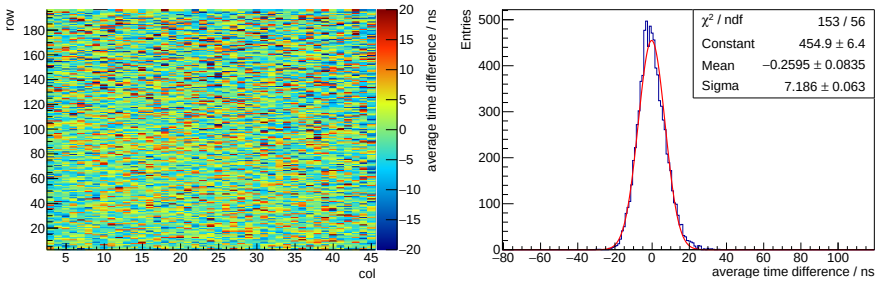

(a) Average time difference map (b) Average time difference histogram

Figure 10.21: Average delay after the linearised delay correction for sensor 084-3-25 at a bias voltage of –50 V. The histogrammed delays are fitted with a Gaussian.

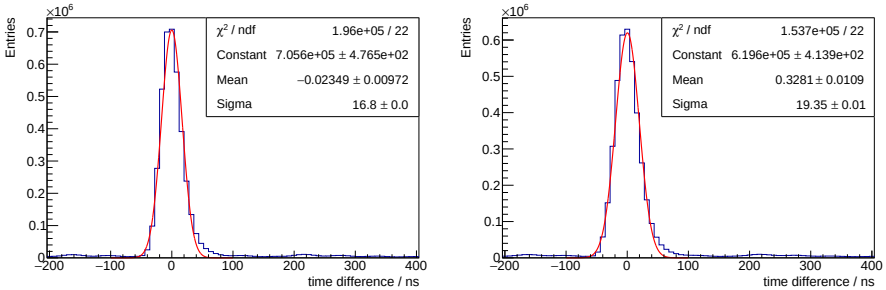

(a) Row corrected

(b) Column corrected

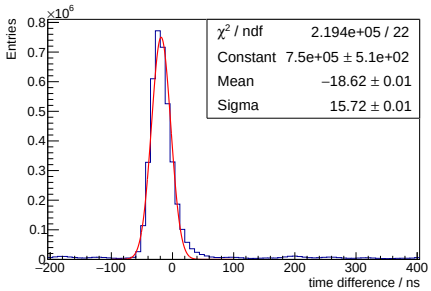

(c) Linearized corrected

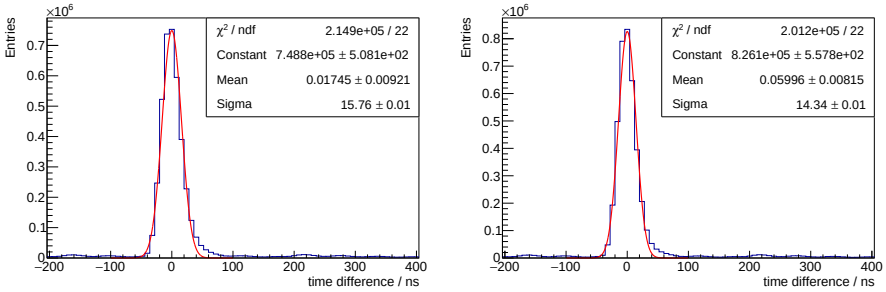

(d) Sectors corrected

(e) Pixel corrected

Figure 10.22: Time resolution of matched clusters of sensor 084-3-25, operated with an bias of –50 V, for the different delay correction methods. All distributions are fitted with a Gaussian. The methods are described in the text.

pared to the other global approaches is explained by pixel-to-pixel variations, which cannot be corrected in global methods.

$$\sigma_{global} = \sqrt{\sigma^2_{pixel} + \sigma^2_{delay}} \tag{10.11}$$

Using $\sigma_{delay} = 7.18\,\text{ns}$ (figure 10.21b) and $\sigma_{pixel} = 14.34\,\text{ns}$ (figure 10.22e) leads to $\sigma_{global} = 16.04\,\text{ns}$, well in agreement with the other correction methods.
The individual pixel correction is the best correction algorithm, which can be used in an offline data analysis.
Online delay corrections can be used to reduce combinatorics as tighter cuts on the allowed timestamp difference of hits can be applied for improved time resolutions. The sector correction method is suited best for online corrections, as it requires only little resources. A possible implementation is to define a lookup table containing the average delays in units of the timestamps (8 ns for MUPIX8). Grouping into 8×8 blocks has the advantage, that one can directly use the column/row address shifted by three bits to the right to access the lookup tables.

Threshold and bias dependency

Time resolution is threshold dependent, as higher thresholds increase time-walk. The pixel corrected time resolution is shown as a function of the threshold in figure 10.23. The time resolution is improving towards lower thresholds. For a threshold of 70 mV and a bias voltage of –50 V, the time resolution is fulfilling the *Mu3e* sensor specifications. Extrapolating to lower thresholds in figure 10.23 shows, that there is still room to improve the time resolution.

Time resolution improvements

The DAC values used for the above studies are not optimized with respect to time resolution. The time resolution is influenced by the applied threshold, the switching characteristic of the comparator, signal shaping and time-walk. MUPIX8 allows for an optimization of each component by a DAC setting adjustment. The following studies are conducted in the scope of a master thesis [54].
The threshold dependence is reduced by using the 2 threshold approach. The threshold to sample the timestamp of a hit can be lower than the threshold to rise the hit flag. An optimal threshold of $25 - 30\,\text{mV}$ has been determined for the tested sensor.
The switching characteristic of the comparator can be adjusted with a dedicated DAC, `VPComp`, which is set to a value of 5 in the default configuration. Increasing `VPComp` enhances the available currents in the comparator, which allows for a faster and more precise switching behavior and less voltage drop induced column dependence **??**. Tuning the sensor has less effect

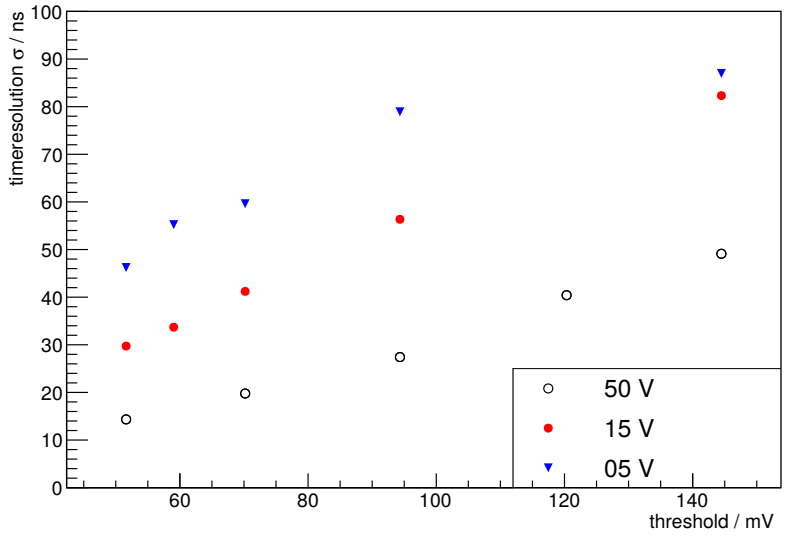

Figure 10.23: Time Resolution as function of the threshold after individual pixel corrections for sensor 084-3-25 at different bias voltages.

for higher values of VPComp.
The signal shape can be influenced by the configuration of the pixel amplifier. A systematic variation of these DACs showed, that the default DACs are already close to the optimum. Only adjustments of the amplifier feedback capacity via VPLoadPix have a significant potential to improve the timing.
Time-walk corrections can reduce the influence of variations in the deposited charge. Due to a design problem ToT information cannot be reliably provided at typical readout speeds and requires a severe reduction of the readout speed, see section 4.2. Therefore it could not be used in MUPIX TELESCOPE studies.
At reduced readout speeds, time-walk can be corrected based on a ToT measurement. Figure 10.24a shows the ToT versus the delay corrected time difference, where time-walk becomes clearly visible. To correct for the time-walk, the arithmetic mean of the corrected time difference $\mu(ToT)$ is calculated for each ToT bin, based on seven time difference bins around the maximum. The time-walk corrected time difference Δt_{twc} is then given as

$$\Delta t_{twc} = \Delta t_{delay} - \mu(ToT_{hit}). \tag{10.12}$$

The ToT versus the delay corrected time difference after time-walk correction is shown in figure 10.24b. No ToT dependence can bee seen anymore.

Dedicated laboratory studies [54] at a bias voltage of –60 V with sensor 084-1-5 show that significant improvements of the time resolution are possible by optimizing the DAC settings. VPComp is increased in a first step. The delay dependence on the column is reduced and goes to zero for higher VPComp values – the comparator is less effected by the small voltage drop along the columns for higher values of VPComp. The results for

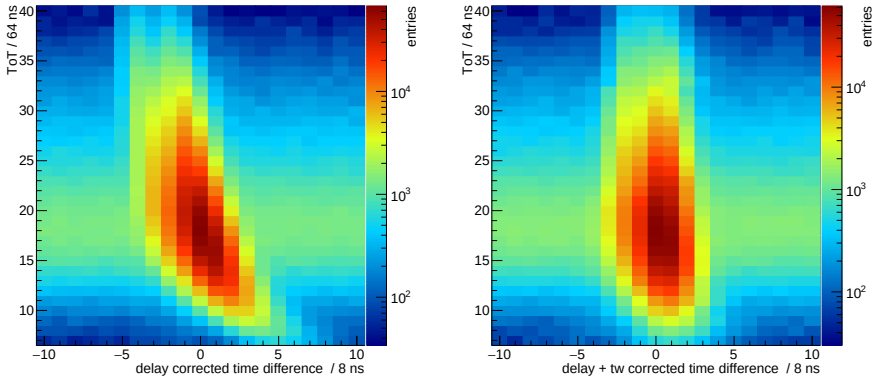

(a) Before time-walk correction (b) After time-walk correction

Figure 10.24: ToT versus the delay corrected time difference between hit and trigger before and after time-walk correction. Based on data from [54].

a scan of VPComp are shown in figure 10.25 for the full matrix and a subset with row numbers below 36 to reduce the influence of crosstalk. For the full sensor a minimum of the time resolution is found for VPComp of 20. For higher values (above 26) the time resolution starts to decrease again. Without any corrections a time resolution of approximately 12 ns can be achieved, compared to 15 ns for the default settings. The improved resolution compared to the previous study is a result of using the 2 threshold method. A linearized correction, as shown above, further improves the resolution to 10 ns for VPComp of 15-20. Adding the time-walk correction leads to a time resolution of approximately 7.5 ns for the full sensor.

Selecting only rows below 36 results in an improved time resolution for all steps. The uncorrected time resolution is 9 ns and not significantly improved by the delay correction, which is dominated by the row correction for the improved settings. Correcting also for time-walk leads to a time resolution of 6.5 ns.
In a next step, VPLoadPix is varied for a VPComp of 18. The results are summarized in figure 10.26 for the full matrix and rows below 19 as the crosstalk is enhanced for higher VPLoadPix values. The default value of 5 is not optimal, the resolution improves by roughly 1 ns after all corrections and is rather constant for VPLoadPix values above 9.

Additional DACs are further varied in [54] without significant improvements. Tests with a 200 Ωcm substrate sensor also do not show an improvement. Therefore, the limitations in the time resolution seem to be not induced by the signal size, but rather created in the circuitry of the senor.
The individual pixel resolutions of the full sensor and the mean delay after the correction is studied, see figure 10.27. The spread has a width of σ =4.16(3) ns, significantly smaller as the spread at default settings. The

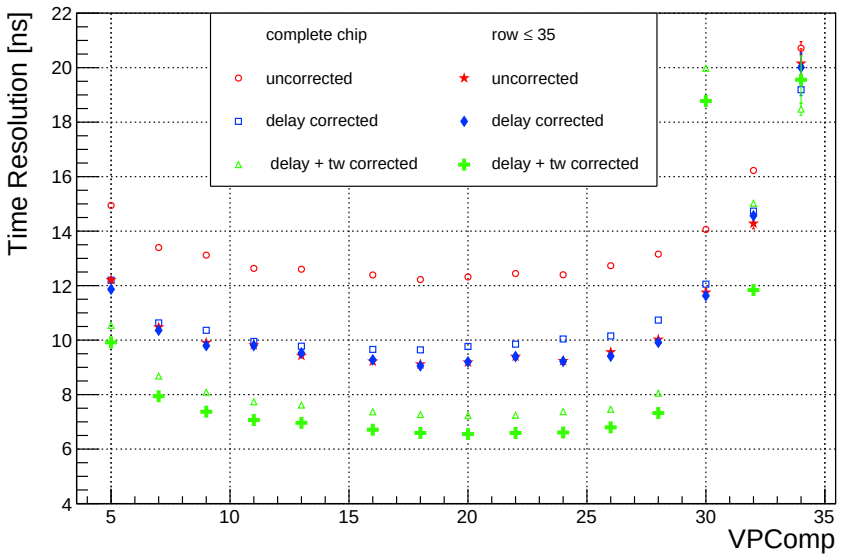

Figure 10.25: Time resolution of sensor 084-1-05 for different values of `VPComp` and a bias of –60 V. Solid markers show the results for rows below 36 and empty markers for the full sensor. The color encodes the correction: No correction (red), delay corrections (blue) and delay and time-walk corrections (green). Taken from [54]

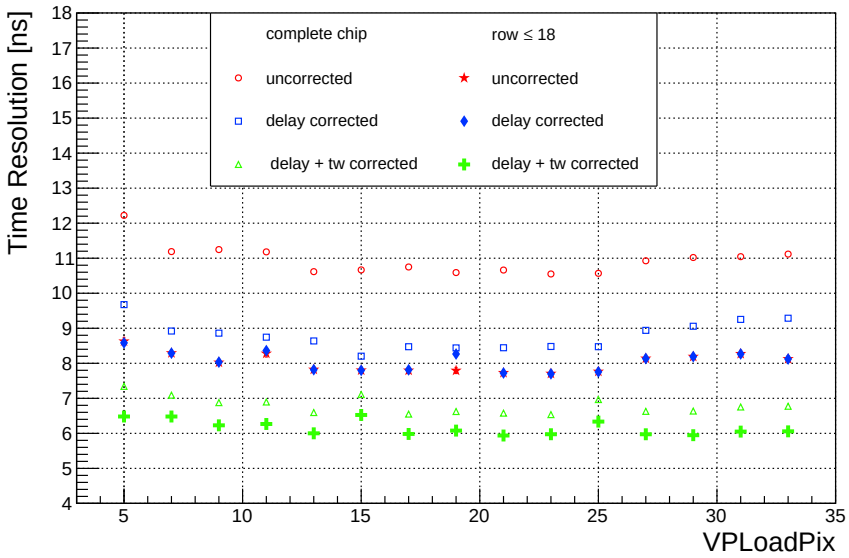

Figure 10.26: `VPLoadPix` scan for sensor 084-1-05 at a bias of –60 V and `VPComp` set to 18. Solid markers show the results for rows below 19 and empty markers for the full sensor. The color encodes the correction: No correction (red), delay corrections (blue) and delay and time-walk corrections (green). Taken from [54].

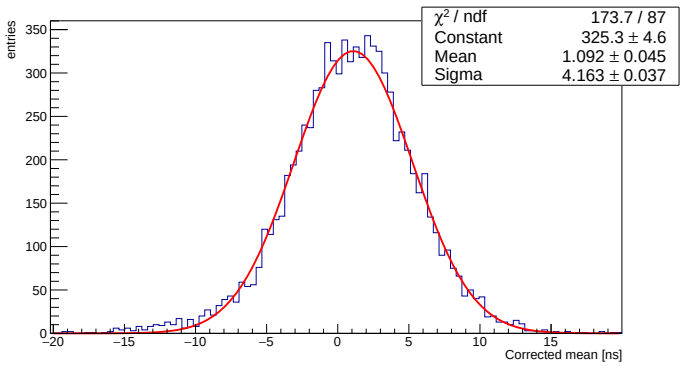

(a) Average time difference

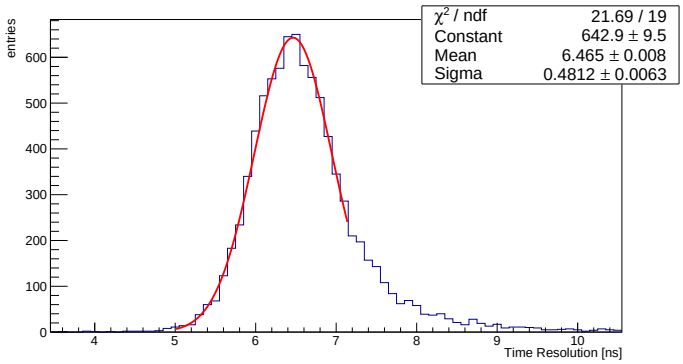

(b) Time resolution

Figure 10.27: Average time difference after delay- and time-walk correction and single pixel resolution for sensor 084-1-05 at a bias of –60 V. The core of both distributions is fitted with a Gaussian. Taken from [54].

individual time resolution after a global time-walk correction is 6.465(1) ns with a spread of only 0.48(1) ns, also a large improvement compared to the default settings.

The resolution of single pixels, see figure 10.27b, is not influenced by delays over the sensor, but only by pixel-to-pixel variations. A global time-walk correction cannot recover these variations. This effect is similar to to the delay corrections. However, a high statistics calibration sample would be required to apply an individual time-walk correction for each pixel, which could not be collected with a radioactive source in the laboratory. A high statistics sample from a testbeam campaign has been collected recently and will be analyzed. Threshold tuning of the pixels can be used to achieve a more uniform response, which should significantly reduce the pixel-to-pixel variations.

The increase in power dissipation due to optimized DAC settings is moderate. The sensor needs 199 mW/cm^2 instead of 180.8 mW/cm^2, an increase of only 10 % and still significantly below the cooling limits for *Mu3e*.

sensorID	resistivity [Ωcm]	thickness [µm]	bias [-V]	threshold [mV]
084-3-25	200	100	50	50
			30	50
			30	50
			3	100
			3	50
084-1-05	80	725	50	50
			15	50

Table 10.2: Listing of all sensors used in the EUDET-telescopes alongside their thickness and resistivity as well as the bias and threshold settings. Sensor 084-1-05 is studied with a beam energy of 4 GeV, 84-3-25 with an energy of 2.8 GeV.

10.4 SUB-PIXEL STUDIES

Studying global efficiencies is only a first step in sensor characterization. Observed inefficiencies need to be tracked down to their origin. Therefore it is crucial to also study effects within the pixel. Does the sensor diode structure influence the response? Is charge-sharing causing inefficiencies? Is there any other structure visible in the pixel? The answer to these questions relies on sub-pixel studies, which are based on a high spatial resolution reference telescope.

In the following, results obtained with the EUDET-telescopes DATURA and DURANTA at the DESY testbeam areas TB 21 and TB 22 are presented. The pointing resolution as well as the alignment has been evaluated in section 7.3.1. During two testbeam campaigns in March 2018 and June/July 2018, two MUPIX8 prototypes have been studied at different bias and threshold voltages. Table 10.2 lists the sensors and settings. An alignment was performed and the post alignment unbiased residuals are below 2 µm and stable over time, with a rotation below 1.8 µm over the full sensors height.

Due to the readout architecture of the EUDET-type telescopes and the missing timing reference for the reconstructed track, no explicit time-cut is applied on the data. However, only hits in the same readout frame as the reference track and the next one are accepted for analysis. This limits the time window to two readout frames and 720 µs. The maximal distance between the pixel and extrapolated track position is set to 100 µm for hit matching. For clusters with hit multiplicity larger one, all hits in the clusters are compared with the extrapolated position and the closest hit is chosen as matched. As region of interest, the outer three columns and rows are excluded and only tracks, which are extrapolated to the region of interest

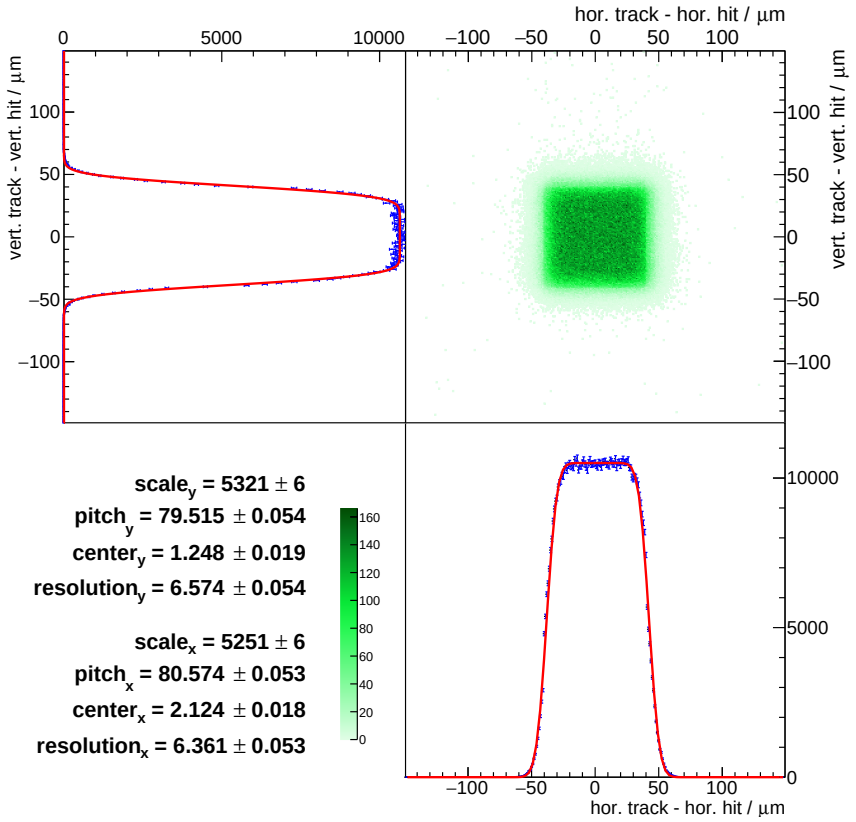

Figure 10.28: Difference between extrapolated track position and pixel center for the 15 V data sample of sensor 084-1-05. The projections along the column and row axis are fitted with a double sided error function to obtain the pointing resolutions. Only rows 0-80 are shown.

are accepted for the analysis.
In the following, the sub-pixel studies are presented in detail for sensor 084-1-05, with a thickness of 725 µm and a resistivity of 80 Ωcm. These sets are chosen as they have the highest statistics and the resolution improvement due to the thinner sensor 084-3-25 is small due to the reduced beam momentum and the track reconstruction method. The pointing resolution of the telescope for the data set at –15 V is summarized in figure 10.28 by plotting the unbiased distance between extrapolated position and hit center. Fitting the x/y projections with a Gaussian smeared box, see equation 7.3, gives the pointing resolution of the telescope of 6.39(4) µm (6.53(4) µm) along $x(y)$.

Efficiency studies

Efficiency maps for the sensor are shown in figure 10.29 for two bias voltages. Figure 10.30 shows the efficiency projection on the row address for

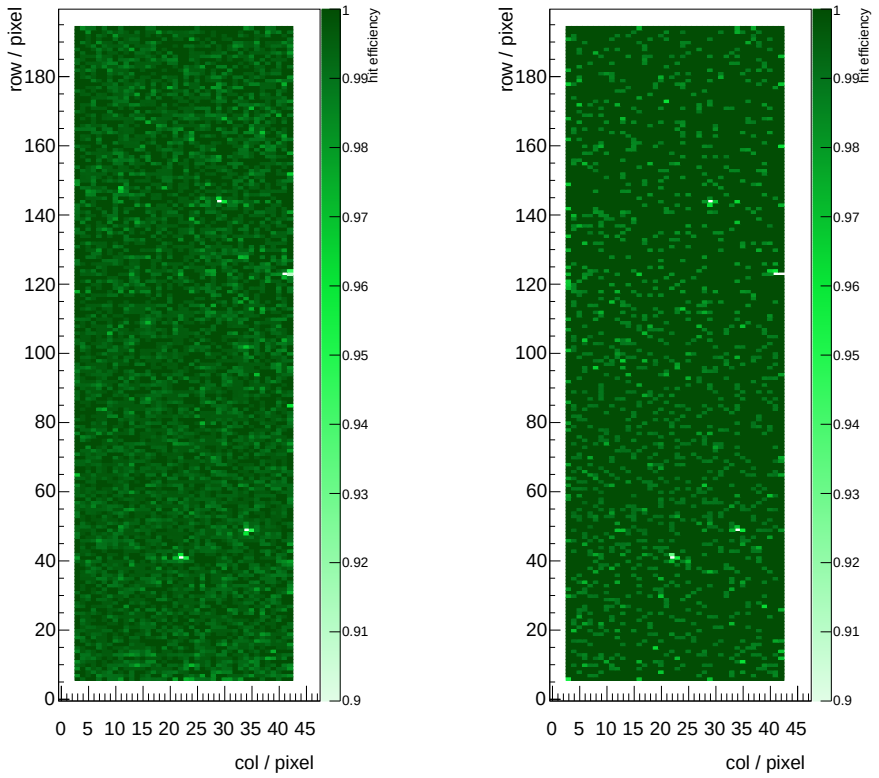

(a) 15 V (b) 50 V

Figure 10.29: Efficiency map of MUPIX8 with sensor ID 84-1-05 at different bias voltages. The inefficient points, drawn in white, are due to masked pixels, which are identical for both bias voltages. Note that the z-scale starts at an efficiency of 90 %.

both sensors. Neither in the 2D plot, nor in the projection, any position dependent effects can be seen. The efficiency remains high over the complete sensor, excluding the masked pixels, which are of course not efficient: the inefficiency of 2.5 % for the rows 42 and 51 is consistent with one pixel out of 42 being inactive and the above discussed average cluster sizes. The smaller inefficiency of masked pixels in higher rows is partially recovered by crosstalk, as the masking turns off the comparator in the digital periphery on the bottom of the sensor. The amplifier and line driver are still active and create crosstalk, compare sketch in figure 4.3.

For –15 V bias, the average hit efficiency is 99.53 % with negligible statistical uncertainty. The average hit efficiency for a bias voltage of –50 V is 99.77 %. The high resolution of the reference telescope is used to study the efficiency with sub-pixel precision. To increase the available statistics, the efficiencies of the sensor are folded back to a 2x2 pixels matrix.

The results for a bias of –15 V is shown in figure 10.31a and for –50 V in figure 10.31b. A clear inefficiency in the pixel corners for a bias of –15 V becomes visible, with some very small inefficiency along the pixel edges. Both effects cannot be seen for a bias of –50 V, leading to the interpreta-

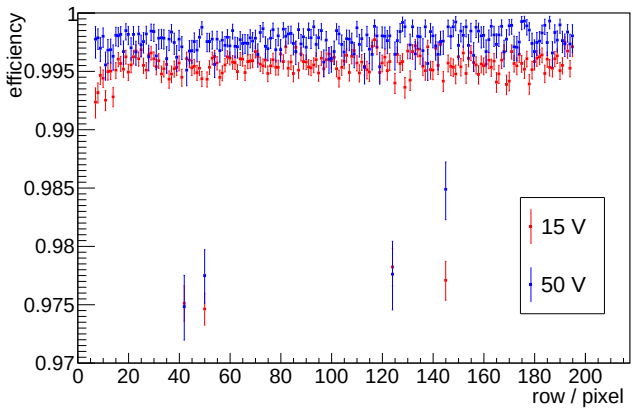

Figure 10.30: Row projection of the efficiency for bias voltages of –15 V and –50 V. The less efficient points correspond to rows with one masked pixel.

tion, that there is no charge sharing induced inefficiency at a bias of –50 V and a threshold of 50 mV.
Figure 10.32 shows the efficiency for –15 V bias folded to a single pixel to further increase the available statistics. The efficiency in the central part of the pixel, ranging from 15 µm to 65 µm along both axis is 99.75 %, consistent with the global efficiency of the –50 V data set, showing, that the efficiency decrease is explained only by inefficiencies in the corners due to charge sharing.

The remaining 0.23 % average hit inefficiency are not created by charge sharing. Four pixels have been masked for the presented study and create an inefficiency of 0.04 %. The remaining inefficiency is either created by mis-reconstructed tracks, see section 5.4 or hits on the DUT, which are lost during the readout[6]. Edge-effects can be excluded because of the larger size of the reference system compared to the MUPIX8 sensor size, the excellent pointing resolution of the reference telescope and the region of interest cut on the data.
From the corner inefficiency the Gaussian σ_{ion} of the ionization width can be inferred under the assumption that the sensor is also depleted in the corners and along the edges. A second approach, based on the width of double clusters is discussed later. Figure 10.33 shows a 3D plot of the in-pixel efficiencies folded to the size of one pixel, with the pixel corner being the center of the plot. The inefficiency in the center can be fitted with

$$E(x,y) = E_0 - g(\theta_x, \theta_y). \tag{10.13}$$

E_0 is the efficiency in the pixel center and $g(\theta_x, \theta_y)$ the 2-dimensional Gaussian defined in equation 7.5. The width of the Gaussian is the superposi-

6 The hit sorter on the FPGA is capable of high rates but a large number of hits per column from a δ-electron can still cause a hit to arrive too late at the sorter.

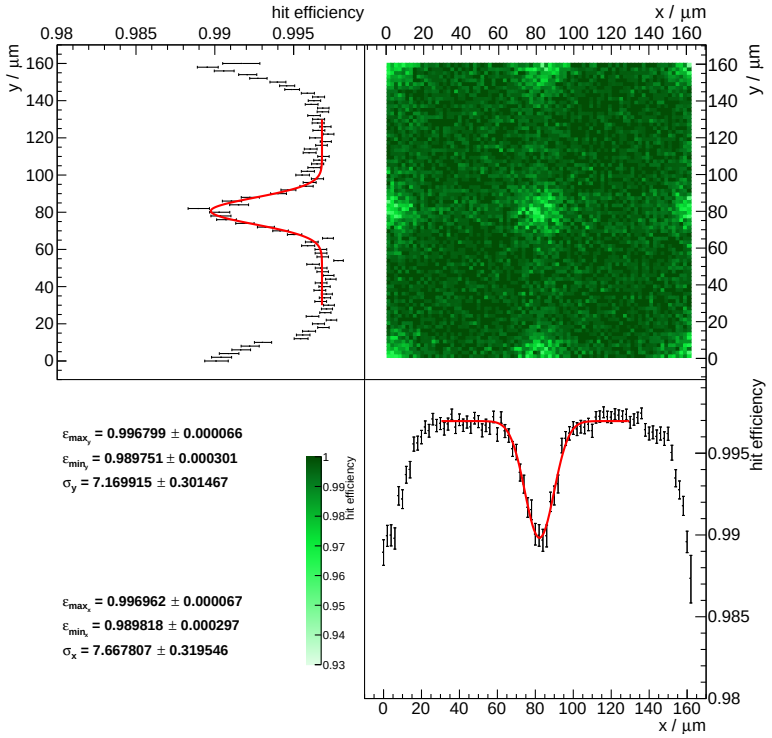

(a) -15 V

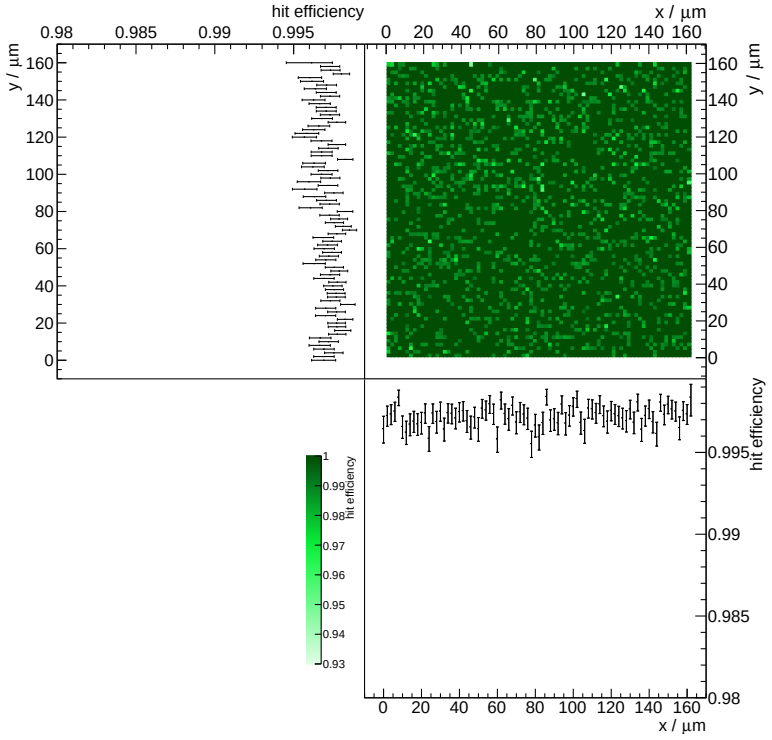

(b) -50 V

Figure 10.31: Efficiency folded to 2x2 pixels at a global threshold of 50 mV, together with the column and row projections. For –15 V structures at the corners and edges become visible. The projections of the –15 V set are fitted with a Gaussian to quantize the inefficiencies. For –50 V no substructure is visible.

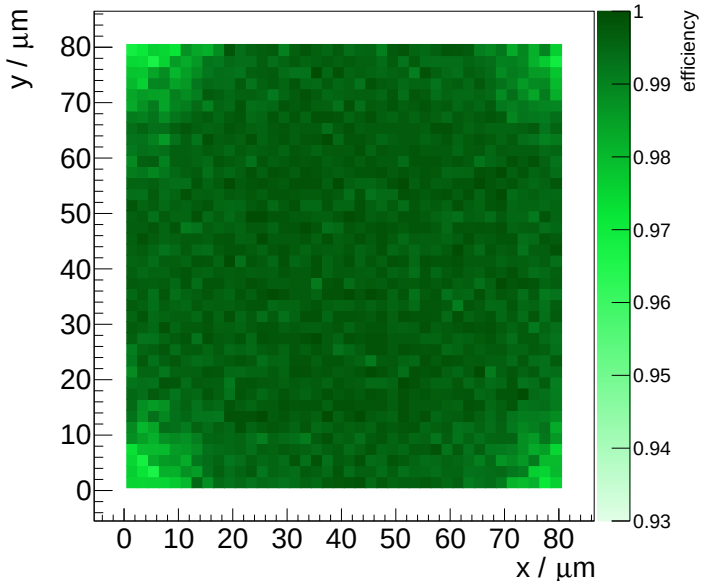

Figure 10.32: Efficiency folded to a single pixel for a bias of −15 V and a threshold of 50 mV.

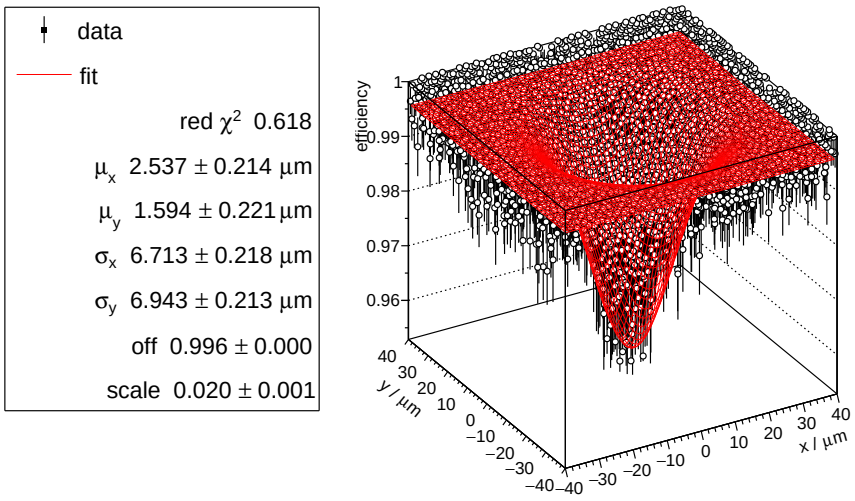

Figure 10.33: Efficiency folded to a single pixel for a bias of −15 V and a threshold of 50 mV. The pixel corner is in the center. The distribution is fitted with a two dimensional Gaussian.

tion of the pointing resolution of the reference telescope σ_{res}, the ionization σ_{ion} and the charge fraction required to create a hit in a pixel. The latter is not exactly known. Observed small inefficiencies in the corners, together with insignificant losses along the edges suggest a small required fraction of charge. For a constant charge signal the fraction would be between 25 % (corner) and 50 % (edges). However, charge deposition is not constant and will further smear out the limits, see also the charge sharing and clustering Monte Carlo in Appendix E. Ignoring the finite fraction of the charge required to detect a hit, the total width of the fit can be split up:

$$\sigma^2_{fit_{x/y}} = \sigma^2_{res_{x/y}} + \sigma^2_{ion_{x/y}} \tag{10.14}$$

σ_{res_x} is measured to be 6.39(4) µm, as described in section 7.3.1. The fitted width σ_{fit_x} is 6.71(22) µm. The width of the ionization σ_{ion_x} is given by

$$\sigma_{ion_x} = \sqrt{\sigma^2_{res_x} - \sigma^2_{fit_x}} = 2.1(7)\,\mu\text{m}. \tag{10.15}$$

σ_{ion_y} can be calculated accordingly to be 2.37(6) µm. In principle, no difference between the x and y is expected. Combining both measurements leads to $\sigma_{ion} = \sqrt{2} \cdot 2.21(16)\,\mu\text{m} = 3.13(23)\,\mu\text{m}$. This is only an estimate on the ionization σ_{ion}, as the detection threshold is ignored.

Clustering

The size of track assigned clusters is shown in figure 10.34, including crosstalk. For higher bias voltages and therefore larger depletions, the mean cluster size is larger. Clusters with a size of larger than four are either an overlay of two particles or created by a δ-electron. The distributions are consistent with the previous results.

Clusters created by charge sharing are expected to be located closer to the pixel edges. Figure 10.35 shows the extrapolated track intersection for matched clusters of different size for the data set with –15 V bias. Single clusters, see figure 10.35a, are located typically in the central part of the pixels. Clusters with a size of two, see figure 10.35b, are located on the pixel edges. For cluster sizes larger than two, the available statistics are limited. However, they tend to be created by particles passing through the corners of pixels, compare figures 10.35c and 10.35d.

The extrapolated track positions for double clusters can be used to extract the size of the charge cylinder. Figure 10.36a (10.36b) shows the 2x2 folded extrapolated track intersections for double clusters projected to the x(y)- axis. The central part is fitted with a Gaussian. The mean values of the fit correspond to the positions of the pixel edges. The width of the distribution is a superposition of the pointing resolution, the ionization width σ_{ion} and the charge fraction required to detect a signal. The pointing resolution is known from the fits in figure 10.28. To calculate σ_{ion} the absolute probability to create a double cluster and charge required to trigger a hit

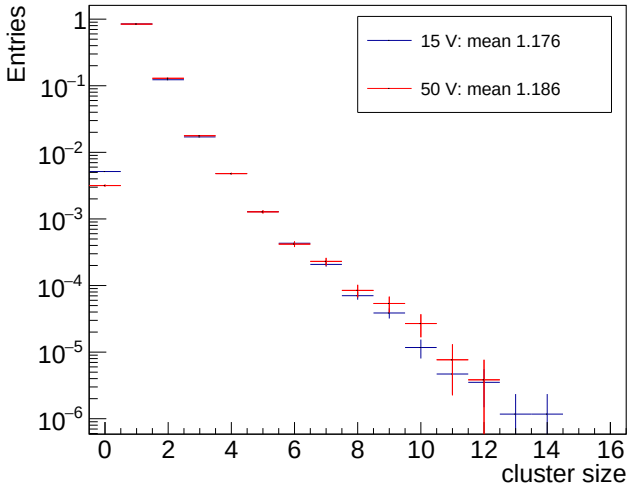

Figure 10.34: Size of track assigned clusters with −15 V and −50 V bias voltage at a threshold of 50 mV. The integral of both distributions is normalized to one. Crosstalk events are included. A cluster size of zero corresponds to sensor inefficiencies.

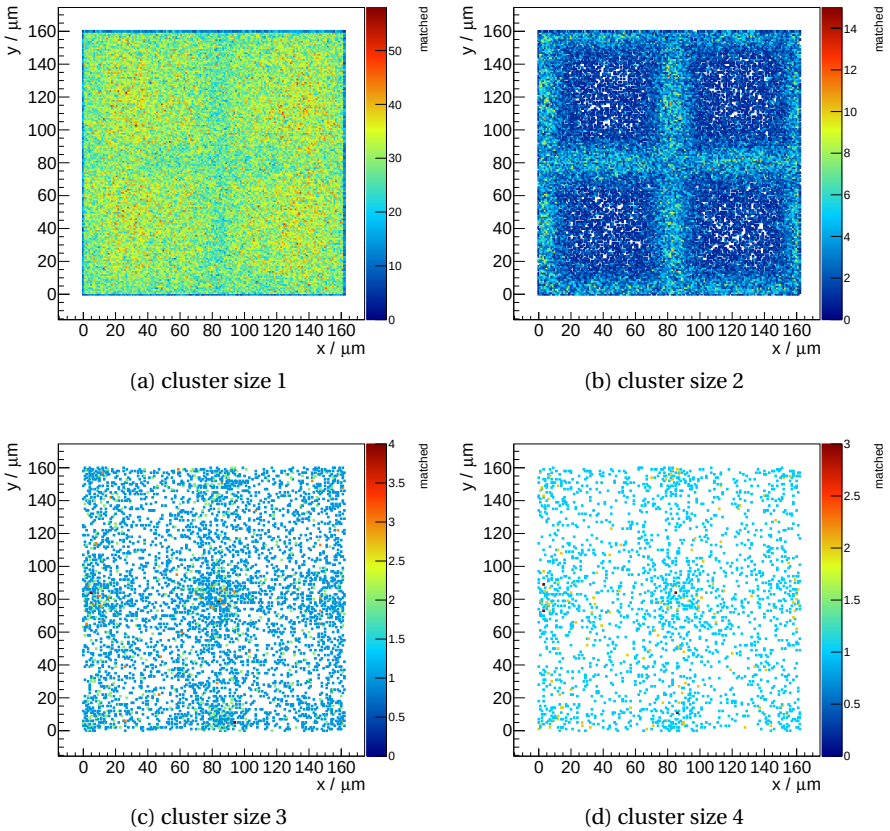

(a) cluster size 1

(b) cluster size 2

(c) cluster size 3

(d) cluster size 4

Figure 10.35: Extrapolated track position folded to a 2x2 pixel matrix for matched clusters with different size. Only rows 0-80 are shown, as they are not affected by crosstalk.

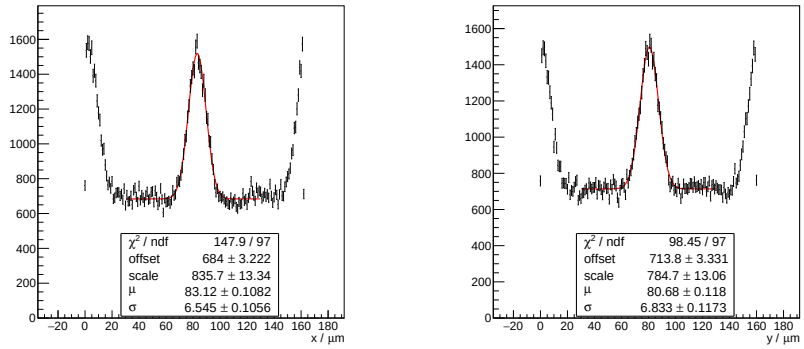

(a) X Projection (b) Y Projection

Figure 10.36: Extrapolated track position for double clusters projected on the x and y axis. Both projections are fitted with a Gaussian.

have to be known. The latter relies on simulation input. From a toy Monte-Carlo, see Appendix E, the required signal fraction can be extracted and the corresponding ionization width σ_{ion} can be read off for combinations of cluster size and efficiency. The efficiency is as aforementioned 99.53 %. The probability to create a double cluster is 6.87 %. From the simulation, the ionization width $\sigma_{x/y} = 2.8\,\mu\text{m}$ can be extracted for the given efficiency and cluster size as well as a detection threshold of 35 % of the most probable charge deposition. The expected double cluster width $\sigma_{expected_{x/y}}$ can be also obtained from simulation, compare Appendix E. The fitted width is

$$\sigma^2_{fit_x} = \sigma^2_{res_{x/y}} + \sigma^2_{expected_{x/y}}. \tag{10.16}$$

The resolution σ_x is 6.36(4) µm, see figure 10.28 and $\sigma^2_{expected_{x/y}}$ is 1.696(1) µm. Thus the expected σ_{fit_x} is 6.6(4) µm. σ_{fit_y} is then 6.8(5) µm. Within the uncertainties, both expected values agree with the fit results in figure 10.36. $\sigma_{ion} = \sqrt{2}\sigma_{x/y} = 3.8\,\mu\text{m}$ is slightly larger than the extracted ionization width from the inefficiencies in the pixel edges, because the required charge to create a hit is correctly taken into account.

Comparison of all samples tested with sub-pixel resolution

The analysis discussed in detail above is carried out for all samples and settings from table 10.2. The results are summarized in table 10.3.

For the used DAC settings sensor 084-1-05 is overall more efficient compared to the sensor 084-3-25, see also section 10.5. The pointing resolution of the telescope is slightly varying between the different data sets, attributed to statistical fluctuations and slightly different alignments – nevertheless it always stays below 9 µm, allowing for sub-pixel analysis. Higher bias voltages lead to larger depletion zones and higher efficiencies, as expected. For a bias voltage of –50 V no position dependence on the sensor edges is observed for sensor 084-1-05 and sensor 084-3-25 shows only 0.1 %

sensor	084-1-05		084-3-25				
bias [-V]	15	50	3	3	30	30	50
threshold [mV]							
	550	550	550	600	550	650	550
$\bar{\epsilon}$	99.5	99.8	95.8	65.4	99.24	77.0	99.3
$\epsilon_{central}$	99.7	99.8	97.8	73.0	99.28	81.9	99.3
ϵ_{edge}		99.8			99.24		
ϵ_{corner}	99.0	99.8	88.2	50.8	99.21	60.9	99.2
Double cluster							
σ_x [µm]	6.5(1)	7.0(2)	6.7(6)	5.8(6)	5.3(6)	7.6(6)	5.9(6)
σ_y [µm]	6.8(1)	7.0(2)	5.9(7)	4.2(9)	6.2(5)	6.1(8)	6.5(5)
telescope resolution							
σ_x[µm]	6.39(2)	6.45(3)	6.91(6)	8.50(4)	6.58(5)	7.82(2)	6.67(4)
σ_y[µm]	6.53(1)	6.16(3)	6.87(6)	8.58(4)	6.46(5)	8.09(2)	6.19(5)

Table 10.3: Overview of the results from the sub-pixel studies.

efficiency decrease in the pixel corner. For higher thresholds/lower depletion voltages, the overall efficiency is reduced. The decrease is smaller in the pixel center, while the efficiency reduction at the corner and edges is more severe, as expected from charge sharing.

The sub-pixel analysis showed that the sensor is homogeneously efficient within the pixel cell for corresponding settings. At increased thresholds, inefficiencies occur first in the sensor corners and then at the edges proving that charge sharing causes inefficiencies first. Additionally it could be confirmed that the ionization width is in the range of $3-4\,\mu m$.

The corners with four pixels touching can be avoided by a change in the pixel cell layout. Changing it to a brick layout, where every second column is shifted by half a pixel avoids charge sharing between four cells, which is expected to increase the efficient threshold range. A honeycomb structure has a similar effect with an increased number of three pixel corners.

10.5 SENSOR-TO-SENSOR VARIATIONS

Building a functional large-scale detector requires not only good individual sensor performance, but also minimal variations between different sensors, as well as highest possible production yield. Ideally, all sensors in a detector can be operated with identical DAC settings.

The MUPIX8 was produced in the first engineering run during the development of the *Mu3e* pixel sensor. Therefore, sensors from several wafers are available and can be compared. Figure 10.37a shows the efficiency of all scanned sensors as a function of the threshold and figure 10.37c zooms

into the most important region. Strong variations between the sensors are present, which need to be understood in detail. The threshold range in which the sensors stay above 99 % efficient varies from over 100 mV to 0 mV. Possible differences are the sensor resistivity, wafer and production variations and the senor thinning and handling, as well as the used DAC settings.

Resistivity dependence

The MUPIX8 is produced on four different substrates with a resistivity of 20 Ωcm, 80 Ωcm, 200 Ωcm and 1 kΩcm. Higher resistivity leads to a larger depletion zone and therefore more collectible charge as well as a higher efficiency over a larger threshold range. Unfortunately, sensors with the standard 20 Ωcm substrate have not become available in time for this study and the 1 kΩcm sensors have not been functional at bias voltages beyond –30 V. The remaining two substrates are compared in figure 10.38 and behave as expected. The high efficiency region is larger for 200 Ωcm compared to 80 Ωcm. Thinning to 100 µm is not degrading the performance.

Production and processing

Figures 10.39a and 10.39b show the efficiency as a function of the threshold for sensors originating from pre- and final production. The thick sensor from the pre-production performs better than the thin sensors from the final production for an 80 Ωcm substrate. For 200 Ωcm, the behavior is exactly the opposite: The final production run sensor performs significantly better than the sensor from the pre-production, which has not been thinned. The production process is monitored using test structures and stayed within the specifications for the final production run. The differences between the behavior of the 80 Ωcm and 200 Ωcm indicates, that the difference is not related with the production process. The handling and processing of the wafers has been different for the pre- and final production. The final production has been thinned and cut by a method called *dicing before grinding*, where the wafer is cut along the die edges with a diamond saw blade in a first step and thinned afterwards. This method is a standard method. The pre-production wafers are laser cut and not thinned.

Wafer-to-wafer variations

Figure 10.40 summarizes all tested samples at an threshold of 50 mV and a bias of –50 V. There are clear differences between sensors from different wafers - especially wafer 22 seems to be best. Also the impressions from figure 10.39 are confirmed: There is no significant difference between the pre- and final production. Sensors originating from the same wafer seem to have similar characteristics - for a final conclusion sensors from more

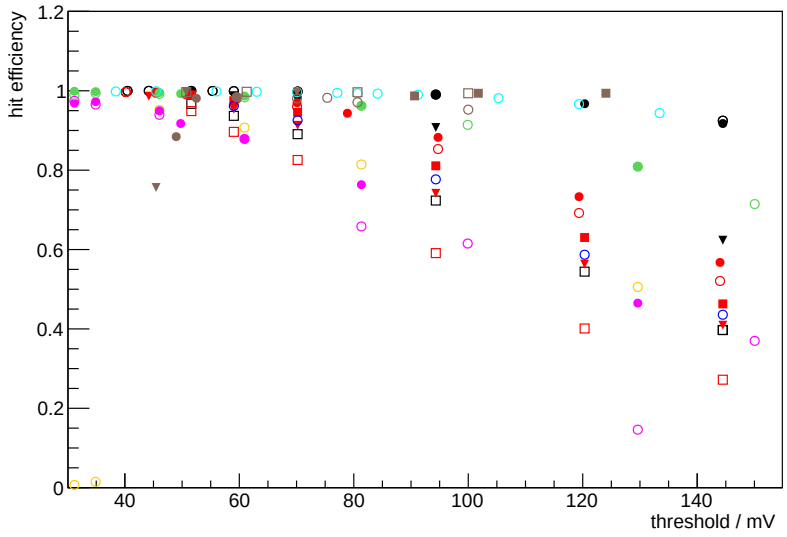

(a) Efficiency

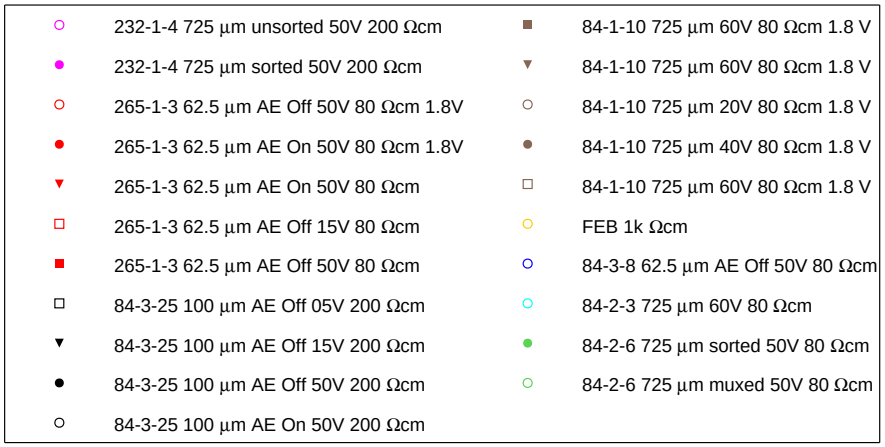

(b) Legend

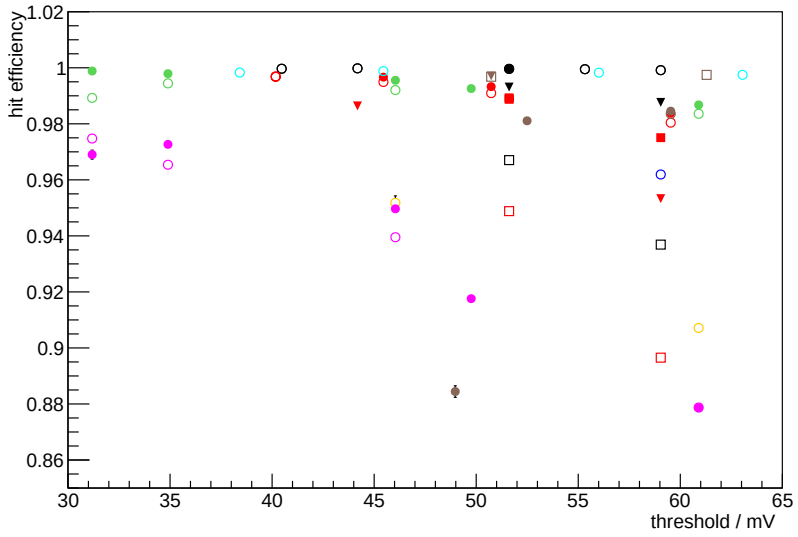

(c) Efficiency zoom

Figure 10.37: Efficiency as a function of the threshold for all tested MUPIX8 sensors and settings. The sensors are color encoded and different settings are indicated by different symbols. Binomial errors are included.

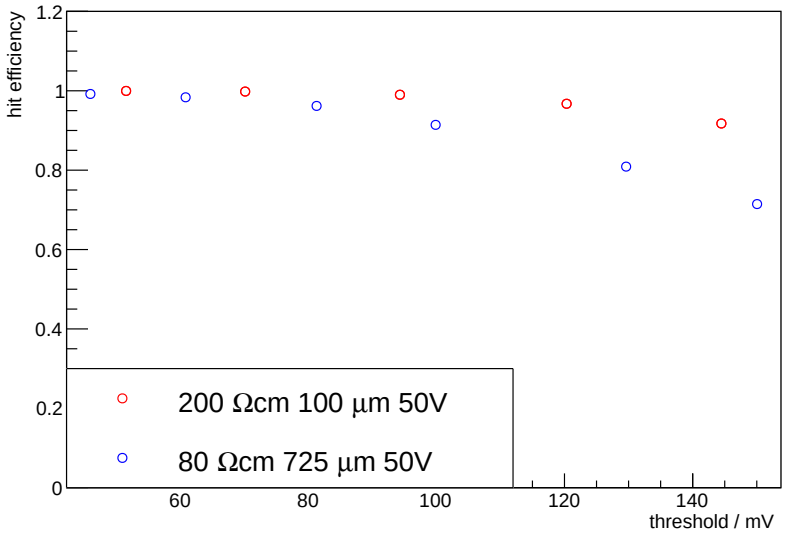

Figure 10.38: Comparison between an exemplary sensor with a resistivity of 80 Ωcm and 200 Ωcm.

wafers are required and additional resistivity wafers need to be added to this comparison.

DAC settings

A possible cause for sensor variations is, that process variations require different DAC settings for the sensors. It is also possible that the used DAC configuration is not optimal and only suitable for a subset of sensors/wafers. Detailed studies on DAC optimization are ongoing while writing this theses.
Two reference voltages for the sensor are sensitive to small production variations. A low source voltage in the source follower limits the currents in the driver and the line capacity cannot be fully charged, reducing the efficiency [92]. Increasing the levels of these reference is expected to reduce the influence of variations in the production. First laboratory measurements show, that the signal of the amplifier is significantly increased, if these levels are increased for senors with a bad performance [55], making it very likely, that the variations can be attributed to a non optimal reference voltage. However, a confirmation in a testbeam measurement is required for a final conclusion. This measurement is planned just after the hand in of this thesis.

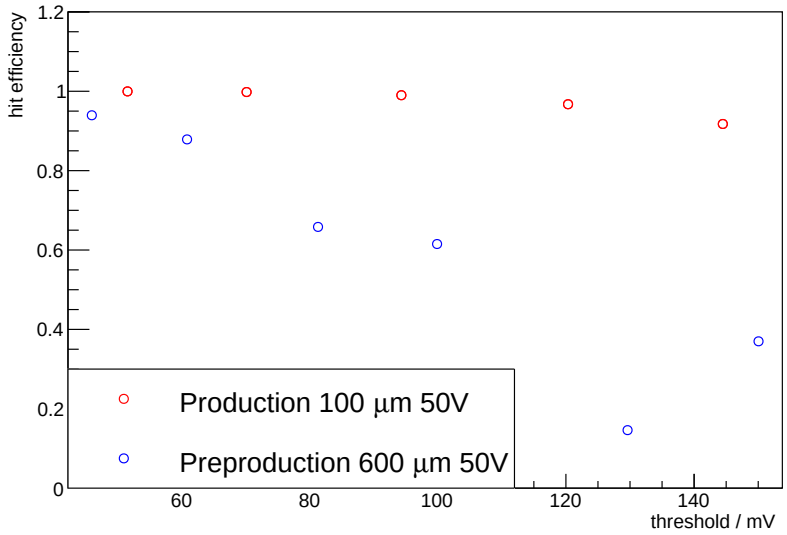

(a) 200 Ωcm

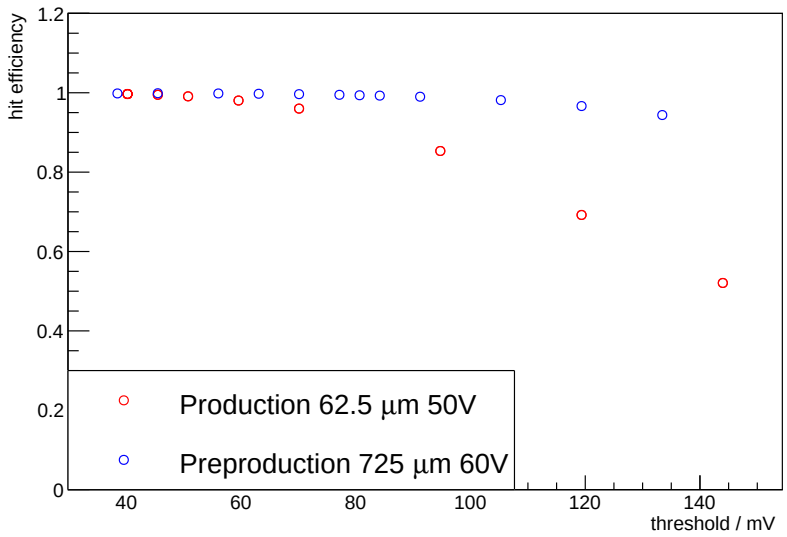

(b) 80 Ωcm

Figure 10.39: Comparison between pre- and final production of sensors with an resistivity of 80 Ωcm and 200 Ωcm.

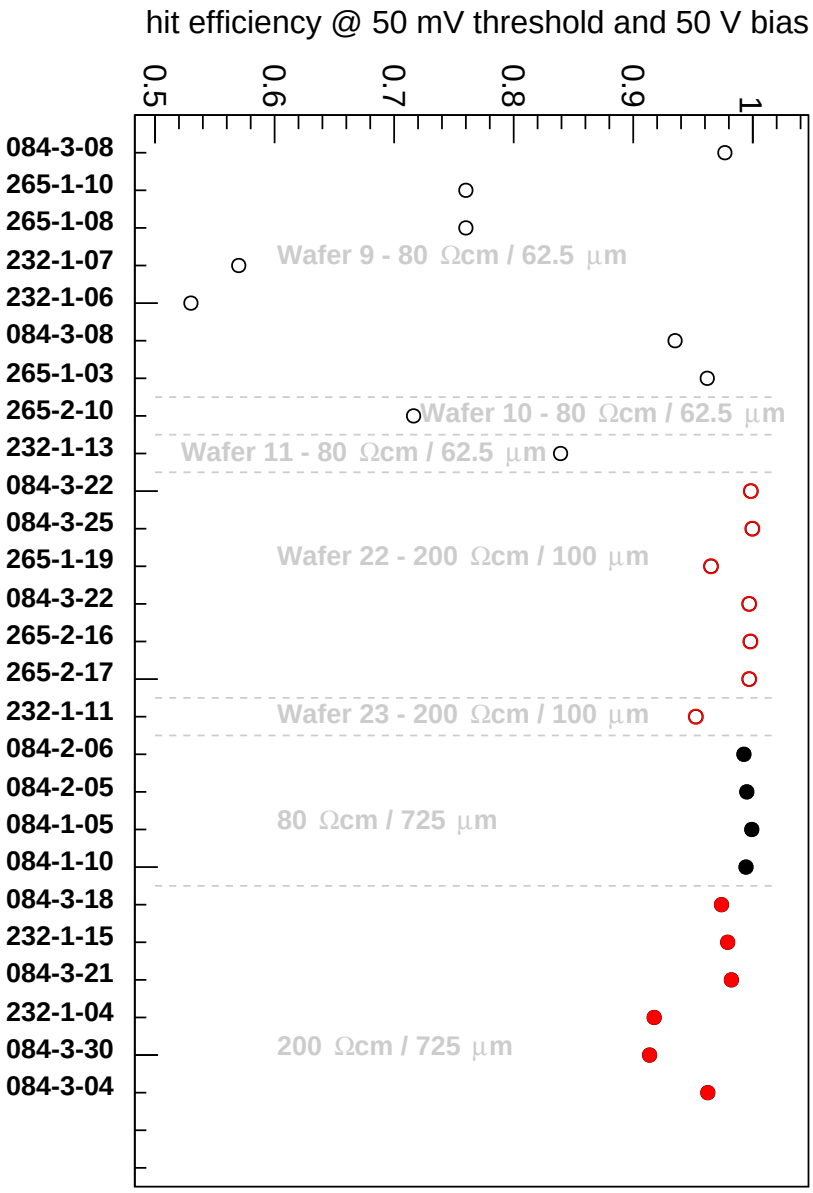

Figure 10.40: Comparison between all wafers. For 725 µm thick sensors it is not possible to assign sensors to wafers. It is known that the sensors originate from three wafers. Filled symbols represent the pre-production and empty ones the final batch. Red symbols are 200 Ωcm samples, black 80 Ωcm.

11

IRRADIATION STUDIES

Modern high-energy and luminosity hadron colliders create numerous particles during collisions. The large amount of created particles leads to significant amounts of radiation, especially close to the collision points. Pixel sensors have to be at least radiation tolerant enough to survive the planned runtime. ATLAS expects a total dose of about $1.31 \cdot 10^{16}\,n_{eq}/cm^2$, with a dose of 7.2 MGy for layer 0, while keeping the in-bunch crossing efficiency above 97 % [94]. Monolithic approaches might be of interest for LHC trackers, as they are extraordinarily thin, fast and less expensive. To test the potential of the AMS/IBM H18 process, a batch of 10 MUPIX7 sensors was irradiated with protons and neutrons at SPS and Ljubljana. As no cooling was developed before irradiation, all samples have been stored at room temperature for one year.
The following measurements have been published in [95] and the majority of this chapter is a copy of it using the exactly same wording.

Irradiated samples

MUPIX7 sensors have been irradiated with protons and neutrons according to table 11.1. During irradiation, the sensors have not been biased and not cooled. The prototypes had not been characterized beforehand. The samples have sensor thicknesses between 60 µm and 75 µm. The studies have been performed after one year of annealing at room temperature and therefore complete annealing of the ionizing damage is expected. The non-ionizing damage responsible for charge trapping and bulk damage, however, is expected to be left unchanged and is the primary focus of this study.

11.1 SETUP

The proton irradiated sensors are directly glued and wire-bonded to a printed-circuit-board (PCB)[1]. The neutron irradiated sensors are glued and wire-bonded to a ceramic carrier, which is connected to the same PCB type via a socket[2]. The PCB provides stable and ripple-free power, filters the high voltage and converts the differential slow control signals to single ended signals required by the MUPIX7. Baseline and threshold reference for the sensor are generated on the PCB where also test pulses to mimic signals can be generated.

1 The PCB is developed for the MUPIX7 and the predecessor of the MuPix8 mother board
2 Due to limited availability of PCBs only the proton irradiated sensors were directly bonded to PCBs.

Sensor ID	N00	N514	N115	N515
Facility	TRIGA	TRIGA	TRIGA	
NIEL Fluence [1 MeV n_{eq}/cm^2]	0	$5 \cdot 10^{14}$	$1 \cdot 10^{15}$	$5 \cdot 10^{15}$
Proton Fluence [24 GeV/c p/cm^2]	-	-	-	-

(a) Neutron irradiadted

Sensor ID	P00	P814	P1515	P7815
Facility	-	PS	PS	PS
NIEL Fluence [1 MeV n_{eq}/cm^2]	0	$4.8 \cdot 10^{14}$	$9 \cdot 10^{14}$	$4.7 \cdot 10^{15}$
Proton Fluence [24 GeV/c p/cm^2]	0	$0.8 \cdot 10^{15}$	$1.5 \cdot 10^{15}$	$4.7 \cdot 10^{15}$

(b) Proton irradiadted

Table 11.1: List of irradiated sensors. The quoted fluences are averaged over the sensor area. A hardness factor of 0.6 n_{eq}/p [37] is used to calculate the NIEL fluences for the proton irradiated samples. The sample P814 was not characterized during the test beam. Taken from [95].

The testbeam setup is sketched in figure 11.1. The sensors under test are actively cooled to reduce leakage currents and noise while also preventing thermal runaway. The proton irradiated sensors are cooled by cold nitrogen gas flowing over the backside of the sensor. The neutron irradiated sensors are cooled using a Peltier element, connected with an aluminum chuck. The Peltier element in turn is cooled by cold nitrogen gas. Two thermal baths are used to cool the nitrogen gas to –20 °C for both setups. The cooling power of the setup is controlled by the applied gas flow. A combined nitrogen flow of 2.5 m^3/h is used to cool the two sensors under test. The temperature of both devices-under-test (DUTs), as well as the humidity in the box, are continuously monitored to guarantee safe and constant operation conditions. Two reference tracking telescopes [66], consisting of three non-irradiated MUPIX7 sensors each, are used to measure efficiencies, noise and time resolution.

Temperature calibration

The temperature of the proton irradiated MUPIX is monitored by measuring the gas temperature close to the MUPIX. The temperature of the neutron irradiated prototypes is monitored by measuring the cooling chuck temperature. For both devices the MUPIX temperature T_{MuPix} is calculated

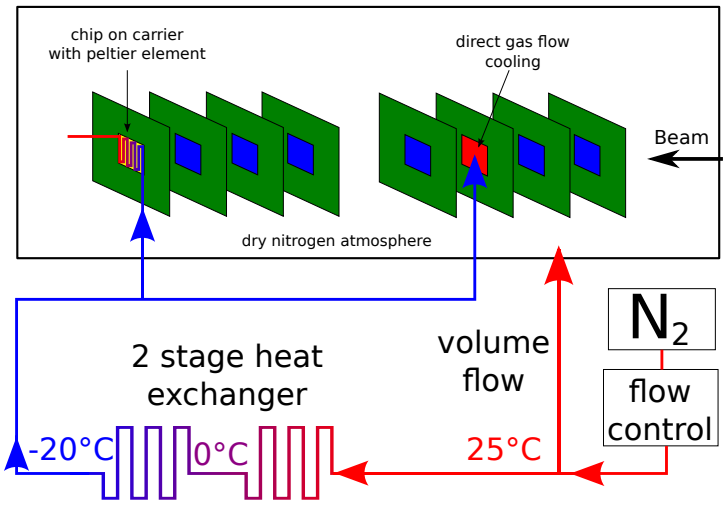

Figure 11.1: Sketch of the cooling setup in test beam. The red squares represent the devices under test. The blue squares represent reference sensors used for performance studies. Taken from [95].

from the measured temperatures T_{meas} by applying a correction obtained from an IR-camera[3]. The correction $T_{MuPix} - T_{meas}$ is about 5(−6) °C for the proton (neutron) irradiated prototypes. The uncertainty on the absolute temperature is dominated by the reproducibility of the thermal coupling between MUPIX and temperature sensor and estimated to be ± 2 °C. The relative uncertainty of the measured temperature over time is small and mainly given by the temperature sensor's uncertainty of 0.7 °C. The temperature is stable on the ± 1 °C level for measurement periods of 15 hours, see figure 11.2. The MUPIX temperature for both, proton and neutron irradiated, sensors is approximately 8 °C.

11.2 CHARACTERIZATION OF IRRADIATED SENSORS

11.2.1 *Laboratory results*

All irradiated MUPIX7 are fully operational after irradiation: the PLL can be locked to an external 125 MHz reference oscillator and the serial data output runs without 8 bit/10 bit errors. All hit addresses and timestamps transmitted to the FPGA are checked to be logically correct, thus indicating a fully functional readout state machine and serializer.

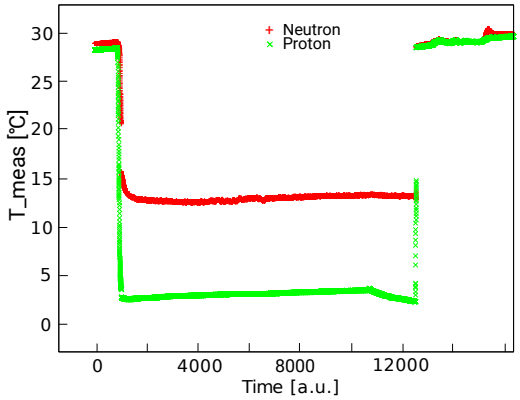

Figure 11.2: Monitored temperature T_{meas} of the gas flow close to the proton irradiated MUPIX (*green*) and the cooling chuck of the neutron irradiated MUPIX (*red*) over a 15 hours period. Taken from [95].

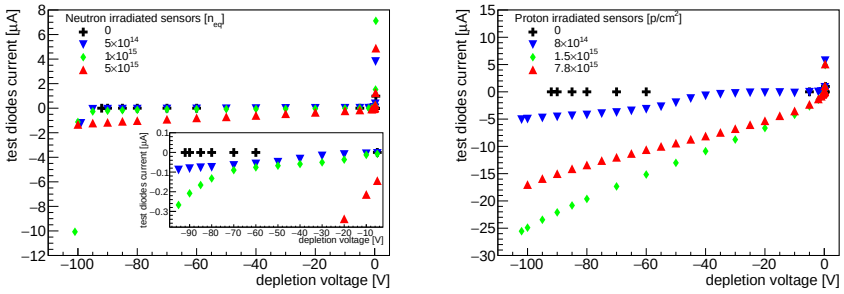

(a) Neutron irradiated samples.

(b) Proton irradiated samples.

Figure 11.3: Leakage currents of 32 test diodes with a total area of $9.9 \cdot 10^3\,\mu m^2$ as function of the depletion voltage for different irradiation levels. The measurements are performed at room temperature without cooling at $T_{MuPix} \approx 24\,°C$. Taken from [95].

Leakage currents

The leakage currents of non-irradiated and irradiated sensors are measured as a function of the depletion voltage. Figures 11.3a and 11.3b show the current-voltage characteristic (IV curve) for the neutron- and proton-irradiated sensors at room temperature when only depletion voltage is applied to a set of dedicated test diodes. As expected the measured leakage current significantly increases with the particle fluence and applied voltage. However, the absolute leakage current increase for the proton irradiated sensors is about twenty times higher than for the neutron irradiated sensors for similar fluences. A possible explanation is that the hardness factor for 24 GeV protons is significantly larger than expected for low-

3 The IR-camera in turn had been calibrated using a Pt1000 [96] glued on a heatable reference silicon surface.

ohmic silicon wafers and the AMS-H18 process[4]. Additionally, the hardness factor is assuming a constant thickness of the depletion zone, as it scales with the irradiated volume, see section 3.1.3. For classical fully depleted pixel sensors this assumption is justified. HV-MAPS are not fully depleted before irradiation and show increased depletion thicknesses after irradiation. Therefore, the conversion is biased. It is also a bit surprising that the $7.8 \cdot 10^{15}$ protons/cm^2 sample shows less leakage currents than the $1.5 \cdot 10^{15}$ protons/cm^2 sample. From edge-TCT measurements [97] it is known that the depletion thickness has a maximum for a fluence of about $1.5 \cdot 10^{15}$ protons/cm^2 which possibly could explain the higher leakage currents.

The diode breakdown voltage is below –100 V for all irradiated samples[5] and is significantly lower than the non-irradiated sensors, which have a typical breakdown voltage of about –90 V. This is consistent with an increased depletion thickness after irradiation [97].

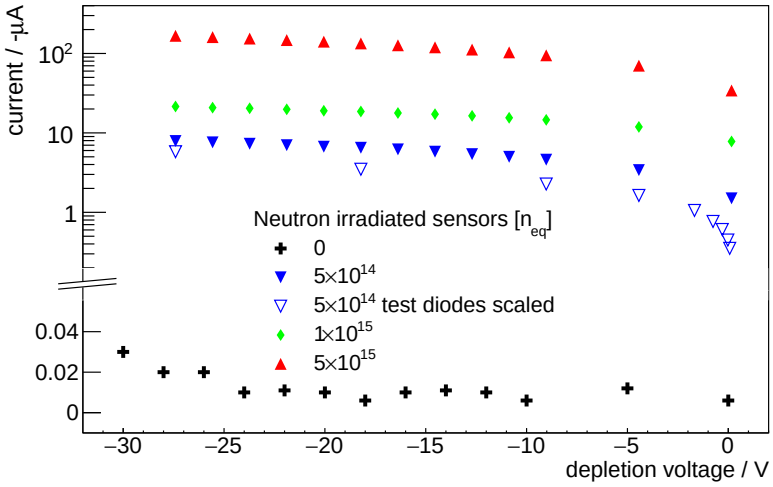

Figure 11.4: Leakage currents of the complete 32x40 pixel matrix for neutron irradiated sensors in full operation for a sensor temperature $T_{MuPix} \approx 40\,°C$. Each pixel encloses 9 diodes. The currents for the non-irradiated sensors are below 40 nA. The guard rings are shorted to the bias. The test diode current from figure 11.3a is scaled by the diode size increase and shown for comparison. Taken from [95].

The leakage currents of all irradiated sensors in full operation are shown in figure 11.4 as a function of the depletion voltage. The slightly larger current compared to the measurements of the test diodes in figure 11.3a can be explained by the higher temperature of the sensor in full operation, see figure 11.5. Without active cooling it is not possible to operate the sensors

4 Similar effects have been reported by other groups and are under investigation.

5 The exact value of the breakdown voltage was not measured to minimize the risk of damage.

with depletion voltages below –30 V due to thermal runaway. With cooling, for $T_{MuPix} \lesssim 15\,°C$, the MUPIX can be operated up to a depletion voltage of –85 V. The following measurements are obtained with the active cooling system described in section 11.1 at a MUPIX temperature of about 8 °C.

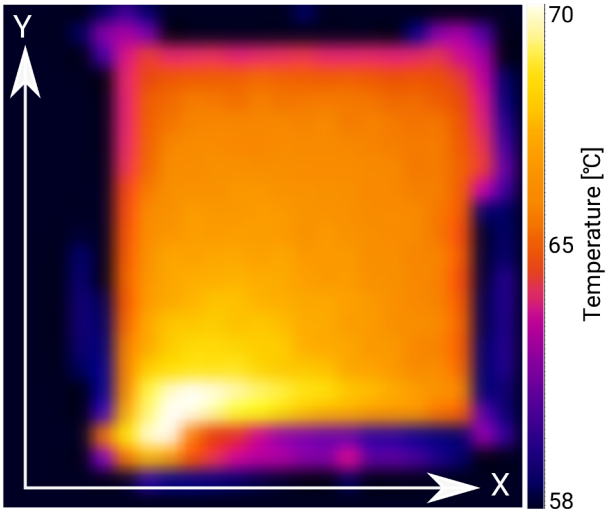

Figure 11.5: IR camera picture of the $1.5 \cdot 10^{15}\,n_{eq}/cm^2$ irradiated MUPIX in full operation. The fast digital logic of the state machine and the serializer is located in the bottom left part of the chip which shows with 85 °C (70 °C uncalibrated) the highest temperature. Taken from [95].

Pixel tuning

In MUPIX7, pixel-to-pixel variations can be corrected for with a 4– bit tuning DAC (TDAC), by adjusting the discriminator threshold. A global DAC (VPDAC) selects from the externally provided threshold reference the tuning range covered by the TDACs. Higher TDAC values correspond to higher effective thresholds, i.e. the separation between threshold and baseline is increased. The pixel response adjustment is based on a noise measurement and an automated software calibration scheme is used. The threshold reference and the VPDAC value are selected such that all pixels are below a certain noise rate at the maximal TDAC value. Afterwards, each individual TDAC value is adjusted such that the noise rate of every pixel is just below the target noise rate (1 Hz without beam). The thresholds obtained by the automated tuning routine strongly vary between sensors and depend on the applied depletion voltage and the irradiation fluence. A summary of the tested sensors, the corresponding tune thresholds and VPDAC values is given in table 11.2. For the proton irradiated samples, the described tuning procedure does not work properly for the complete matrix because of too large pixel-to-pixel variations caused by the inhomo-

geneities in the irradiation process (see below). Therefore, up to 5% of all pixels[6] are excluded in the presented analysis.

ID	HV [-V]	THR [mV]	VPDAC	ID	HV [-V]	THR [mV]	VPDAC
P00	40	735	38	N00	40	700	19
	60	725	21		60	718	20
	70	740	21		70	725	19
	85	734	20		85	725	19
P1515	60	700	19	N514	60	740	18
	70	680	19	N115	40	711	23
	85	568	20		60	711	22
P7815	40	770	26		70	740	23
	60	755	26		85	730	24
	70	760	28	N515	40	675	22
	75	740	27		60	675	21
					70	690	25
					85	690	25

Table 11.2: HV and configuration parameters used for chip characterization. THR stands for threshold reference. The target noise rate for the pixel tuning is 1 Hz/pixel at the given threshold references. The beam is switched off during tuning. The baseline is externally applied and set to about 800 mV for all settings. 100 mV signal height correspond to approximately 800 primary electrons [87]. Taken from [95].

The TDAC values and their distribution over the chip after tuning are shown in figure 11.6 for three sensors. The TDAC map of the neutron irradiated MUPIX (figure 11.6b) looks similar to the TDAC map for a non-irradiated MUPIX (figure 11.6a). For the proton irradiated sensors (figure 11.6c) a non-uniform distribution of the TDACs is obtained which we attribute to a non-uniform irradiation beam profile. The observed non-uniform radiation damage causes position dependent depletion and varying noise levels [98]. The distribution of the TDAC values (figure 11.6c) has a shoulder towards lower values which originate from the bottom right part of the TDAC map where the irradiation beam center was probably located[7]. The inhomogeneous proton irradiation prevented us from optimally tuning the sensors, thus compromising the following characterization studies.

6 Pixels cannot be masked in the MUPIX7.

7 Dosimetry results of the facility suggest a 10% dose varition over the sensor.

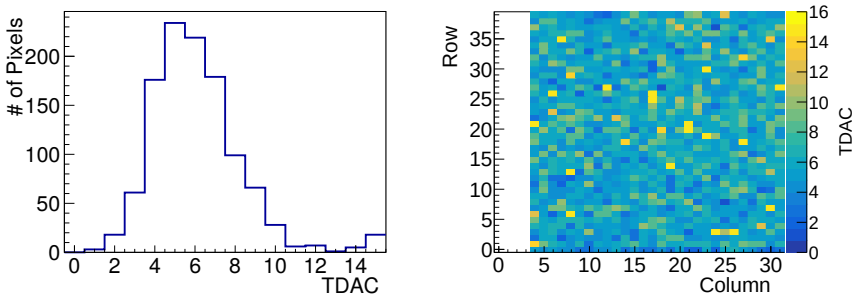

(a) non-irradiated (ID P00)

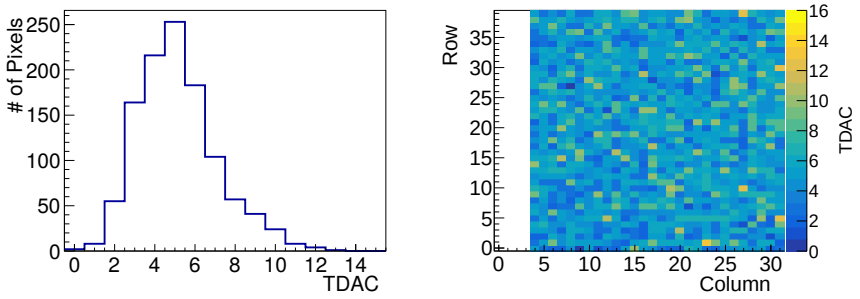

(b) $1 \cdot 10^{15}$ n_{eq}/cm^2 neutron irradiated (ID N115)

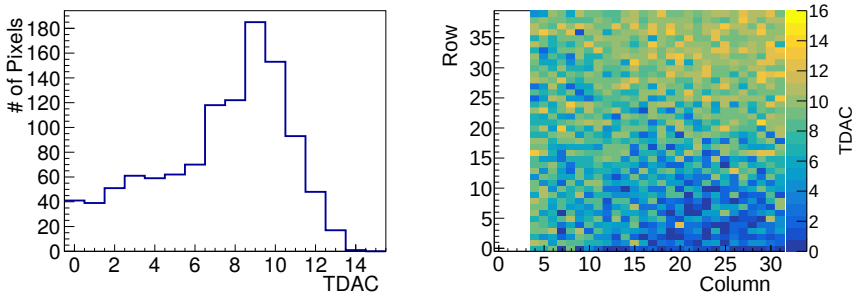

(c) $1.5 \cdot 10^{15}$ p $/cm^2$ irradiated (ID P1515)

Figure 11.6: **Left:** Pixel TDAC values for a non-irradiated, a neutron-irradiated and a proton-irradiated sensor. **Right:** Corresponding TDAC value shown as pixel matrix. Taken from [95].

11.2.2 *Test beam results*

Two MUPIX TELESCOPES [66] are used as tracking reference for a test beam performed at the πM1 beam line at PSI in November 2016. One telescope is used to characterize the proton irradiated MUPIX, see figure 11.1. The other telescope is used to characterize the neutron irradiated MUPIX.

The πM1 beam consists of a mixture of π^+, e^+, μ^+ and protons, with π^+ being the dominant beam component. The momentum is set to 365 MeV/c to select minimum ionizing π^+, which are expected to produce 1200 primary electrons in the depletion zone of a non-irradiated MUPIX7 sensor at a depletion voltage of –85 V. The particle rate of the beam is set to about 100 kHz of which only about 10 kHz are reconstructed by the telescopes due to limited acceptance. Both MUPIX TELESCOPES are mechanically aligned with a precision of better than 250 µm relative to each other. A software alignment procedure is applied to correct for residual offsets with a precision of ± 10 µm.

Efficiency and noise study

To study efficiency and noise, reference tracks are extrapolated to the DUT. On the DUT, clustering and crosstalk removal is applied. A search window of 800 µm radius and a time window of ± 64 ns around the extrapolated track intersection is used to match hit clusters. The hit finding efficiency is defined as the number of matched tracks divided by the total number of extrapolated tracks and corrected for random coincidences. The quoted efficiencies include all components of the readout system: hit digitization, on-chip readout state machine, data transmission over the serial link and front-end processing on the readout FPGA, i.e. timestamp sorting and merging of data from the four telescope layers. Figure 11.7 shows exemplary results for the efficiency and noise of the tested samples as a function of the applied threshold reference. The noise consists of all unmatched clusters and is corrected for small inefficiencies of the reference planes. Due to the small size of the sensors in the reference planes (about 1/10 of the beam profile) and large angle scatterers a significant fraction of beam particles entering the DUT cannot be reconstructed. This adds a constant noise floor of about 20 Hz/pixel (7 Hz/pixel) for the proton (neutron) irradiated sensors.

The noise of the $5 \cdot 10^{14}$ n_{eq}/cm^2 neutron irradiated sensor is similar to the non-irradiated sensor: up to a reference threshold of about 720 mV the noise stays below 10 Hz/pixel; for higher threshold references (lower thresholds) the noise increases exponentially.

The noise of the $1.5 \cdot 10^{15}$ protons/cm^2 proton irradiated sensor increases more rapidly and already starts at low reference threshold (high thresholds). Proton and neutron irradiated sensors with a depletion voltage of –60 V reach efficiencies of about 95 %, similar to the non-irradiated sensor, however, at the expense of factor 10-100 higher noise levels and

increased leakage currents. Higher efficiencies can be reached by further increasing the depletion-voltage.

The influence of the depletion voltage on the efficiency and noise as a function of the threshold reference is shown in figure 11.8 for a neutron irradiated sensor with $5 \cdot 10^{15}$ n_{eq}/cm^2 which was operated at a sensor temperature of about 8 °C. The sensor efficiency increases with the applied depletion voltage, consistent with the expectation that the active depletion zone grows proportional to $\sqrt{U_{HV}}$, leading to higher signals. At very high negative voltages additional avalanche effects contribute to charge amplification, which sets in at about –80 V for non-irradiated sensors and shifts to slightly higher negative voltages for irradiated sensors [98]. For a depletion voltage of –85 V an efficiency of about 90 % is measured at a threshold reference of 715 mV and a noise rate of about 100 Hz per pixel. The noise significantly increases for larger threshold references. The shift of the threshold curves for the different depletion voltages can be explained by tuning effects: different VPDAC values and tune thresholds are used for the –70 V and –85 V measurements compared to the –40 V and –60 V measurements, as seen in table 11.2. This results in a shift of the effective threshold by about 15 mV.

For the different irradiated samples the efficiency and noise measurements are summarized in figure 11.9 as a function of threshold value. Data samples with a common, but reduced, HV of –60 V are chosen here to allow for a systematic comparison of all irradiated sensors[8]. Small differences in the efficiency are expected from the different telescope geometries: The neutron irradiated samples are glued on a carrier and placed behind the three reference layers. They have by 0.3 % to 0.8 % reduced efficiencies due to undetected particle losses with large angle scattering in the third layer.

In general, neutron and proton irradiated samples show similar performance, considering the threshold variations due to different VPDAC settings and the limited threshold scan for the neutron-irradiated sensor which does not reach very low effective thresholds. Accounting for these differences the data show overall an efficiency loss and noise increase for increasing neutron and proton fluences. Although the MUPIX irradiated to $1.5 \cdot 10^{15}$ p /cm^2 reaches almost similar efficiencies than the non-irradiated one, it shows a significant noise increase. At very low threshold values (high thresholds) a beam induced noise floor of 20 Hz and 7 Hz is measured for the proton and neutron irradiated sensors, respectively.

The automated threshold tuning procedure leads to strong correlations between the efficiency and noise measurements and the threshold used for tuning, also visible as shifts of the threshold curves in figures 11.8 and 11.9. To compare the different samples in a more setting independent way, the efficiencies are determined for fixed average noise rates of 40 Hz (200 Hz) per pixel[9]. The noise floor of 7 Hz (20 Hz) for the neutron (proton) irra-

8 Sensor N514 was accidentally damaged after taking data at –60 V.

9 For LHC experiments noise occupancies are typically required to be below $1 \cdot 10^{-6}$, corresponding to 40 Hz noise per pixel at 40 MHz bunch crossing frequency.

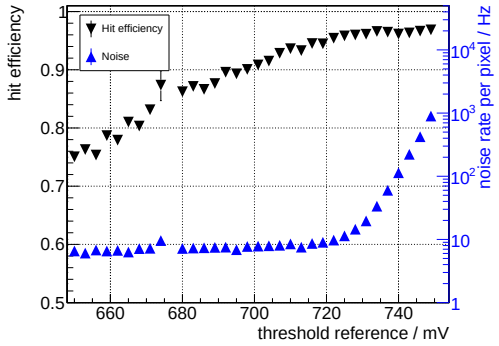

(a) non-irradiated

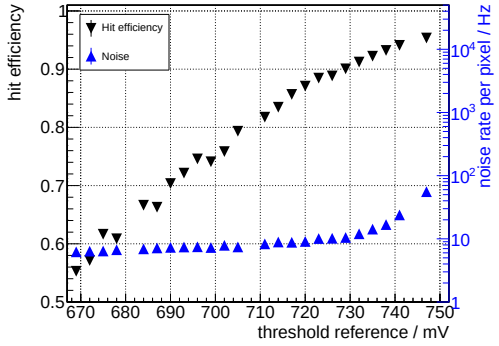

(b) $5 \cdot 10^{14}\,\mathrm{n_{eq}/cm^2}$

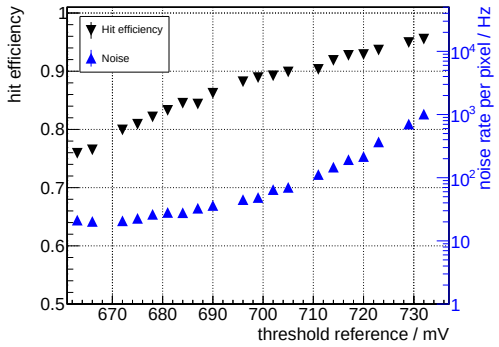

(c) $1.5 \cdot 10^{15}\,\mathrm{p/cm^2}$

Figure 11.7: Efficiency and noise as function of the threshold reference for a depletion voltage of –60 V at $T_{MuPix} \approx 8\,^{\circ}C$ for non-, neutron- and proton irradiated sensors. Taken from [95].

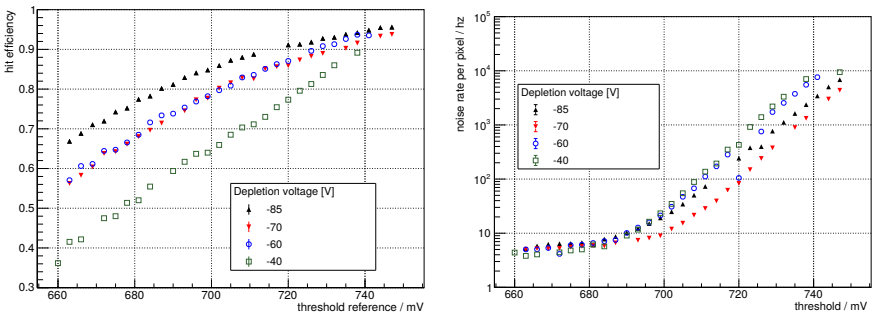

(a) Efficiency (b) Noise rate

Figure 11.8: Efficiency and noise rate as a function of the threshold reference for the $5 \cdot 10^{15}\,n_{eq}/cm^2$ neutron-irradiated MUPIX7 sensor. Results are shown for different HV settings at $T_{MuPix} \approx 8\,°C$. Note that the sensor was configured at different tune thresholds and different tuning strength (VPDAC) for the different depletion voltages, see table 11.2 leading to threshold curve shifts of about 15 mV. Binomial errors included. Taken from [95].

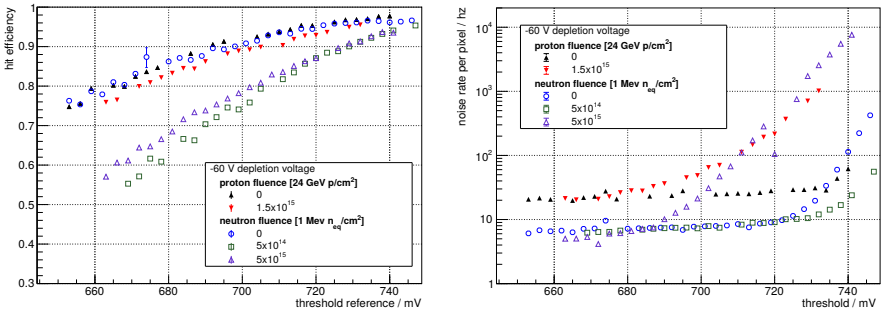

(a) Efficiency (b) Noise rate

Figure 11.9: Efficiency and noise rate as a function of the threshold reference for all tested samples for HV = –60 V and $T_{MuPix} \approx 8\,°C$. 60 V is chosen, as one sensor was damaged after taking data at 60 V. Note that the sensors were configured at different tune thresholds and with different tuning strength (VPDAC), see table 11.2), leading to threshold curve shifts of about 50 mV. Binomial errors included. Taken from [95].

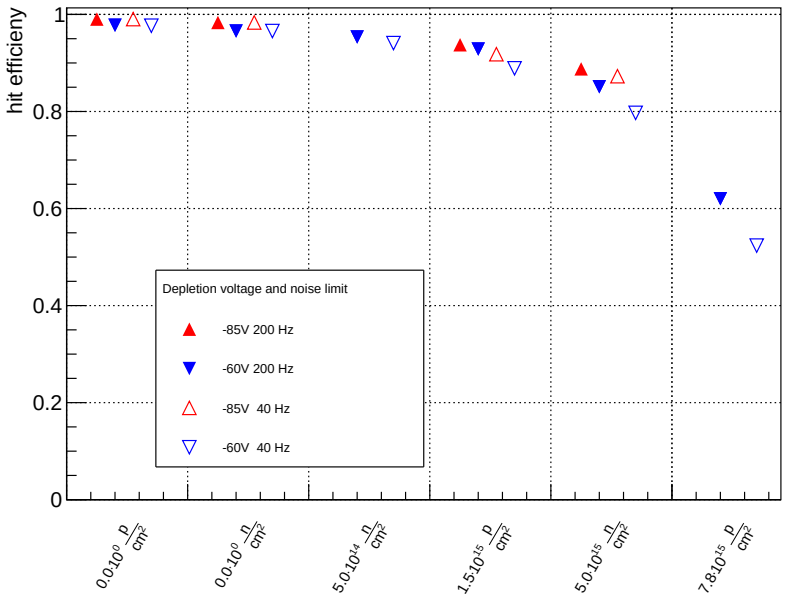

Figure 11.10: Efficiencies as function of the fluence for depletion voltages of –60 V (*blue* symbols) and –85 V (*red* symbols) and $T_{MuPix} \approx 8\,°C$. The filled triangles show the results for an average per pixel noise rate of 200 Hz and the empty ones for 40 Hz. The beam induced noise floor is subtracted. Binomial error bars are too small to be seen. Taken from [95].

diated samples is subtracted. The resulting efficiencies are shown in figure 11.10 for depletion voltages of –60 V and –85 V. The efficiencies of the proton- and neutron-irradiated sensors show a moderate reduction up to a fluence of $1.5 \cdot 10^{15}\,/\mathrm{cm}^2$. For higher fluences $> 1.5 \cdot 10^{15}\,/\mathrm{cm}^2$ the efficiency decreases more strongly and falls below 90 %. The efficiency difference between the average per pixel noise rates of 40 Hz and 200 Hz indicates the possible efficiency gain if the sensors are cooled to even lower temperatures.

Time resolution

The time resolution of the MuPix7 DUT is measured relative to the averaged timestamps of the hits from reference tracks. A Gaussian fit is applied to a histogram of the time differences. The standard deviation, σ, of the fit defines the time resolution, which is corrected for the limited resolution of the reference sensors

$$\sigma^2{}_{DUT} = \sigma^2{}_{Fit} - \sigma^2{}_{Ref} \tag{11.1}$$

assuming a time resolution of $\sigma_{MuPix} = 14.2\,\mathrm{ns}$ for the non-irradiated MuPix7 [50, 88]. Using $\sigma_{Ref} = \frac{1}{3}\sqrt{3 \cdot \sigma^2{}_{MuPix}}$ the time resolution of the DUT is measured for all MuPix and for different depletion voltages, see figure 11.11. The time resolution of the non-irradiated MuPix of about 15 ns

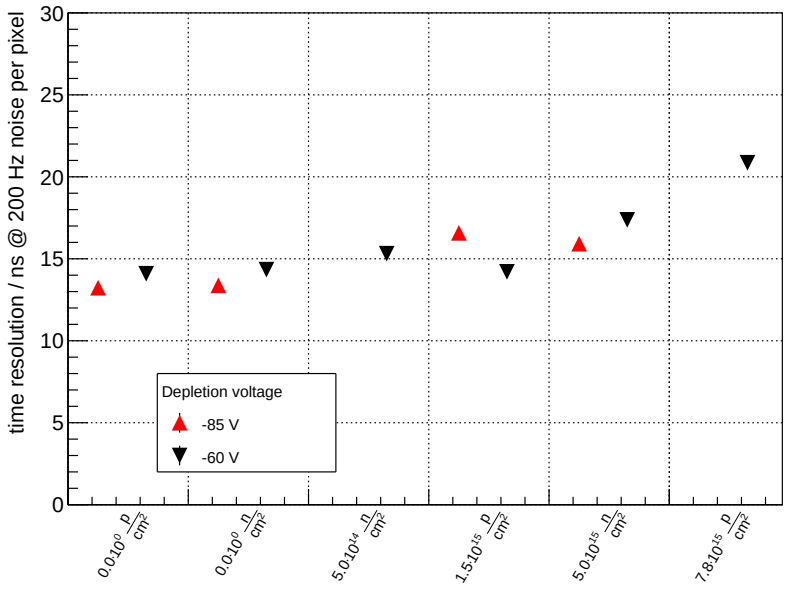

Figure 11.11: Time resolution expressed in Gaussian σ as function of the irradiation dose for depletion voltages of –60 V and –85 V at an exemplaric average noise rate of 200 Hz and $T_{MuPix} \approx 8\,^{\circ}C$. Error bars are too small to be seen. Taken from [95].

is in agreement with previous measurements [50]. It stays constant for fluences up to $1.5 \cdot 10^{15}$ p/cm^2 and is also rather independent of the threshold setting and therefore the noise limit. For higher proton and neutron fluences, the time resolution of the sensor becomes significantly worse, consistent with the observation of reduced signal detection efficiency in this region and the interpretation of larger time walk effects due to the reduced signal amplitude.

11.3 SUMMARY OF THE IRRADIATION STUDIES

Proton and neutron irradiated samples of HV-MAPS prototypes with a particle fluence of up to $7.8 \cdot 10^{15}$ p/cm^2 were tested in the laboratory and at a PSI test beam. All sensors are fully functional after one year of annealing at room temperature.

The MUPIX7 samples have a non-radiation-hard design and were realized on a $10-20\,\Omega$cm substrate with a depletion zone of $10-14\,\mu$m at a depletion voltage –85 V before irradiation. For the irradiated samples increased noise rates and leakage currents in the pixel matrix are observed. The proton irradiated samples show significantly higher leakage currents as the neutron irradiated sensors for similar particle fluences in the laboratory.

At PSI, efficiency and noise studies with sensors cooled down to 8 °C have been carried out. At an optimal depletion voltage of –85 V and at a maxi-

mum noise limit of 40 Hz /pixel efficiencies ≥90 % are measured for all sensors with a dose of up to $1.5 \cdot 10^{15}$ p/cm^2. For higher proton and neutron fluences a significant performance degradation is observed. The time resolution for all irradiated sensors is below 22 ns, compared to about 15 ns time resolution of the non-irradiated references. Only a small time resolution decrease for fluences of up to $5 \cdot 10^{15}$ n_{eq}/cm^2 is observed. During full operation in the test beam the overall noise seems to be strongly influenced by bulk damage induced charge trapping.

Despite the non-radiation-hard design and the very small depletion zone of the standard AMS H18 process, the MUPIX7 shows high radiation tolerance emphasizing the potential of the AMS H18 process for usage in harsh radiation environments. The radiation tolerance of the synthesized and fast readout state machine logic is demonstrated for the first time for a fully monolithic prototype realized in HV-CMOS technology.

12 SUMMARY AND OUTLOOK

The search for physics beyond the Standard Model is one of the biggest challenges in modern particle physics. Charged Lepton flavor violation is a promising portal to new physics. The decay $\mu^+ \rightarrow e^+e^-e^+$ is one possible channel and suppressed in the Standard Model to an unobservable branching ratio. Hence, any observation is a clear sign for new physics. The *Mu3e* experiment is searching for this decay with a target branching ratio sensitivity of $1 \cdot 10^{-16}$. Efficient background suppression requires a fast, precise and extraordinarily lightweight spectrometer, which is based on high-voltage monolithic active pixel sensors.
The work discussed in this thesis describes two interconnected steps on the way towards the first HV-MAPS pixel tracker: Prototype characterization and the further development of a particle tracking telescope consisting of HV-MAPS and scintillating tiles. The particle tracking telescope is used as a tool to characterize prototypes and to prove the feasibility of integrating prototypes into more complex systems. The telescope additionally serves as an excellent test for the *Mu3e* DAQ. It has been adapted for two prototype generations and used as a reference system for HV-MAPS studies during 14 test beam campaigns at PSI, SPS-CERN, DESY-II and MAMI.

12.1 PARTICLE TRACKING TELESCOPES

The MUPIX TELESCOPE has been adapted for two MUPIX prototype generations – MUPIX7 and MUPIX8 – and improved significantly in the scope of this thesis. It is running in a non-triggered data acquisition mode and has been intensively used to study the performance and scalability of HV-MAPS prototypes in the past years. It features an easy-to-use GUI, online data merging and monitoring. Online tracking and efficiency determination has been added to provide optimal feedback for characterization studies. During 14 testbeam campaigns, the telescope has been running flawlessly in different configurations and provided crucial input to understand, improve and develop HV-MAPS prototypes not only in the context of *Mu3e* but also for a monolithic sensor proposed for the ATLAS upgrade, the ATLASPIX sensor which has been used as DUT in a telescope with MUPIX8 as reference. It has been shown, that up to eight sensors can be operated synchronously in one setup, marking a milestone towards the *Mu3e* pixel tracker and underlining the feasibility of the DAQ concept of *Mu3e*.
Two track fits, a straight line fit ignoring multiple Coulomb scattering and a general broken line fit taking multiple Coulomb scattering into account, are implemented in the analysis framework developed for telescope data

in the scope of this thesis. The fits are evaluated and compared and the use of a fast straight line fit for the MUPIX TELESCOPE is validated. It needs less computational time while tracking efficiency and background suppression are comparable.
The rate capabilities of the MUPIX TELESCOPE have been measured during a dedicated campaign, with fast data transmission to the DAQ computer via direct-memory-access and total hit rates in the telescope of above 80 MHz. For hit rates up to approximately 10 MHz, the DAQ is able to process the data as fast as it is received. For higher rates, the DAQ cannot cope with the hit rate anymore and needs up to four times longer to write the data to disk as it takes to acquire the data. Up to 100 MB/s can be written to disk. The online monitoring can process up to 500 kHz of particle hits.
Online efficiency calculation provides important feedback on the sensor's performance in real-time. It is proven to be fully functional by comparing the results from the on- and offline analysis, which are found to be identical. A track rate of 22.5 kHz has been processed online, limited by the slow polling data transmission scheme to the DAQ computer during the beam time.
The MUPIX TELESCOPE will be an excellent test bench for the next prototypes and is expected to be heavily used in upcoming beam times. Developments towards the *Mu3e* DAQ requires moving away from the current graphical interface to a implementation closer to the proposed final *Mu3e* detector control and readout system. This requires to replace the current GUI by a browser based control, which is foreseen for the *Mu3e* experiment and an update in the data format.

To perform precise studies of effects below the size of a pixel, a high resolution tracking telescope at DESY has been used. An interface to the telescope DAQ has been implemented into the MUPIX DAQ. During the analysis, it has been demonstrated that pointing resolutions of 6 µm can be achieved with the EUDET telescopes, independent of the material budget of the DUT by using track extrapolation from both sides. This method provides similar resolutions as previously used method, a straight line fit through all six layers, but enhances the available statistics by more than two orders of magnitude. The significant improvement is achieved by also reconstructing tracks with scattering on the DUT, which cannot pass the tight χ^2 cut, which is required for a good resolution with a straight line fit.

12.2 PIXEL SENSOR STUDIES

Two prototypes have been studied: The small-scale MUPIX7 and its successor, the large-scale MUPIX8. Both sensors show an excellent performance. Efficiencies above 99 % at noise rates below 10 Hz per pixel are observed, fulfilling the *Mu3e* requirements.
Power optimization studies show that the MUPIX7 has an optimal working point at a power dissipation of 300 mW/cm^2, 25 % below the cooling limit

of *Mu3e*. The time resolution is measured to be 14 ns. Capacitive coupling on the connection lines between analog and digital part of the sensor leads to a crosstalk probability of roughly 15 % at a typical operation point. Additionally, it has been shown, that the operational region is enlarged significantly by tilting the sensor due to increased charge deposition. All measurements are done with tuned MUPIX7 sensors.
Scaling the size of the sensor, together with additional time-walk circuits and minor changes led to the MUPIX8, with roughly 6 times the active height. All measurements conducted in this thesis used untuned sensors. The design of the supply voltage distribution is much more challenging, due to the increased size and it is not perfectly implemented on the MUPIX8, leading to position dependencies in the signal delays, efficiency, and threshold behavior. Nevertheless, the increased substrate resistivity from 20 Ωcm to 80 – 200 Ωcm significantly enhances the detection efficiency due to the enlarged active depletion thickness. An efficiency of above 99 % is measured at average pixel noise rates below 0.4 Hz. Operational regions of over 100 mV in threshold have been found at bias voltages of only –50 V. An improved biasing will allow for higher bias voltages in the order of –100 V and even larger signals. The larger signal will further increase the operational region.
The power dissipation of the MUPIX8 is reduced to approximately 200 mW/cm^2, which is a factor 2 below the cooling limit.
The time resolution is affected strongly by the delay differences over the sensor. A resolution of only 20 ns at default DAC settings is measured. Sacrificing dynamic range in the tuning of the sensor allows for optimized settings with a time resolution of 12 ns. Correcting for individual pixel variation of the mean time difference to the reference system improves the time resolution to 10 ns, which is significantly better than for MUPIX7. Variations in the signal height cause an additional variation of the hit timestamp, so called time-walk, which influences the time resolution. An on-chip charge measurement in form of a time-over-threshold measurement, which is supposed to be used to correct for this effect could not be utilized in the presented testbeam analysis as the hit data is likely to be read out before the ToT can be sampled, due to an issue in the design. The issue could in principle be solved in upcoming designs by either using a faster shaping or by using the falling edge to validate a hit. Dedicated laboratory test are conducted to study the time-walk. It was shown that a time resolution of 6.5 ns can be achieved with considerably reduced readout frequencies and a global time-walk correction. A per pixel time-walk compensation and a sensor tuning can potentially improve the results further. The 2 threshold method is the optimal time-walk compensation for upcoming HV-MAPS, as it allows for reduced time-walk and a charge measurement at the same time.
Crosstalk on the analog signal lines from the active pixel to the periphery has also been studied. For the longest lines, crosstalk probabilities of 50 % are observed. A more elaborated line layout can suppress crosstalk

effects by two orders of magnitude and should be considered for the next prototypes. An improved voltage distribution for the next generations potentially increases the operational region further.
Sub-pixel studies have shown that no position dependent inefficiencies are observed at typical operational thresholds of 50 mV and a depletion voltage of –50 V. For reduced depletion voltages and/or higher thresholds, charge sharing induced inefficiencies at the edges and corners become visible. The effect is enhanced in the corners as the charge is shared between four pixel cells.
The MuPix8 fulfills the *Mu3e* detector requirements already and the next large-scale sensor, with the improvements mentioned above, should be well suited for the construction of a full pixel tracker. Especially, the large operational region relaxes constraints on the noise of supply voltages, simplifying detector fabrication.
To conclude the sensor studies, tests with proton and neutron irradiated MuPix7 on the standard 20 Ωcm substrate have been conducted during a beam campaign. Increased leakage currents and noise rates are observed without severe efficiency and time resolution degradation for fluences of up to $1.5 \cdot 10^{15}$ 24 GeV p/cm^2. For a fluence of $7.8 \cdot 10^{15}$ 24 GeV p/cm^2, a significant efficiency decrease is observed. The intrinsic radiation tolerance of the MuPix7 emphasizes the potential of the MuPix8, which features a radiation tolerant design. MuPix8 samples should be irradiated to LHC phase-II doses for further verification.

Part IV

APPENDIX

A

TRACK RECONSTRUCTION AND EXTRAPOLATION

SOFTWARE IMPLEMENTATION OF THE COORDINATE TRANSFORMATION

The coordinate transformations are implemented utilizing the GenVector package of ROOT [60]. A human readable configuration file stores all important parameters for each plane. The transformation is implemented via the following snippet:

```
ROOT::Math::Transform3D _to_global;
ROOT::Math::Transform3D _to_local;
Rotation3D pitch(diag(_pitch_col, _pitch_row, 1));
RotationZYX rotation(_rot_z, _rot_y, _rot_x);
Translation3D translation(_off_x, _off_y, _off_z);

_to_global = translation * rotation * pitch;
_to_local = _to_global.Inverse();
```

HIT MATCHING INCLUDING ROTATIONS

The simple matching for unrotated DUTs is already discussed in section 5.3.2. For a rotated DUT the matching is different. However, the DUT rotation is typically only around one axis, which simplifies the matching. Assuming an intersection point **p** and hit **h**, the hits on the DUT are still grouped into three categories: Hits with the pixel center inside the projected search ellipsoid:

$$\sqrt{\sum_{k=0}^{1}\left(\frac{\mathbf{p}_k-\mathbf{h}_k}{a_k}\right)^2} < 1 \tag{A.1}$$

a_k being the semi-minor and semi-major axes of the ellipsoid representing the cut radius. The second category are hits, with the distance between extrapolated intersection and pixel center being larger than the search radius plus half a pixel diagonal $d_{p/2}$:

$$\sqrt{\sum_{k=0}^{1}\left(\frac{\mathbf{p}_k-\mathbf{h}_k}{a_k+d_{p/2}}\right)^2} >= 1 \tag{A.2}$$

The last category of hits are located in between the first two and the intersection of the ellipsoid with one of the edges. Four line segments, based on the four pixel corners are compared to the ellipse. The equation system

$$\begin{aligned} y &= \mathbf{p}_{m\,y} + \frac{x - \mathbf{p}_{m\,x}}{\mathbf{p}_{m\,y} - \mathbf{p}_{n\,y}} \\ {r_c}^2 &= \frac{(x - \mathbf{p}_{i\,x})^2}{a^2} + \frac{(y - \mathbf{p}_{i\,y})^2}{b^2}, \end{aligned} \tag{A.3}$$

with $\mathbf{p}_{m/n}$ being pixel corner coordinates, $\mathbf{p}_i$ the intersection coordinates, r_c the search radius and a, b parameters describing the rotation induced deformation of the cylinder projection. The equation can be solved analytically for x and y, if the line segment is not vertical. In this case, x and y need to be swapped. In parallel a and b also need to be swapped. If equations A.3 have a real solution, the line intersects with the ellipse. The intersection point is on the pixel edge if

$$\begin{aligned} 0 < x - \mathbf{p}_{m\,x} < \mathbf{p}_{n\,x} - \mathbf{p}_{m\,x} \text{ , if } \mathbf{p}_{n\,x} > \mathbf{p}_{m\,x} \\ 0 > x - \mathbf{p}_{m\,x} > \mathbf{p}_{n\,x} - \mathbf{p}_{m\,x} \text{ , if } \mathbf{p}_{n\,x} < \mathbf{p}_{m\,x}, \end{aligned} \tag{A.4}$$

holds for at least one of the solutions. Otherwise, the intersection is outside the pixel and the hit will not be assigned to the track.

B

DATA FORMAT

Depending on the readout mode and the data type, there are different blocks which are packed on the FPGA an transmitted to the PC memory. Triggerblock, see table B.1, contain external trigger reference information. Hitblocks contain hit information, which is either sorted (table B.2) or multiplexed (B.3).

Word offset	Value	Comment
0	0xCAFECAFE	Beginning block marker
1	b0 Block counter	
2	timestamp 0 1 [61:31]	500 MHz
3	timestamp 0 2 [30:0]	
...		
2N + 0	timestamp N 1 [61:31]	
2N + 1	timestamp N 1 [30:0]	
2N + 2	0xCAFEBABE	End of block marker

Table B.1: Structure of a trigger block: Beginning and end of block markers frame the trigger information. The Block counter counts the number of read trigger blocks to crosscheck for readout errors. The trigger timestamp is sampled with 500MHz an stored in two words. The most significant bits of all words are set to zero, excluding the begin and end of block markers to detect bit errors during transmission.

Word offset	Value	Comment
0	0xFABEABBA	Beginning block marker
1	b0 Block counter	
2	b0 FPGA timestamp [61:31]	125 MHz
3	b0 FPGA timestamp [30:0]	
4	b0 Counter of sent blocks	
5	data word 0 1	
6	data word 0 2	
...		
2N + 4	data word N 1	
2N + 5	data word N 2	
2N + 6	0xBEEFBEEF	End of block marker
data word i 1	0b00 & Chip[3:0] & 0b0 & Overflow & Hitlabel[3:0] & Matrix identifier[3:0] & Row[7:0] & Column[7:0]	
data word i 2	0b00 & Chip[3:0] & 0b0 & Overflow & Timelabel[3:0] & Matrix identifier[3:0] & TS2[5:0] & TS1[9:0]	

Table B.2: Block structure of the sorter output for MuPix8 data: Each hit is split into two 32-bit words, a time and an address word. The first 16-bits are used as markers: Chip marks the sensor and the matrix identifier marks the link of the sensor. Hit and Time label distinguish between address and time information. Overflow indicates if an overflow of the current timestamp TS1 has been observed. The 16 lowest bit encode the column and row address of hit or the two timestamps.
The most significant bits of all words are set to zero, excluding the begin and end of block markers to to detect bit errors during transmission.

Word offset	Value	Comment
0	0xFABEABBA	Beginning block marker
1	b0 Block counter	
2	b0 FPGA timestamp [61:31]	125 MHz
3	b0 FPGA timestamp [30:0]	
4	b0 Counter of sent blocks	
5	data word 0 1	
6	data word 0 2	
...		
2N + 3	data word N 1	
2N + 4	data word N 2	
2N + 5	0xBEEFBEEF	End of block marker
data word i 1	0b00 & Chip[3:0] & 0b0 & Overflow & Hitlabel[3:0] & Matrix identifier[3:0] & Row[7:0] & Column[7:0]	
data word i 2	0b00 & Chip[3:0] & 0b0 & Overflow & Timelabel[3:0] & Matrix identifier[3:0] & TS2[5:0] & TS1[9:0]	

Table B.3: Block structure of the multilink readout for MuPix8 data: Each hit is split into two 32-bit words, a time and an address word. The first 16-bits are used as markers: Chip marks the sensor and the matrix identifier marks the link of the sensor. Hit and Time label distinguish between address and time information. Overflow indicates if an overflow of the current timestamp TS1 has been observed. The 16 lowest bit encode the column and row address of hit or the two timestamps.
The most significant bits of all words are set to zero, excluding the begin and end of block markers to detect bit errors during transmission.

C

MUPIX7

DAC VALUES

The DAC settings for the different power dissipation settings are summarized in figure C.1. The varied DACs are highlighted in red.

DAC	1000 mW/cm^2	400 mW/cm^2	300 mW/cm^2	225 mW/cm^2
inverted Resets	1	1	1	1
BlRes	10	10	10	10
BlRes2	10	10	10	10
ckdivend	1	1	1	1
division factor	5	5	5	5
enpll	1	1	1	1
maxcycend	4	4	4	4
resetckdivend	8	8	8	8
slowdownend	0	0		
thres	60	60	60	60
timerend	0	0	0	0
VN	60	30	20	5
VN2	60	30	20	5
VNdcl	12	12	12	12
VNdel	10	10	10	10
VNdeldcl	6	6	6	6
VNdeldclmux	6	6	6	6
VNdelpreemp	6	6	6	6
VNfb	10	10	8	3
VNfb2	10	10	8	3
VNfoll	10	10	10	10
VNload	5	5	4	2
VNload2	5	5	4	2
VNlvds	60	60	60	60
VNlvdsdel	0	0	0	0
VNvco	10	10	10	10
VPcomp	60	30	20	10
VPdac	25	19	17	11
VPdcl	24	24	24	24
VPdeldcl	12	12	12	12
VPdeldclmux	12	12	12	12
VPdelpreemp	12	12	12	12
VPpump	20	20	20	20
VPvco	10	10	10	10

Table C.1: Overview over the DAC settings used for the MuPix7. DACs, which have been optimized in beam are highlighted.

D

MUPIX8 ANALYSIS

A collection of additional plots for the MuPix8 analysis.

AVERAGE TIMESTAMP DIFFERENCE CORRECTIONS

The linear corrections are shown in section 10.3.3. To check, if linear corrections are sufficient, the corrected delay is plotted as function of $\texttt{colum}^2$, $\texttt{row}^2$ and $\texttt{colum}\cdot\texttt{row}$. The results are summarized in figure D.1. The structure in the two dimensional plots on the top is induced by the 8 ns timestamp binning, compared to the higher resolution for the corrections. The projections on the bottom plots reveal tiny effects, which can be added to the corrections. However, the overall effect is negligible and therefore not included in the time corrections.

DAC VALUES USED FOR MUPIX8 STUDIES

The default DAC values of the MuPix8 sensors in a four layer telescope are summarized in tables D.1 and D.2. Analog pixel DACs, digital pixel DACs, general DACs and state machine DACs are grouped together, to improve the readability. A sketch of the circuitry is shown in figure 4.3.

MASKED PIXELS

In software masked pixels for the studies presented in figure 10.15 are shown in figure D.2 for completeness. Note, that some thresholds, which occur in the masked pixel plot are excluded in figure 10.15 as they have been mis-configured.

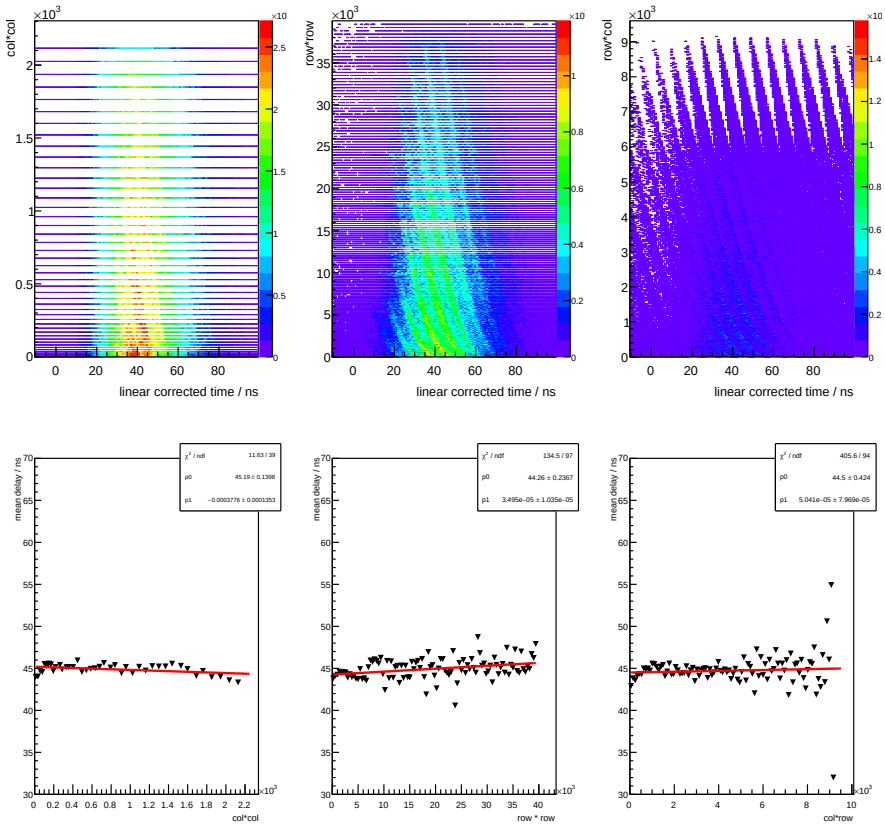

Figure D.1: Second order correction of the delays. There are no significant shifts over the sensor visible.

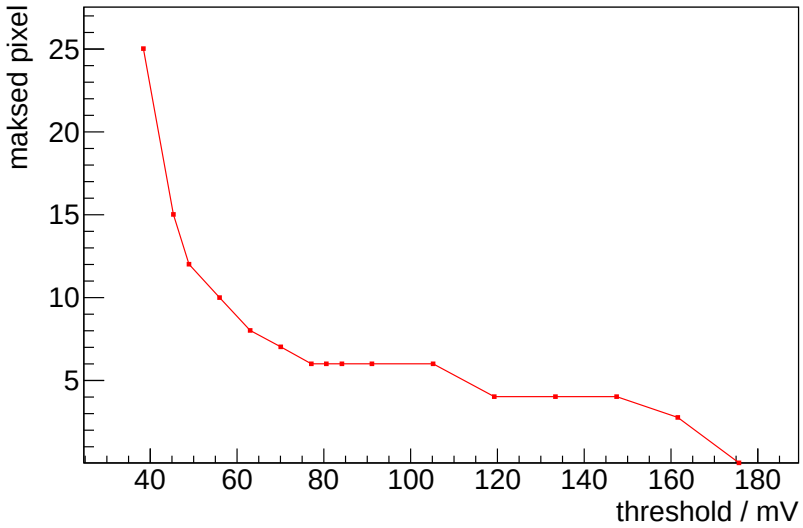

Figure D.2: Number of masked pixels

Layer	0	1	2	3
BLResPix	5	5	5	5
VNPix	20	20	20	20
VNFBPix	10	10	10	10
VNFollPix	10	10	10	10
VNPix2	0	0	0	0
VNBiasPix	0	0	0	0
VPLoadPix	5	5	5	5
VNOutPix	10	10	10	10
VNRegCasc	0	0	0	0
VDel	16	16	16	16
VPComp	5	5	5	5
VPDAC	0	0	0	0
BLResDig	5	5	5	5
VPRegCasc	0	0	0	0
VPRamp	0	0	0	0
VPBiasReg	0	0	0	0
VNBiasReg	0	0	0	0
enable2threshold	0	0	0	0
enableADC	1	1	1	1
AlwaysEnable	0	0	0	0

Table D.1: Default DACs for a four layer MUPIX TELESCOPE. **Top:** Analog pixel DACs. **Bottom:** Digital part DACs

Layer	0	1	2	3
resetckdivend	15	15	15	15
maxcycend	63	63	63	63
slowdownend	0	0	0	0
timerend	1	1	1	1
tsphase	0	0	0	0
ckdivend2	7	7	7	7
ckdivend	0	0	0	0
Readout reset n	1	1	1	1
Serializer reset n	1	1	1	1
Aurora reset n	1	1	1	1
sendcounter	0	0	0	0
Bandgap1 on	0	0	0	0
Biasblock1 on	5	5	5	5
VNLVDS	24	24	24	24
VNLVDSDel	0	0	0	0
Linkselect	1	1	1	1
Termination	0	0	0	0
SelectTest	0	0	0	0
SelectTestOut	0	0	0	0
DisableHitbus	1	1	1	1
Bandgap2 on	0	0	0	0
Biasblock2 on	5	5	5	5
VPFoll	10	10	10	10
VNDACPix	0	0	0	0
ThLow	291	291	291	291
ThPix	437	437	437	437
BLPix	448	448	448	448
BLDig	248	248	248	248
ThHigh	297	297	320	297

Table D.2: Default DACs for a four layer MUPIX TELESCOPE. **Top:** State machine DACs.**Middle:** General configuration DACs. **Bottom:** Voltage DACs

E

TOY MONTE-CARLO FOR CLUSTERING

To estimate the width of the ionization charge cloud, a toy Monte-Carlo simulation study is performed. Single particles, which traverse the sensor perpendicular are simulated. The ionization cloud is assumed to be Gaussian shaped around the particles path. The overall charge deposit is modeled with a Landau distribution, with a most probable energy loss of 15. The position of particles is simulated uniformly distributed over a 3×3 pixel matrix. The charge collection in a 5×5 pixel matrix is analyzed. The charge deposit in each pixel is calculated by integrating the two dimensional Gaussian over the pixel range numerically. $5 \cdot 10^5$ particles are simulated with one dimensional ionization width σ_{ion} ranging from $0.8 - 3.5\,\mu m$ in steps of $0.1\,\mu m$.
A exemplary cluster size map is shown in figure 3.9. The simulated charge next to a comparison between reconstructed and simulated charge is shown in figure E.1 to validate the integration algorithm.

The detection efficiency and the average cluster size is studied as a function of the detection threshold relative to the most probable charge deposition for the different σ_{ion}. Larger ionization σ_{ion} result in a larger average cluster size as well as reduced efficiency for a constant threshold.

The cluster size versus efficiency is plotted for different detection thresholds in figure E.3. Cluster size and efficiency can be determined experimentally and used to extract the corresponding ionization σ_{ion}.
As an example, the results from the –15 V data samples in section 10.4 can be used as reference: A measured efficiency of 99.53 % and an average cluster size of 1.07 corresponds to an ionization σ_{ion} of $2.8\,\mu m$. From figure E.1, a charge detection threshold of 35 % can be extracted.

Using these values and the pointing resolution of the reference telescope, the intersection points of particles, which create a double cluster can be

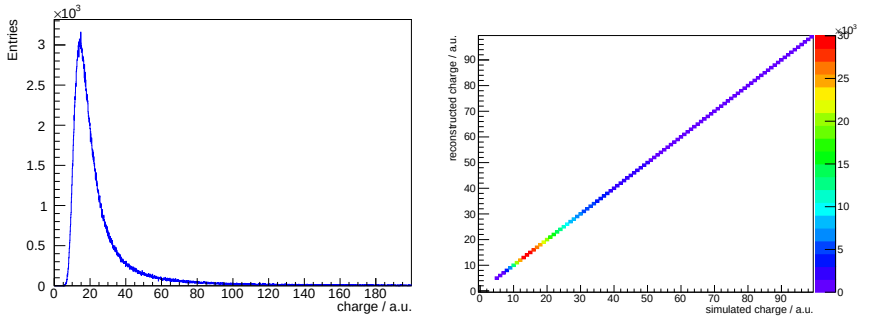

(a) Simulated charge (b) Reconstructed- versus simulated charge

Figure E.1: Simulated charge for an ionization sigma σ_{ion} of $2.8\,\mu m$.

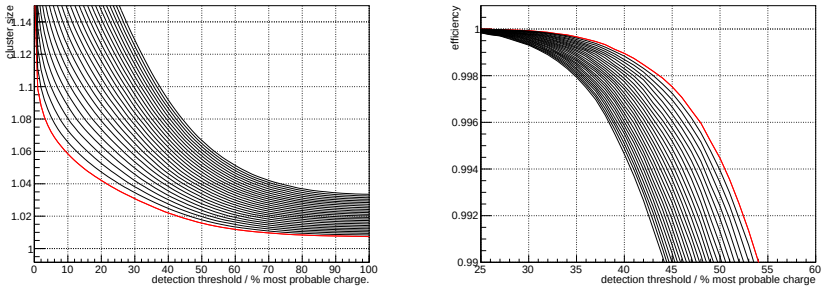

(a) Clustersize (b) Efficiency

Figure E.2: Simulated efficiency and cluster size for charge ionization σ_{ion} from 0.8 to 3.5 µm as a function of the detection threshold. The red highlighted line is the result for 0.8 µm.

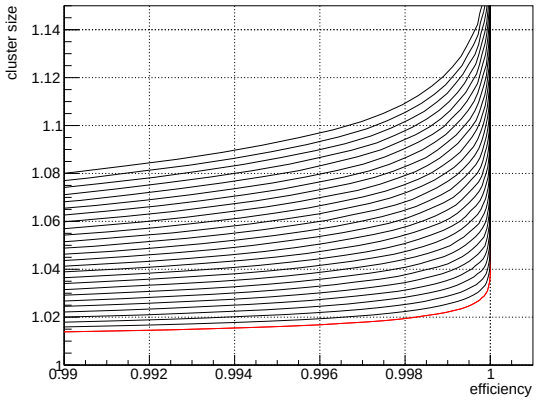

Figure E.3: Efficiency versus cluster size for different ionization widths. The red curve is again $\sigma_{ion} = 0.8$ µm.

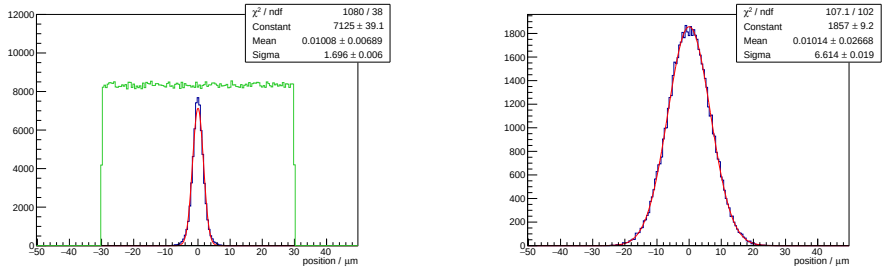

(a) Position of double cluster in blue, simulated particles in green.

(b) Position of double cluster folded with a reference resolution of 6.39 µm.

Figure E.4: Simulated one dimensional cluster distribution for a detection threshold of 35 % and $\sigma_{ion} = 2.8\,\mu\text{m}$. The pixel edge is located at zero.

simulated, based on the same charge model as above. The results are summarized in figure E.4, for uniformly distributed particles in a range from –30 mum to 30 mum. The pixel edge is located at zero. The distribution of double clusters, shown in figure E.4a is well described by a Gaussian and has a width of 1.696(1) µm. For completeness, the position of all simulated particles is also drawn in green. Folding a pointing resolution of 6.39 µm to the double cluster distribution leads to figure E.4b, which is also described by a Gaussian. The total width is

$$\sigma_{tot}^2 = \sqrt{\sigma_{expected}^2 + \sigma_{res}^2} = 6.61(2)\,\mu\text{m}. \tag{E.1}$$

F

PUBLICATIONS

Parts of the ideas and work presented in this thesis have appeared previously in the following list of journal articles and conference proceedings.

Technical design of the Phase I Mu3e Experiment
A. Blondel et al.
to be published

MuPix8 — Large area monolithic HVCMOS pixel detector for the Mu3e experiment
H. Augustin et al.
In: *Nucl. Instrum. Meth.* A (2018)
https://doi.org/10.1016/j.nima.2018.09.095

Irradiation Study of a Fully Monolithic HV-CMOS Pixel Sensor Design in AMS 180 nm
H. Augustin et al.
In: *Nucl. Instrum. Meth.* A905(2018)53-60
arXiv: 1712.03921[physics.ins-det] (2017)

Efficiency and Timing Performance of the MuPix7 High Voltage Monolithic Active Pixel Sensor
H. Augustin et al.
In: *Nucl. Instrum. Meth.* A902(2018)158-163
arXiv: 1802.09851[physics.ins-det]

The MuPix Telescope: A Thin, High Rate Tracking Telescope
H. Augustin et al.
In: *JINST* 12.01 (2017), C01087. DOI: 10.1088/1748-0221/12/01/C01087. arXiv: 1611.03102[physics.ins-det]

MuPix7—A Fast Monolithic HV-CMOS Pixel Chip for Mu3e
H. Augustin et al.
In: *JINST* 11.11 (2017), C11029. DOI: 10.1088/1748-0221/11/11/C11029. arXiv: 1610.02210[physics.ins-det]

The MuPix System-on-Chip for the Mu3e Experiment
H. Augustin et al.
In: *Nucl. Instrum. Meth.* A845 (2017), 194-198. DOI: 10.1016/j.nima.2016.06.095. arXiv: 1603.08751[physics.ins-det]

Overview of HVCMOS Pixel Sensors
I. Perić et al.
In: *JINST* 10.05 (2015), C05021. DOI: 10.1088/1748-0221/10/05/C05021.

The following publication is related to a research internship prior to my PhD study

Characterization of Silicon Photomultipliers for nEXO
I. Ostrovskiy et al.
In: *IEEE Trans.Nucl.Sci. 62 (2015) no.4, 1825-1836*

G

BIBLIOGRAPHY

[1] S. L. Glashow. “Partial Symmetries of Weak Interactions”. In: *Nucl. Phys.* 22 (1961), pp. 579–588.

[2] A.-K. Perrevoort. “Sensitivity Studies on New Physics in the Mu3e Experiment and Development of Firmware for the Front-End of the Mu3e Pixel Detector”. PhD thesis. Heidelberg University, 2018.

[3] C. Burgard and D. Galbraith. *Standard Model of Physics*. CERN Webfest. 2012. URL: http://davidgalbraith.org/portfolio/ux-standard-model-of-the-standard-model/.

[4] G. Aad et al. *Observation of a new particle in the search for the Standard Model Higgs boson with the ATLAS detector at the LHC*. 2012. arXiv: 1207.7214 [hep-ex].

[5] S. Chatrchyan et al. “Observation of a new boson at a mass of 125 GeV with the CMS experiment at the LHC”. In: *Phys.Lett.B* (2012). arXiv: 1207.7235 [hep-ex].

[6] M. et al. Tanabashi. “Review of Particle Physics”. In: *Phys. Rev. D* 98 (3 2018), p. 030001. DOI: 10.1103/PhysRevD.98.030001.

[7] Q. R. Ahmad et al. “Measurement of the charged current interactions produced by B-8 solar neutrinos at the Sudbury Neutrino Observatory”. In: *Phys. Rev. Lett.* 87 (2001), p. 071301. eprint: nucl-ex/0106015.

[8] F.P. An et al. “Observation of electron-antineutrino disappearance at Daya Bay”. In: *Phys.Rev.Lett.* 108 (2012), p. 171803. DOI: 10.1103/PhysRevLett.108.171803. arXiv: 1203.1669 [hep-ex].

[9] Y. Fukuda et al. “Evidence for oscillation of atmospheric neutrinos”. In: *Phys. Rev. Lett.* 81 (1998), pp. 1562–1567. eprint: hep-ex/9807003.

[10] W. Rodejohann and A. Schöning. “The Standard Model of Particle Physics”. Lecture notes. 2012. URL: http://www.mpi-hd.mpg.de/manitop/StandardModel/index.html.

[11] A. de Gouvea and P. Vogel. “Lepton Flavor and Number Conservation, and Physics Beyond the Standard Model”. In: *Prog.Part.Nucl. Phys.* 71 (2013), pp. 75–92. DOI: 10.1016/j.ppnp.2013.03.006. arXiv: 1303.4097 [hep-ph].

[12] Y. Kuno and Y. Okada. “Muon decay and physics beyond the standard model”. In: *Rev. Mod. Phys.* 73 (2001), pp. 151–202. eprint: hep-ph/9909265.

[13] A. Blondel et al. *Letter of Intent for an Experiment to Search for the Decay $\mu \to eee$*. 2012.

[14] L. Calibbi, A. Faccia, A. Masiero, and S.K. Vempati. "Running U(e3) and BR(mu —> e + gamma) in SUSY-GUTs". In: *JHEP* 0707 (2007), p. 012. DOI: 10.1088/1126-6708/2007/07/012. arXiv: hep-ph/0610241 [hep-ph].

[15] J. C. Pati and A. Salam. "Lepton Number as the Fourth Color". In: *Phys. Rev.* D10 (1974), pp. 275–289.

[16] J. Bernabeu, E. Nardi, and D. Tommasini. "$\mu - e$ conversion in nuclei and Z' physics". In: *Nucl. Phys.* B409 (1993), pp. 69–86. eprint: hep-ph/9306251.

[17] U. Bellgardt et al. "Search for the Decay $\mu^+ \to e^+e^+e^-$". In: *Nucl.Phys.* B299 (1988), p. 1. DOI: 10.1016/0550-3213(88)90462-2.

[18] W. J. Marciano, T. Mori, and J. M. Roney. "Charged Lepton Flavor Violation Experiments". In: *Ann.Rev.Nucl.Part.Sci.* 58 (2008), pp. 315–341. DOI: 10.1146/annurev.nucl.58.110707.171126.

[19] A. M. Baldini et al. "Search for the lepton flavour violating decay $\mu^+ \to e^+\gamma$ with the full dataset of the MEG experiment". In: *Eur. Phys. J.* C76.8 (2016), p. 434. DOI: 10.1140/epjc/s10052-016-4271-x. arXiv: 1605.05081 [hep-ex].

[20] P.-R. Kettle. In: PSI-internal, LTP Filzbach Meeting, June 2010.

[21] R. M. Djilkibaev and R. V. Konoplich. "Rare Muon Decay $\mu^+ \to e^+e^-e^+\nu_e\bar{\nu}_\mu$". In: *Phys.Rev.* D79 (2009), p. 073004. DOI: 10.1103/PhysRevD.79.073004. arXiv: 0812.1355 [hep-ph].

[22] Mu3e collaboration. "Mu3e Technical Design Report". In: *internal document* (2017).

[23] *High Intensity Proton Accelerators*. Online, accessed 01-September-2018. URL: https://www.psi.ch/ltp/facilities.

[24] F. Berg. "CMBL - A High-intensity Muon Beam Line & Scintillation Target with Monitoring System for Next-generation Charged Lepton Flavour Violation Experiments". PhD thesis. ETH Zürich, 2017.

[25] S. Corrodi. "A Timing Detector based on Scintillating Fibres for the Mu3e Experiment". PhD thesis. ETH Zürich, 2018.

[26] P. Eckert. "The Mu3e Tile Detector". PhD thesis. Heidelberg University, 2015.

[27] M. Oinonen et al. "ALICE Silicon Strip Detector module assembly with single-point TAB interconnections". In: *Proceedings, eleventh Workshop on Electronics for LHC and Future Experiments, Heidelberg, Germany, 12-16 September 2005*. 2005, pp. 92–98. DOI: 10.5170/CERN-2005-011. URL: http://lhc-workshop-2005.web.cern.ch/lhc%2Dworkshop%2D2005/PlenarySessions/15-MOinonen.pdf.

[28] D. vom Bruch. “Pixel Sensor Evaluation and Online Event Selection for the Mu3e Experiment”. PhD thesis. Heidelberg University, 2017.

[29] H. Bethe and W. Heitler. “On the Stopping of Fast Particles and on the Creation of Positive Electrons”. In: *Proc. Roy. Soc.* A 146 (1934), p. 83.

[30] H. Bichsel. “A method to improve tracking and particle identification in TPCs and silicon detectors”. In: *Nucl. Instrum. Meth.* A562 (2006), pp. 154–197. DOI: 10.1016/j.nima.2006.03.009.

[31] S. M. Seltzer and M. J. Berger. “Improved Procedure for Calculating the Collision Stopping Power of Elements and Compounds for Electrons and Positrons”. In: *The International Journal of Applied Radiation and Isotopes* 35 (1984).

[32] Yung-Su Tsai. “Pair production and bremsstrahlung of charged leptons”. In: *Rev. Mod. Phys.* 46 (4 1974), pp. 815–851. DOI: 10.1103/RevModPhys.46.815.

[33] Handel Davies, H. A. Bethe, and L. C. Maximon. “Theory of Bremsstrahlung and Pair Production. II. Integral Cross Section for Pair Production”. In: *Phys. Rev.* 93 (4 1954), pp. 788–795. DOI: 10.1103/PhysRev.93.788.

[34] Virgil L. Highland. “Some Practical Remarks on Multiple Scattering”. In: *Nucl. Instrum. Meth.* 129 (1975), p. 497. DOI: 10.1016/0029-554X(75)90743-0.

[35] M.S. Lazo et al. “Silicon and Silicon dioxide neutron damage functions”. In: *Proceedings of the Fast Burst Reactor Workshop held in Albuquerque* (1986).

[36] G. Lindström, M. Moll, and E. Fretwurst. “Radiation hardness of silicon detectors – a challenge from high-energy physics”. In: *Nuclear Instruments and Methods in Physics Research Section A: Accelerators, Spectrometers, Detectors and Associated Equipment* 426.1 (1999), pp. 1 –15. DOI: https://doi.org/10.1016/S0168-9002(98)01462-4.

[37] *"EP - DT Irradiation Facilities", talk at the DD Section Meeting: https://indico.cern.ch/event/545592/contributions/2213686/attachments/1306077/1952192/2016_07_08_EP_DT_DD_Section_Meeting_Ravotti.pdf*. (Visited on 03/20/2017).

[38] N Wermes. *Teilchendetektoren*. 1st. Springer Spektrum, 2016.

[39] H. Augustin. “Charakterisierung von HV-MAPS”. Bachelor Thesis. Heidelberg University, 2012.

[40] A.-K. Perrevoort. “Characterisation of High Voltage Monolithic Active Pixel Sensors for the Mu3e Experiment”. Master Thesis. Heidelberg University, 2012.

[41] Spieler. H. *Semiconductor Detector Systems*. Oxford University Press, 2014.

[42] Ulrich Husemann. *A New Pixel Detetcor for the CMS Experiment*. Online, accessed 01-October-2018. 2012. URL: http://ekpwww.etp.kit.edu/~husemann/talks/husemann_cms_pixel_heidelberg_20120508.pdf.

[43] L. Greiner et al. "A MAPS based vertex detector for the STAR experiment at RHIC". In: *Nucl. Instr. Meth.* A 650 (2011). International Workshop on Semiconductor Pixel Detectors for Particles and Imaging 2010, pp. 68 –72. DOI: 10.1016/j.nima.2010.12.006.

[44] I. Perić. "A novel monolithic pixelated particle detector implemented in high-voltage CMOS technology". In: *Nucl.Instrum.Meth.* A582 (2007), p. 876. DOI: 10.1016/j.nima.2007.07.115.

[45] A. Herkert. PhD Thesis. Heidelberg University, in preparation.

[46] Gabriel Vidal-Álvarez, Eloi Marigó, Francesc Torres, and Núria Barniol. "Fabrication and Measurement of a Suspended Nanochannel Microbridge Resonator Monolithically Integrated with CMOS Readout Circuitry". In: *Micromachines* 7.3 (2016). DOI: 10.3390/mi7030040.

[47] J.C. Ashley. "Energy loss rate and inelastic mean free path of low-energy electrons and positrons in condensed matter". In: *Journal of Electron Spectroscopy and Related Phenomena* 50.2 (1990), pp. 323 – 334. DOI: https://doi.org/10.1016/0368-2048(90)87075-Y.

[48] *AMS AG, Tobelbader Strasse 30, 8141 Unterpremstaetten (Austria)*.

[49] N. Berger. *MUPIX7 Data Format*. Mu3e internal note 0010, Version 0.2. 2018.

[50] H. Augustin et al. "MuPix7 - A fast monolithic HV-CMOS pixel chip for Mu3e". In: *Journal of Instrumentation* 11.11 (2016), p. C11029. URL: http://stacks.iop.org/1748-0221/11/i=11/a=C11029.

[51] D. Immig. "Charakterisierung des VCO, der PLL und der Pulsform des MuPix7 in Abhängigkeit der Umgebungstemperatur". Bachelor Thesis. Heidelberg University, 2016.

[52] N. Berger. *MUPIX8 Data Format*. Mu3e internal note 0024, Version 0.2. 2018.

[53] S. Dittmeier. "Fast data acquisition for silicon tracking detectors at high rates". PhD thesis. Heidelberg University, 2018.

[54] J. Hammerich. "Analog Characterization and Time Resolution of a large scale HV-MAPS Prototype". Master thesis. Heidelberg University, 2018.

[55] H. Augustin. *Private Communication*.

[56] A Weber. "Design of a Pixel Sensor Chip for Particle Physics". Master thesis. Karlsruher Institut für Technologie, 2016.

[57] P.V.C. Hough. "Method and means for recognizing complex patterns". In: *Patent 3,069,654, Dec. 18, 1962* (Dec. 1962).

[58] Rudolph Emil Kalman. “A New Approach to Linear Filtering and Prediction Problems”. In: *Transactions of the ASME–Journal of Basic Engineering* 82.Series D (1960), pp. 35–45.

[59] Ardakani H. & Bridges T. J. *Review of the 3-2-1 EulerAngles: a yaw-pitch-roll sequence*. URL: http://personal.maths.surrey.ac.uk/st/T.Bridges/SLOSH/3-2-1-Eulerangles.pdf.

[60] R. Brun and F. Rademakers. “ROOT: An object oriented data analysis framework”. In: *Nucl. Instrum. Meth.* A389 (1997), pp. 81–86. DOI: 10.1016/S0168-9002(97)00048-X.

[61] C. Kleinwort. “General Broken Lines as advanced track fitting method”. In: *Nucl.Instrum.Meth.* A673 (2012), pp. 107–110. DOI: 10.1016/j.nima.2012.01.024. arXiv: 1201.4320 [physics.ins-det].

[62] M. Kiehn. “Pixel Sensor Evaluation and Track Fitting for the Mu3e Experiment”. PhD thesis. Heidelberg University, 2015.

[63] U. Hartenstein. “Track Based Alignment for the Mu3e Tracking Detector”. PhD thesis. Mainz University, in preperation.

[64] Eric W. Weisstein. *"Moiré Pattern." From MathWorld–A Wolfram Web Resource*. URL: http://mathworld.wolfram.com/MoirePattern.html.

[65] L. Huth. “Development of a Tracking Telescope for Low Momentum Particles and High Rates consisting of HV-MAPS”. Master thesis. Heidelberg University, 2014.

[66] H. Augustin et al. “The MuPix Telescope: A Thin, High-Rate Tracking Telescope”. In: *Journal of Instrumentation* 12.01 (2017), p. C01087. URL: http://stacks.iop.org/1748-0221/12/i=01/a=C01087.

[67] Intel. *Stratix IV - Features*. https://www.intel.com/content/dam/altera-www/global/en_US/pdfs/literature/pt/stratix-iv-product-table.pdf visited on 21.08.2018.

[68] J. Kroeger. “Readout Hardware for the MuPix8 Pixel Sensor Prototype and a Firmware-based MuPix8 Emulator”. Master Thesis. Heidelberg University, 2017.

[69] Dirk Wiedner et al. “Readout Electronics for the First Large HV-MAPS Chip for Mu3e”. In: *Proceedings of the Topical Workshop on Electronics for Particle Physics (TWEPP17)*. 2018, PoS TWEPP–17 099.

[70] C. Grzesik. “Fast Optical Readout for the Mu3e Experiment”. Bachelor thesis. Heidelberg University, 2014.

[71] *The qt4 library*. URL: https://www.qt.io.

[72] Boost. *Boost c++ libraries*. [Online; accessed 30-August-2018]. 2014. URL: http://www.boost.org/.

[73] N. Berger. *Personal communication*. 2018.

[74] H. Augustin. PhD thesis. Heidelberg University, in preperation.

[75] J. Philipp. “Efficienzanalyse von HV-MAPS anhand des MuPix-Teleskops”. Bachelor thesis. Heidelberg University, 2015.

[76] R. Schmidt S. Ritt. *MSCB (MIDAS Slow Control Bus)*. 2001. URL: http://midas.psi.ch/mscb.

[77] *Diener R, Meyners N, Potylitsina-Kube N, Stanitzki M (2018) Test Beams at DESY, Accessed 01 Aug 2018.* URL: http://testbeam.desy.de.

[78] Hendrik et al. Jansen. “Performance of the EUDET-type beam telescopes”. In: *EPJ Techniques and Instrumentation* 3.1 (2016), p. 7. DOI: 10.1140/epjti/s40485-016-0033-2.

[79] Baudot J, et al. “First test results of MIMOSA-26, a fast CMOS sensor with integrated zero suppression and digitized output”. In: *Nuclear Science Symposium Conference Record 2009, 1169–1173.. IEEE, Orlando. 10.1109/NSSMIC.2009.5402399.* (). DOI: 10.1109/NSSMIC.2009.5402399.

[80] *EUDAQ Software Developers (2016) EUDAQ Website. Accessed 01 Aug 2018.* URL: http://eudaq.github.io.

[81] S. Spannagel. “Test Beam Measurements for the Upgrade of the CMS Pixel Detector and Measurement of the Top Quark Mass from Differential Cross Sections”. PhD thesis. Hamburg University, 2016.

[82] V. Blobel. “Software alignment for tracking detectors”. In: *Nucl. Instrum. Meth.* A566 (2006), pp. 5–13. DOI: 10.1016/j.nima.2006.05.157.

[83] H. Herminghaus, A. Feder, K. H. Kaiser, W. Manz, and H. Von Der Schmitt. “The Design of a Cascaded 800-MeV Normal Conducting CW Racetrack Microtron”. In: *Nucl. Instrum. Meth.* 138 (1976), pp. 1–12. DOI: 10.1016/0029-554X(76)90145-2.

[84] K. H. Kaiser et al. “The 1.5-GeV harmonic double-sided microtron at Mainz University”. In: *Nucl. Instrum. Meth.* A593 (2008), pp. 159–170. DOI: 10.1016/j.nima.2008.05.018.

[85] H. Augustin. “Characterization of a novel HV-MAPS Sensor with two Amplification Stages and first examination of thinned MuPix Sensors”. Master Thesis. Heidelberg University, 2014.

[86] R. Hagdorn. “Performance Optimization of the MuPix7 Sensor Prototype”. Master thesis. Heidelberg University, 2015.

[87] K. Simmoteit. “Development of an X-Ray based Energy Calibration Method for High Voltage Monolithic Active Pixel Sensors”. Bachelor thesis. Heidelberg University, 2015.

[88] Augustin H. et al. “Efficiency and timing performance of the MuPix7 high-voltage monolithic active pixel sensor”. In: *Nuclear Instruments and Methods in Physics Research Section A: Accelerators, Spectrometers, Detectors and Associated Equipment* 902 (2018), pp. 158 –163. DOI: 10.1016/j.nima.2018.06.049.

[89] D. Immig. Master Thesis. Heidelberg University, in preparation.

[90] *Iron-55 on wikipedia*. Online - accessed 10.10.2018. URL: https://en.wikipedia.org/wiki/Iron-55.

[91] *Sr-90 on wikipedia*. Online - accessed 10.10.2018. URL: https://en.wikipedia.org/wiki/Strontium-90.

[92] I. Perić. *Private Communication*.

[93] G. Kramberger, V. Cindro, I. Mandic, M. Mikuz, M. Milovanovic, M. Zavrtanik, and K. Zagar. "Investigation of Irradiated Silicon Detectors by Edge-TCT". In: *IEEE Transactions on Nuclear Science* 57.4 (2010), pp. 2294–2302. DOI: 10.1109/TNS.2010.2051957.

[94] S. Terzo. "The Phase-II ATLAS ITk pixel upgrade". In: *Journal of Instrumentation* 12.07 (2017), p. C07023. URL: http://stacks.iop.org/1748-0221/12/i=07/a=C07023.

[95] H. Augustin et. al. "Irradiation study of a fully monolithic HV-CMOS pixel sensor design in AMS 180 nm". In: *Nuclear Instruments and Methods in Physics Research Section A: Accelerators, Spectrometers, Detectors and Associated Equipment* 905 (2018), pp. 53 –60. DOI: 10.1016/j.nima.2018.07.044.

[96] *Labfacility Pt1000: Data sheet (online, accessed 2017-05-30, http://www.farnell.com/datasheets/1918818.pdf?_ga=2.73347419.911411872.1496222551-845443501.1496222551)*.

[97] M. Fernández García, C. Gallrapp, M. Moll, and D. Muenstermann. "Radiation hardness studies of neutron irradiated CMOS sensors fabricated in the ams H18 high voltage process". In: *Journal of Instrumentation* 11.02 (2016), P02016. URL: http://stacks.iop.org/1748-0221/11/i=02/a=P02016.

[98] Affolder et al. "Charge collection studies in irradiated HV-CMOS particle detectors". In: *Journal of Instrumentation* 11.04 (2016), P04007. URL: http://stacks.iop.org/1748-0221/11/i=04/a=P04007.

DANKSAGUNG

Die letzte Seite dieser Arbeit widme ich allen die mich auf der Reise durch mein Studium und bei meiner Doktorarbeit unterstützt haben.
Bei meinem Doktorvater André Schöning bedanke ich mich herzlichst für die Möglichkeit zur Bearbeitung dieses Themas, sowie der exzellenten Betreuung mit unzähligen Diskussionen und Anregungen die grundlegend zum Erfolg dieser Arbeit beigetragen haben.
Norbert Herrmann gilt mein Dank für die freundliche Bereitschaft das Zweitgutachten für meine Arbeit zu übernehmen.
Vielen Dank an die gesamte Mu3e-Arbeitsgruppe für die gute allgemeine Stimmung, gegenseitige Rückendeckung und natürlich die essentiellen Daten die in den letzten Monaten meiner Doktorarbeit gesammelt wurden.
Ein ganz dickes Dankeschön geht an meine langjährigen Doktorandenkollegen Heiko Augustin, Sebastian Dittmeier, Adrian Herkert, Ann-Kathrin Perrevoort und Dorothea vom Bruch. Die intensive Zusammenarbeit mit euch hat wesentlich zum Gelingen dieser Arbeit beigetragen und die Gespräche mit euch, sowohl die fachlichen als auch die unterhaltsamen, werde ich nie vergessen. Ihr seid für mich mehr als nur Arbeitskollegen!
Mein Dank gilt Nik Berger, der immer einen guten Rat zu allen Lebenslagen zur Hand hatte und von dem ich sehr viel über Soft- und Firmware gelernt habe.
Ich bedanke mich bei Dirk Wiedner für die Unterstützung in Hardware-Belangen und Anregungen bei Fragen.
Jan Hammerich gilt mein Dank für die fruchtbare Zusammenarbeit bei Sensor Charakterisierung.
Eine Doktorarbeit ohne Korrekturleser wäre vermutlich unlesbar – daher gilt mein Dank allen die mich lesend unterstützt haben: Heiko Augustin, Nik Berger, Sebastian Dittmeier, Jan Hammerich, Adrian Herkert, David Immig, Ann-Kathrin Perrevoort, Dorothea vom Bruch und Dirk Wiedner.
Bei allen Mitgliedern der Werkstatt des Physikalischen Instituts, insbesondere Rudi Hotz, möchte ich mich dafür bedanken, dass alle meine Ideen, und wenn sie noch so grob auf einem Zettel verfasst waren, schnell, zuverlässig und gut umgesetzt wurden.
Ein langes Studium ohne Unterstützung der Familie ist nur schwer vorstellbar. Daher möchte ich mich herzlich bei meinen Eltern und meinem Bruder bedanken, die immer ein offenes Ohr für mich und meine Probleme hatten und mich gelegentlich wieder in die Realität zurück geholt haben.
Am Ende möchte ich mich noch bei Katahrina Alter bedanken, die mich über mein ganzes Studium unterstützt hat, mir insbesondere in der letzten Schreibphase den kompletten Alltag abgenommen hat und sich dazu entschieden hat gemeinsam mit mir nach Hamburg zu ziehen. Vielen Herzlichen Dank für alles, du bist großartig!